การกำจัดการกระจายตามความถี่อันดับที่สามและความไม่เสถียรของไซด์แบนด์ในระบบสื่อสัญญาณผ่านเส้นใยแสงความเร็วสูงยิ่งระยะไกลยิ่งที่ใช้การสังยุคเฟสแสงตรงจุดกึ่งกลาง

นาย พสุ แก้วปลั่ง

วิทยานิพนธ์นี้เป็นส่วนหนึ่งของการศึกษาตามหลักสูตรปริญญาวิศวกรรมศาสตรดุษฎีบัณฑิต
สาขาวิชาวิศวกรรมไฟฟ้า ภาควิชาวิศวกรรมไฟฟ้า
คณะวิศวกรรมศาสตร์ จุฬาลงกรณ์มหาวิทยาลัย
ปีการศึกษา 2546
ISBN 974-17-3957-5

SUPPRESSION OF THIRD-ORDER DISPERSION AND SIDEBAND INSTABILITY IN ULTRA-LONG-HAUL ULTRA-HIGH-SPEED OPTICAL FIBER TRANSMISSION USING MIDWAY OPTICAL PHASE CONJUGATION

Mr. Pasu Kaewplung

A Dissertation Submitted in Partial Fulfillment of the Requirements
for the Degree of Doctor of Philosophy in Electrical Engineering

Department of Electrical Engineering
Faculty of Engineering
Chulalongkorn University

Academic year 2003
ISBN 974-17-3957-5

Thesis Title	Suppression of Third-Order Dispersion and Sideband Instability in Ultra-Long-Haul Ultra-High-Speed Optical Fiber Transmission Using Midway Optical Phase Conjugation
By	Mr. Pasu Kaewplung
Field of Study	Electrical Engineering
Thesis Advisor	Assistant Professor Dr. Tuptim Angkaew
Thesis Co-advisor	Professor Dr. Kazuro Kikuchi

Accepted by the Faculty of Engineering, Chulalongkorn University in Partial Fulfillment of the Requirements for the Doctor's Degree

…….. Dean of Faculty of Engineering
(Professor Dr. Somsak Panyakaew)

THESIS COMMITTEE

…….. Chairman
(Professor Dr. Prasit Prapinmongkolkarn)

……. Thesis Advisor
(Assistant Professor Dr. Tuptim Angkaew)

…….. Thesis Co-advisor
(Professor Dr. Kazuro Kikuchi)

…….. Member
(Associate Professor Dr. Somchai Jitapunkul)

…….. Member
(Associate Professor Dr. Watit Benjapolakul)

…….. Member
(Associate Professor Dr. Athikom Roeksabutr)

พสุ แก้วปลั่ง: การกำจัดการกระจายตามความถี่อันดับที่สามและความไม่เสถียรของไซด์แบนด์ในระบบสื่อสัญญาณผ่านเส้นใยแสงความเร็วสูงยิ่งระยะไกลยิ่งที่ใช้การสังยุคเฟสแสงตรงจุดกึ่งกลาง (Suppression of Third-Order Dispersion and Sideband Instability in Ultra-Long-Haul Ultra-High-Speed Optical Fiber Transmission Using Midway Optical Phase Conjugation) อ.ที่ปรึกษา: ผู้ช่วยศาสตราจารย์ ดร. ทับทิม อ่างแก้ว, อ.ที่ปรึกษาร่วม: Professor Dr. Kazuro Kikuchi, ๑๘๘ หน้า, ISBN 974-17-3957 -5.

วิทยานิพนธ์ฉบับนี้รายงานผลการศึกษาการเพิ่มสมรรถนะของระบบสื่อสัญญาณผ่านเส้นใยแสงซึ่งใช้การสังยุคเฟสแสง (OPC) ตรงจุดกึ่งกลางโดยการกำจัดการกระจายตามความถี่อันดับที่สามและความไม่เสถียรของไซด์แบนด์ สำหรับการชดเชยการกระจายตามความถี่อันดับที่สามนั้น เราได้แสดงว่าการสะสมของการกระจายตามความถี่อันดับที่สามในระบบ OPC นั้นค่อนข้างเป็นแบบเชิงเส้น เราได้สาธิตความเป็นไปได้ในการสื่อสัญญาณความเร็ว ๑๐๐ กิกะบิตต่อวินาทีในระยะทางกว่า ๑๐,๐๐๐ กิโลเมตรโดยใช้เพียงแค่การชดเชยการกระจายตามความถี่อันดับที่สามเท่านั้น สำหรับการกำจัดความไม่เสถียรของไซด์แบนด์นั้น เรานำเสนอทฤษฎีการวิเคราะห์ความไม่เสถียรของไซด์แบนด์ที่สมบูรณ์ที่สุดในกรณีที่นำเส้นใยแสงสองเส้นที่มีคุณสมบัติต่างกันมาต่อกันเพื่อจัดการการกระจายตามความถี่ ผลจากการวิเคราะห์พบว่าขนาดอัตราการขยายของความไม่เสถียรของไซด์แบนด์ลดลงเมื่อเพิ่มค่าการกระจายตามความถี่อันดับที่สองของส้นใยแสงที่นำมาจัดการการกระจายตามความถี่

เนื่องจากการจัดการการกระจายตามความถี่โดยใช้เส้นใยแสงแบบแผนคลื่นเดียว (SMF) กับเส้นใยแสงแบบกลับการกระจายตามความถี่ (RDF) ซึ่งทั้งคู่มีค่าการกระจายตามความถี่อันดับที่สองที่สูงนั้น สามารถใช้กำจัดการกระจายตามความถี่อันดับที่สองและสามในเวลาเดียวกันได้ เราจึงนำคู่ของ SMF และ RDF นี้มาใช้ในระบบ OPC เพื่อกำจัดทั้งการกระจายตามความถี่อันดับที่สามและความไม่เสถียรของไซด์แบนด์ในเวลาเดียวกัน จากการคำนวณด้วยวิธีเชิงเลขพบว่าระบบที่ใช้วิธีที่นำเสนอนี้สามารถส่งสัญญาณความเร็วสูงถึง ๒๐๐ กิกะบิตต่อวินาทีในระยะทางกว่า ๑๐,๐๐๐ กิโลเมตรได้เมื่อค่าความถี่ของการจัดการการกระจายตามความถี่และค่ากำลังของสัญญาณได้รับการเลือกให้อยู่ในค่าที่เหมาะสม

สำหรับการกำจัดความไม่เสถียรของไซด์แบนด์ เราเสนอการใช้การขยายสัญญาณแสงแบบแจกแจงผ่านปรากฏการณ์รามาน (DRA) เพื่อสร้างการแจกแจงของกำลังสัญญาณแบบกลับด้านในช่วงครึ่งที่สองของระบบ OPC ซึ่งจะทำให้เกิดการแจกแจงของกำลังสัญญาณที่สมมาตรทั้งระบบเมื่อเทียบกับจุดกึ่งกลาง จากการคำนวณด้วยวิธีเชิงเลขพบว่าสามารถสื่อสัญญาณความเร็ว ๒๐๐ กิกะบิตต่อวินาทีในระยะทางกว่า ๑๐,๐๐๐ กิโลเมตรได้เช่นกัน

ในการคำนวณสัญญาณพัลส์ที่เดินทางในเส้นใยแสง เราได้พัฒนาวิธีหลายวิธีจากวิธีไฟไนต์ดิฟเฟอเรนซ์เชิงเวลา (FDTD) ผลของการคำนวณด้วยวิธีที่พัฒนาขึ้นมาใหม่ถูกนำมาเปรียบเทียบกับวิธี split-step Fourier ซึ่งเป็นที่นิยมใช้กันทั่วไปในการคำนวณสัญญาณที่เดินทางในเส้นใยแก้วนำแสง เราพบว่าวิธี FDTD ต่างๆ ที่ได้พัฒนาขึ้นมานั้นแสดงความเป็นไปได้ที่จะนำมาใช้คำนวณสัญญาณเดินทางในเส้นใยแสงได้ไกลหลายสิบกิโลเมตรภายใต้ความผิดพลาดที่ยังยอมรับได้

ภาควิชา วิศวกรรมไฟฟ้า ลายมือชื่อนิสิต.....

สาขาวิชา วิศวกรรมไฟฟ้า ลายมือชื่ออาจารย์ที่ปรึกษา.....

ปีการศึกษา ๒๕๔๖ ลายมือชื่ออาจารย์ที่ปรึกษาร่วม.....

4471819921 : MAJOR: ELECTRICAL ENGINEERING
KEY WORDS: OPTICAL FIBER COMMUNICATION / OPTICAL AMPLIFICATION / DISPERSION COMPENSATION / NONLINEAR FIBER-OPTICS / NUMERICAL SIMULATION

PASU KAEWPLUNG : THESIS TITLE (SUPPRESSION OF THIRD-ORDER DISPERSION AND SIDEBAND INSTABILITY IN ULTRA-LONG-HAUL ULTRA-HIGH-SPEED OPTICAL FIBER TRANSMISSION USING MIDWAY OPTICAL PHASE CONJUGATION) THESIS ADVISOR: ASSISTANT PROFESSOR DR. TUPTIM ANGKAEW, THESIS CO-ADVISOR: PROFESSOR DR. KAZURO KIKUCHI, 189 pp. ISBN 974-17-3957 -5.

In this dissertation, the performance improvement of the optical phase conjugation (OPC) systems by suppressing the third-order dispersion (TOD) and the sideband instability (SI) is studied. For the TOD compensation, we predict that the accumulation of TOD in OPC systems is almost linear. We demonstrate the possibility of a 100-Gbit/s data transmission over 10,000 km by only performing the TOD compensation. For the SI suppression, we derive the complete theoretical analysis of the SI that occurs when two fibers with different characteristics are concatenated to form a dispersion-managed fiber link. We find that the magnitude of the SI gain reduces with the increase in the strength of dispersion management.

Since the strong dispersion management link using the combination of a standard single-mode fiber (SMF) and a reverse dispersion fiber (RDF) can realize the simultaneous compensation of the second-order dispersion (SOD) and the TOD, we employ this combination of SMF and RDF to simultaneously suppress both TOD and SI in OPC systems. By computer simulation, we demonstrate the possibility of a 200-Gbit/s data transmission over 10,000 km by only optimizing the dispersion map and the input signal power.

For alternative method for compensation of SI, we propose the use of distributed Raman amplification (DRA) to construct a reverse power distribution in the second half of OPC systems, in order to form the entirely symmetrical distribution of signal power with respect to the system midpoint. The result of our simulation also shows that the 200-Gbit/s data can successfully transmit over 10,000 km.

For computing pulse propagation in optical fiber, we develop several algorithms based on the finite-difference time-domain (FDTD) method. The results of the simulations are compared with the results obtained from the split-step Fourier method (SSFM), which is the common method used for calculating signal propagation in optical fibers. Our developed FDTD algorithms show a possibility of the calculation over several ten kilometers with acceptable accuracy.

Department	Electrical Engineering	Student's signature……..
Field of study	Electrical Engineering	Advisor's signature…….
Academic year	2003	Co-advisor's signature…….

ACKNOWLEDGEMENTS

At first, I wish to express my utmost gratitude to Assistant Professor Dr. Tuptim Angkaew and Professor Dr. Kazuro Kikuchi, my research advisors for providing me fruitful advice together with valuable discussion. Without their professional guidance and continuous encouragement throughout the course of present study, this work can hardly be completed.

I am very thankful to Professor Dr. Prasit Prapinmongkolkarn, Associate Professor Dr. Somchai Jitapunkul, Associate Professor Dr. Watit Benjapolakul, and Associate Professor Dr. Athikom Roeksabutr for their reviews and comments on this dissertation.

To my family, I could have never achieved this goal without inspiration and financial support from my parents and my sister.

Finally, I would like to give a special thank with all of my heart to my beloved persons for their forbearance and encouragement, my wife, Dr. Orapin Kaewplung and my daughter, Miss Alisara Kaewplung.

TABLE OF CONTENTS

Page

TABLE OF CONTENTS (Continued)

Page

TABLE OF CONTENTS (Continued)

Page

TABLE OF CONTENTS (Continued)

Page

LIST OF TABLES

LIST OF FIGURES

Figure Page

LIST OF FIGURES (Continued)

Figure Page

LIST OF FIGURES (Continued)

Figure Page

LIST OF FIGURES (Continued)

Figure Page

LIST OF FIGURES (Continued)

Figure Page

LIST OF FIGURES (Continued)

Figure Page

LIST OF FIGURES (Continued)

Figure Page

LIST OF FIGURES (Continued)

Figure Page

LIST OF FIGURES (Continued)

LIST OF FIGURES (Continued)

Figure Page

LIST OF FIGURES (Continued)

Figure Page

LIST OF FIGURES (Continued)

Figure Page

ABBREVIATION LIST

ASE – Amplified Spontaneous Emission Noise

BER – Bit-Error Rate

BPF – Band-Pass Filter

CN – Crank-Nicholson

CW – Continuous Wave

DDF – Dispersion-Decreasing Fiber

DM – Dispersion Management

DRA – Distributed Raman Amplification

DSCF – Dispersion Slope Compensating Fiber

DSF – Dispersion-Shifted Fiber

DWDM – Dense Wavelength Division Multiplexing

EDFA – Erbium-Doped Fiber Amplifier

FFT – Fast Fourier Transform

FRA – Fiber Raman Amplifiers

FDTD – Finite-Difference Time-Domain

FWHM – Full-Width-Half-Maximum

FWM – Four-Wave Mixing

Gb/s – Giga-Bit per Second

GHz – Giga-Hertz

GVD – Group-Velocity Dispersion

$i = \sqrt{-1}$

km – Kilometer

LPF – Low-Pass Filter

MI – Modulation Instability

mW – Milli-Watt

NLSE - Nonlinear Schrodinger Equation

NRZ – Non-Return-to-Zero

OBPF – Optical Band-Pass Filter

OPC – Optical Phase Conjugation

OSNR – Optical Signal-to-Noise Ratio

OTDM – Optical Time Division Multiplexing

ABBREVIATION LIST (Continued)

PMD – Polarization Mode Dispersion

ps – Pico-Second

RDF – Reverse Dispersion Fiber

RK4 – Fourth-Order Runge-Kutta

RZ – Return-to-Zero

SBS – Stimulated Brillouin Scattering

SI – Sideband Instability

SMF – Standard Single-Mode Fiber

SNR – Signal-to-Noise Ratio

SOD – Second-Order Dispersion

SPM – Self Phase Modulation

SRS – Stimulated Raman Scattering

SSFM – Split-Step Fourier Method

THz – Tera-Hertz

TOD – Third-Order Dispersion

Tb/s – Tera-Bit per Second

W - Watt

WDM – Wavelength Division Multiplexing

XPM – Cross Phase Modulation

CHAPTER 1
INTRODUCTION

1.1 General Background

Rapid growth of demand on both transmission data rate and distance in this decade for supporting the multimedia information is very remarkable. The promising system which has a potential to respond such demand is the optical fiber transmission system. However, at present, most of the installed long-haul fiber systems still operate with electronic repeaters at very low bit rate. During the propagation in the transmission fiber, the peak power of the optical signal decreases due to the fiber loss, as well as the signal waveform becomes distorted due to the fiber characteristics such as the fiber second-order dispersion (SOD) and the fiber nonlinearity [1]-[10]. The SOD causes the signal pulse broadening while the fiber nonlinearity results in signal spectra broadening during signal transmission in the fiber [3]-[5]. The interaction of SOD and nonlinearity will cause more severe distortion of both pulse and spectra [4]-[10].

Figure 1.1 shows the configuration of the electronic repeater [2]. In electronic-repeated scheme, after launching to the repeater, such distorted optical signal is converted to electrical signal. The distortion is removed out of signal by mean of electronic signal processing, and then is converted back to optical signal again. By this scheme, the capacity of system is limited by speed of the electronic circuit, which is well known as “electronic bottle neck”, at the speed of around 40 GHz or at the bit rate of 40 Gbit/s [4], [5], [11]. Therefore, to operate the system with bit rate higher than 40 Gbit/s, all optically signal-processed repeater, which uses light processes light, is necessary.

The invention of the Erbium-doped fiber optical amplifier (EDFA) [4], [5], [12]-[15] has significantly opened the possibility of the data transmission at the bit rate higher than 40 Gbit/s. EDFA has many beneficial properties [4], such as polarization independent gain, slow recovery time which prevents the pattern effect, low insertion loss and high saturation output power. The most important thing may be the fact that EDFA is operating in the 1550 nm region where the optical fibers exhibit minimum loss. Moreover, the gain bandwidth of EDFA is sufficiently wide enough so that it realizes a possibility of amplifying the ultra high bit rate signal up to over Tbit/s and a large number of WDM signals. EDFA can also serve as excellent receiver pre-amplifiers, as they can provide very nearly the theoretical quantum-

limited 3-dB noise figure [4]. This is because EDFA can be coupled very efficiently to the single-mode fibers with insertion loss of about 0.1dB, and almost full population inversion can be achieved.

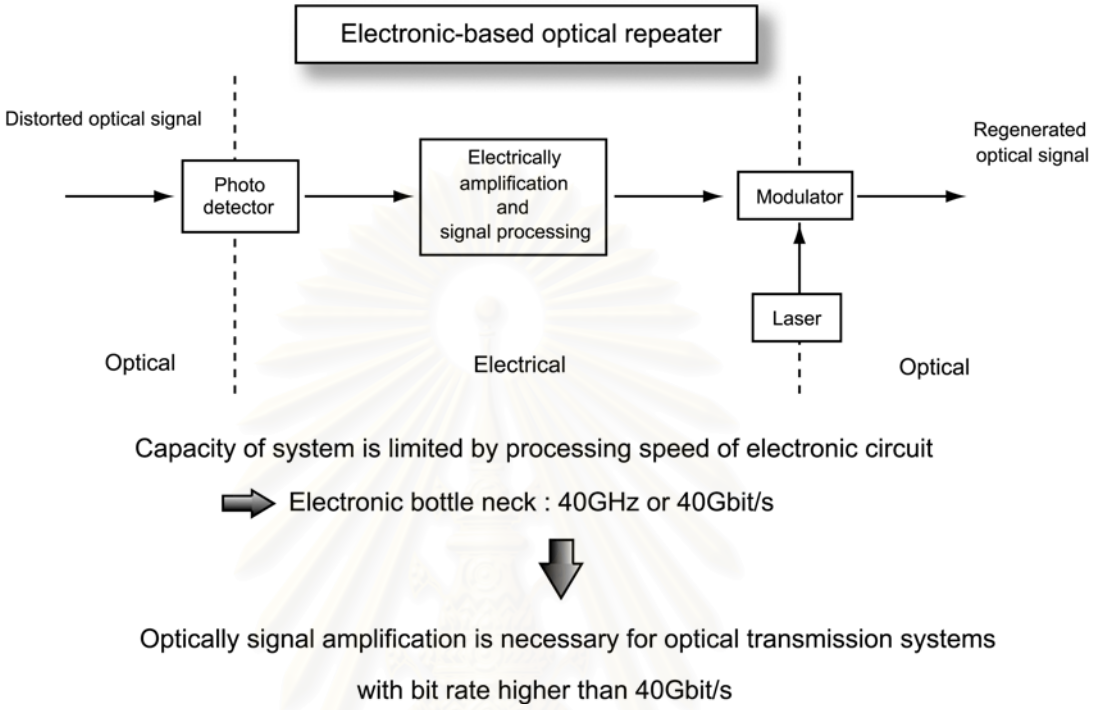

Figure 1.1: Configuration of electronic repeater.

Figure 1.2 shows the configuration of the EDFA, which is commonly used in optically amplified systems. High output power semiconductor laser diode with operating wavelength 1480 nm or 980 nm is used for stimulating the Stimulated Brillouin scattering effect to occur inside the Er^{3+}-doped optical fiber for coherently amplifying 1550 nm signal input into the fiber. Usually, the EDFA is equipped with two optical isolators. The first is placed at the input in order to eliminate possible disturbances caused by the backward traveling amplified spontaneous emission (ASE) on the upstream span, while the second, at the output, protects the device against possible back reflections from the downstream line. The signal is launched into the active fiber together with the pump radiation through a wavelength division multiplexer (WDM) coupler which minimizes the power losses of both input beams.

The gain bandwidth of EDFA ranges approximately from 1520 nm to 1570 nm so that it is well tuned with the system operating at wavelength near 1550 nm region.

Typical values for the small-signal gain are 30-40dB for pump powers of 50-100 mW. Output powers range from +13dBm up to +20dBm, while the noise is generally very close to the minimum theoretical limit which can be derived from the fundamental laws of physics such as Heisenberg's Uncertainty principle.

However, the EDFA can only amplify the optical signal. Unlike the electronic repeater, the waveform distortion induced from SOD and fiber nonlinearity can not be removed from the signal at the output of EDFA. Therefore, in order to upgrade the electronic-repeated to the optically amplified system, the signal distortion induced from the SOD and nonlinearity must be seriously taken into account.

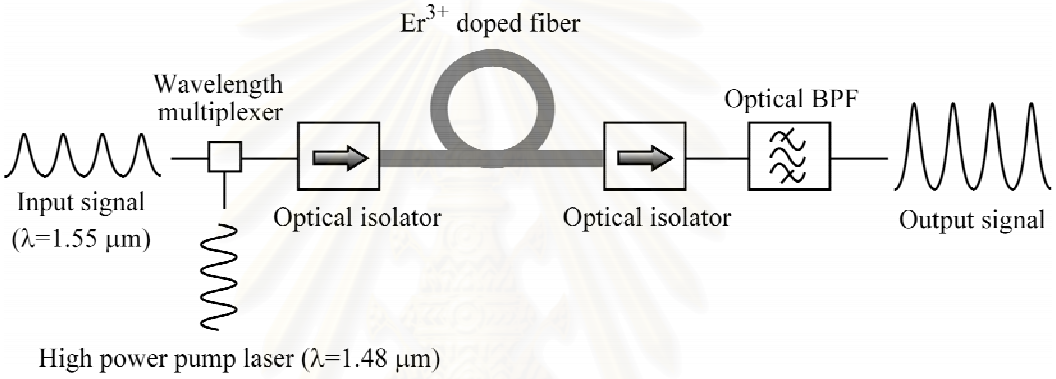

Figure 1.2: Configuration of EDFA.

There are many transmission methods have been proposed in order to overcome the SOD. The zero-dispersion wavelength transmission [16]-[20] is to set an operation wavelength of the system at zero-dispersion point so that the pulses can propagate without broadening. The SOD management [21]-[35] is to arrange the various sections of fiber in such a way that none or only very few of them have zero SOD wavelengths that coincide with the carrier wavelength while the total fiber exhibits zero SOD on average. The optical soliton [36]-[47] is to create the signal pulses that can propagate in optical fiber without broadening by balancing the SOD and the nonlinear self-phase modulation (SPM) effect in anomalous dispersion region [4], [5], [36]. Quantitatively, this can be achieved by launching optical pulses with proper input power and width into the fiber. The midway optical phase conjugation [48]-[52] is to perform the optical phase conjugation (OPC) at the midpoint of system in order to achieve the perfect compensation of both SOD and nonlinear effects if the

condition that all of the system characteristics are symmetric with respect to the midway OPC.

Although the SOD is completely compensated, when the ultra-high-bit-rate data is transmitted through an optical fiber, the third-order dispersion (TOD) shows up and influences transmission characteristics. Moreover, the TOD interplays with the SPM, causing severe distortion of both signal waveform and signal spectrum [4].

In the dispersion-managed system where the SOD map is properly designed but the TOD is not compensated, the bit rate of the 10,000-km transmission system is limited only about 10Gbit/s because of the interplay of the TOD with the SPM. It has been shown, by numerical simulations, that when TOD is compensated periodically at the interval quite shorter than the nonlinear scale of the system, the speed limit is possibly raised up over 20Gbit/s [25].

On the other hand, in soliton systems, a recent numerical study shows that the eigen solution to solitons can exist in the transmission line with TOD, and that is stable against the perturbation of TOD [53]. Even without TOD compensation, 40Gbit/s, 10,000km transmission has been actually demonstrated by using DM solitons [54].

For further expansion both in capacity and distance, dispersion management to eliminate both SOD and TOD will be one of the key issues. For this purpose, several TOD compensators have been proposed and demonstrated such as chirped fiber grating [55], [56], all-pass optical filter [57] and also special dispersion compensating fibers called the reverse dispersion fiber (RDF) [58]-[60]. Among these devices, the RDF seems to be more practical and attractive than others. Figure 1.3 shows schematically the dispersion characteristics of the RDF and the SMF. Since the RDF exhibits low negative TOD with large negative SOD value, therefore, by the combination with conventional single-mode fiber (SMF) in each span, the dispersion flattened fiber link with low average dispersion for simultaneously compensating both SOD and TOD is achieved. The combination of SMF and RDF can be applied for both OTDM and WDM transmission schemes as shown in Fig. 1.3(a) and (b) respectively. Several recent OTDM transmission experiments have demonstrated very attractive results of this SMF+RDF combination based systems such as the transmission of 640 Gbit/s over 92km [61] and even the data rate as high as 1.28 Tbit/s over 70 km [62]. In the other hand, the success of 320 Gbit/s over 200km transmission using SMF combined with DSCF has been reported [63]. Following by

a numerical simulation, the possibility of 320 Gbit/s soliton transmission over 6,000 km employing short period SOD and TOD management has been shown [64].

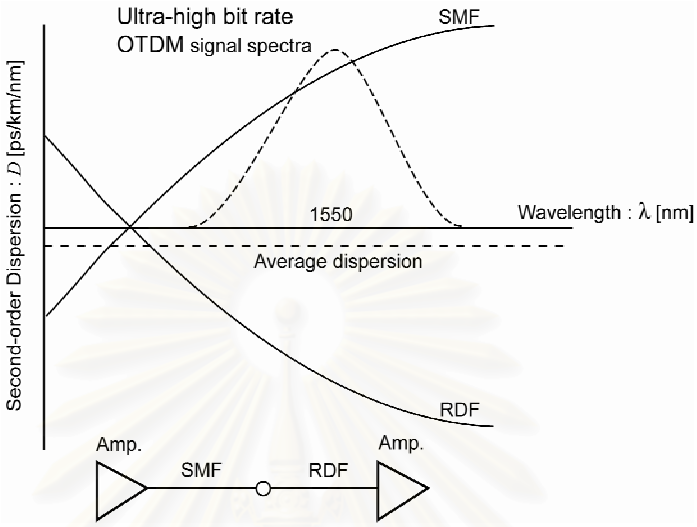

(a)

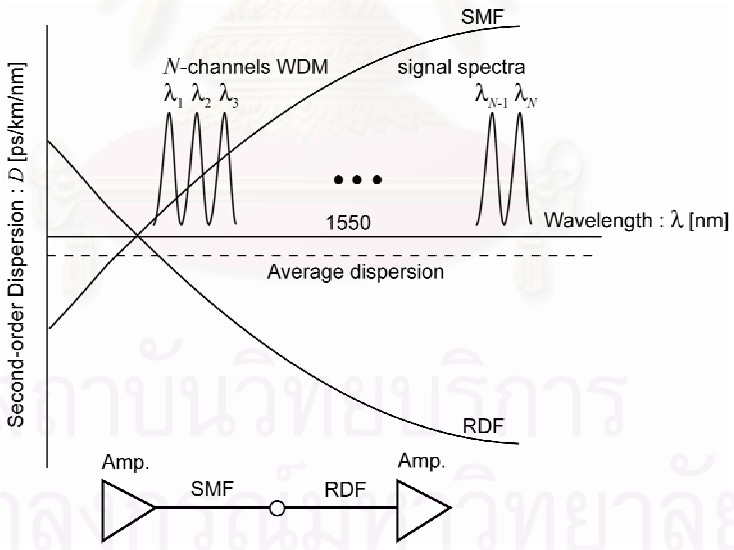

(b)

Figure 1.3: Dispersion characteristics of SMF and RDF for using in (a) OTDM scheme and (b) WDM scheme.

As an alternative approach for ultrahigh-bit-rate long-haul transmission, midway optical phase conjugation (OPC) is an attractive solution to compensating for the distortion induced from the interplay between the SOD and the SPM [65]. Several recent works have reported the broadband, wavelength-shift-free, and polarization-independent optical phase conjugators [66], [67]. This intensively may bring the OPC systems into a commercial world. However, the ultimate performance of OPC systems is also limited by TOD together with a nonlinear resonance at well-defined signal sideband frequencies induced by periodic amplification process called sideband instability (SI) effect [68].

Propagation of slowly varying envelope optical signal in optical fibers is governed by the well-known partial differential equation called nonlinear Schrodinger equation (NLSE) [4]. Since the NLSE does not have an analytic solution, the use of numerical method is necessary. The most commonly used numerical algorithm for solving the NLSE is the split-step Fourier method (SSFM) [4], in which the fiber is divided into small sections with a length called the step size. Each section exhibits only the dispersive or nonlinear effects, which act on the propagating signal separately. The accuracy of the SSFM solution increases with the reduction of the step size.

Although the SSFM has become the standard method for analyzing almost all problems of signal propagating in optical fibers, in order to obtain the NLSE, several approximations are applied to Maxwell's equations, and also, the SSFM consumes a lot of computation time. Moreover, it is quite inconvenient for those who are not good at computer programming, and also who only aim to study simple problems and want to know the approximate solutions immediately. This is because it is very complicated and tough to implement the SSFM algorithm into computational program. It can take more than a week to develop several hundred lines of a simulation program based on SSFM algorithm and then validating it before it starts to work properly.

As an alternative method for studying optical field propagation, the finite-difference time-domain (FDTD) method [69] has been widely used for analyzing and designing several structures of short-scale optical waveguides and devices [70], [71]. Since the FDTD algorithm is much easier and simpler for implementing than the SSFM, by using the FDTD, it is possible to develop the calculation program that consumes not more than 20 lines in only an hour. The basic principle of FDTD is to

discretize both time and space into small cells and then applying the central difference approximations for both temporal and spatial derivatives. Recently, 12fs ultra-broadband optical pulse propagation in optical fiber is also studied using the FDTD for directly solving Maxwell's equations [72]. Nevertheless, the algorithm used in this previous work cannot be applied to the propagation of slowly varying envelope optical pulse in relatively long fibers due to the accumulation of the truncation error caused by the sampling width of transmission distance.

1.2 Purpose of This Study

The aim of this study is to improve the performance of midway OPC transmission systems by proposing and evaluating practical schemes to suppress two main problems, TOD and SI, which limit the transmission performance of the systems. Two methods are proposed in this thesis for overcoming these two problems in OPC system. First is the use of the combination of SMF and RDF in OPC system in order to achieve the simultaneous suppression of both TOD and SI. Second is the suppression of both TOD and SI by using a lump TOD compensator and the distributed Raman amplification (DRA) to construct the reverse power distribution in the second-half of OPC system to obtain the entirely symmetrical power distribution with respect to the system midpoint. Moreover, we will propose the optimum system design theories for achieving maximum system performance for each proposed scheme.

Furthermore, in this study, the numerical method based on the SSFM will be mainly used to prove our derived theory and to evaluate our designed systems. However, for the sake of simplicity, this study also aims to develop numerical analysis algorithms based on the FDTD method for calculating signal propagation in optical fiber and to perform a comparison among them.

1.3 Study Methods and Plans

The research will start with studying the accumulation characteristic of TOD in OPC systems and finding the most suitable scheme to compensate it. Next, we consider two possible ways to eliminate the SI. First is the use of periodic perturbation to perturb the Fourier components of the virtual grating constructed by periodic power variation. The periodic perturbation will modulate the magnitudes of those

components which results the desirable decrease of SI gain. Second is the use of distributed gain such as Raman amplifier in the second half of the system to form the desirable symmetrical signal power distribution with respect to the midway OPC.

According to the above research plan, the research methods of this work are mainly based on the derivation of analytical theories, and then evaluating their possibilities and accuracies by the method of computer numerical simulations.

The study plan can be divided into 16 steps.

1) Studying on the TOD accumulation characteristic and the most suitable TOD compensating scheme in OPC systems. Then, proposing the optimum system design strategies to achieve maximum performance and confirming the performance improvement of the systems when the TOD is compensated.
2) Summarizing the results, presenting the work in international conferences or publishing the work in periodical journal.
3) Proposing the simultaneous suppression of TOD and SI by higher-order dispersion compensating fiber link composed of SMF and RDF. Deriving the complete mathematical expression of SI gain concerning periodic dispersion management fiber link when two different fibers are connected together. Verifying the derived theory with the computer simulations. Confirming the possibility of reducing SI gain with the fiber link consisted by SMF and RDF.
4) Summarizing the results, presenting the work in international conferences or publishing the work in periodical journal.
5) Proposing and studying the implementation of the dispersion management using SMF and RDF on OPC systems in terms of possible installing profiles. Theoretically making the comparison the advantages and disadvantages among the proposed schemes. Finding out the most suitable scheme.
6) Using the computer simulation to confirm the performance improvement of higher-order dispersion-managed OPC system by the simultaneous suppression of both TOD and SI.
7) Summarizing the results, presenting the work in international conferences or publishing the work in periodical journal
8) Theoretically finding the optimum higher-order dispersion-managed OPC system design strategies in terms of designing system operating parameters such as input signal power, dispersion management period, and average dispersion value, etc. in order to achieve maximum system performance.

9) Using computer simulations to evaluate the maximum performance of higher-order dispersion-managed OPC transmission system employing the derived optimum system design strategies.
10) Summarizing the results, presenting the work in international conferences or publishing the work in periodical journal
11) Studying the suppression of SI using DRA. Designing the Raman gain in order to obtain symmetrical signal power distribution with respect to the system midpoint when the Raman amplifiers are applied to the second-half of the system.
12) With the DRA in combination with lump TOD compensators, confirming by the computer simulations the performance improvement of the OPC transmission systems.
13) Summarizing the results, presenting the work in international conferences or publishing the work in periodical journal
14) Studying numerical computations of the propagation of optical signal in optical fiber using the FDTD method with several algorithms such as the explicit FDTD, the implicit FDTD, and the Crank-Nicholson scheme, comparing the calculation results using these FDTD methods with those obtained from the SSFM.
15) Summarizing the results, presenting the work in international conferences or publishing the work in periodical journal.
16) Writing the doctoral dissertation.

1.4 Studying Scopes

1) Focusing only on the suppressing two main problems, TOD and SI, of OPC systems.
2) Proposing, studying and evaluating only the two possible ways to eliminate the TOD and SI.
   - The use of higher-dispersion compensated fiber link composed of single-mode fiber and reverse dispersion fiber. This combination yields the compensation of TOD and at the same time induces the periodic perturbation to the system. Therefore, by this scheme, the simultaneous suppression of both TOD and SI is expectable.

- The use of distributed gain from Raman amplifiers with the combination of lumped gain from EDFA. With this combination, the periodic power variation in the second half of OPC system can be made symmetrical with respect to midway point when the distributed gain of the Raman amplifier is carefully designed. Therefore, in combination with lump TOD compensators the vanishing of both TOD and SI can also be expected.

3) Proposing, studying and evaluating the OPC system optimum design theory focusing only the systems using the above two schemes.
4) As this research aims to study the performance improvement of ultra-long-haul ultra-high-speed OPC systems, therefore, we focus on OPC systems with transmission length of 10,000 km and with data rate higher than 100 Gbit/s.
5) The computer simulation is only one method to verify the derived theories because it is still not possible to perform such ultra-long haul ultra-high bit rate transmission experiments except in large telecommunication companies such as NTT, KDD and AT&T.
6) The numerical methods developed for computer simulations in this study are the SSFM and the FDTD method.

1.5 Benefits

1) The accumulation characteristic of TOD in OPC systems and the most suitable scheme for compensating the TOD on OPC systems.
2) First time in our knowledge, the complete theory of SI when two different characteristics of fibers are connected together.
3) The use of dispersion-management in OPC system which will be proposed for the first time in our knowledge.
4) The design of Raman amplifier gain that yields the lowest effect of SI to the signal transmission.
5) The performance improvement of OPC systems that is expected to be improved close to the linear SNR limit.
6) Very simple numerical analysis algorithms for calculating signal propagation in relatively long optical fiber using the FDTD method that gives both accuracy and least calculation time at the same time.
7) Three publications in proceedings of domestic conferences.

8) Three publications in proceedings of international conferences.
9) Publications of two full papers and one letter in international periodical journals.
10) Best paper award in domestic conference

1.6 Organization of this Dissertation

This thesis is organized as follows. Chapter 2 gives the review of basic knowledge about single-mode fiber characteristics and their effects on signal propagation. In chapter 2, we also describe about the NLSE and the principle of the SSFM which is the numerical method used for solving the NLSE. Chapter 3 is the literature review about the theory of the OPC and its limitations, together with other transmission schemes for overcoming the SOD effect. Our contributions start from chapter 4 where we discuss about the TOD compensation scheme in OPC systems. We show that the accumulation characteristic of the TOD in OPC transmission systems is almost linear. By assuming the ideal TOD compensator, the computer simulation result has shown the possibility of 100-Gbit/s, 10,000-km transmission based on TOD compensated OPC systems.

In chapter 5, the complete theoretical analysis of SI focusing on the case when two different characteristic fibers connected together is made. In our analysis, not only the periodic power variation but the periodic dispersion management, periodic fiber loss coefficient variation, and periodic nonlinear coefficient variation are also included. We derive the analytical SI gain and the SI frequency considering three cases: (a) when the dispersion management period is larger than the amplifier spacing, (b) when the two lengths are equal, and (c) when the amplifier spacing is larger than the dispersion management period. The derived theory is evaluated its accuracy by computer simulations.

We also focus on a dispersion managed transmission system consisting of SMF and RDF. Our computer simulation results show that, when two or more channels produce SI at the same frequency, SI significantly causes a serious problem to the channel whose carrier is positioned just at that superposition resonance frequency. We also demonstrate that, by re-arranging the channel position or channel spacing in such a way that none of the SI resonance frequency falls inside the channel signal bandwidth, the transmission performance is significantly improved.

In chapter 6, the reduction of the SI gain by employing the combination of SMF and RDF is shown. We then discuss an implementation of dispersion management in OPC systems. We suggest that a symmetric dispersion profile with respect to the mid-point of the system is preferable in order to avoid nonlinear accumulation of amplifier noise when the system operates with relatively high signal intensity. The performance improvement of the dispersion-managed 100-Gbit/s OPC system using the symmetric dispersion profile is confirmed by numerical simulations even when the dispersion map is not optimized.

Next, we discuss the optimum dispersion map design for obtaining the maximum performance in OPC systems. We demonstrate that, a 200-Gbit/s data transmission over a 10,000 km distance can be achieved by simultaneously suppressing TOD and SI in OPC systems using the dispersion-managed fiber link consisting of SMF and RDF whose dispersion map is properly designed.

Chapter 7 devotes to the use of bi-directional pumped DRA in the second-half of the OPC system to obtain the symmetrical signal power distribution with respect to the system midpoint. We show that the reverse power distribution can be formed by carefully choosing the forward pump power and backward pump power. In combination with one lump TOD compensator, we demonstrate by the computer simulation that the transmission of a 200-Gbit/s data over 10,000 km can also be made possible.

In chapter 8, we propose the use of FDTD for solving the NLSE and demonstrate that the FDTD can be sufficiently applied to simulate the optical pulse propagation in relatively long fiber under acceptable accuracy. In this chapter, three main FDTD algorithms, the explicit FDTD, the implicit FDTD, and the FDTD with Crank-Nicholson scheme are studied. We modify these algorithms to be the implicit-1, implicit-2, CN-1, CN-2, CN-3, CN-4, and CN-5 FDTD in order to make them suitable for solving the NLSE. Then, using these proposed methods, the comparison among the simulation results based on the model of single pulse propagation in optical fiber, together with those obtained from the SSFM are shown and discussed.

Finally, the conclusion of this thesis, the discussion considered the minor factors, which can also affect the performance of the proposed schemes, and the suggestion for future works are made at chapter 9.

CHAPTER 2
SIGNAL PROPAGATION IN SINGLE-MODE FIBER AND NUMERICAL METHOD

For understanding the evolution of optical pulses propagation in an optical fiber, it is necessary to understand the properties and characteristics of single-mode fibers which are generally used as transmission medium in fiber-optic systems.

Optical fibers are always considered as the lossless mediums because of their extremely small value of a loss coefficient (minimum 0.2 dB/km at an operation wavelength 1.55 μm) [4], [73]. This will lead to the extension of repeater spacing for more than 100 km while in the systems employing coaxial cables whose repeater spacing is limited to a few kilometers. Furthermore, according to the fact that optical fibers are made of SiO_2 glass, so optical fibers will have robustness against the disturbances from the surrounding circumstance more than those systems that use metal wires as transmission mediums. The above reasons make the fiber-optic systems the most expectable systems for nowadays and also, future telecommunication.

The behavior of optical signal when propagating in single-mode optical fiber is mainly determined by three main effects: fiber loss, dispersion, and fiber nonlinearity. The fiber loss causes the exponentially decrease of signal power during the propagation, which is necessary to be compensated by repeater for long distance transmission. The dispersion results a broadening of optical pulse, while the nonlinearity of fiber yields a broadening of signal spectrum. In fact, the dispersion and the nonlinearity interplay with each other, resulting in the distortion of both signal and its spectrum.

In this chapter, we describe about these fiber characteristics and their effects on signal propagating in optical fiber. Next, the concept of a numerical method called the split-step Fourier method which is mainly used for simulating signal propagating in optical fiber in this dissertation is shown.

2.1 Single-Mode Fiber Characteristics

2.1.1 Fiber Loss

Let P_i is the power launched at the input of a fiber length L, the transmitted power: P_T is given by

$$P_T = P_i \exp(-\alpha L), \tag{2-1}$$

where α is the attenuation constant, commonly referred to as the fiber loss. It is customary to express the fiber loss in units of dB/km by using the relation

$$\alpha_{dB} = -\frac{10}{L}\log\left(\frac{P_T}{P_i}\right) = 4.343\alpha, \tag{2-2}$$

where α_{dB} is the attenuation constant in dB/km expression. The fiber loss depends on the wavelength of light. Figure 2.1 shows the optical loss characteristic of single-mode fibers as a function of the operation wavelength.

The factors that are mainly contributed to the fiber loss are material absorption induced by OH ion and Rayleigh scattering [4], [73]. Other factors that cause additional loss is bending losses and boundary losses (due to scattering at the core-cladding boundary). The total loss of a fiber link on optical communication systems also includes the splice loss that occurs when two fiber pieces are joined together. The fiber loss causes the exponential decrease of optical signal power without giving rise to any change in signal shape also its spectrum.

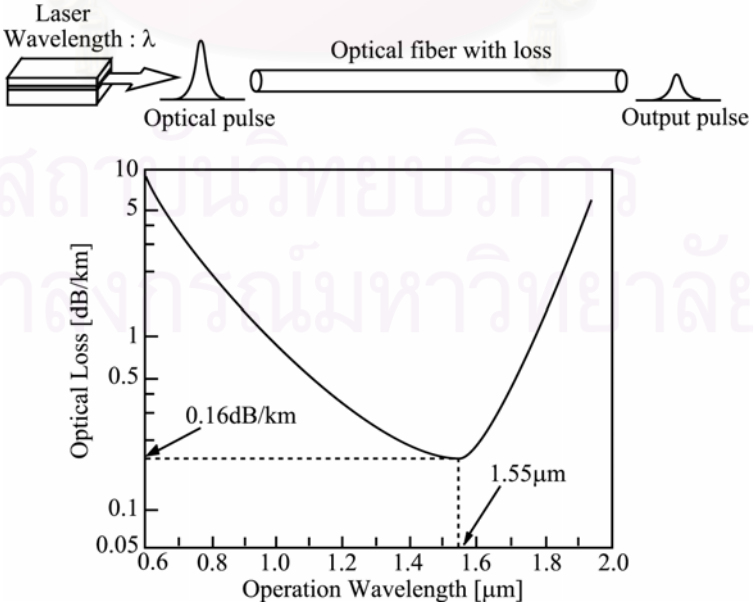

Figure 2.1: Optical loss characteristic of single-mode fibers.

2.1.2 Second-Order Dispersion [4]

When an optical pulse is launched to the fiber, its different frequency components associated with the pulse travel at different speeds. It will lead to the pulse broadening induced by the delay of transit time of each frequency component. This effect is well known as the chromatic dispersion, which may be one important limitation of a bit-rate or a distance in fiber-optic communication systems.

In the case if we consider optical fiber as a medium, dispersion play a critical role in propagation of short optical pulses since different spectral components associated with the pulse travel at different speeds given by $c/n\omega$ and the shorter pulses will have broader spectrum width.

Mathematically, the effects of fiber dispersion are accounted for by expanding the signal propagation constant β in a Taylor series about the lightwave carrier frequency ω_0.

$$\beta(\omega) = \beta_0 + \beta_1(\omega - \omega_0) + \frac{1}{2}\beta_2(\omega - \omega_0)^2 + \frac{1}{6}\beta_3(\omega - \omega_0)^3 \ldots, \qquad (2\text{-}3)$$

where β_1 in Eq. (2-3) refers to the inverse of group-velocity of the pulse envelope and also be known as first-order group-velocity dispersion (GVD) parameter. The second-order GVD parameter β_2 is responsible for pulse broadening, and the third-order GVD β_3, which relates to the TOD, causes signal waveform distortion in ultra-high bit rate signal transmission.

There is another parameter called second-order dispersion (SOD) or dispersion parameter D that is commonly used in the fiber-optics literature in place of β_2. It is related to β_2 by the relation

$$D = -\frac{2\pi c}{\lambda^2}\beta_2 . \qquad (2\text{-}4)$$

Figure 2.2 shows schematically the variation of β_2 and D with wavelength λ for optical fibers. The most notable feature in Fig. 2.2 is that β_2 and D vanishes at a wavelength λ_D. λ_D is often referred to as zero-dispersion wavelength which is about 1.3 μm in the case of standard single-mode fibers (SMF) and becomes 1.55 μm where the fiber loss is minimum in dispersion-shifted fibers (DSF).

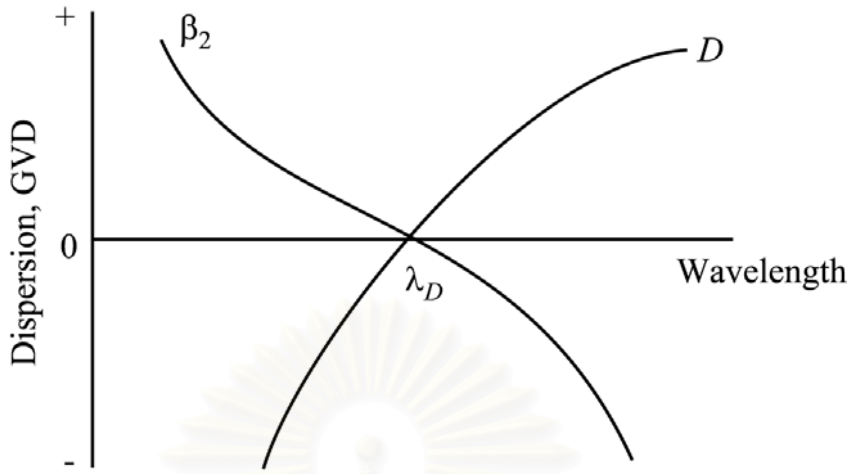

Figure 2.2: Dispersion characteristics of single-mode fibers.

The pulse can propagate without broadening in the zero-dispersion region, and the systems which operate at the zero-dispersion wavelength are known as zero-dispersion transmission systems which are expected to achieve high bit-rate and long transmission distance since the performance of the systems no longer limited by the SOD-induced broadening. However, it should be noted that total dispersion does not vanish at λ_D. Pulse propagation near λ_D requires the inclusion of the third-order dispersion effects β_3. Their inclusion is however necessary only when the pulse wavelength approaches λ_D to within a few nanometers.

According to Figure 2.2, for wavelength such that $\lambda < \lambda_D$, $\beta_2 > 0$, the fiber is said to exhibit normal dispersion. In the normal-dispersion regime, the higher frequency (blue-shifted) components of an optical pulse travel slower than the lower frequency (red-shifted) components. By contrast, the opposite occurs in the so-called anomalous-dispersion regime in which $\lambda > \lambda_D$, $\beta_2 < 0$. The anomalous-dispersion regime gives an interest for the study of nonlinear effects because it is in this regime that optical fibers can support nonlinear optical pulse soliton through a balance between the dispersive and nonlinear effects.

It should be noted here that the SOD-induced pulse broadening does not depend on the signs of β_2. Different signs but same values of SOD will lead to the same magnitude of broadening. Moreover, although the dispersion results in pulse

broadening, it does not cause the change in the spectrum of the pulse. Figure 2.3 shows the propagation of single optical pulse propagates along the optical fiber in the presence of the effect of dispersion.

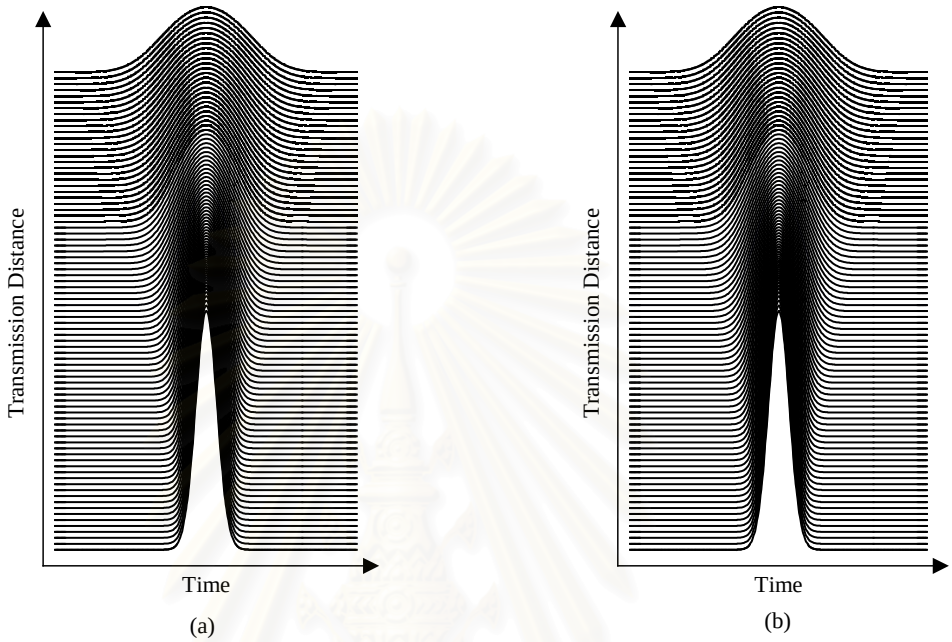

Figure 2.3: Evolution of single optical pulse in single-mode fiber with the effect of dispersion, (a) in normal dispersion regime ($\beta_2 > 0$), (b) in anomalous dispersion regime ($\beta_2 < 0$).

In general the extent of broadening is governed by the SOD length by

$$T_{out} = T_0 \left(1 + \left(\frac{z}{L_D} \right)^2 \right)^{\frac{1}{2}}, \tag{2-5}$$

where T_{out} denotes the transmitted pulse width. The SOD length L_D is defined as

$$L_{d2} = \frac{T_0^2}{|\beta_2|}. \tag{2-6}$$

L_D is the parameter which determines the length scale over which the dispersive effect becomes important for pulse evolution along a fiber length L when $L_{d2} < L$.

The difference between propagation of a pulse in normal-dispersion region and in anomalous-dispersion region is the sign of linear phase modulation of the

transmitted pulse. This linear phase modulation can be expressed as the time dependence of the optical phase $\phi(z,T)$ caused by the effect of β_2.

$$\phi(z,T) = -\frac{\mathrm{sgn}(\beta_2)(z/L_{d2})T^2}{1+(z/L_{d2})^2 T_0^2} + \tan^{-1}\left(\frac{z}{L_{d2}}\right), \tag{2-7}$$

where $\mathrm{sgn}(\beta_2) = \pm 1$ depending on the sign of the GVD parameter β_2. The time dependence of the phase $\phi(z,T)$ implies that the instantaneous frequency differs across the pulse from the central frequency ω_0. The difference $\Delta\omega$ is just the time derivative $-\partial\phi/\partial T$ and is given by

$$\Delta\omega = -\frac{\partial\phi}{\partial T} = \frac{2\,\mathrm{sgn}(\beta_2)(z/L_D)T}{1+(z/L_D)^2 T_0^2}. \tag{2-8}$$

The phenomenon that frequency changes across the pulse is generally known as the frequency chirp. Although the incident pulse is unchirped but after propagating in dispersive fiber the pulse will be chirped. The chirp $\Delta\omega$ depends on the sign of β_2. Figure 2.4 shows the difference between frequency chirp in normal-dispersion regime $(+\beta_2)$ and anomalous-dispersion regime $(-\beta_2)$.

In the normal-dispersion regime, $\Delta\omega$ is negative at the leading edge $T < 0$ and increases linearly across the pulse. The opposite occurs in the anomalous-dispersion regime.

2.1.3 Third-Order Dispersion [4], [74]

SOD-induced pulse broadening discussed above is due to the second-order GVD term proportional to β_2 in the expansion (3). Although the contribution of this term dominates in most cases of practical interest, it is sometimes necessary to include the higher-order term proportional to β_3 in this expansion.

Since β_3 is the derivative of β_2 by the frequency ω: $\beta_3 = d\beta_2/d\omega$. The effect of β_3 can be explained in term of the effect of dispersion slope. As shown in Fig. 2.5, for broadband optical signal such as ultra-short pulses or OTDM signal [75], different signal spectral component will experience different dispersion values due to the slope of the dispersion curve. Therefore, it is often necessary to include β_3 for such signal.

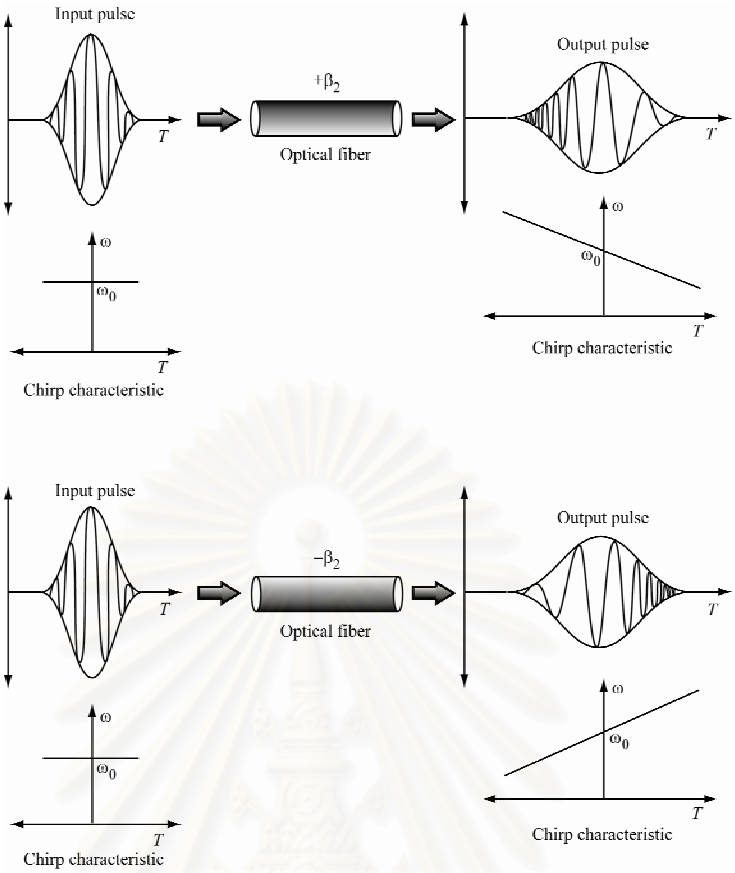

Figure 2.4: Linear frequency chirps induced by fiber SOD, (a) in normal dispersion regime ($+\beta_2$), (b) in anomalous dispersion regime ($-\beta_2$).

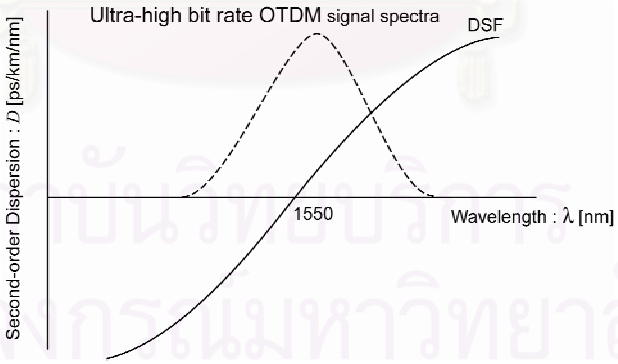

Figure 2.5: Broadband optical signal on fiber dispersion band.

The important parameter widely used representing the effect of β_3 is the third-order dispersion (TOD) or the dispersion slope, which is defined by the derivative of the dispersion value D by wavelength λ: TOD = $dD/d\lambda$. Typically,

near zero-dispersion wavelength of DSF, $\beta_3 \approx 0.2\text{ps}^3/\text{km}$ and TOD = 0.06ps/km/nm^2. In order to compare the relative importance of the dispersion and the TOD terms, it is useful to introduce a dispersion length associated with the TOD term defined as

$$L_{d3} = \frac{T^3}{|\beta_3|}. \tag{2-9}$$

The higher-order dispersive effects play a significant role only if $L_{d3} \le L_{d2}$.

Figure 2.6(a) shows the single optical pulse propagates along the optical fiber with the effect of higher-order dispersion in the case of positive TOD and Fig. 2.6(b) and (c) shows the initial pulse shape and the output pulse, respectively. The output optical pulse is distorted such that it becomes asymmetry with an oscillatory structure near one of its edges. It should be noted that the dispersive effect does not cause any change in the output spectrum. For the case of positive TOD shown in Fig. 2.6, the oscillation appears near the trailing edge of the pulse.

For the case of $D = 0$, oscillations are deep with intensity dropping to zero between successive oscillations. However, these oscillations damp significantly even for the relatively small values of D.

2.1.4 Kerr Effect [4]

Most of the nonlinear effects in optical fibers originate from nonlinear refraction. Nonlinear refraction is a phenomena that refers to the intensity dependence of the refractive index. This phenomena is known as the Kerr effect. The expression of the refractive index, which includes the term of light intensity dependence, becomes

$$\bar{n}\left(\omega, |A|^2\right) = n(\omega) + n_2 |A|^2 \tag{2-10}$$

where $n(\omega)$ is the linear part. $|A|^2$ is the optical signal intensity inside the fiber, and n_2 is the nonlinear-index coefficient.

The intensity dependence of the refractive index leads to a large number of interesting nonlinear effects. The one most widely studied are self-phase modulation (SPM) [4]. SPM refers to the self-induced phase shift experienced by optical field during its propagation in optical fibers. Its magnitude can be obtained by changes of the phase of an optical field by

$$\phi = \bar{n} k_0 L = \left(n(\omega) + n_2 |A|^2\right) k_0 L \ , \tag{2-11}$$

where $k_0 = 2\pi/\lambda$ and L is the fiber length. The intensity-dependent nonlinear phase shift caused by SPM is

$$\phi_{nl} = \bar{n} k_0 L |A|^2 \ . \tag{2-12}$$

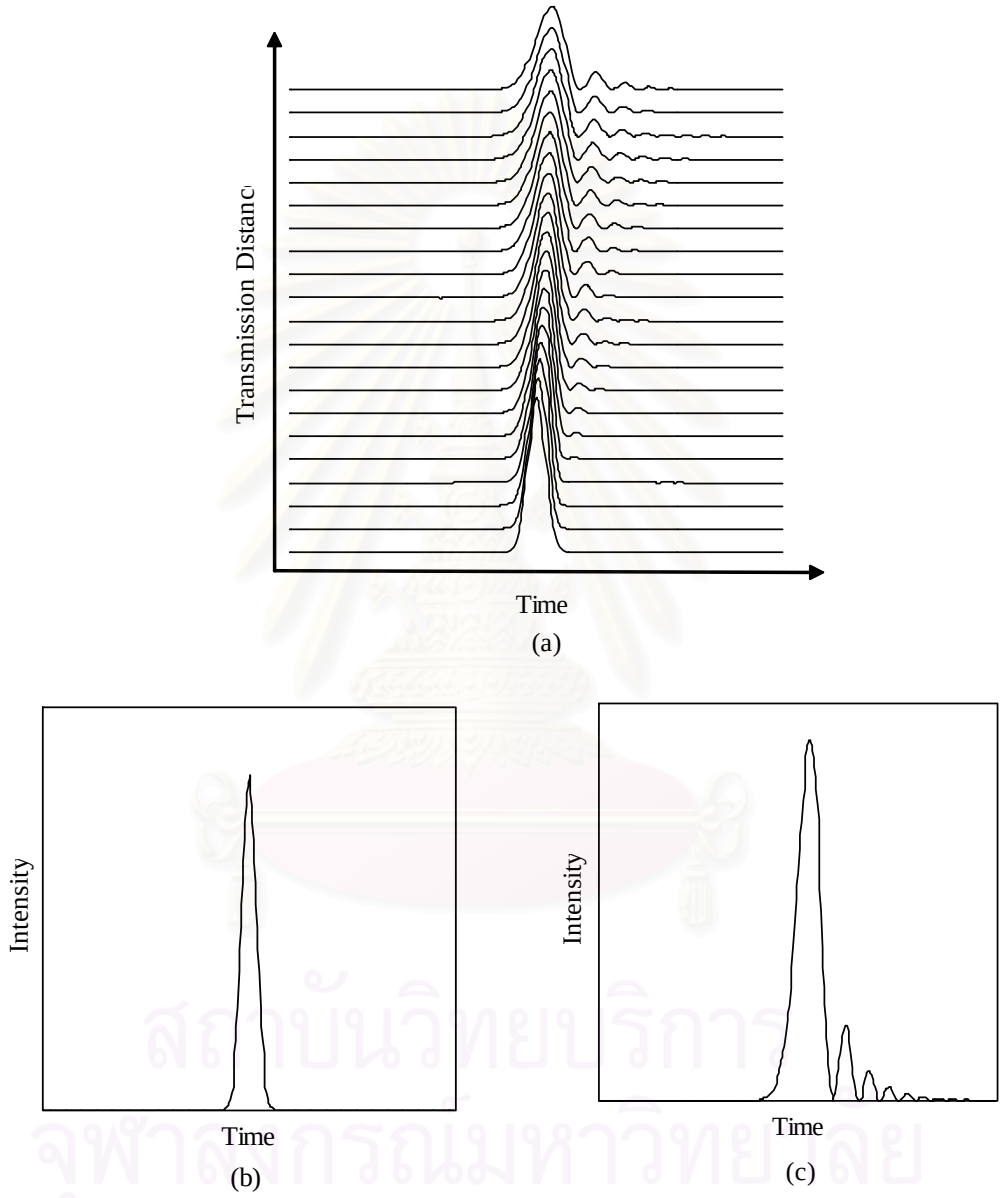

Figure 2.6: Transmission of an optical pulse and in single-mode fiber with the effect of TOD, (a) pulse evolution, (b) initial pulse shape, (c) pulse at output end of fiber.

SPM is responsible for spectral broadening of optical pulses. When the SPM interacts with the SOD effect in the normal-dispersion regime, it will lead to the

breaking of the optical pulse. By contrast, If the SPM balances with the SOD effect in anomalous-dispersion regime, this will lead to the existence of optical solitons.

If we consider the pulse propagation in lossless optical fibers, $U(z,t)$ now represents the normalized envelope function of the optical pulses, Eq. (2-12) should be modulated to time-distance-depended equation which fits to the description of pulse propagation in fiber,

$$\phi_{nl}(z,t) = |U(z,t)|^2 z / L_{nl} \quad , \tag{2-13}$$

where the nonlinear length L_{NL} which represents the length of fiber at which the nonlinearity becomes the dominant effect is defined as

$$L_{nl} = \frac{1}{\gamma P_0}, \tag{2-14}$$

where P_0 denotes the input peak power of the pulse and γ is the nonlinear coefficient which is proportional to the nonlinear refractive index n_2. $U(z,t)$ appearing in Eq. (2-13) is the optical field normalized by peak power.

Equation (2-13) shows that SPM gives rise to an intensity-dependent phase shift while the pulse shape governed by $|U(z,t)|^2$ remains unchanged. Furthermore, this nonlinear phase shift $\phi_{nl}(z,t)$ given by Eq. (2-13) increases with the propagated distance z. SPM-induced spectral broadening is a consequence of the time dependence of $\phi_{nl}(z,t)$. This can be understood by nothing that a temporally varying phase implies that the instantaneous optical frequency differ across the pulse from its central value ω_0. The difference $\Delta\omega$ is given by

$$\Delta\omega = -\frac{\partial \phi_{NL}}{\partial t} = -\frac{\partial |U(z,t)|^2}{\partial t}\frac{z}{L_{nl}}, \tag{2-15}$$

and the frequency of the pulse now becomes time-depend function. Figure 2.7 shows the modulation of optical carrier frequency of the pulse obtained from Eq. (2-15).

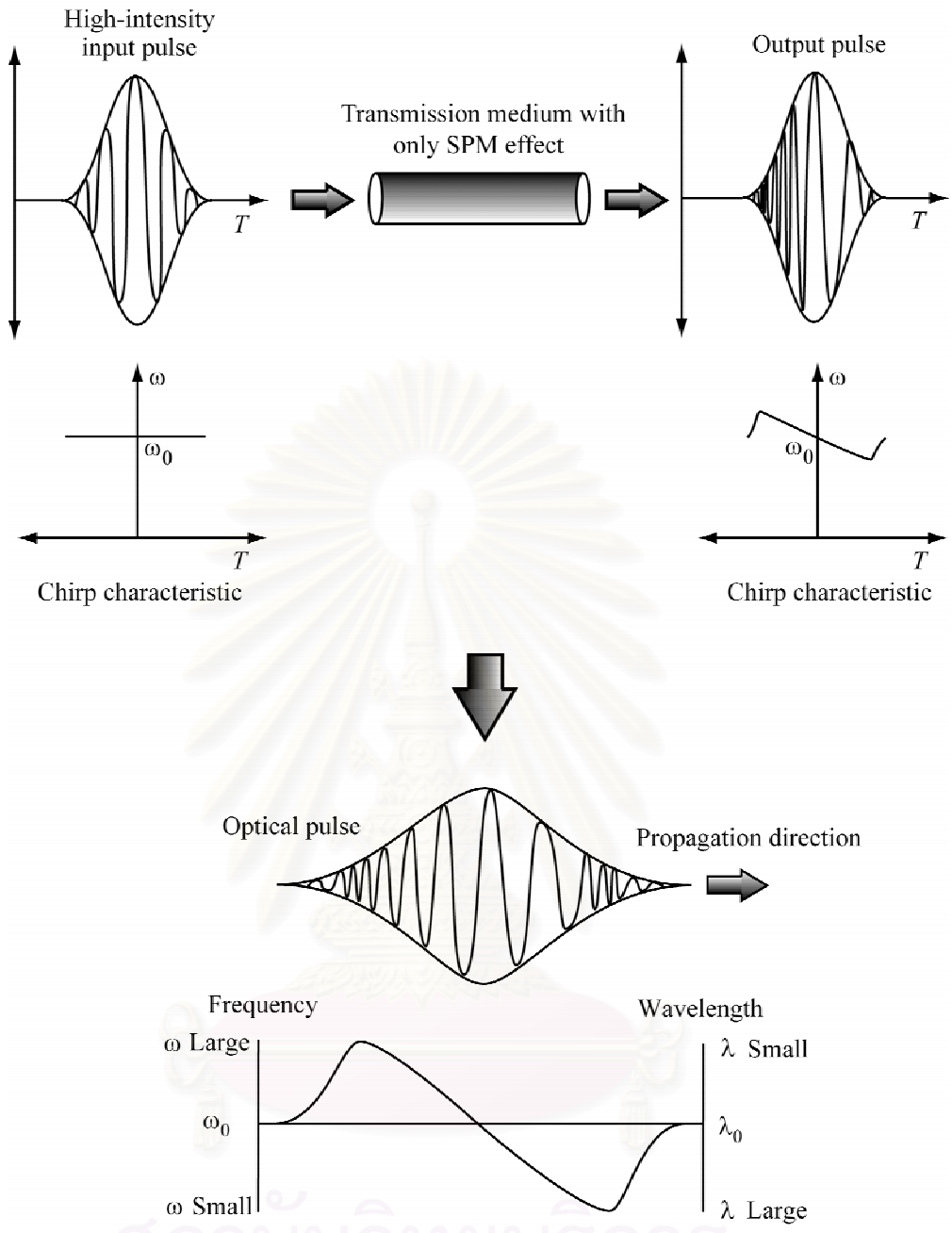

Figure 2.7: Modulation of optical frequency inside the pulse due to nonlinear self-phase modulation.

The modulation of frequency or the time dependence of $\Delta\omega$ can be viewed as a frequency chirp. The chirp is induced by SPM and increases in magnitude with the propagated distance. The temporal variation of the SPM-induced chirp in $\Delta\omega$ in Fig. 2.7 has two interesting features. First, $\Delta\omega$ is negative near the leading edge (red shift) and becomes positive near the trailing edge (blue shift). Second, the chirp is linear and positive (up-chirp) over the large central region. Since the characteristic of

the SPM-induced frequency chirp is similar to the linear up-chirp, we should call this chirp the nonlinear up-chirp.

Figure 2.8 shows the spectrum of single optical pulse propagating along the optical fiber with only the effect of SPM. The most notable feature of Fig. 6 is that SPM-induced spectral broadening is accompanied by an oscillatory structure covering the entire frequency range. In general, the spectrum consists of many peaks and the outermost peaks are the most intense.

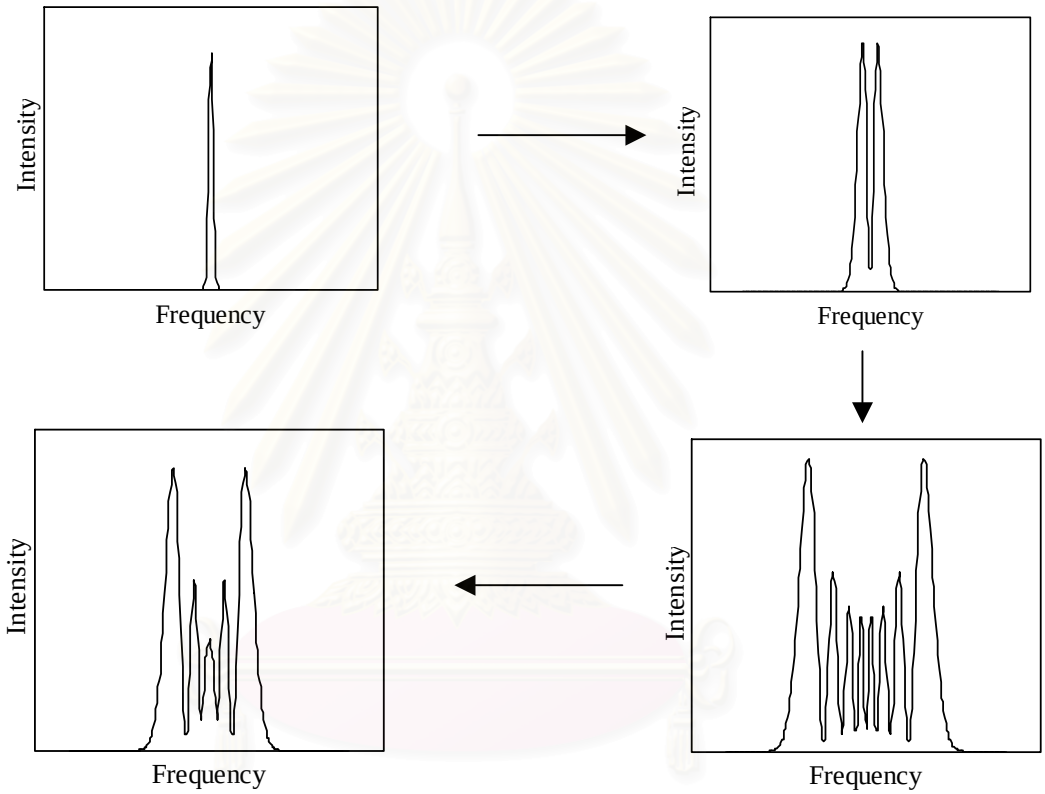

Figure 2.8: Evolution of optical spectrum in the presence of nonlinear self-phase modulation.

2.1.5 Stimulated Inelastic Scattering

Stimulated inelastic scattering is the nonlinear effect in which the optical field transfers part of its energy to the nonlinear medium. Two important nonlinear effects in optical fiber fall in this category are known as stimulated Raman scattering (SRS) [4], [6] and stimulated Brillouin scattering (SBS) [4], [6], [76]. Both of them are related to vibrational excitation modes of silica. The main difference between the two is that optical phonons participate in SRS while acoustic phonons participate in SBS.

2.1.5.1 Stimulated Raman Scattering

Stimulated Raman scattering (SRS) is an important nonlinear process that can turn optical fibers into broadband Raman amplifiers. When the intense optical beam is inputted into the fiber, part of its energy coverts to another optical beam at a frequency downshifted by an amount determined by the vibrational modes of the medium. This process is called the Raman effect and is described quantum-mechanically as a scattering of the incident photon by a molecule to a lower-frequency photon while the same time the molecule makes a transition between vibrational states. The incident light acts as a pump to generate the frequency-shifted light called Stokes wave.

Under the steady state or CW operation of the pump light, the initial growth of the Stokes wave is described by the relation

$$\frac{dI_S}{dz} = g_R I_P I_S, \tag{2-16}$$

where I_S is the stokes intensity, I_P is the pump intensity, and g_R is the Raman gain coefficient. Figure 2.9 shows g_R as a function of the frequency shift for fused silica at a pump wavelength of 1000 nm. The most significant feature of the Raman gain in silica fiber is that g_R extends over a large frequency range up to 40 THz with a broad dominant peak near 13 THz (440 cm^{-1}). As a result, optical fibers can act as the broadband amplifiers.

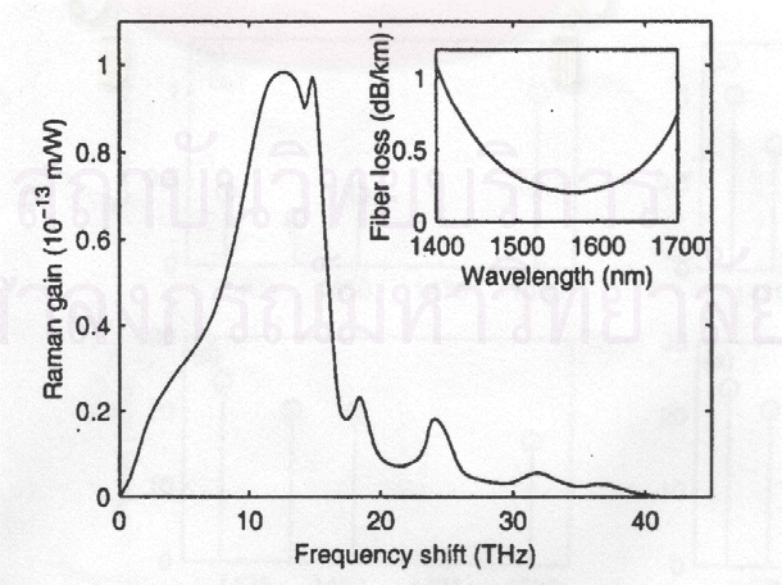

Figure 2.9: Raman gain coefficient g_R as a function of the frequency shift for fused silica at a pump wavelength of 1000 nm (After Ref.[4]).

Considering a cw pump beam propagating inside the fiber at the optical frequency ω_P. If the probe beam at the frequency ω_S is coincident with the pump at the fiber input, it will be amplified because of the Raman gain as long as the frequency difference $\omega_P - \omega_S$ lies within the bandwidth of the Raman gain spectrum. If only the pump beam is incident at the fiber input, spontaneous Raman scattering provides a weak signal which acts as a probe and is amplified with propagation. Since spontaneous Raman scattering generates photons within the entire bandwidth of the Raman gain spectrum, all frequency components are amplified. However, the frequency component for which g_R is maximum build up most rapidly. In the case of pure silica g_R is maximum for the frequency by about 13.2 THz (440 cm^{-1}). It turns out that when the pump power exceeds a threshold value, this component builds up almost exponentially. Thus, SRS leads to generation of the Stokes wave whose frequency is determined by the peak of the Raman gain. The corresponding frequency shift is sometimes called the Raman shift or the Stokes shift.

To find the Raman threshold in the CW case, two coupled equations of the interaction between the pump and Stokes waves should be considered as follow:

$$\frac{dI_s}{dz} = g_R I_P I_S - \alpha_S I_S , \tag{2-17}$$

$$\frac{dI_P}{dz} = \frac{\omega_P}{\omega_S} g_R I_S I_P - \alpha_P I_P , \tag{2-18}$$

where the absorption coefficients α_S and α_P account for the fiber loss at the Stokes and pump frequencies. For estimating the Raman threshold, the first term on the right-hand side of Eq. (2-18), which is responsible for pump depletion, can be neglected. Then the solution of the coupled equations are obtained

$$I_S(L) = I_S(0)\exp\left(g_R I_0 L_{eff} - \alpha_S L\right), \tag{2-19}$$

where

$$L_{eff} = \frac{1}{\alpha_P}\left(1 - \exp(-\alpha_P L)\right) \tag{2-20}$$

is the effective interaction length and I_0 is the incident pump intensity at $z = 0$. The use of Eq. (2-19) requires an input intensity $I_S(0)$ at $z = 0$. In practice, SRS can build up from spontaneous Raman scattering.

The Raman threshold is defined as the input pump power at which the Stokes power becomes equal to the pump power at the fiber output, or

$$P_S(L) = P_P(L) = P_0 \exp(-\alpha_P L), \tag{2-21}$$

where

$$P_0 = I_0 A_{eff}\,, \tag{2-22}$$

P_0 is the input power and A_{eff} is the effective fiber core area. By assuming $\alpha_S \approx \alpha_P$, the threshold pump power P_0^{th} is calculated to be

$$P_0^{th} \approx \frac{16 A_{eff}}{g_R L_{eff}}. \tag{2-23}$$

If polarization is not preserved the Raman threshold is increased by a factor whose value lies between 1 and 2. For long fiber such that $\alpha_P L << 1, L_{eff} \approx 1/\alpha_P$. At λ_P = 1550 nm, a wavelength near which the fiber loss in minimum. If we use a typical value $A_{eff} = 50\mu\,\mathrm{m}^2$, the predicted Raman threshold is P_0^{th} = 600 mW. Since the power launched into the fiber is typically 1 mW, SRS is not likely to occur in single-channel optical communication systems. The soliton-based optical communication systems would require higher power levels in the range 40-50 mW. This range is still well below the critical value. Moreover, to estimate how the Raman effect affects the lightwave system, the CW theory of SRS needs modification when optical pulses are used at the pump since the optical power launched into the fiber is the pulses not the CW.

In this case, if the Raman threshold is reached and if the pulse width is much smaller than the Raman response time of the medium ($\tau_R \approx$ 10 fs in silica fiber), each pump pulse then generates a Stokes or Raman pulse.

Optical fiber can be used to amplify a weak signal if it is propagated together with a strong pump wave and if its wavelength lied within the bandwidth if the Raman gain spectrum of the pump. Such amplifiers are called fiber-Raman amplifiers. The signal intensity at the amplifier output at $z = L$ is then given by Eq. (2-19). Since $I_S(L) = I_S(0)\exp(-\alpha_S L)$ in the absence of pump, the amplifier gain or the amplification factor is given by

$$G_R = \frac{I_S(L)}{I_S(0)\exp(-\alpha_S L)} = \exp\left(g_R P_0 L_{eff} / A_{eff}\right), \tag{2-24}$$

Fiber-Raman amplifier can easily amplify the signal by a factor of 1000 (30 dB gain) at a pump power of about 1 W. An attractive feature of the fiber-Raman amplifiers is their broad bandwidth ($\geqq$ 5 THz). It can be used to amplify several channels simultaneously in a multi-channel communication system and it is possible to apply to the amplification for transmitting ultra-short pulses such soliton pulses.

Raman amplifier using optical fiber can be realized by forward, backward, and also bi-directional pumping scheme. In chapter 7, we apply the distributed Raman gain produced through the bi-directional pumped SRS in optical fiber for constructing the reverse power distribution in order to achieve the perfect compensation of signal distortion in OPC system.

2.1.5.2 Stimulated Brillouin Scattering

Stimulated Brillouin scattering (SBS) is a nonlinear process that occurs in optical fibers at input power levels much lower than those needed for stimulated Raman scattering (SRS). The difference against SRS is that the direction of generated Stokes wave is backward while SRS is occurred in both direction, and an amount of the frequency shift of the Stokes wave is determined by the acoustic phonons instead of optical phonons. Similarly, SBS can be useful through fiber-Brillouin amplifiers and laser [77], [78].

SBS manifests through the generation of a backward Stokes wave downshifted from the frequency of the incident pump wave by an amount determined by the nonlinear medium. The stoke shift in SBS ($\approx$ 10 GHz) is smaller by three orders of magnitude compared with the occurring in SRS. The threshold power for SBS depends on the spectral width associated with the pump wave. It can be as low as ≈ 1 mW for a CW pump. By contrast, SBS nearly ceases to occur for short pump pulses with widths shorter than 10 ns.

The process of SBS can be described as a parametric interaction among the pump wave, the Stokes wave, and an acoustic wave. The pump wave generates acoustic waves through the process of electrostriction which in turn causes a periodic modulation of the refractive index. The pump-induced index grating scatters the pump light through Bragg diffraction. The scattered light is downshifted in frequency because of the Doppler shift associated with a grating moving at the acoustic velocity v_A. The frequency shift ν_B in the backward is given by

$$\nu_B = \frac{2n\nu_A}{\lambda_P}, \tag{2-25}$$

where n is the refractive index, and λ_P is the pump wavelength. If we use ν_A = 5.96 km/s and n = 1.45, the values appropriate for silica fibers, $\nu_B \approx$ 11.1 GHz at λ_P = 1550 nm. Similar to the case of SRS, the growth of the Stokes wave is characterized by the Brillouin gain coefficient $g_B(\nu_B)$ whose peak value occurs at $\nu = \nu_B$. However in contrast with the SRS case, the spectral width $\Delta\nu_B$ of the Brillouin-gain spectrum is very small ($\approx$ 10 MHz). The Brillouin-gain coefficient g_B is nearly independent of the pump wavelength. For fused silica, $g_B = 5\times10^{-11}$ m/W.

Similar to the SRS case, the development of SBS in optical fibers requires the consideration of mutual interaction between the pump and Stokes waves. Assuming that the fiber loss is the same for the pump and Stokes waves $(\alpha_P = \alpha_S = \alpha)$, under the steady-state conditions, the interaction couple-intensity equations is given by

$$\frac{dI_S}{dz} = g_B I_P I_S - \alpha I_S, \tag{2-26}$$

$$\frac{dI_P}{dz} = -g_B I_S I_P + \alpha I_S. \tag{2-27}$$

The solution of the couple equations about the Stokes intensity is found to grow exponentially in the backward direction according to the relation

$$I_0(0) = I_S(L)\exp\left(\left(g_B P_0 L_{eff} / A_{eff}\right) - \alpha L\right), \tag{2-28}$$

where $P_0 = I_P(0)A_{eff}$, A_{eff} is the effective core area, and the effective interaction length is given by

$$L_{eff} = \frac{1}{\alpha}\left(1 - \exp(-\alpha L)\right). \tag{2-29}$$

Equation (2.28) shows how a Stokes signal incident at $z = L$ grows in the backward direction because of Brillouin amplification occurring as a result of SBS. In practice, no such signal is generally fed, and the Stokes wave grows from noise or spontaneous Brillouin scattering occurring throughout the fiber. The Brillouin threshold is found to occur at a threshold pump power P_0^{th} obtained by using the relation

$$g_B P_0^{th} L_{eff} / A_{eff} \approx 21. \tag{2-30}$$

The numerical factor of 21 can also increase by a factor between 1 and 2 depending on whether the pump and Stokes waves maintain their polarization along the fiber or not. If we used the typical values for fibers used in 1550 nm optical communication systems, A_{eff} = 50 μm^2, L_{eff} ≈ 20 km, and $g_B \approx 5\times10^{-11}$ m/W, the predicted threshold pump power P_0^{th} ≈ 1 mW. It is such a low threshold that makes SBS a dominant nonlinear process in optical fibers.

The Brillouin gain of an optical fiber can be used to amplify a weak signal whose frequency is shifted from the pump frequency by an amount equal to the Brillouin shift ν_B. The fiber-Brillouin amplifier gain G_B is given by

$$G_B = \exp\left(g_B P_0 L_{eff} / A_{eff}\right). \tag{2-31}$$

Since amplification of fiber-Brillouin amplifiers can be achieved at the pump power of only a few milliwatts, such a semiconductor laser can be used as a pump source. The narrow bandwidth of the amplifiers can also be advantageous for some fiber-optic applications requiring selective amplification of only a narrow portion of the incident signal spectrum.

The most important development in optical fiber communication in this decade may be the invention of EDFA. Such kind of fiber amplifier has Erbium doped in the core and utilizes SBS to provide a gain for optical amplification. EDFA is the most attractive and has a great potential for lightwave system not only for linear systems but also can be applied for amplifying nonlinear pulses such as optical soliton in nonlinear systems [79]-[81].

2.1.6 Parametric Processes and Four-Wave Mixing

In the stimulated scattering processes, the optical fiber play and active role through the participation of molecular vibrations or acoustic phonons. In many nonlinear phenomena the fiber plays a passive role except for mediating the interaction among several optical waves through a nonlinear response of bound electrons. Such processes are referred to as the parametric processes as they originate from light-induced modulation of a medium parameter such as the refractive index [4]. These processes include the nonlinear phenomena such as second-harmonic generation which will not occur in the mediums such as optical fibers, four-wave mixing [4], [82], and parametric amplification [8], [83].

Four-wave mixing and parametric amplification refer to the interaction among four optical waves. Four-wave mixing in optical fibers has been studied extensively since it can be quite efficient in generating new waves. Its main features can be understood by considering the third-order polarization term given as

$$\vec{P}_{NL} = \varepsilon_0 \chi^{(3)} \vec{E} \cdot \vec{E} \cdot \vec{E} \,, \tag{2-32}$$

where $\vec{E}$ is the electric field, $\vec{P}_{NL}$ is the induced nonlinear polarization, and ε_0 is the vacuum permitivity. Consider four optical waves oscillating at frequencies $\omega_1, \omega_2, \omega_3$, and ω_4 and linearly polarized along the same axis *x*. The total electric field can be written as

$$\vec{E} = \hat{x} \frac{1}{2} \sum_{j=1}^{4} E_j \exp\left(i\left(k_j z - \omega_j t\right)\right) + c.c., \tag{2-33}$$

where

$$k_j = n_j \omega_j / c \,, \tag{2-34}$$

n_j is the refractive index, *c.c.* represents the complex conjugate, and four waves are assumed to be propagating in the same direction *z*. Substituting Eq. (2-33) in Eq. (2-32), $\vec{P}_{NL}$ can be expressed as

$$\vec{P}_{NL} = \hat{x} \frac{1}{2} \sum_{j=1}^{4} P_j \exp\left(i\left(k_j z - \omega_j t\right)\right) + c.c., \tag{2-35}$$

we find that P_j for j = 1-4 consists of a large number of terms involving the products of three electric fields. For example, P_4 can be expressed as

$$P_4 = \frac{3\varepsilon_0}{4} \chi^{(3)}_{xxxx} \left\{ \left(|E_4|^2 + 2\left(|E_1|^2 + |E_2|^2 + |E_3|^2 \right) \right) E_4 + 2E_1 E_2 E_3 \exp\left(i\theta^+\right) + 2E_1 E_2 E_3^* \exp\left(i\theta^-\right) + \ldots \right\} \tag{2-36}$$

where

$$\theta^+ = \left(k_1 + k_2 + k_3 - k_4\right) z - \left(\omega_1 + \omega_2 + \omega_3 - \omega_4\right) t \,, \tag{2-37}$$

$$\theta^- = \left(k_1 + k_2 - k_3 - k_4\right) z - \left(\omega_1 + \omega_2 - \omega_3 - \omega_4\right) t \,. \tag{2-38}$$

The term proportional to E_4 in Eq. (2-36) is responsible for self-phase modulation (SPM) and cross-phase modulation (XPM) effects respectively. The remaining terms are responsible for FWM. The efficiency of FWM depends on the phase difference between E_4 and P_4 as described in Eq. (2-37) and Eq. (2-38). Significant FWM occurs only if the phase difference nearly vanishes. This requires matching of frequencies as well as of the wave vectors. The latter requirement is often referred to as phase matching. Phase matching condition requires a specific choice of the

frequencies and the refractive indices for parametric processes to occur. There are two types of FWM terms in Eq. (2-36). First, the case which three photons transfer their energy to a single photon by the following condition,

$$\omega_4 = \omega_1 + \omega_2 + \omega_3 . \tag{2-39}$$

This process can also refers to the phenomena such as third-harmonic generation when $\omega_1 = \omega_2 = \omega_3$ or frequency conversion to the wave at $2\omega_1 + \omega_3$ when $\omega_1 = \omega_2 \neq \omega_3$. In general, it is difficult to satisfy the phase matching condition for these processes to occur in optical fibers with high efficiencies.

The process which is able to occur in optical fiber is the second type of FWM described by the following condition,

$$\omega_3 + \omega_4 = \omega_1 + \omega_2 , \tag{2-40}$$

where two photons at frequencies ω_1 and ω_2 are annihilated with a simultaneous creation of two photons at frequencies ω_3 and ω_4.

The phase-matching requirement for this process to occur is that $\Delta k = 0$, where

$$\Delta k = k_3 + k_4 - k_1 - k_2 = \left(n_3\omega_3 + n_4\omega_4 - n_1\omega_1 - n_2\omega_2\right)/c . \tag{2-41}$$

The description of this process is illustrated in Fig. 2.10. It is relatively easy to satisfy the phase matching condition for the case in which $\omega_1 = \omega_2$. This case is similar to SRS.

A strong pump wave at ω_1 creates two side bands at lower frequency ω_3 and higher frequency ω_4. ω_3 and ω_4 are referred to as the Stokes and anti-Stokes respectively in direct analogy with SRS and are also be called the signal and idler bands when an input signal at ω_3 is amplified through the process of FWM.

FWM will affect the multi-channel fiber-optics systems such WDM systems since once the phase matching is satisfied, one channel transfers its energy to other two channels [84], [85]. Even the single-channel systems, the degradation by FWM process occurs since the signal transfers its energy to spontaneous noise whose their frequencies satisfy the phase matching condition [86]-[93]. The degradation of single-channel systems will be stronger if the signal wavelength is set at the zero-dispersion wavelength since it has been shown that phase-matching is easily to justify at zero-dispersion wavelength of optical fibers [4], [82]. In this case, the FWM

interacts with the SPM effect causing an enhancement of the spontaneous noises resulting in spreading of spectrum which will degrade a bit-error rate of the systems [86]-[93].

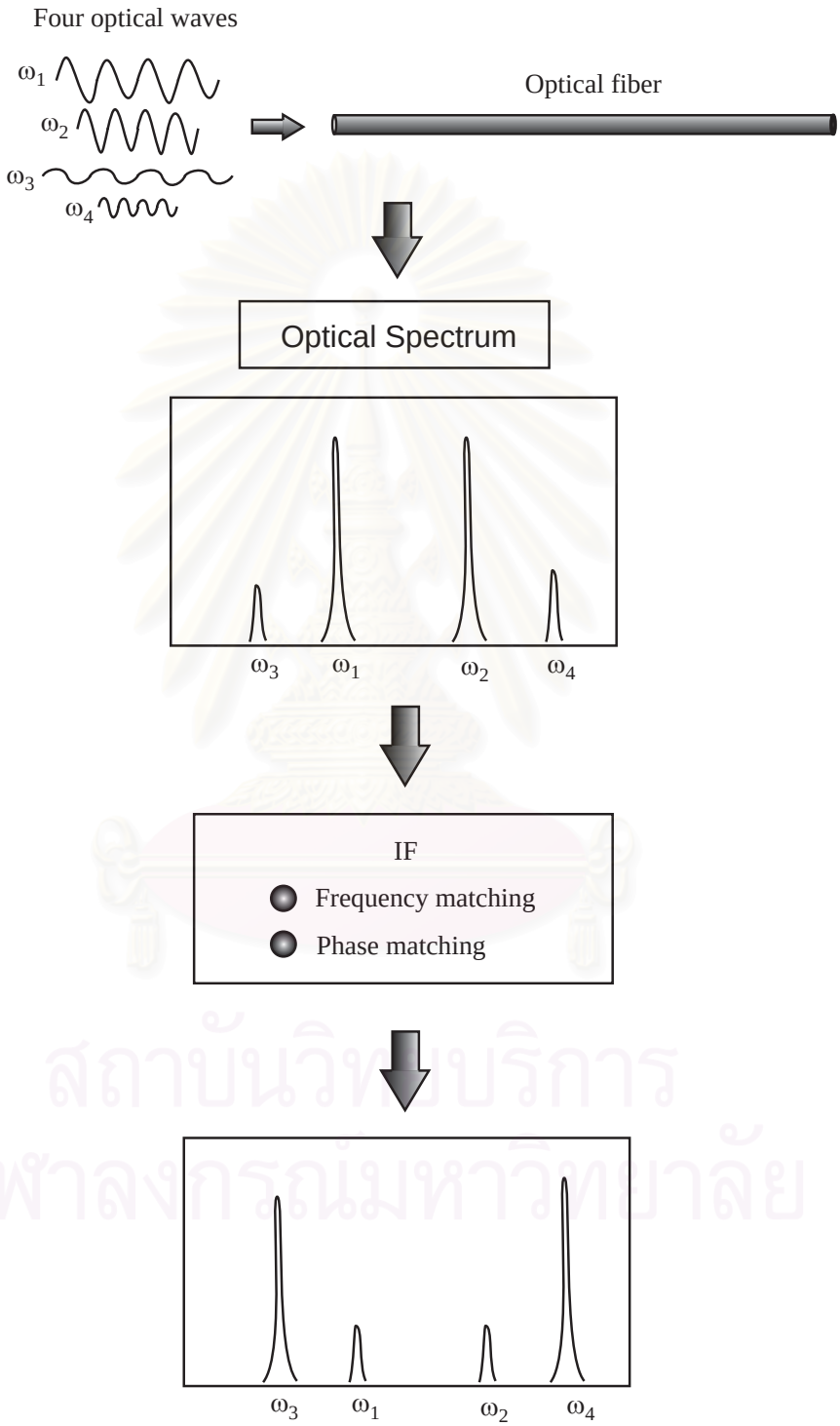

Figure 2.10: Process of Four-wave mixing in optical fiber.

2.2 Derivation of Basic Propagation Equation

In order to study signal propagation in optical fiber both analytically and numerically, the nonlinear Schrodinger equation (NLSE) which governs the signal propagation in optical fiber must be solved. In this section, we show the derivation of basic equation that governs the propagation of optical signal in single-mode fibers which is based on Maxwell's equations and important concepts such as the linear and nonlinear parts of the induced polarization, the frequency-dependent dielectric constant, and the theory of pulse propagation in nonlinear dispersive media in the slowly-varying-envelope approximation with the assumption that the pulse is much smaller than the frequency of the incident radiation. Next, we describe a simulation method which is employed in this research for solving the propagation equation since there is no analytic solution available except a special case such as soliton. As we use the algorithm of FFT so that the initial optical field must be sampled to discrete function, this sec ends with the preparation before performing the numerical simulation.

Like all electromagnetic phenomena, the propagation of optical fields in fibers is governed by Maxwell's equations. In the case that considers optical fibers as a medium, Maxwell's equations will be

$$\nabla \times \vec{E} = -\frac{\partial \vec{B}}{\partial t}, \tag{2-42}$$

$$\nabla \times \vec{H} = \vec{J}_f + \frac{\partial \vec{D}}{\partial t}, \tag{2-43}$$

$$\nabla \cdot \vec{D} = \rho_f, \tag{2-44}$$

$$\nabla \cdot \vec{B} = 0, \tag{2-45}$$

where $\vec{E}$ and $\vec{H}$ are electric and magnetic field vectors respectively, and $\vec{D}$ and $\vec{B}$ correspond to electric and magnetic flux densities.

In the medium such as optical fibers, the relations between $\vec{D}$ and $\vec{E}$, and, $\vec{B}$ and $\vec{H}$ are

$$\vec{D} = \varepsilon_0 \vec{E} + \vec{P}, \tag{2-46}$$

$$\vec{B} = \mu_0 \vec{H}, \tag{2-47}$$

where ε_0 is the vacuum permitivity, μ_0 is the vacuum permeability, and $\vec{P}$ is the induced electric polarization. If we include third-order nonlinear effects governed by

the third-order susceptibility $\chi^{(3)}$, the induced polarization will separate into two parts such that

$$\vec{P} = \vec{P}_L + \vec{P}_{NL}, \tag{2-48}$$

where the linear part $\vec{P}_L$ and the nonlinear part $\vec{P}_{NL}$ are related to the electric field by the following relations

$$\vec{P}_L = \varepsilon_0 \chi^{(1)} \vec{E}, \tag{2-49}$$

$$\vec{P}_{NL} = \varepsilon_0 \chi^{(3)} \vec{E} \cdot \vec{E} \cdot \vec{E}. \tag{2-50}$$

To derive the basic propagation equation that governs the propagation of optical pulses in nonlinear dispersive fibers, the starting point is to take the curl of Eq. (2-42) and using Eq. (2-43), (2-46), (2-47) and (2-48), then we will obtain

$$\nabla^2 \vec{E} - \frac{1}{c^2}\frac{\partial^2 \vec{E}}{\partial t^2} = -\mu_0 \frac{\partial^2 \vec{P}_L}{\partial t^2} - \mu_0 \frac{\partial^2 \vec{P}_{NL}}{\partial t^2}. \tag{2-51}$$

To solve Eq. (2-51), it is necessary to make several simplifying assumptions such the following items

1. $\vec{P}_{NL}$ is treated as a small perturbation to $\vec{P}_L$.

2. The optical field is assumed to maintain its polarization along the fiber length so that a scalar approach is valid.

3. The center frequency of the optical field is assumed to locate at ω_0 and has the spectral width $\Delta\omega$ such that $\Delta\omega/\omega_0 << 1$. This assumption is valid for pulses whose width is $\leq$ 0.1 ps.

4. Assuming that the slow-varying envelope approximation can be applied to this case.

By the last item of the above assumptions, we can separate the rapidly varying part of the electric field and the induced polarization components by writing them in the form

$$\vec{E}(\vec{r},t) = \frac{1}{2}\hat{x}E(\vec{r},t)\{\exp(-i\omega_0 t) + \exp(i\omega_0 t)\}, \tag{2-52}$$

$$\vec{P}_L(\vec{r},t) = \frac{1}{2}\hat{x}P_L(\vec{r},t)\{\exp(-i\omega_0 t) + \exp(i\omega_0 t)\}, \tag{2-53}$$

$$\vec{P}_{NL}(\vec{r},t) = \frac{1}{2}\hat{x}P_{NL}(\vec{r},t)\{\exp(-i\omega_0 t) + \exp(i\omega_0 t)\}, \tag{2-54}$$

where $\hat{x}$ is the polarization unit vector of the light assumed to be linearly polarized along the *x*-axis, and $E(\vec{r},t)$ is a slowly varying function of time.

To obtain the wave equation for the slowly varying amplitude $E(\vec{r},t)$, it is more convenient to work in the Fourier domain. Substituting Eq. (2-52)-(2-54) into Eq.(2-51), using the relation between electric fields and induced polarization given by Eq. (2-53) and then taking the Fourier transform, we will obtain

$$\nabla^2 \tilde{E}(\vec{r},\omega-\omega_0)-\varepsilon(\omega)k_0^2\tilde{E}(\vec{r},\omega-\omega_0)=0, \tag{2-54}$$

where $\tilde{E}(\vec{r},\omega-\omega_0)$ is the envelope function in Fourier domain defined by

$$\tilde{E}(\vec{r},\omega-\omega_0)=\int_{-\infty}^{\infty}E(\vec{r},t)\exp(i(\omega-\omega_0)t)dt, \tag{2-55}$$

k_0 is the wave number, and the dielectric constant $\varepsilon(\omega)$ is given by

$$\varepsilon(\omega)=1+\tilde{\chi}^{(1)}(\omega)+\varepsilon_{NL}, \tag{2-56}$$

where $\tilde{\chi}^{(1)}(\omega)$ is the Fourier transform of $\chi^{(1)}(t)$, and the nonlinear part ε_{NL} is given by

$$\varepsilon_{NL}=\frac{3}{4}\chi^{(3)}\left|E(\vec{r},t)\right|^2. \tag{2-57}$$

The dielectric constant can be used to define the refractive index $\bar{n}$ and the absorption α by the relation

$$\varepsilon=(\bar{n}(\omega)+i\alpha/2k_0)^2, \tag{2-58}$$

so that $\bar{n}$ will be intensity dependent by the relation

$$\bar{n}(\omega)=n(\omega)+n_2\left|E\right|^2, \tag{2-59}$$

where n_2 is defined as the nonlinear refractive index given by

$$n_2=\frac{3}{8n}\chi^{(3)}. \tag{2-60}$$

If we assume a solution of Eq. (2-54) has the form

$$\tilde{E}(\vec{r},\omega-\omega_0)=F(x,y)\tilde{A}(z,\omega-\omega_0)\exp(i\beta_0 z), \tag{2-61}$$

where $\tilde{A}(z,\omega-\omega_0)$ is a slowly varying function of z, and $F(x, y)$ is the modal distribution of the optical field in an optical fiber. Substituting Eq. (2-61) into Eq. (2-54) then the two equations for $\tilde{A}(z,\omega-\omega_0)$ and $F(x, y)$ will be obtained as

$$\frac{\partial^2 F}{\partial x^2}+\frac{\partial^2 F}{\partial y^2}+\left\{\varepsilon(\omega)k_0^2-\bar{\beta}^2\right\}F=0, \tag{2-62}$$

$$2i\beta_0 \frac{\partial \tilde{A}}{\partial z} + \{\bar{\beta}^2 - \beta_0^2\}\tilde{A} = 0 . \tag{2-63}$$

Eq. (2-62) can be solved by using first-order perturbation theory. However, we should concentrate to the more important Eq. (2-63) that can explain pulses propagation in optical fibers.

The eigen value $\bar{\beta}(\omega)$ has the form

$$\bar{\beta}(\omega) = \beta(\omega) + \Delta\beta , \tag{2-64}$$

where

$$\Delta\beta = \frac{k_0 \int_{-\infty}^{\infty}\int \Delta n |F(x,y)|^2 \, dxdy}{\int_{-\infty}^{\infty}\int |F(x,y)|^2 \, dxdy} . \tag{2-65}$$

and

$$\Delta n = n_2 |E|^2 + \frac{i\alpha}{2k_0}, \tag{2-66}$$

By using Eq. (2-64), Eq. (2-63) can be written as

$$\frac{\partial \tilde{A}}{\partial z} = i(\beta(\omega) + \Delta\beta - \beta_0)\tilde{A} . \tag{2-67}$$

where we approximated $\bar{\beta}^2 - \beta_0^2$ by $2\beta_0(\bar{\beta} - \beta_0)$.

The inverse Fourier transform of Eq. (2-67) provides us the propagation equation for $A(z,t)$. For this purpose, it is useful to expand $\beta(\omega)$ in a Taylor series about the carrier frequency ω_0,

$$\beta(\omega) = \beta_0 + \beta_1(\omega - \omega_0) + \frac{1}{2}\beta_2(\omega - \omega_0)^2 + \frac{1}{6}\beta_3(\omega - \omega_0)^3 \ldots , \tag{2-68}$$

where

$$\beta_n = \left(\frac{d^n \beta}{d\omega^n}\right)_{\omega=\omega_0} . \tag{2-69}$$

As mentioned above, β_2 and β_3 are responsible for the second-order and third-order dispersion, respectively. In the zero-dispersion region, only the effect of β_2 vanishes, however, it is necessary to include the high-order terms of dispersion. The higher-order terms in this expansion are negligible if the spectral width $\Delta\omega/\omega_0$ << ω_0 corresponding to the pulse width > 0.1 ps. Substituting Eq. (2-68) in Eq. (2-67) and

considering only to the third-order dispersion term, the inverse Fourier transform of Eq. (2-67) will be

$$\frac{\partial A}{\partial z} = -\beta_1 \frac{\partial A}{\partial t} - \frac{i}{2}\beta_2 \frac{\partial^2 A}{\partial t^2} + \frac{1}{6}\beta_3 \frac{\partial^3 A}{\partial t^3} + i\Delta\beta A, \tag{2-70}$$

where A is the inverse Fourier transform of the envelope function $\tilde{A}$. By substituting Eq. (2-66) and Eq. (2-65) in Eq. (2-70), we will obtain

$$\frac{\partial A}{\partial z} + \beta_1 \frac{\partial A}{\partial t} + \frac{i}{2}\beta_2 \frac{\partial^2 A}{\partial t^2} - \frac{1}{6}\beta_3 \frac{\partial^3 A}{\partial t^3} + \frac{\alpha}{2}A = i\gamma |A|^2 A, \tag{2-71}$$

where the nonlinear coefficient γ is defined by

$$\gamma = \frac{n_2 \omega_0}{c A_{eff}}. \tag{2-72}$$

The parameter A_{eff} is known as the effective core area and is given by

$$A_{eff} = \frac{\left(\int_{-\infty}^{\infty} \int |F(x,y)|^2 \, dxdy \right)^2}{\int_{-\infty}^{\infty} \int |F(x,y)|^4 \, dxdy}. \tag{2-73}$$

For a single-mode fiber, the modal distribution $F(x,y)$ corresponds to the distribution of the fundamental fiber mode HE_{11} given by the expression of Bessel functions which is too complicated for calculating. In practice, the fundamental fiber mode is often approximated by a Gaussian distribution of the form

$$F(x,y) = \exp\left(-\frac{x^2 + y^2}{a^2} \right), \tag{2-74}$$

where a is the fiber core radius.

Equation (2-71) describes the propagation of an optical pulse in single-mode fibers. It includes the effects of fiber loss through α, of chromatic dispersion through β_1, β_2, and β_3, and of fiber nonlinearity through γ. However, if we consider an ultra-short pulse whose width is shorter than 0.1 ps or a pulse whose peak power is larger than the threshold level of stimulated inelastic scattering such as SRS and SBS, it may need modification for supplying these effects.

Before attempting to solve the propagation equation (2-71), it is useful to employ a frame of reference moving with the pulse at the group velocity v_g $\left(v_g = 1/\beta_1\right)$. By making the transformation

$$T = t - \frac{z}{v_g} = t - \beta_1 z\,, \tag{2-75}$$

Equation (2-72) can be written as

$$\frac{\partial A}{\partial z} = -\frac{\alpha}{2}A - \frac{i}{2}\beta_2 \frac{\partial^2 A}{\partial T^2} + \frac{1}{6}\beta_3 \frac{\partial^3 A}{\partial T^3} + i\gamma |A|^2 A\,. \tag{2-76}$$

Equation (2-76) is sometimes called the generalized nonlinear Schrodinger equation. In the special case of $\alpha = 0$ and $\beta_3 = 0$, Eq. (2-76) is well known as the nonlinear Schrodinger equation which has been extensively studied in the context of soliton.

2.3 Numerical Method: the Split-Step Fourier

To understand the propagation of the pulse in an optical fiber, it is necessary to solve Eq. (2-76). However, the propagation equation (2-76) generally does not have the analytic solutions except for some specific cases such as the soliton case which the inverse scattering method can be employed. Because of this reason, a numerical method is therefore necessary for solving this equation. In this thesis, we used the numerical method called split-step Fourier method (SSFM) [4], [74] which has been extensively used to solve the nonlinear equation. By this method, a fiber length is divided into a large number of small segments of width δ where each segment is assumed to have the effects of nonlinearlities or the dispersive effects only. Thus, by using an iterative procedure, we can utilize the Fourier transform to solve the propagation of the pulse that is disturbed only by the effects of dispersions and the effects of nonlinearities separately. This separation of the calculation of dispersion effects and nonlinearity leads to a possibility for solving Eq. (2-76)

Equation (2-76) can be written as

$$\frac{\partial A}{\partial z} = \left(\hat{D} + \hat{N}\right)A\,, \tag{2-77}$$

where the differential operator $\hat{D}$ includes the first two terms involving loss and dispersion while $\hat{N}$ consists of the last nonlinear term, i. e. ,

$$\hat{D} = -\frac{\alpha}{2} - \frac{i}{2}\beta_2 \frac{\partial^2}{\partial T^2} + \frac{1}{6}\beta_3 \frac{\partial^3}{\partial T^3}\,, \tag{2-78}$$

$$\hat{N} = i\gamma |A|^2\,. \tag{2-79}$$

As mentioned above, in general dispersion and nonlinearity act together along the length of the fiber. The SSFM obtains an approximate solution by assuming that

in propagating the optical field over a small distance δ, the dispersive and nonlinear effects can be pretended to act independently. More specifically, propagation from *z* to $z+\delta$ is carried out in two steps. In the first step, dispersion acts alone, and $\hat{D}$ = 0 in Eq. (2-77). In the second step, dispersion acts alone, and $\hat{N}$ = 0 in Eq. (2-77). Mathematically, the approximate solution can be obtain as

$$A(z+\delta,T) \approx \exp(\delta\hat{D})\exp(\delta\hat{N})A(z,T). \tag{2-80}$$

Figure 2.11 shows the propagation of optical field $A(z,T)$ in a small segment of fiber δ when the nonlinearity and dispersion are assumed to act independently.

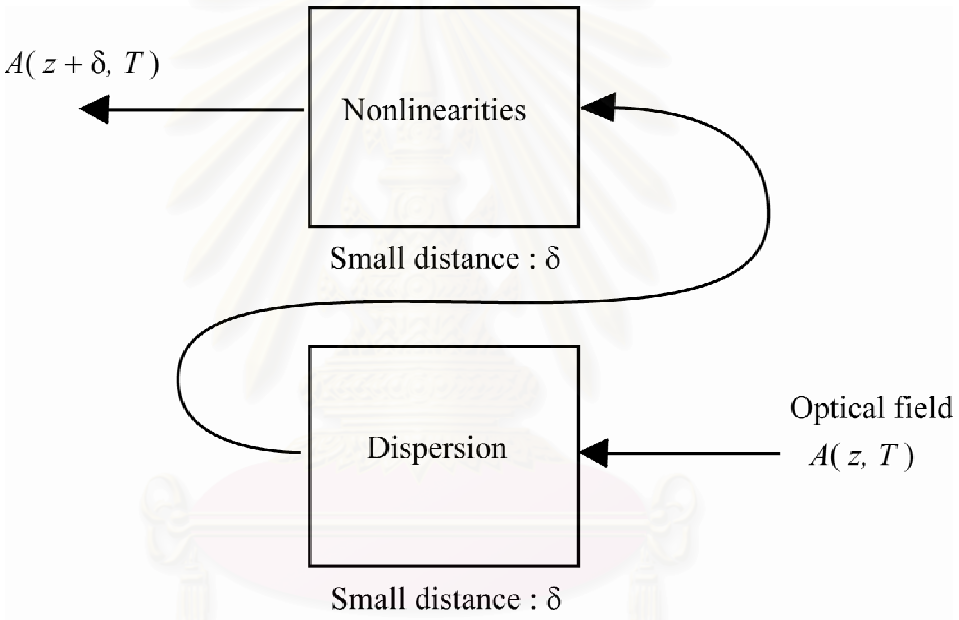

Figure 2.11: Propagation of optical field $A(z,T)$ in a small segment of fiber δ when the nonlinearity and dispersion are assumed to act independently.

To perform the SSFM, it is necessary to use the differential operation $\hat{D}$ in Fourier domain. By replacing $\frac{\partial}{\partial T}$ with $i\omega$, we will obtain

$$F\left\{\hat{D}\right\} = -\frac{\alpha}{2} + \frac{i}{2}\beta_2\omega^2 - \frac{i}{6}\beta_3\omega^3, \tag{2-81}$$

where *F* denotes the Fourier-transform operation. Equation (2-80) can be written in the form of SSFM as

$$A(z+\delta,T)=F^{-1}\left\{\exp\left(\delta\hat{D}(i\omega)\right)F\left\{\exp\left(\delta\hat{N}\right)A(z,T)\right\}\right\}. \quad (2\text{-}82)$$

Figure 2.12 shows the calculation route of optical field propagating in fiber based on SSFM for the case that the fiber is divided into 4 small segments.

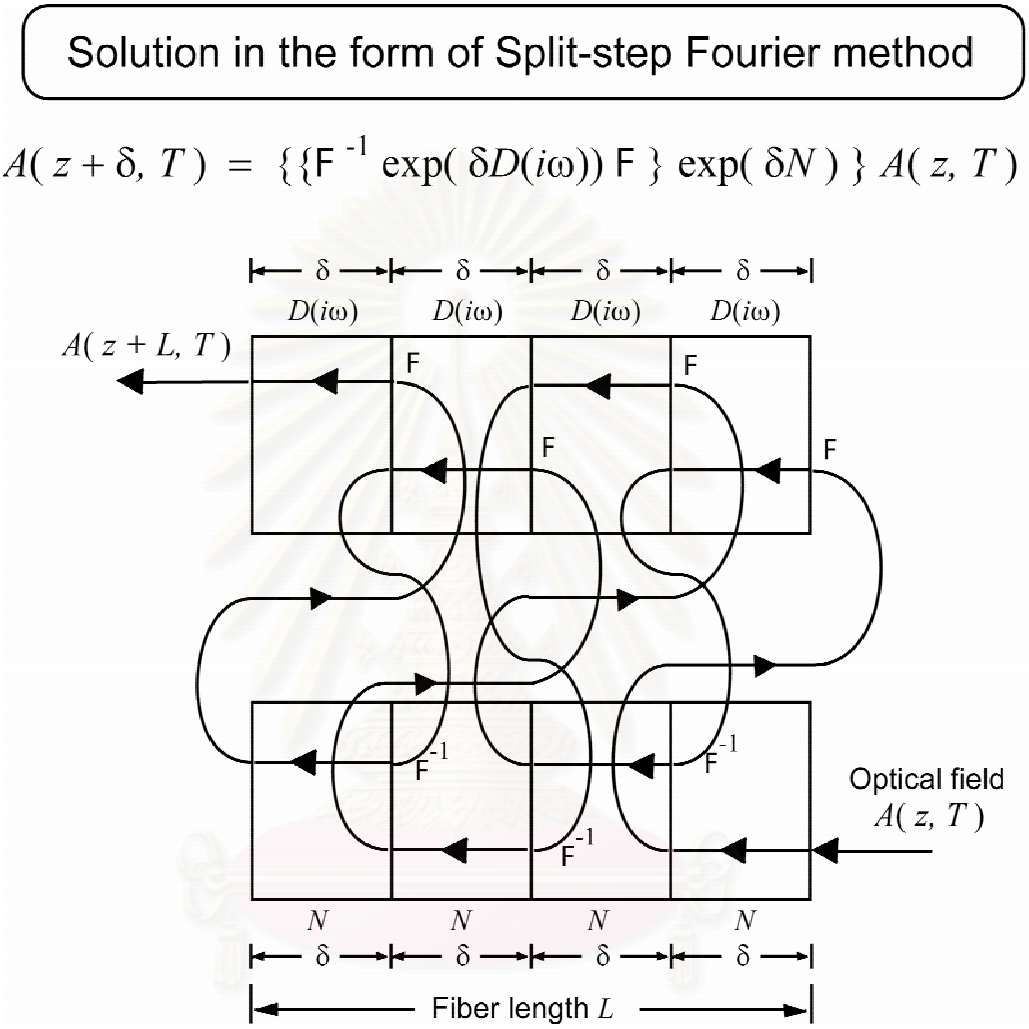

Figure 2.12: Calculation route of optical field propagating in fiber based on SSFM for the case that the fiber is divided into 4 small segments.

The speed of this SSFM directly depends on an algorithm of Fourier-transform. In this thesis, we use the algorithm of FFT(Fast Fourier Transform) [94] which can makes this numerical evaluation of Eq. (2-82) relatively fast. About the accuracy of the SSFM, the dominant error term is found to result from the single commutator [4]

$$\frac{1}{2}\delta^2\left(\hat{D}\hat{N}-\hat{N}\hat{D}\right). \quad (2\text{-}83)$$

From the result of Eq. (2-83), the SSFM is accurate to second order in the step size δ, thus the improvement of accuracy of this method can be perform by reducing the step width. Furthermore, The accuracy of the SSFM can be improved by adopting a different procedure which includes the effect of nonlinearity only at the midplane and uses an iterative calculation performed on each half step. In this procedure Eq. (2-84) is replaced by

$$A(z+\delta,T) \approx \exp\left(\frac{\delta}{2}\hat{D}\right)\exp\left(\int_{z}^{z+\delta}\hat{N}(z')dz'\right)\exp\left(\frac{\delta}{2}\hat{D}\right)A(z,T). \tag{2-85}$$

Because of the symmetric from of the exponential operators in Eq. (2-85), this method is known as the symmetrized SSFM. The integral in the middle exponential is useful to include the *z* dependence of the nonlinear operator $\hat{N}$. If the step size δ is small enough, it can be approximated by $\exp(\delta\hat{N})$. The accuracy of the SSFM can be further improved by evaluating the integral in Eq. (2-85) more accurately than approximating it by $\delta\hat{N}(z)$. A simple approach is to approximate the integral by

$$\int_{z}^{z+\delta}\hat{N}(z')dz' \approx \frac{h}{2}\left\{\hat{N}(z)+\hat{N}(z+\delta)\right\}. \tag{2-86}$$

However, the implementation of Eq. (2-86) is not simple since $\hat{N}(z+\delta)$ is unknown at the midsegment located at $z+\delta/2$. It is necessary to follow an iterative procedure that is initiated by replacing $\hat{N}(z+\delta)$ by $\hat{N}(z)$. Equation (2-85) is then used to estimate $A(z+\delta,T)$, which in turn is used to calculate the new value of $\hat{N}(z+\delta)$. Although the iteration procedure is time-consuming, it can still reduce the overall computing time if the step size δ can be increased because of the improved accuracy of the numerical algorithm. Two iterations are generally enough in practice.

In this dissertation, the SSFM is mainly used for simulating signal propagation in optical fibers. The implementation of the SSFM in this thesis is conceptually shown in Fig. 2.13. The fiber length is divided into a large number of segments that need not to be equi-spaced. The optical signal is propagated from the segment to segment using the prescription of Eq. (2-85). More specifically, the optical field $A(z,T)$ is first propagated for a distance midplane $z+\delta/2$, the field is multiplied by a nonlinear term that represents the effect of nonlinearity over the whole segment length δ. Finally, the field is propagated the remaining distance $\delta/2$ with dispersion

only to obtain $A(z+\delta,T)$. In effect, the nonlinearity is assumed to be lumped at the midplane of each segment.

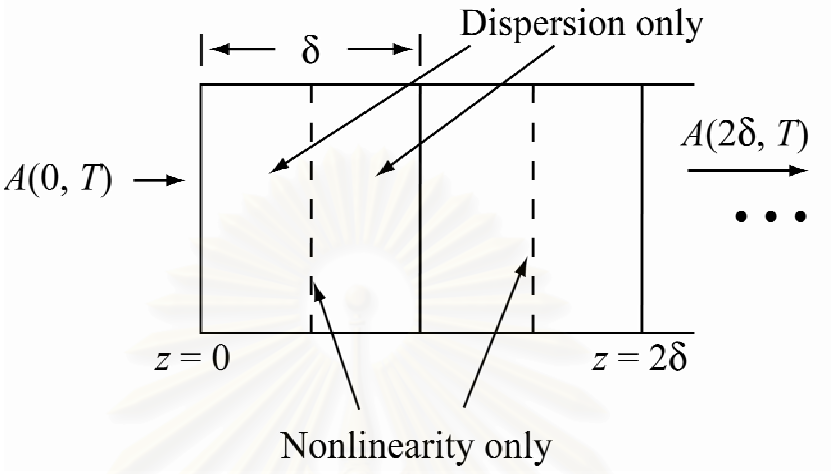

Figure 2.13: Calculation procedure of the symmetric SSFM.

2.4 Preparation before Simulation

Because we concern both amplitude and phase of the optical field $A(z,T)$, so that $A(z,T)$ is assumed to be the complex function.

$$A(z,T) = A_r(z,T) + iA_i(z,T). \tag{2-87}$$

For initial field of simulation, since we use the algorithm of fast-Fourier transform (FFT) in the SSFM, $A(0,T)$ is sampling with the sampling interval ΔT to be the discrete function consists of *n*-data: $A^*(n\Delta T)$. Initially, it is convenient to set the relative phase of the optical field to zero thus the discrete field can be written as

$$A^*(0,n\Delta T) = A_r^*(0,n\Delta T). \tag{2-88}$$

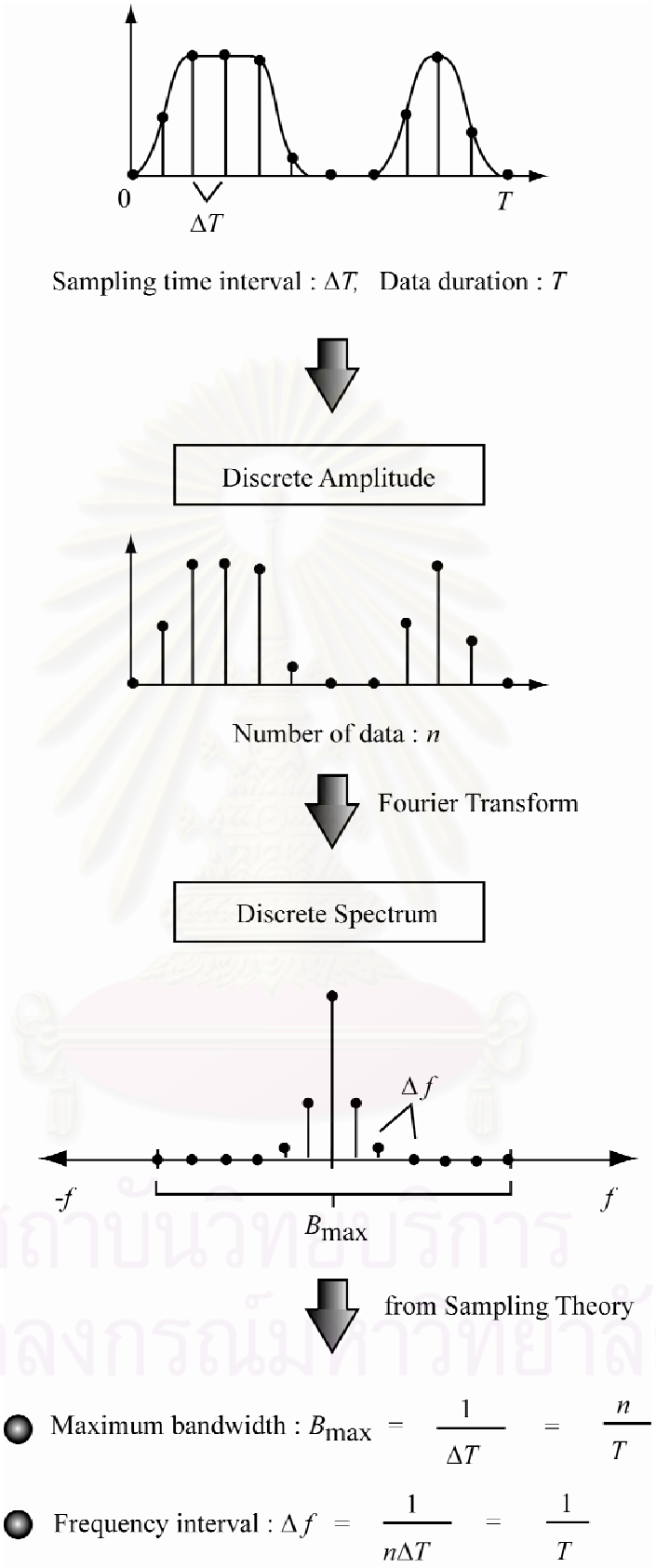

Figure 2.14: Relation between sampling interval and maximum spectral bandwidth according to sampling theory.

As shown in Fig. 2.14, according to the sampling theory, after performing Fourier transform of $A^*(z, n\Delta T)$, the maximum bandwidth of its discrete spectral window $B_{\max}$ will be limited by the sampling interval ΔT or the number of data *n* by the relation [97]

$$B_{\max} = \frac{1}{\Delta T} = \frac{n}{T}, \tag{2-89}$$

where *T* denotes the duration of discrete field $A^*(z, n\Delta T)$. Using the above relations, the frequency interval Δf of discrete spectrum of $A^*(z, n\Delta T)$ is obtained by

$$f = \frac{1}{n\Delta T} = \frac{1}{T}. \tag{2-90}$$

The relation between maximum bandwidth and number of sampled data predicts that it is impossible to assume the free-space bandwidth since the bandwidth is limited by the number of sampled data. To increase the maximum bandwidth, it is necessary to increase the number of sampled data. In this dissertation we use the number of sampled data *n* = 2048 for all calculations.

CHAPTER 3
OPTICAL TRANSMISSION SCHEMES FOR SYSTEM USING OPTICAL AMPLIFICATION

When the electronic repeaters are replaced with the optical amplifiers, the problem which is necessary to be overcome first is considerably originated from fiber dispersion that causes the broadening of the signal pulses during propagation inside the fiber. There are many systems that have been proposed in order to overcome the dispersion effect.

3.1 Zero-Dispersion Wavelength Transmission [17]-[20]

According to the dispersion characteristic of optical fibers shown in Fig. 2.2, the group-velocity dispersion (GVD) parameter β_2 and the second-order dispersion (SOD) parameter D vanish at the wavelength of λ_D which is referred to 1.55 μm for the DSF. The idea of this kind of system is simple: setting an operation wavelength of the system at zero-dispersion (SOD) point so that the pulses can propagate without broadening. The advantages of the zero-dispersion systems arise from their simple construction and the avoidance from dispersion-limited performance. However, it is considerably difficult to set the operation wavelength exactly at the zero-dispersion point.

The problems of the zero-dispersion systems, as discussed above, grow up from the third-order dispersion (TOD) resulting in pulse distortion and broadening [4], [17]. When the input power of the signal becomes intense, the nonlinearity of the fiber mainly causes the problems in zero-dispersion transmission. The two main problems in zero-dispersion transmission induced from fiber nonlinearity are the interaction between SPM and TOD and the enhancement of optical amplifier noise due to SPM [18]-[20]. The above two problems seriously result the signal waveform distortion and the rapid spreading of signal spectra.

3.2 Dispersion Management [21]-[35].

As discussed above, fiber systems whose operation wavelength is located directly at the zero-dispersion point encounter problems mainly induced by the nonlinearity of optical fibers. Since the SOD length defined by Eq. (2-6) becomes infinity and no

longer is compared to the nonlinear length at zero-dispersion point, the nonlinearity becomes stronger and pays important role in limiting the system performance. In order to avoid the nonlinear problems, a very slight displacement of a carrier wavelength from zero-dispersion wavelength may be one way to alleviate the problems [21]-[35].

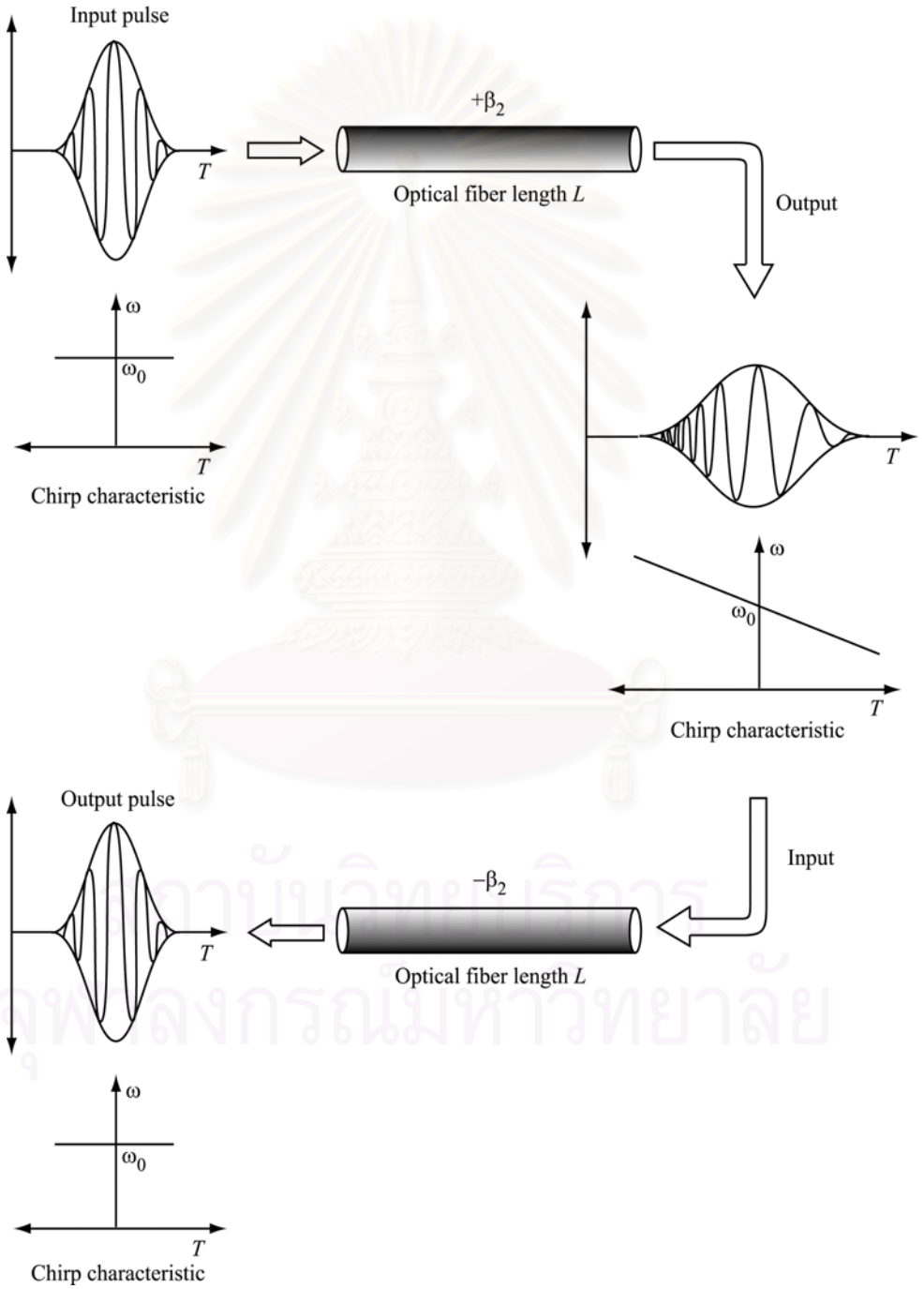

Figure 3.1: Concept of dispersion management method.

Furthermore, the more sufficient method is to arrange the various sections of fiber in such a way that none or only very few of them have zero-dispersion wavelengths that coincide with the carrier wavelength while the total fiber exhibits zero SOD on average. A method for construction a fiber system which consists of fiber sections that are arranged such that the SOD of each amplifiers span is zero at the operation wavelength are generally called dispersion management.

The idea of dispersion management comes from the completely cancellation of the frequency chirp resulting in the recovery of the pulse shape. If we consider the fiber section consisting of two pieces of fibers with the same value of SOD but different symbols (+ and -) shown in Fig. 3.1. This section of fiber exhibits the zero SOD on average. An optical pulse launched to this fiber will be frequency-chirped induced by the SOD. The pulse will be broadened due to the SOD-induced pulse broadening. However, when the pulse is entered to the fiber which exhibits the opposite SOD symbol, the frequency-chirping occurs in the opposite direction so that it will cancel the chirp induced by the first fiber resulting in pulse compression.

3.3 Optical Soliton [36]-[47]

Soliton refers to special kind of waves that can propagate undistorted over long distances and remain unaffected after collision with each other. Optical soliton in optical fiber is conformed by balancing the fiber dispersion and nonlinear self-phase modulation (SPM) in anomalous dispersion region [4], [5], [36]. Quantitatively, this can be achieved by launching optical pulses with proper input power and width into the fiber. The most attractive characteristic of optical soliton is that they can propagate in optical fibers without pulse shape distortion over a long distance if the fiber loss is negligible. There are other several other reasons why soliton is attractive for optical communication systems generally and therefore why they should be considered as a possible route for system upgrades. In particular, soliton is compatible with all optical switching and routing technologies [11]. The ability to optically process signal is essential if the bottleneck problems encountered at switching nodes are to be overcome for the high data rates.

The generation of optical soliton in optical fibers based on the idea of dispersion compensation which is achieved by the frequency-chirp cancellation occurring by transmitting optical pulses in two pieces of optical fibers whose symbols

of SOD are opposite. In the case of nonlinear effect, if we launch an intense optical pulse to the fiber with operating wavelength situating at anomalous dispersion region, the nonlinear up-chirp will occur through the SPM and at the same time the linear down-chirp will be induced by the anomalous dispersion. Since the chirp induced by SPM and chirp induced by the SOD exhibit opposite symbols, they will cancel each other during propagation inside resulting in pulse compression or broadening depending on the input power of the pulse. If we enter the optical pulse to the fiber with an appropriated power which is related to the value of β_2 and pulse width, the nonlinear up-chirp and linear down-chirp will cancel each other in such a way that no pulse compression and pulse broadening during propagation. Such the optical pulse which can travel inside the fibers with no change in pulse shape and spectrum by balancing the effect of SPM and SOD refers to the optical soliton.

Figure 3.2 illustrates how the soliton can maintain its shape during the propagation by the balance of frequency chirp by SPM and chirp by fiber SOD in anomalous dispersion region. Qualitatively, in the absence of fiber loss, such soliton phenomena can be met at the balance point of SOD effect and SPM via the condition: $L_{nl} = L_{d2}$, which yields the input power P_0 required for conforming the soliton for given β_2 and pulse width T.

The problems in soliton transmission systems are roughly classified into the following three problems: the fiber loss, [4], [5], [42]-[44] the mutual interaction between adjacent solitons [4], [45], and the Gordon-Haus effect [46], [47]. To transmit soliton pulses through actual optical fibers, especially for a long distance, it is necessary to consider the fiber loss. The fiber loss results in exponentially increase of soliton width and decrease of soliton peak. It is necessary to amplify the soliton periodically to maintain its power. With the EDFA, the soliton power is amplified to amplitude larger than that required for forming the fundamental soliton (the soliton in lossless fibers) so that its average power along the fiber is still the fundamental soliton power. Such a soliton called the guiding-center soliton [42] or average soliton [43], which is stable when the ratio of the amplifier spacing and the soliton period is much less than unity [44].

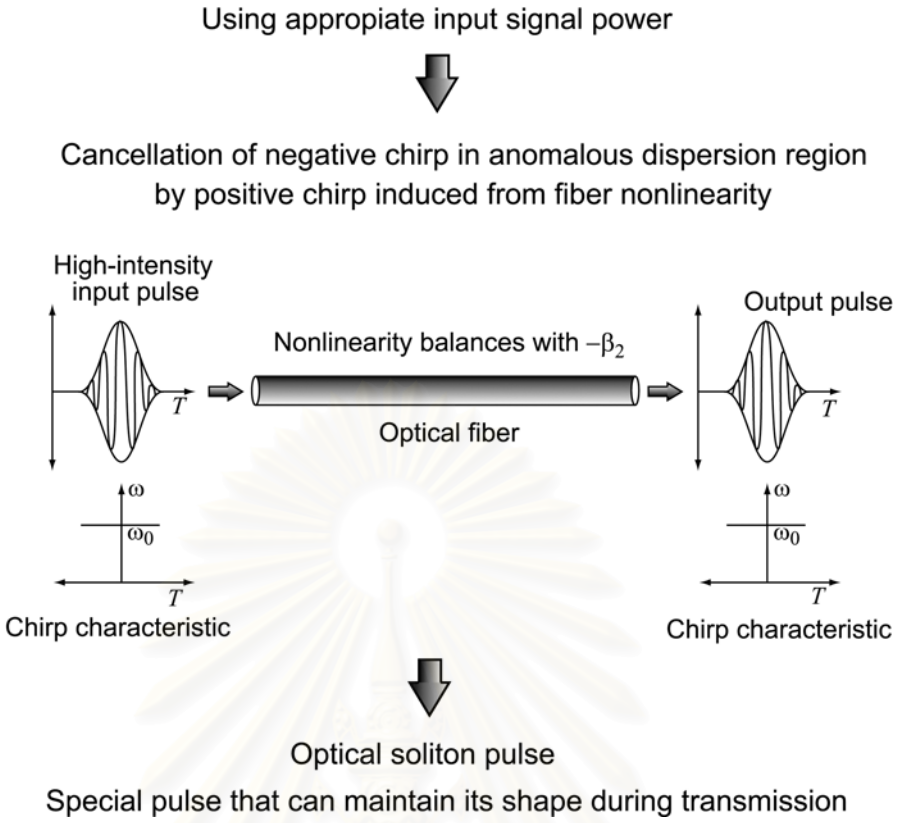

Figure 3.2: Soliton generated by the balance of SPM and fiber SOD in anomalous dispersion region.

In addition to the stability requirement, there are two other effects limiting the capacity of soliton transmission. When the solitons are closely spaced, the mutual interaction changes the velocity of the solitons and causes the soliton to move out of the detection window [4], [45]. On the other hand, the noise introduced by the optical amplifier randomly modulates the carrier frequency of the soliton, and the group velocity varies. This effect leads to the timing jitter and is known as the Gordon-Haus effect [46], [47].

3.4 Midway Optical Phase Conjugation [48]-[52].

This kind of system performs optical phase conjugation (OPC) at the midpoint of system in order to compensate both dispersive and nonlinear effects. If all of the system characteristics in the first half is symmetrical to the second half with respect to the midway OPC, when we generate the conjugate signal of the first-half-transmitted signal at the midway of the system, all of the phase distortions induced in the first half

are completely compensated via the self-recovery effect of the conjugate signal when transmitting through the second half of the system.

Figure 3.3 shows schematically the midway OPC system. The optical phase conjugator is placed at the midpoint of the system. Under the condition that all of the system characteristics are symmetric with respect to the midway OPC, generating the conjugate signal of the first-half-transmitted signal at the midway of the system, all of the phase distortions induced in the first half are completely compensated via the self-recovery effect of the conjugate signal when transmitting through the second half of the system. However, in real transmission, three problems including one from an asymmetric system characteristic occur and limit a performance of OPC systems.

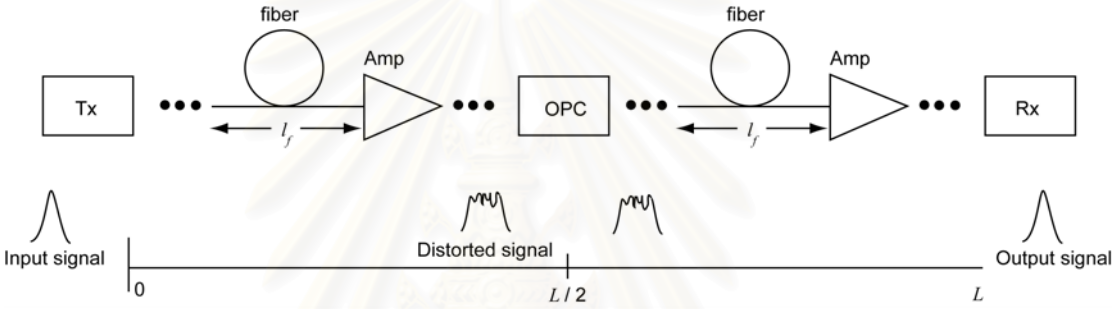

Figure 3.3: Optical transmission system with midway OPC.

According to the nonlinear Schrodinger equation (NLSE) (Eq. (2-76), which governs the propagation of signal pulses in an optical fiber, taking the complex conjugation of NLSE, we obtain

$$-\frac{\partial A^*}{\partial z} = +\frac{\alpha}{2}A^* - \frac{i}{2}\beta_2\frac{\partial^2 A^*}{\partial T^2} - \frac{1}{6}\beta_3\frac{\partial^3 A^*}{\partial T^3} + i\gamma\left|A^*\right|^2 A^*, \qquad (3\text{-}1)$$

where * denotes the complex conjugate operation. Eq. (3-1) describes the complex conjugate amplitude of the signal A propagating in backward direction through the fiber which exhibit reverse sign of α and β_3. According to Eq. (2-76) and (3-1) indicates that if we generate the complex conjugate of the distorted pulses at the midway of a transmission link and let them travel through the second half of the link, we will obtain the complex conjugate of the undistorted input pulses at the output end. The nonlinear waveform distortion caused by the fiber nonlinearity and the dispersion is thus perfectly compensated at the output end. However, to achieve the perfect compensation two conditions are needed. First, the transmission fiber of the second

half must have negative β_3 while its β_2 still keeps the same sign as that of first half. Second, the propagation of signal through the second half requires a distributed gain instead of distributed loss since the sign of α must be reversed.

According to the first requirement, the widely-used transmission fibers such as SMF and dispersion-shifted fiber (DSF) both exhibit positive TOD. Therefore, similar to other systems, the TOD in OPC systems cannot be compensated by OPC but it just accumulates along the system length and will also cause the signal waveform distortion [48], [49]. On the other hand, the second condition can be satisfied only in an ideal lossless medium. In real system with long distance transmission, a periodic lumped amplification must be used for maintain signal power in order to obtain good signal-to-noise ratio (SNR) at receiver. The fiber loss and this periodic amplification forms a periodic signal power distribution along the system length and at the same time produces a periodic variation of fiber refractive index through the nonlinear Kerr effect of an optical fiber. By this process, it seems like a grating is virtually constructed in the transmission fiber. As shown in Fig. 3.4, a resonance between the virtual grating and the signal will occur at the signal sideband component whose wave vector matches the wave vector of this virtual grating resulting in exponential growth of that component with transmission length. This phenomenon is known as the sideband instability (SI), which causes signal waveform distortion if SI arises at frequency inside the signal bandwidth, which cannot be eliminated by using optical bandpass filter [50]-[52].

Qualitatively, SI can be considered as four-wave mixing (FWM) effect which is quasi-phase-matched by the assistance of the periodic power variation induced virtual grating as the condition

$$k_+ + k_- = 2k_0 + k_f . \tag{3-2}$$

In Eq. (3-2), k_0 denote the wave number of the signal which acts as a pump, $k_\pm$ the sideband wave numbers, and k_f the wave number of the virtual grating which is given as

$$k_f = \frac{2\pi n}{l_f}, \tag{3-3}$$

where $n = 0,\pm1,\pm2,...,$ and l_f is the amplifier spacing. The sideband frequency ω_n shifted from the carrier frequency, at which SI arises is obtained from Eq. (3-2) and (3-3) as

$$\omega_n = \pm\sqrt{\frac{1}{|\beta_2|}\left(k_f n - 2\,\mathrm{sgn}(\beta_2)\overline{P}\right)}. \tag{3-4}$$

where $\overline{P}$ is the path-averaged signal power. The power gain $\lambda(\omega_n)$ of SI at each *n*-order resonance frequency is

$$\lambda(\omega_n) = 2P_0|F_n|, \tag{3-5}$$

where P_0 denotes the signal input power and F_n the *n*-order of the Fourier series coefficient of the periodic function $\alpha(z)$ whose period is equal to l_f.

In order to avoid the signal distortion due to the SI, C. Lorattanasane et al. has introduced the optimum system design strategies, which is shown conceptually in Fig. 3.5. Figure 3.5 shows the magnitude of signal degradation in OPC system as a function of the SOD in the absence of the TOD. In Fig. 3.5, two transmission windows are observed at relatively large anomalous dispersion region and at relatively low normal dispersion. The SI causes the serious signal distortion when the operation SOD becomes larger because the SI will occur at inner signal bandwidth according to Eq. (3-4). Therefore, the use of relatively low SOD is preferred. However, the lowest SOD that can be used is limited by the effect of the SOD fluctuation around zero-dispersion point. In anomalous dispersion region, the use of low SOD induces the modulation instability effect which will result in much signal degradation. Thus, for anomalous dispersion region, the optimum operation SOD is located at relatively large value.

As alternative method for reducing the effect of SI, Watanabe and Shirasaki have given a condition for perfect SI compensation [95] as shown below.

$$\frac{\beta_2(-z_1')}{\gamma(-z_1')P(-z_1')} = \frac{\beta_2(z_2')}{\gamma(z_2')P(z_2')}, \tag{3-6}$$

where the GVD parameter β_2, the nonlinear coefficient γ , and the signal power P are the function of distance *z*.

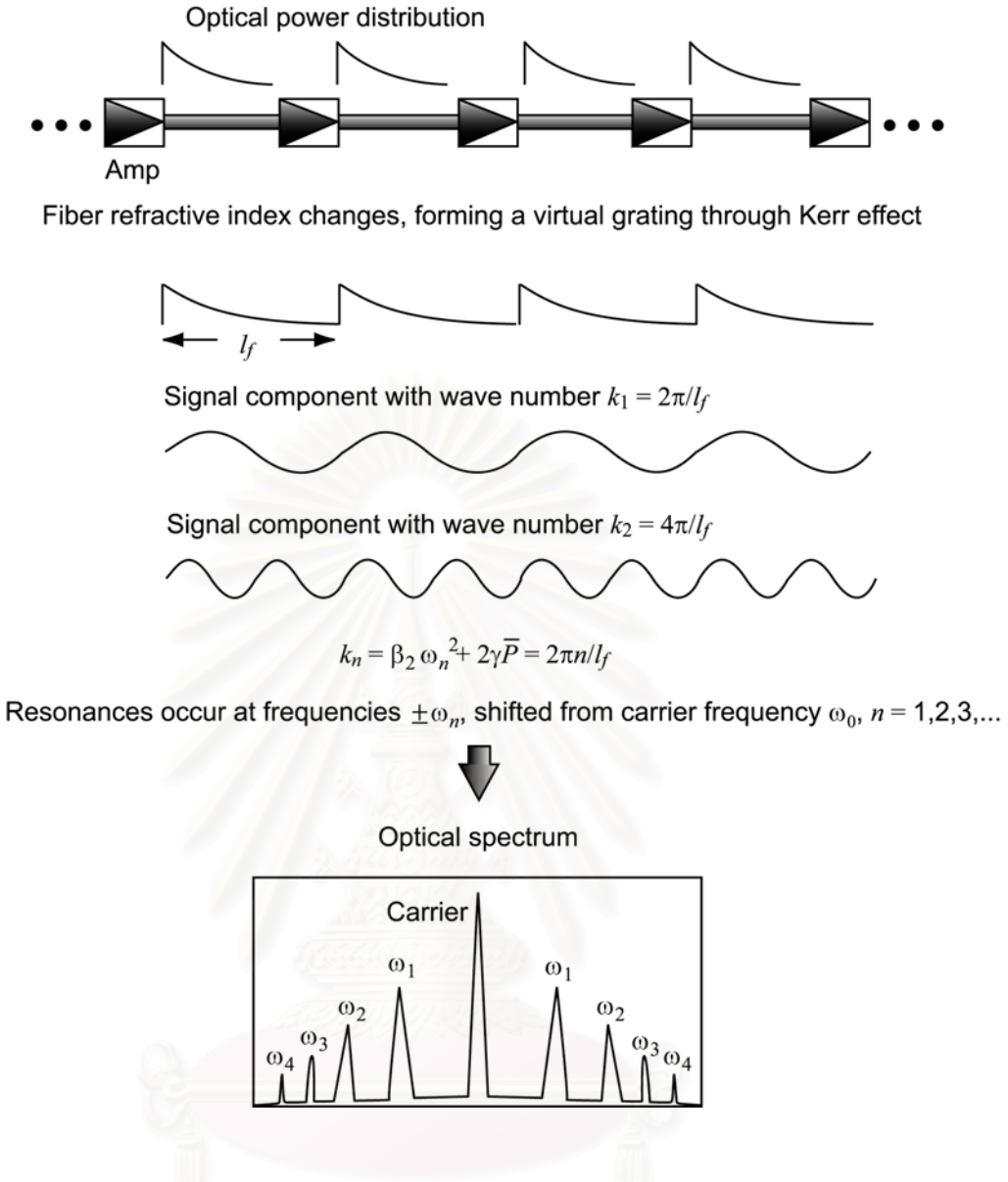

Figure 3.4: The occurrence of SI in chain of periodic amplification.

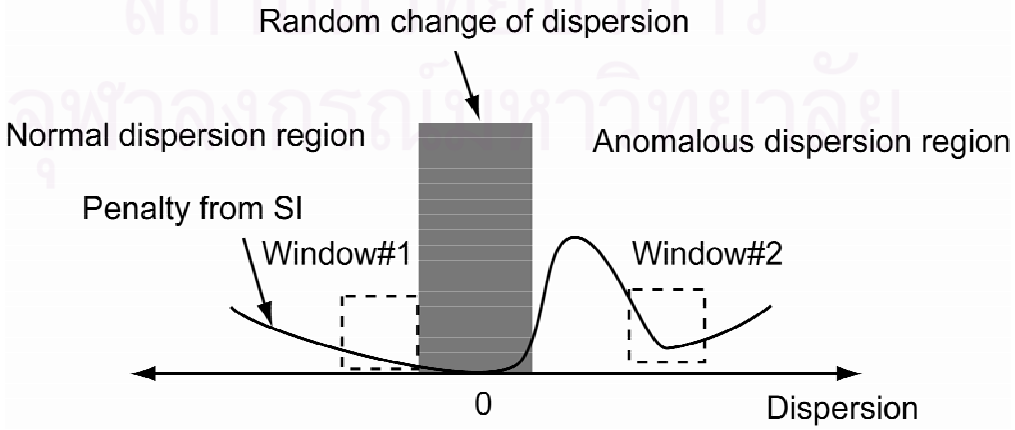

Figure 3.5: Operation windows for OPC systems.

Equation (3-6) indicates that the perfect suppression of SI is achieved when the cumulative SOD-induced chirp and the cumulative nonlinearity-induced chirp integrated from the OPC position at $z' = 0$ to $-z_1'$ and z_2' are equal. This relation means that providing the equal ratio of the SOD and the nonlinearity at the corresponding position symmetrical from the system midpoint, perfect distortion compensation can be obtained. This relation gives us the following freedoms for the OPC system design.

1) The OPC needs not be placed at the midway of the system. Assuming that the SOD value, the signal power, and the system length of the first half are D_A, P_A, and L_A, respectively, and those of the second section are D_B, P_B, and L_B, respectively. We find that Eq. (3-6) holds provided that $D_A = kD_B$, $P_A = kP_B$, and $kL_A = L_B$.
2) The power distribution needs not to be uniform. Equation (3-6) holds when the SOD value is properly tailored to follow attenuation of the signal power.

In order to satisfy the condition, a dispersion-decreasing (SOD) fiber (DDF), whose SOD-decreasing coefficient is proportional to a fiber loss coefficient, must be installed throughout the entire OPC system length. A good transmission result of 20 Gbit/s over 3,000 km [95] was demonstrated by using a quasi-DDF in which short fibers with different dispersion values were concatenated to form the dispersion-decreasing profile. However, such the approach sounds too impractical to be employed in real systems. Moreover, for both two proposed schemes the uncompensated TOD will show up to affect the long-haul transmission with the bit rate higher than 40 Gbit/s.

CHAPTER 4
THIRD-ORDER DISPERSION COMPENSATION IN OPC SYSTEMS

In this chapter, we prove that, in optical phase conjugation systems, the third-order dispersion of fibers almost linearly accumulates along the transmission distance, and the distortion induced from the third-order dispersion can be perfectly compensated by using a linear third-order dispersion compensator placed at any point of the system. We demonstrate by numerical simulations that 100-Gbit/s single-channel transmission can be achieved over a 10,000-km distance in midway optical phase conjugation transmission system by compensating the third-order dispersion using only one third-order dispersion compensator placed anywhere in the system [49].

4.1 Introduction

In ultra-high bit-rate optical-time-division multiplexed (OTDM) transmission systems, the second-order dispersion (SOD) of fibers for transmission must be completely compensated. With SOD averaged to zero, the third-order dispersion (TOD) shows up and influences transmission characteristics. Moreover, the TOD interplays with the self-phase modulation (SPM) of optical pulses, causing severe distortion of both signal waveform and signal spectrum [4].

In the dispersion-managed system using non-return-to-zero (NRZ) pulse format, where the SOD map is properly designed but the TOD is not compensated, the bit rate of the 10,000km transmission system is limited only about 10Gbit/s because of the interplay of the TOD with the SPM. It has been shown, by numerical simulations, that when the TOD is compensated periodically at the interval quite shorter than the nonlinear scale of the system, the speed limit is possibly raised up over 20Gbit/s [25].

On the other hand, in dispersion-managed (DM) soliton systems, a recent numerical study shows that the eigen solution to DM solitons can exist in the transmission line with the TOD, and that is stable against the perturbation of the TOD [40]. Even without TOD compensation, 40Gbit/s, 10,000km transmission has been actually demonstrated by using DM solitons [54].

As an alternative approach for high-bit-rate long-distance transmission, midway optical phase conjugation (OPC) is an attractive solution to compensating for

the distortion induced from the interplay between the SOD and the SPM [65]. The ultimate performance of the OPC systems is also limited by the TOD together with a nonlinear resonance at well-defined signal sideband frequencies induced by periodic amplification process called sideband instability (SI) effect [65]. However, the accumulation characteristic of the TOD and the TOD compensation scheme suitable for OPC systems have not been studied yet.

In this chapter, we show, for the first time to our knowledge, the linear accumulation characteristics of the TOD in OPC systems under ordinary operation conditions, and demonstrate that the performance of the OPC system can be improved beyond the above TOD limitation only by linearly compensating the TOD. Numerical simulation results show that the 100Gbit/s, 10,000km transmission is made possible by the OPC system incorporated with the TOD compensation.

4.2 TOD Accumulation Characteristic in OPC Systems

First, it should be noted that, to discuss the accumulation of TOD in OPC systems, it is necessary to use three characteristic scales: the SOD length L_{d2}, the TOD length L_{d3}, and the nonlinear length L_{nl}, which are defined in [4] for forecasting signal behaviors in optical fiber transmission systems. The effect whose scale becomes the shortest plays a dominant role in limiting the system performance.

Dispersion-managed NRZ transmission systems require the SOD compensation interval, which is quite shorter than L_{nl}, in order to avoid the interaction of the SOD and SPM. If the SOD compensation interval becomes much shorter than L_{d3}, which is usually the case, the pulse behaves in the TOD scale as if it propagates through a uniformly zero-dispersion fiber. In such a system, in order to prevent the interaction between the TOD and the SPM, it is necessary to place TOD compensators at the interval much shorter than L_{nl} so that TOD can be compensated before interacting with SPM.

Also in OPC systems, TOD cannot be compensated by OPC and it just accumulates along the system length. However, the accumulation of TOD in OPC systems has different characteristics from the above system. In OPC systems, SOD exists along the entire transmission length; therefore, L_{d2} becomes many times shorter than L_{nl} for the case of high bit-rate transmission. When L_{d2} is much shorter than L_{nl} and L_{d3}, the signal pulses are rapidly broadened by the SOD effect, and their peak power decreases after transmitting for several L_{d2}. This means that the broadened

pulses almost do not experience the effect of the fiber nonlinearity, and we can thus expect that the accumulation of the TOD-induced phase shift increases almost linearly with the transmission length.

However, if L_{nl} becomes comparable to L_{d2}, both the pulses and spectrum will first be distorted by the interaction between SPM and SOD and subsequently being attacked by TOD. In this case, even though the pulse waveform and spectrum can be restored to their initial shapes at the end of the system, since OPC can compensate for the SPM+SOD interaction, the amount of TOD-induced phase shift is no longer linearly proportional to the transmission length because the spectral shape changes during the transmission. However, to obtain the condition $L_{nl} \approx L_{d2}$, we need an extremely high input signal power which will not be practically used in ordinary operating states. Thus, we can conclude from this fact that the TOD accumulation in OPC systems is almost linear. The linear TOD accumulation enables us to place only one TOD compensator at any point in the link instead of periodically placing TOD compensators at the interval much shorter than L_{nl}.

4.3 Computer Simulations

To confirm the prediction, the computer simulations have been performed. The main parameters used in the simulation are typical dispersion-shifted fiber parameters: SOD: D = -1 ps/km/nm, TOD = 0.06 ps/km/nm, and the nonlinear coefficient γ = 2.6 $W^{-1}km^{-1}$. The fiber loss and amplification process are neglected in order to focus only on the TOD accumulation characteristics. The TOD compensator used in simulations is assumed to be an ideal device that multiplies the complex amplitude of the signal with a negative amount of linearly accumulated phase shift caused by TOD. This compensator is placed only at the end of system.

The optical pulse at the midway of the system is conjugated by an ideal infinite-bandwidth optical phase conjugator. The propagation of the optical pulse is calculated by solving the nonlinear Schrodinger (NLS) equation by the split-step Fourier method [4]. In the first calculation, L_{nl} is set at 280 km which is equal to L_{d3} and is approximately 40 times longer than L_{d2} (≈ 7 km).

Figures 4.1(a) and (b) shows the waveform and spectrum of a single 5-ps FWHM optical pulse. The dotted curves show those of input pulse, whereas the dash-dotted curves those of the input pulse which propagates a 2000-km distance in the OPC system with the effect of TOD. The pulse waveform is distorted after

propagation, while any change in its spectrum is not observed. The solid curves are those of 2,000-km transmitted pulse after compensating TOD. The pulse waveform recovers to the initial shape by TOD compensation. The results shown in Fig. 4.1 indicate that the accumulation of TOD is linear and the compensation is done perfectly as we expected in the previous section.

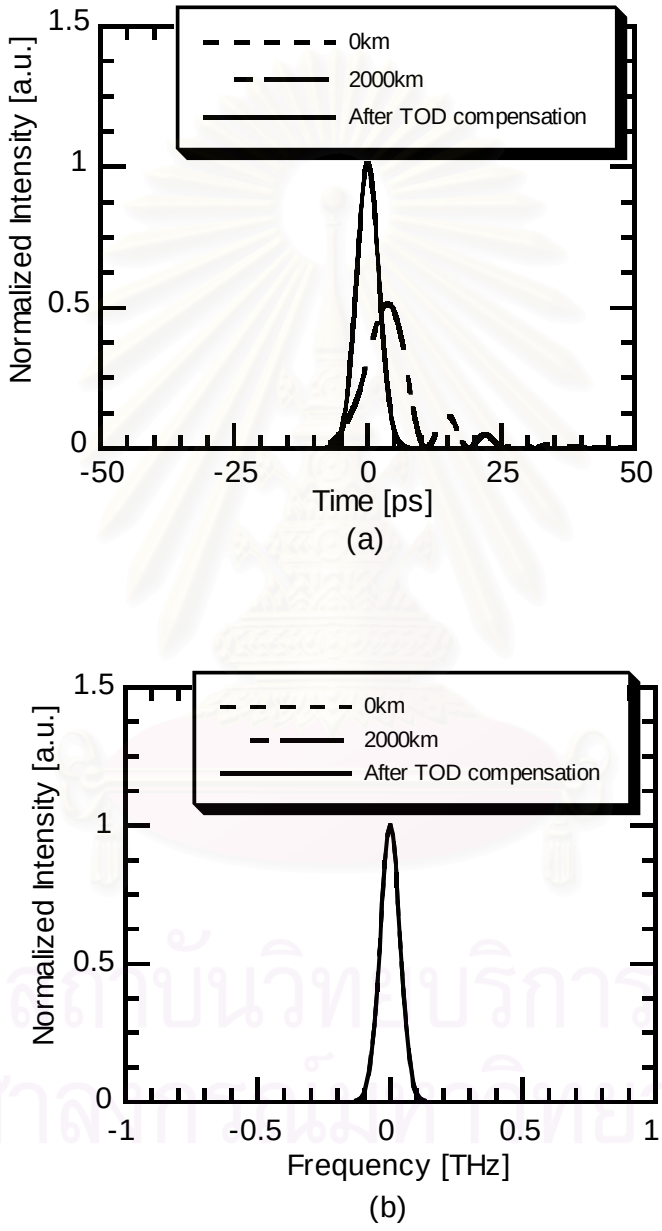

Figure 4.1: Waveform and spectrum of an optical pulse propagating a 2,000-km distance in the OPC system where the nonlinear length is set equal to the TOD length; (a) optical pulse, (b) optical spectrum. The dotted curves show those of the input pulse, the dash-dotted curves those of the pulse transmitted with the effect of TOD, and the solid curves are those of the transmitted pulse after compensating the TOD.

Figures 4.2(a) and (b) show the calculated results of the case when L_{nl} is equal to L_{d2} (≈ 7 km). As we have mentioned, the interaction between TOD and SPM appears in OPC systems. Both the pulse shape and spectrum becomes distorted and the TOD compensation is almost failed.

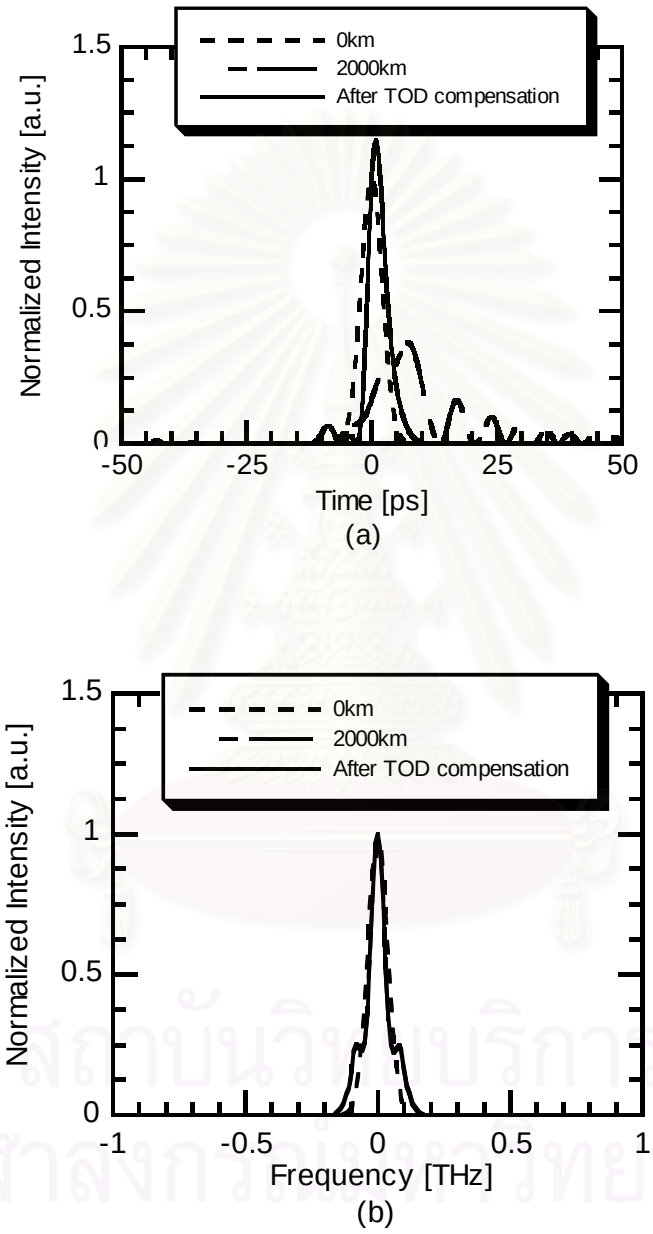

Figure 4.2: Waveform and spectrum of an optical pulse propagating a 2,000-km distance in the OPC system where the nonlinear length is equal to the GVD length; (a) optical pulse, (b) optical spectrum. The dotted curves show those of the input pulse, the dash-dotted curves those of the pulse transmitted with the effect of TOD, and the solid curves are those of the transmitted pulse after compensating the TOD.

Figure 4.3 shows the calculated bit-error rate (BER) of the TOD compensated OPC system. The input power of all curves is set at 3 mW. In this case, L_{nl} becomes almost equal to L_{d3} at 280 km while L_{d2} is around 7 km. An input optical signal consists of a pseudorandom 32-bit Gaussian RZ pulse train whose bit rate is equal to 100 Gbit/s. The fiber loss of 0.2 dB/km and amplification of 8 dB at every 40 km interval are included in the calculations. The optical amplifier produces ASE noise through a process of amplification with noise figure of 5.3 dB (n_{sp} = 1.7). The ideal infinite bandwidth TOD compensator is placed at the output end of the fiber. We assume the use of an optical band-pass filter with a 1 THz bandwidth in front of a receiver with a bandwidth of 50-GHz-cutoff-low-pass filter. The system performance is evaluated in terms of the bit-error rate (BER) calculated by repeating 128 times the transmission of the same pulse train and assuming Gaussian noise distribution [25].

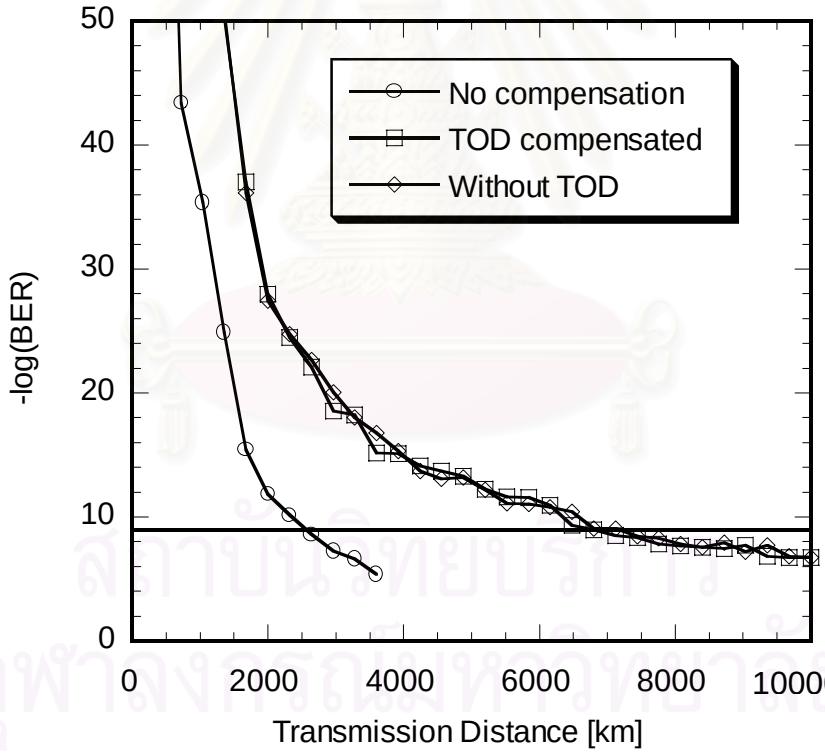

Fig. 4.3: BER of the 100-Gbit/s TOD compensated OPC systems where the nonlinear length becomes equal to the TOD length. The BER of TOD compensated OPC system is shown by squares, that of the system neglecting the TOD is shown by diamonds, and that of the system without TOD compensation is shown by circles.

According to the calculation results, the BER curve obtained from the TOD compensated OPC system (shown by squares) almost fits with that obtained from the system that neglects TOD (shown by diamonds), showing that the accumulation of the TOD is almost linear even L_{d3} is comparable to L_{nl} so that the linear TOD compensation is done perfectly. Without TOD compensation (shown by circles) the maximum achievable length for 100-Gbit/s OPC transmission is limited about 2,500 km at BER = 10^{-9} as shown by the across line. The TOD compensated OPC system gains more 4,000-km transmission length up to 6,500 km. This proves the effectiveness of TOD compensation on improving transmission performance in OPC systems.

4.4 100-Gbit/s, 10,000-km Transmission by Optimum Input Power

If we increase the power of the signal, the achievable transmission distance will increase due to the improvement of SNR. At the same time, the increase in power gives rise to the degradations from the SI effect and the reduction of the corresponding nonlinear length. Therefore, the improvement and degradation will balance each other at an optimum input power in which the system can reach the maximum performance. To find the optimum power, we perform the simulations by increasing the input power of the same system as Fig. 2.4 from 3 mW to 20 mW. Figure 4.4 shows the BER calculated as a function of the transmission distance. The optimum power obtained from the result is approximately 7 mW, and with this input power, we can achieve over 10,000-km transmission at BER = 10^{-9}.

4.5 Conclusion

We have found that the accumulation characteristic of the TOD in OPC transmission systems is almost linear as long as the SOD length is much shorter than the nonlinear length. This fact gives us a possibility to install only one of the linear TOD compensation device at any point in the system for perfect TOD compensation. By assuming the ideal TOD compensator, the computer simulation result has shown the possibility of 100 Gbit/s, 10,000km transmission based on TOD compensated OPC systems.

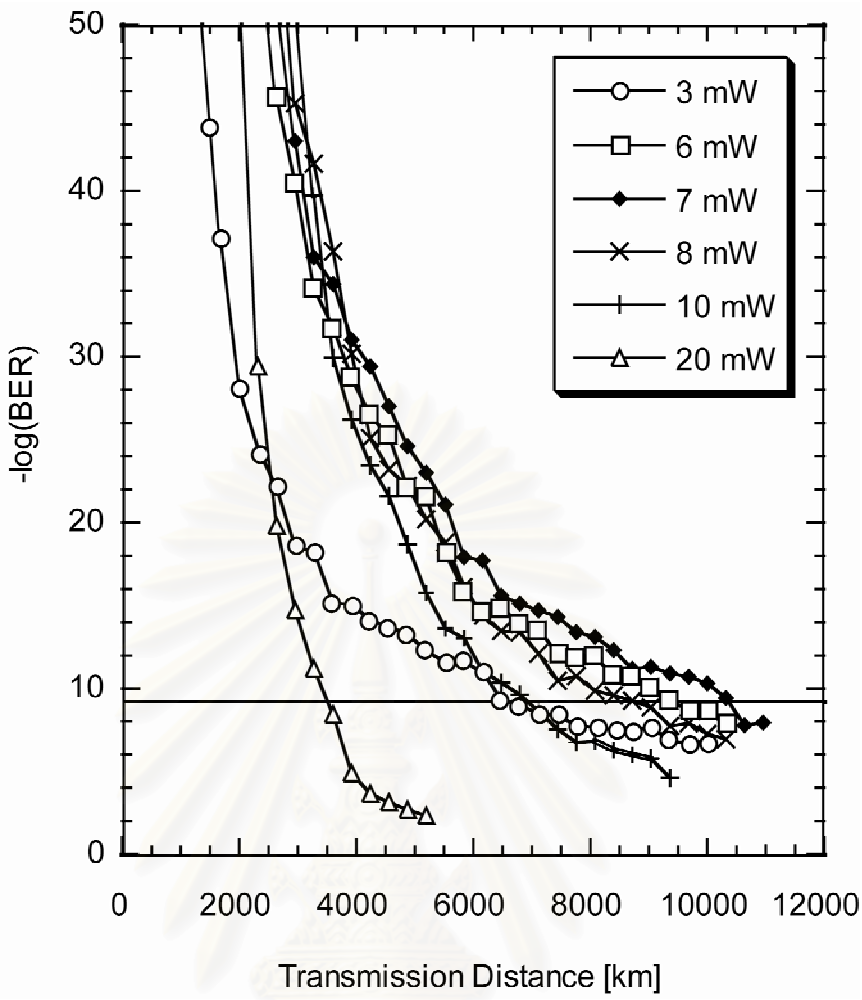

Fig. 4.4: BER curves of 100-Gbit/s TOD compensated OPC systems when an input power increases from 3 to 20 mW. We find that 100-Gbit/s, 10,000-km transmission is achieved by the optimum input power of 7mW when TOD is compensated in the OPC system.

CHAPTER 5
COMPLETE ANALYSIS OF SIDEBAND INSTABILITY IN CHAIN OF PERIODIC DISPERSION-MANAGED FIBER LINK AND ITS EFFECT ON HIGHER-ORDER DISPERSION-MANAGED LONG-HAUL WAVELENGTH DIVISION MULTIPLEXED SYSTEMS

In this chapter, we present for the first time a complete theoretical analysis of sideband instability (SI) that occurs when two kinds of fibers with different characteristics are concatenated to form a dispersion-managed fiber link [52]. In the analysis, the following three cases are taken into account: case (a) when a dispersion management period is larger than an amplification period, case (b) when the two lengths are equivalent, and case (c) when a dispersion management period is smaller than an amplification period.

We find that the SI gain peak appears at frequencies determined by the larger period out of the two variation periods. Moreover, for all the three cases, the magnitude of the SI gain reduces with the increase in strength of dispersion management.

Next, we focus on the fiber link using the combination of standard single-mode fiber (SMF) and reverse dispersion fiber (RDF), which is widely used for simultaneously compensating second-order dispersion (SOD) and third-order dispersion (TOD). By computer simulation, it is shown that, in wavelength-division-multiplexed (WDM) systems, SI still induces significant degradation in channels located at frequencies where SI induced from other channels arises. By re-allocating the channel frequency to avoid the SI frequency, the transmission performance is improved significantly.

5.1 Introduction

Four-wave mixing (FWM) and cross-phase modulation (XPM) in optical fibers have been recognized as the main problems that cause signal waveform distortion in wavelength-division-multiplexed (WDM) systems [4], [96], [97]. FWM induces signal energy transfer among channels, while, through XPM, temporal intensity

variation of every channel modulates the phase of other co-propagating channels. In fact, the use of non-zero dispersion for signal transmission yields relatively different propagating group-velocity among channels, referred as walk-off, which dramatically results in the reduction of channel crosstalk induced from both FWM and XPM. For this purpose, the second-order dispersion (SOD) management method has been proposed and demonstrated [25], [98]-[100]. Through this method, fiber sections are periodically arranged in such a way that the signal carrier wavelengths alternatively fall in normal and anomalous dispersion region, while, for each period, the total fiber exhibits zero or near zero dispersion on average. Therefore, signal pulse propagating in the link will always experience non-zero dispersion while its width is almost preserved at each compensation period due to low average dispersion.

However, such an approach can manage only SOD in only one channel. Therefore, in WDM systems, signal channels far from the average zero-dispersion wavelength experience different amount of dispersion accumulation along the entire system length because of the existence of the dispersion slope or third-order dispersion (TOD).

It has been predicted that the existence of TOD limits the available passband of the WDM systems with the data rates of over 10 Gbit/s [101]-[103]. For further expansion both in capacity and distance, dispersion management to eliminate both SOD and TOD will be one of the key issues. For this purpose, the special dispersion compensating fibers called reverse dispersion fiber (RDF) [58]-[60] has been proposed and demonstrated its potential. Since RDF exhibits low negative TOD with large negative SOD, we can achieve the dispersion flattened fiber link with low average SOD by combining RDF with standard single-mode fiber (SMF) in each compensation interval. The use of such higher-order dispersion compensation fiber link in combination with the optimization of channel spacing realizes the simultaneously reduction of FWM, XPM, and TOD. Transmission experiment shows that using the combination of SMF and RDF can achieve the data rate as high as 1 Tbit/s (104 x 10 Gbit/s) WDM transmission over 10,000 km [104].

In this chapter, we demonstrate that the additional signal distortion to long-haul higher-order-dispersion-managed WDM systems can occur via the quasi FWM phase-match process assisted by periodic variation of the signal power in the chain of lossy fiber intervals and lumped amplifiers incorporated with periodic dispersion management. This parametric process, which occurs in both normal and anomalous

dispersion region, is called sideband instability (SI). Through this process, signal carrier transfers its energy to specific sideband frequencies which grow up exponentially with transmission distance.

It has been shown theoretically that in order to avoid the XPM-induced signal waveform distortion for 10-Gbit/s-based 10,000 km WDM transmission, the use of channel spacing larger than 100 GHz is preferable [105]. Several long-haul transmission experiments also demonstrate attractive results using the channel spacing around this value [101], [104], [106]. With this relatively large channel spacing, the first order SI, which usually exhibits large gain than higher orders, will not arise inside one's channel bandwidth. Therefore, the problem induced from SI has not been yet appeared and can be ignored for such transmissions.

However, with system distance shorter than 10,000 km, the possibility of using smaller channel spacing for signal transmission has been shown [107]-[109]. In this situation, if two different channels produce SI at the same frequency, SI will cause a serious problem to the channels whose carriers are placed just at that frequency, especially for the frequency where the first order SI arises.

Historically, Matera *et al*. first theoretically showed the occurrence of SI in long distance systems through the periodic signal amplification [50]. Kurtzke and Peterman briefly discussed the impact of SI on multi-channel long-distance optical communication systems [110], [111]. In their works, by computer simulations, a serious channel signal distortion was observed when the SI resonance frequency superpositions on the channel frequency. Kikuchi, *et al.* experimentally observed SI in optical amplifier chain using a recirculating fiber loop [112]. Smith and Doran predicted that the periodic dispersion management also leads to the occurrence of SI. They also demonstrated that the gain of SI could be reduced by strong dispersion management [113]. Recently, we have presented a part of the derivation of SI under the existence of both periodic power variation and periodic dispersion variation [51].

However, all of the previous works have not yet included the periodic variation of fiber parameters such as fiber loss coefficient and fiber nonlinear coefficient, which is practically necessary to consider when two different fibers are connected together to form a dispersion-managed transmission line. Moreover, to avoid the problem of SI in WDM systems, it is important to study SI more details and the exact analytical expression of SI must be derived.

In this chapter, the complete theoretical analysis of SI focusing on the case when two different characteristic fibers connected together has been made for the first time. In our analysis, not only the periodic power variation but the periodic dispersion management, periodic fiber loss coefficient variation, and periodic nonlinear coefficient variation are also included. In section 5.2, we derive the analytical SI gain and the SI frequency considering three cases: (a) when a dispersion management period is larger than an amplifier spacing, (b) when the two lengths are equal, and (c) when an amplifier spacing is larger than a dispersion management period. In section 5.3, the derived theory is evaluated its accuracy by computer simulations.

The section 5.4 focuses on dispersion managed transmission system consisting of SMF and RDF. Our computer simulation results show that, when two or more channels produce SI at the same frequency, SI significantly causes a serious problem to the channel whose carrier is positioned just at that superposition resonance frequency. We also demonstrate that, by re-arranging the channel position or channel spacing in such a way that none of the SI resonance frequency falls inside the channel signal bandwidth, the transmission performance is significantly improved. Finally, the summary of this paper is made at section 5.5.

5.2 Derivation of Sideband Instability in the Presence of Periodic Power Variation and Periodic Dispersion Management

In long haul and high-capacity fiber transmission systems, the power of the optical signal must be kept high in order to obtain good signal-to-noise ratio (SNR) at a receiver. In such high power systems, by amplification process, the periodic power variation produces a periodic variation of fiber refractive index through the nonlinear Kerr effect of an optical fiber. By this process, it seems like a grating is virtually constructed in the transmission fiber. As shown in Fig. 3.4, a parametric resonance between the virtual grating and the signal will occur at the signal sideband component whose wave number is half of the wave number of this virtual grating resulting in exponential growth of that component with transmission length. This phenomenon is known as the sideband instability (SI), which causes signal waveform distortion if SI arises at frequency inside the signal bandwidth since it cannot be eliminated by using optical bandpass filter.

Quantitatively, the occurrence of SI can be explained in terms of quasi-phase-matched FWM process that is assisted by the virtual grating induced by the periodic power variation as the condition

$$k_+ + k_- = 2k_0 + k_f . \tag{5-1}$$

In Eq. (5-1), the wave number of the signal, which acts as a pump, is $k_0 = -\gamma\overline{P} + \beta(\omega_0)$, the sideband wave numbers are $k_+ = k_- = \frac{1}{2}\beta_2\omega_n^2 + \beta(\omega_0)$, where $\beta(\omega_0)$ is the wave number at the central carrier frequency ω_0. k_f is the wave number of the virtual grating which is given as

$$k_f = \frac{2\pi n}{l_f}, \tag{5-2}$$

where $n = 0,\pm1,\pm2,...,$ and l_f is the amplifier spacing. The sideband frequency ω_n shifted from the carrier frequency, at which SI arises is obtained from Eq. (5-1) and (5-2) as

$$\omega_n = \pm\sqrt{\frac{1}{|\beta_2|}\left(k_f n - 2\,\mathrm{sgn}(\beta_2)\gamma\overline{P}\right)}. \tag{5-3}$$

where $\overline{P}$ is the path-averaged signal power. The power gain $\lambda(\omega_n)$ of SI at each *n*-order resonance frequency is

$$\lambda(\omega_n) = 2P_0|F_n|, \tag{5-4}$$

where P_0 denotes the signal input power and F_n the *n*-order of the Fourier series coefficient of the periodic function $\alpha(z)$ whose period is equal to l_f.

In fact, not only the periodic power variation, but also all of the periodic perturbation under the Kerr effect, such as the periodic dispersion variation, the periodic fiber loss coefficient variation, and the periodic fiber nonlinear coefficient variation, can also lead to the occurrence of SI. To obtain the general expression of SI considering all of the periodic perturbation, we should start the analytical derivation based on the models of dispersion management systems illustrated in Fig. 5.1. In Fig. 5.1, the signal power and the fiber dispersion is assumed to change periodically with transmission length. As we aim to concentrate to dispersion managed transmission system consisting of SMF and RDF, the fiber link is composed of two different characteristic fibers with the same length. Therefore, the dispersion profile is the simplest type where the dispersion varies every half of period with the same amount

plus and minus around a given average dispersion value. Each fiber has its own nonlinear coefficient and the fiber loss, which is assumed periodic by the period equivalent to the dispersion management period. We consider here three possible cases: (a) when the dispersion management period is longer than the amplifier span, (b) when the two scales become equal, and (c) when the dispersion management period is shorter than the amplifier span.

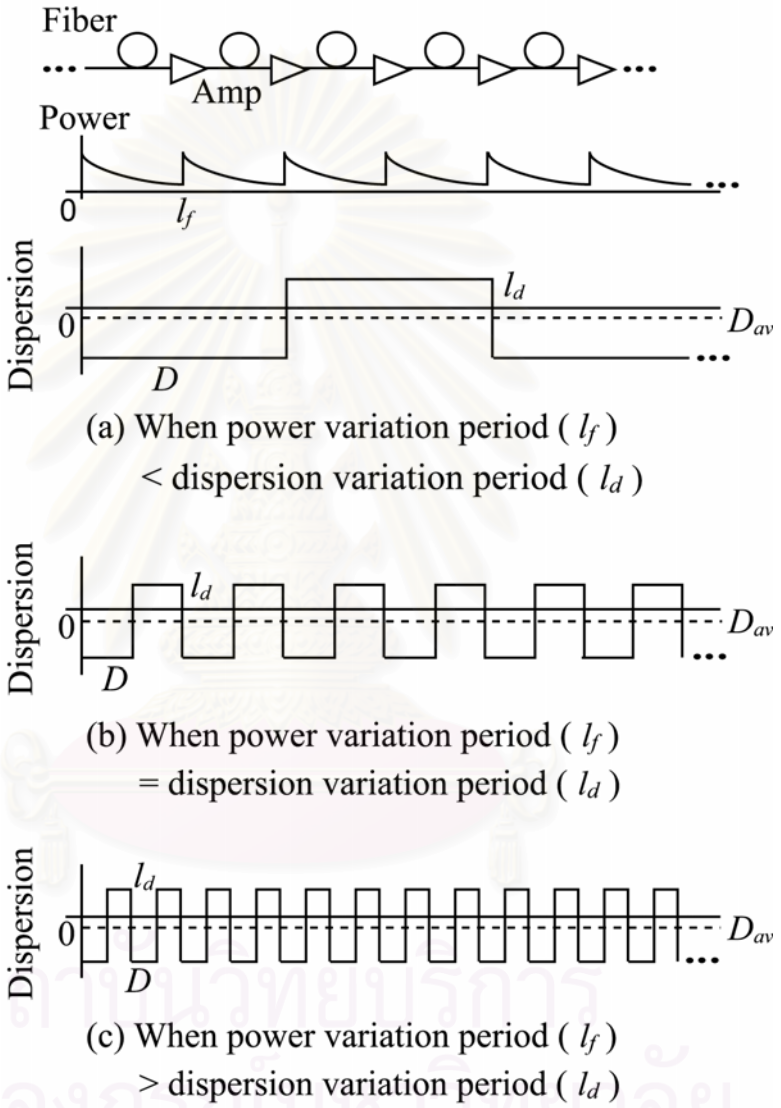

Figure. 5.1: Models of dispersion management system used for the analytical derivation. The signal power and fiber dispersion change periodically with transmission length. The fiber link is consisted of two different characteristic fibers with the same length. Three possible cases are modeled: (a) when the dispersion compensation period l_d is longer than the amplifier span l_f, (b) when the two scales become equal, and (c) when $l_d < l_f$.

The analysis starts from the nonlinear Schrodinger equation for the signal envelope function $U(z,t)$

$$\frac{\partial U}{\partial Z} = -\frac{\alpha(z)}{2}U - \frac{i}{2}\left(\beta_{2av} + \beta_{2fl}(z)\right)\frac{\partial^2 U}{\partial t^2} + i\gamma(z)|U|^2 U \ . \tag{5-5}$$

In Eq. (5-5), The GVD is separated in two parts: the constant average β_{2av} and the fluctuation part $\beta_{2fl}(z)$. The fiber loss coefficient $\alpha(z)$, the nonlinear coefficient $\gamma(z)$ and $\beta_{2fl}(z)$ are the functions of *z* which are assumed periodic with the same period equivalent with the dispersion management period. It should be noted that the GVD parameter β_2 relates to the common dispersion parameter *D* by

$$D = -\frac{\omega_0}{\lambda_0}\beta_2, \tag{5-6}$$

where ω_0 denotes the carrier frequency and λ_0 the carrier wavelength.

At each amplifier, the span loss is compensated so that we can assume the optical field propagating in each amplification period has the form

$$U(z,t) = u(z,t)\exp\left(-\frac{1}{2}\alpha(z)z\right). \tag{5-7}$$

Inserting Eq. (5-7) into Eq. (5-5), we obtain

$$\frac{\partial u}{\partial Z} = -\frac{i}{2}\left(\beta_{2av} + \beta_{2fl}(z)\right)\frac{\partial^2 u}{\partial t^2} + if(z)|u|^2 u, \tag{5-8}$$

where $f(z) = \gamma(z)\exp(-\alpha(z)z)$ is the periodical function whose period is equal to the amplifier spacing. Next, we perturb Eq. (5-8) by a small amplitude fluctuation *a* added to the steady solution of Eq. (5-8),

$$u(z,t) = \left(\sqrt{P_0} + a\right)\exp\left(iP_0\int_0^z f(z')dz'\right) \tag{5-9}$$

where P_0 denotes the input peak power and *a* is defined as

$$a(z,t) = \frac{1}{2}\left\{a(z,\omega)\exp(i\omega t) + a(z,-\omega)\exp(-i\omega t)\right\}. \tag{5-10}$$

Substituting Eq. (5-9) and (5-10) back to Eq. (5-8), then we obtain one set of two differential equations

$$\frac{\partial}{\partial Z}\begin{bmatrix} a(z,\omega) \\ a^*(z,-\omega)\end{bmatrix} = i\begin{bmatrix} \frac{1}{2}\left(\beta_{2av} + \beta_{2fl}(z)\right)\omega^2 + f(z)P_0 & f(z)P_0 \\ -f^*(z)P_0 & -\frac{1}{2}\left(\beta_{2av} + \beta_{2fl}(z)\right)\omega^2 - f^*(z)P_0\end{bmatrix}\begin{bmatrix} a(z,\omega) \\ a^*(z,-\omega)\end{bmatrix} \tag{5-11}$$

where the subscript * indicates the counterpart complex conjugate. By introducing the transformation

$$\begin{bmatrix} a(z,\omega) \\ a^*(z,-\omega) \end{bmatrix} = \begin{bmatrix} \exp\left(i\frac{\omega^2}{2}\int_0^z \beta_{2fl}(z')dz' \right) & 0 \\ 0 & -\exp\left(i\frac{\omega^2}{2}\int_0^z \beta_{2fl}(z')dz' \right) \end{bmatrix} \begin{bmatrix} b(z,\omega) \\ b^*(z,-\omega) \end{bmatrix} \quad (5\text{-}12)$$

Eq. (5-11) becomes

$$\frac{\partial}{\partial Z}\begin{bmatrix} b(z,\omega) \\ b^*(z,-\omega) \end{bmatrix} = i\begin{bmatrix} \frac{1}{2}\beta_{2av}\omega^2 + f(z)P_0 & g(z)P_0 \\ -g^*(z)P_0 & -\frac{1}{2}\beta_{2av}\omega^2 - f^*(z)P_0 \end{bmatrix} \begin{bmatrix} b(z,\omega) \\ b^*(z,-\omega) \end{bmatrix} \quad (5\text{-}13)$$

where

$$g(z) = f(z)\exp\left(-i\omega^2\int_0^z \beta_{2fl}(z')dz' \right). \quad (5\text{-}14)$$

By this transformation, we can remove the fast oscillations in the field envelope, so that only those changes that accumulate over the period of $\beta_{2fl}(z)$ is left. The key step of this analysis is to expand $f(z)$ and $g(z)$ as complex Fourier series:

$$f(z) = \sum_{n=-\infty}^{\infty} F_n \exp\left(ik_f nz\right), \quad g(z) = \sum_{n=-\infty}^{\infty} G_n \exp\left(ik_g nz\right), \quad (5\text{-}15)$$

where k_f and k_g are the fundamental wave constants of $f(z)$ and $g(z)$, and F_n and G_n denote the Fourier series coefficients of $f(z)$ and $g(z)$.

5.2.1 The Case when the Dispersion Compensation Period is Larger than the Amplifier Spacing

First, we consider the case (a) when the dispersion management period l_d is larger than the amplifier spacing l_f. The wave constant k_g in this case can be written as $k_g = 2\pi/l_d = k_d$, where $l_d = 2pl_f$, so that $k_f = 2pk_d$ and p = 1, 2, 3, …. In order to get close to the resonance of the n^{th} Fourier component of the perturbation, we introduce the variable transformation

$$\begin{bmatrix} b(z,\omega) \\ b^*(z,-\omega) \end{bmatrix} = \begin{bmatrix} \exp\left(i\frac{1}{2}k_d nz \right) & 0 \\ 0 & \exp\left(-i\frac{1}{2}k_d nz \right) \end{bmatrix} \begin{bmatrix} c(z,\omega) \\ c^*(z,-\omega) \end{bmatrix} \quad (5\text{-}16)$$

Inserting Eq. (5-15) and (5-16) into Eq. (5-13) and equating only the coefficients of $\exp(ik_d nz/2)$ and $\exp(-ik_d nz/2)$ (for the complex conjugate counterpart), we obtain

$$\frac{\partial}{\partial Z}\begin{bmatrix} c(z,\omega) \\ c^*(z,-\omega) \end{bmatrix} = i\begin{bmatrix} -\frac{1}{2}k_d n + \frac{1}{2}\beta_{2av}\omega^2 + P_0F_0 & P_0G_n \\ -P_0G_n^* & \frac{1}{2}k_d n - \frac{1}{2}\beta_{2av}\omega^2 - P_0F_0^* \end{bmatrix}\begin{bmatrix} c(z,\omega) \\ c^*(z,-\omega) \end{bmatrix}, \quad (5\text{-}17)$$

where F_0 and G_n denote the fundamental and the *n*-th order coefficient of Fourier series of $f(z)$ and $g(z)$, respectively.

From the eigen values of Eq. (5-17), we obtain the power gain $\lambda(\omega)$ for the *n*-order SI effect as

$$\lambda(\omega) = \sqrt{4P_0^2|G_n|^2 - \left(k_d n - \beta_{2av}\omega^2 - P_0|F_0|\right)^2}\,. \quad (5\text{-}18)$$

At each order of SI, λ appears its peak at frequencies defined by

$$\omega_n = \pm\sqrt{\frac{1}{|\beta_{2av}|}\left(k_d n - 2\,\mathrm{sgn}(\beta_{2av})P_0|F_0|\right)}. \quad (5\text{-}19)$$

It is remarkable from Eq. (5-19) that SI occurs at frequencies determined by the dispersion management period l_d and by the averaged GVD β_{2av} independent of the fluctuation part β_{2fl}. For larger l_d, the SI gain position moves closer to signal carrier frequency, which may cause more severe signal waveform distortion. On the other hand, the peak of SI gain at the *n*-order resonance frequency $\lambda(\omega_n)$ depends on β_{2av} through ω_n in $|G_n|$ according to Eq. (5-14) and (5-19).

In order to obtain the expression of the SI gain, F_0 and G_n have to be derived. F_0 can be calculated from

$$F_0 = \frac{1}{l_d}\int_0^{l_d} f(z)dz = \frac{1}{l_d}\int_0^{l_d}\gamma(z)\exp(-\alpha(z)z)dz. \quad (5\text{-}20)$$

Since this paper considers the periodical dispersion compensation, which is constructed by the combination of two fibers in equal length. Each fiber exhibits different values of α and γ which are assumed to be constant along each fiber length. In each compensation interval, let α_1 and γ_1 represent the fiber loss coefficient and the nonlinear coefficient of the first fiber and α_2 and γ_2 represent the fiber loss coefficient and the nonlinear coefficient of the second fiber, respectively, F_0 is obtained through

$$F_0 = \frac{1}{l_d}\sum_{i=0}^{p-1}\left\{\int_{\frac{il_d}{2p}}^{\frac{l_d}{2p}+\frac{il_d}{2p}} \gamma_1 \exp(-\alpha_1 z)dz + \int_{\frac{l_d}{2}+\frac{il_d}{2p}}^{\frac{l_d}{2}+\frac{l_d}{2p}+\frac{il_d}{2p}} \gamma_2 \exp(-\alpha_2 z)dz\right\}$$

$$= p\left\{\gamma_1\left(\frac{1-\exp\left(-\alpha_1\frac{l_d}{2p}\right)}{\alpha_1 l_d}\right) + \gamma_2\left(\frac{1-\exp\left(-\alpha_2\frac{l_d}{2p}\right)}{\alpha_2 l_d}\right)\right\}. \qquad (5\text{-}21)$$

By assuming that $\beta_{2fl}(z)$ follows the profile shown in Fig. 5.1, we have

$$\int_0^z \beta_{2fl}(z')dz' = \begin{cases} \beta_{2fl} z, z = \left[0, \frac{l_d}{2}\right) \\ \beta_{2fl}(l_d - z), z = \left[\frac{l_d}{2}, l_d\right] \end{cases}. \qquad (5\text{-}22)$$

Substituting Eq. (5-22) to the exponential part of Eq. (5-14), G_n can be analytically obtained through the Fourier integration

$$G_n = \frac{1}{l_d}\sum_{j=0}^{p-1}\int_{\frac{il_d}{2p}}^{\frac{ld}{2p}+\frac{jl_d}{2p}} \gamma_1 \exp\left(-\alpha_1 z\right)\exp\left(-i\beta_{2fl}\omega^2 z\right)\exp\left(-ik_d nz\right)dz$$
$$+\frac{1}{l_d}\sum_{j=0}^{p-1}\int_{\frac{l_d}{2}+\frac{il_d}{2p}}^{\frac{l_d}{2}+\frac{ld}{2p}+\frac{jl_d}{2p}} \gamma_2 \exp\left(-\alpha_2 z\right)\exp\left(-i\beta_{2fl}\omega^2\left(l_d - z\right)\right)\exp\left(-ik_d nz\right)dz\,. \qquad (5\text{-}23)$$

Because $f(z)$ is periodical over each fiber length with the period of $\left[j\frac{l_d}{2p}, j\frac{l_d}{2p}+\frac{l_d}{2p}\right)$ for j = 0,1,2,…, it satisfies the following relations

$$f\left(\frac{jl_d}{2p}\right) = \gamma\exp\left(-\alpha\frac{jl_d}{2p}\right) = 1,\ f\left(\frac{l_d}{2p}+\frac{jl_d}{2p}\right) = \gamma\exp\left(-\alpha\frac{l_d}{2p}\right),$$
$$f\left(\frac{l_d}{2}+\frac{jl_d}{2p}\right) = \gamma\exp\left(-\alpha\left(\frac{l_d}{2}+\frac{jl_d}{2p}\right)\right) = 1,\ f\left(\frac{l_d}{2}+\frac{l_d}{2p}+\frac{jl_d}{2p}\right) = \gamma\exp\left(-\alpha\frac{l_d}{2p}\right). \qquad (5\text{-}24)$$

Applying the above conditions to Eq. (5-23), we obtain

$$G_n = \gamma_1 \left\{ \frac{1-\exp\left(-\alpha_1 \frac{l_d}{2p}\right)\exp\left(-i\left(\beta_{2fl}\omega^2 + k_d n\right)\frac{l_d}{2p}\right)}{\alpha_1 l_d + i\left(\beta_{2fl}\omega^2 + k_d n\right) l_d} \right\} \sum_{j=0}^{p-1} \exp\left(-i\left(\beta_{2fl}\omega^2 + k_d n\right)\frac{jl_d}{2p}\right)$$

$$+\gamma_2 \left\{ \frac{\exp\left(i\left(\beta_{2fl}\omega^2 - k_d n\right)\frac{l_d}{2}\right) - \exp\left(-\alpha_2 \frac{l_d}{2p}\right)\exp\left(i\left(\beta_{2fl}\omega^2 - k_d n\right)\left(\frac{l_d}{2} + \frac{l_d}{2p}\right)\right)}{\alpha_2 l_d - i\left(\beta_{2fl}\omega^2 - k_d n\right) l_d} \right\} \quad .(5\text{-}25)$$

$$\times \sum_{j=0}^{p-1} \exp\left(i\left(\beta_{2fl}\omega^2 - k_d n\right)\frac{jl_d}{2p}\right)$$

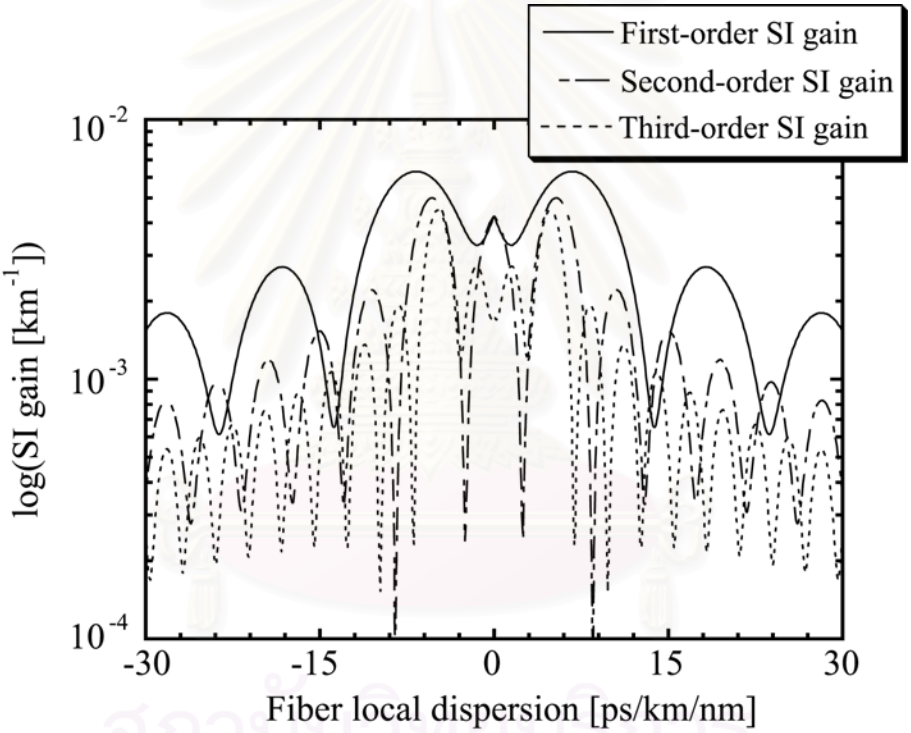

Figure 5.2: Theoretical n = 1, 2, and 3-order SI gain peaks at resonance frequency ω_n as a function of local SOD D, calculated with l_f = 40 km, l_d = 80 km, P_0 = 5 mW, and D_{av} = –5 ps/km/nm. D exhibits a negative value when the arrangement of fiber link changes the order of fiber installation to RDF-SMF instead of SMF-RDF. The gain characteristics for all three orders appear to be decreased and periodically reduced to minimum points with the increase in D.

At resonance frequency ω_n where the *n*-order SI occurs, the *n*-order SI gain becomes $2P_0|G_n|$. Figure 5.2 plots the n = 1, 2, and 3-order SI gain peaks at ω_n as a function of local SOD *D*, calculated by Eq. (5-25) with l_f = 40 km, l_d = 80 km. P_0 is assumed to be 5 mW, D_{av} is –5 ps/km/nm, α_1 and γ_1 of the fiber#1 are 0.2 dB and 1.6 $W^{-1}km^{-1}$, for the fiber#2, α_2, γ_2 are 0.25 dB and 4.8 $W^{-1}km^{-1}$, respectively. It should be noted that *D* exhibits a negative value when the arrangement of fiber link changes the order of fiber installation to fiber#2-fiber#1 instead of fiber#1-fiber#2.

The gain characteristics shown in Fig. 5.2 for all three orders appear to be decreased and periodically reduced to minimum points with the increase in fiber local SOD. The reduction of SI gain with the increase of local SOD has been predicted by Smith and Doran [113]. However, the reason for explaining this phenomena has not been clearly mentioned yet. According to Eq. (5-23), it is obvious that the reduction of SI gain does not come from the linear addition and cancellation of the two Fourier components: one induced from the periodic power variation $P_0\alpha(z)$ and the other from the periodic GVD variation $\beta_{2fl}(z)$. In order to understand the reason, we should rewrite $l_d = 2l_f$ (p = 1) and $\beta_{2fl}\omega_n^2 = ck_d$, where *c* denotes a real number that larger than zero, Eq. (5-23) can be written as

$$|G_n| = \left| \begin{aligned} &\frac{2}{l_f}\int_0^{l_f} \gamma_1 \exp(-\alpha_1 z)\exp\left(-i\frac{(c+n)}{2}k_f z\right)dz \\ &+\frac{2}{l_f}\exp(-i(c+n)\pi)\int_0^{l_f} \gamma_2 \exp(-\alpha_2 z)\exp\left(i\frac{(c-n)}{2}k_f z\right)dz \end{aligned} \right| \quad . \qquad (5\text{-}26)$$

Eq. (5-26) indicates that, for the *n*-order SI, by increasing the local GVD $|\beta_{2fl}|$, the corresponding *c* is increased, resulting in the increase of wave constant k_f by the factor of $(c+n)/2$ for the first term and $(c-n)/2$ for the second term, respectively. Each order of the SI gain, which becomes smaller for large k_f, is correspondingly reduced. Saying in other words, the first term of Eq. (5-26) is similar to the formula of Fourier integration using for obtaining the $(c+n)/2$-order Fourier coefficient of $f(z)$ when the period is l_f, and for the second term, the $(c-n)/2$-order Fourier coefficient. Therefore, this can be also interpreted that the increase of local GVD $|\beta_{2fl}|$ virtually shifts the order of SI induced from the power variation to higher order which exhibits

lower gain than the lower order. Furthermore, the SI gain falls down to minimum points when the virtual order number $(c+n)/2$ and $(c-n)/2$ together become an integer. In Fig. 5.2, agreeing with our prediction, the SI gain reduces to minimum points when $(c+n)/2$ and $(c-n)/2$ becomes |*c*| = 3, 5, 7,..., for the first-order, |*c*| = 4, 6, 8,..., for the second-order, and |*c*| = 5, 7, 9,...., for the third-order, respectively.

5.2.2 The Case when the Dispersion Compensation Period Becomes Equal to, or Shorter than the Amplifier Spacing

In this subsection, we consider the case when l_d is equal to, or shorter than l_f. The wave constant k_g for this case becomes $k_f = 2\pi / l_f$. l_f is assumed to satisfy $l_f = pl_d$, where p = 1, 2, 3,.... The analysis approach for this case is almost similar to that of previous subsection. By only replacing k_d in Eq. (5-15) with k_f. The power gain $\lambda(\omega)$ for n-order SI effect becomes

$$\lambda(\omega) = \sqrt{4P_0^2|G_n|^2 - \left(k_f n - \beta_{2av}\omega^2 - P_0|F_0|\right)^2}\,, \tag{5-27}$$

which exhibit each peak of the SI order at frequencies determined by

$$\omega_n = \pm\sqrt{\frac{1}{|\beta_{2av}|}\left(k_f n - 2\,\mathrm{sgn}(\beta_{2av})P_0|F_0|\right)}. \tag{5-28}$$

From Eq. (5-28), the frequencies where SI arises are determined by the wave constant k_f which is constant even the dispersion management period l_d is changed. This means that, for $l_d \le l_f$, SI will almost arise at the same frequencies independent of the change in l_d, which is different from the previous case. For this case, F_0 can be obtained by

$$F_0 = \frac{1}{l_f}\sum_{j=0}^{p-1}\left\{\int_{jl_d}^{\frac{l_d}{2}+jl_d}\gamma_1\exp(-\alpha_1 z)dz + \int_{\frac{l_d}{2}+jl_d}^{l_d+jl_d}\gamma_2\exp(-\alpha_2 z)dz\right\}$$

$$= \sum_{j=0}^{p-1}\left\{\gamma_1\left(\frac{\exp\left(-\alpha_1 jl_d\right)-\exp\left(-\alpha_1\left(\frac{l_d}{2}+jl_d\right)\right)}{\alpha_1 l_f}\right)+\gamma_2\left(\frac{\exp\left(-\alpha_2\left(\frac{l_d}{2}+jl_d\right)\right)-\exp\left(-\alpha_2\left(l_d+jl_d\right)\right)}{\alpha_2 l_f}\right)\right\}. \tag{5-29}$$

It should be noted that, in fact, ω_n slightly depends on the change of l_d through F_0 in Eq. (5-28) and (5-29). For example, computing the first order SI frequency by substituting the same fiber parameters as the calculation of Fig. 5.2 into Eq. (5-28)

and (5-29), when we reduce l_d from 40 km (= l_f) to 1 km, the first order SI frequency only moves 0.3 GHz closer to the carrier frequency. Therefore, such small amount of frequency shift is negligible comparing to the shift of SI position caused by the change of k_f .

G_n, for this case, can be analytically obtained through the series of Fourier integration

$$\begin{aligned} G_n = \frac{1}{l_f}\sum_{j=0}^{p-1}\int_{jl_d}^{\frac{l_d}{2}+jl_d} \gamma_1 \exp\left(-\alpha_1 z\right)\exp\left(-i\beta_{2fl}\omega^2 z\right)\exp\left(-ik_f nz\right)dz \\ +\frac{1}{l_f}\sum_{j=0}^{p-1}\int_{\frac{l_d}{2}+il_d}^{l_d+il_d} \gamma_2 \exp\left(-\alpha_2 z\right)\exp\left(-i\beta_{2fl}\omega^2\left(l_d - z\right)\right)\exp\left(-ik_f nz\right)dz \ . \end{aligned} \tag{5-30}$$

As $\exp\left(-i\beta_{2fl}\omega^2 z\right)$ in $g(z)$ repeats periodically *p* times over each l_f ,

$$\begin{aligned} &\exp\left(-i\beta_{2fl}\omega^2 jl_d\right)=1,\ \ \exp\left(-i\beta_{2fl}\omega^2\left(\frac{l_d}{2}+jl_d\right)\right)=\exp\left(-i\beta_{2fl}\omega^2\frac{l_d}{2}\right), \\ &\exp\left(-i\beta_{2fl}\omega^2\left(l_d-\left(\frac{l_d}{2}+jl_d\right)\right)\right)=\exp\left(-i\beta_{2fl}\omega^2\frac{l_d}{2}\right), \\ &\exp\left(-i\beta_{2fl}\omega^2\left(l_d-\left(l_d+jl_d\right)\right)\right)=1. \end{aligned} \tag{5-31}$$

Carrying out the integration in Eq. (5-30) by the assistance of the relations in Eq. (5-31) gives

$$\begin{aligned} G_n = &\gamma_1\left\{\frac{1-\exp\left(-\alpha_1\frac{l_d}{2}\right)\exp\left(-i\left(\beta_{2fl}\omega^2+k_f n\right)\frac{l_d}{2}\right)}{\alpha_1 l_f + i\left(\beta_{2fl}\omega^2+k_f n\right)l_f}\right\}\sum_{j=0}^{p-1}\exp\left(-\alpha_1 jl_d\right)\exp\left(-ik_f njl_d\right) \\ &+\gamma_2\left\{\frac{\exp\left(-\alpha_2\frac{l_d}{2}\right)\exp\left(i\left(\beta_{2fl}\omega^2-k_f n\right)\frac{l_d}{2}\right)-\exp\left(-\alpha_2 l_d\right)\exp\left(-ik_f nl_d\right)}{\alpha_2 l_f - i\left(\beta_{2fl}\omega^2-k_f n\right)l_f}\right\} \\ &\times\sum_{j=0}^{p-1}\exp\left(-\alpha_2 jl_d\right)\exp\left(-ik_f njl_d\right) \end{aligned} \ . \tag{5-32}$$

Figure 5.3 shows the relations between the *n* = 1, 2, and 3-order SI gains and *D* at resonance frequency ω_n . All parameters used in Fig. 5.3 are the same as the plot in Fig. 5.2 except l_d is set equal to l_f at 40 km. The gain characteristics in Fig. 5.3

are in similar shapes to Fig. 5.2 where the gain decreases and periodically reduces to minimum points with the increase in *D*.

The similar characteristic is also obtained for the case of $l_d < l_f$ as shown in Fig. 5.4 where l_d is reduced to 10 km. However, in order to achieve the magnitude of SI gain as low as those of the above two cases, relatively large *D* is required.

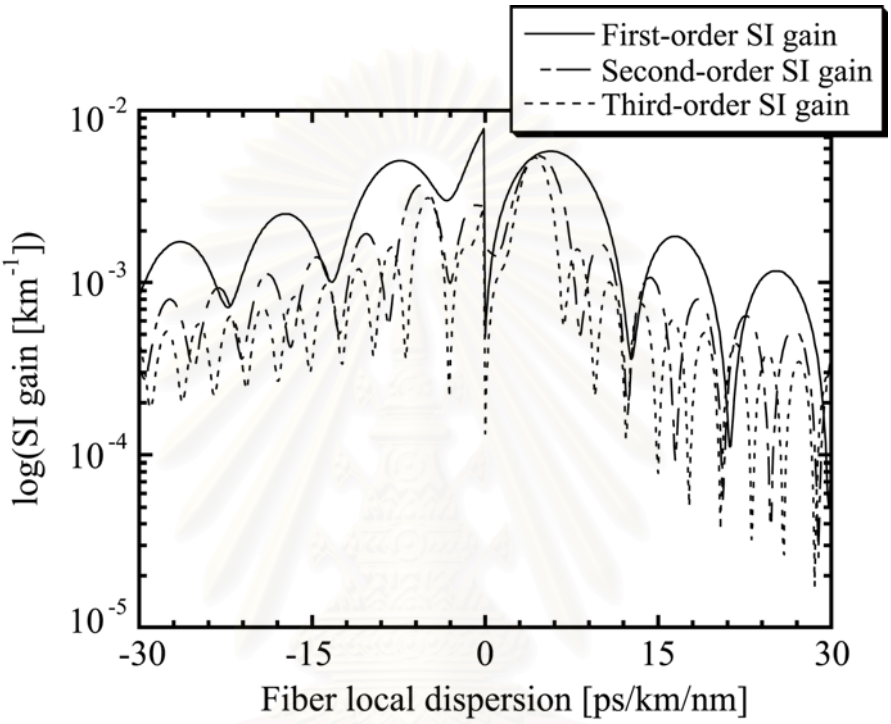

Figure 5.3: Relations between the *n* = 1, 2, and 3-order SI gain peaks and *D* at resonance frequency ω_n. All parameters used in this figure are the same as the plot in Fig. 5.2 except l_d is set equal to l_f at 40 km. The SI gain characteristics for all three orders are similar to Fig. 5.2 where the gain decreases and periodically reduces to minimum points with the increase in *D*.

One interesting thing observed from Fig. 5.2 ($l_d > l_f$), Fig. 5-3 ($l_d = l_f$), and Fig. 5.4 ($l_d < l_f$) is the gain characteristic in Fig. 5.2 is symmetrical with respect to *D* = 0 while those of Fig. 5.3 and Fig. 5.4 are not symmetrical. This can be explained as follows. As described above, when the sign of *D* is reversed, the order of the fiber installation is changed from fiber#1-fiber#2 to fiber#2-fiber#1. For the case of Fig. 5.3 and Fig. 5.4, at least two pieces of fibers is used for constructing the transmission

line between two amplifiers. This means that the fiber which locates at the output of amplifier where the signal power is still high is replaced with the other fiber which has different α , different γ , and different sign of *D*. Therefore, the gain characteristics in Fig. 5.3 and Fig. 5.4 become asymmetrical when the order of the two fibers is changed. On the other hand, for the case of Fig. 5.2, only one fiber is installed over the entire length of one amplifier spacing. Therefore, the arrangement of the two fibers will not result any differences in the gain characteristic.

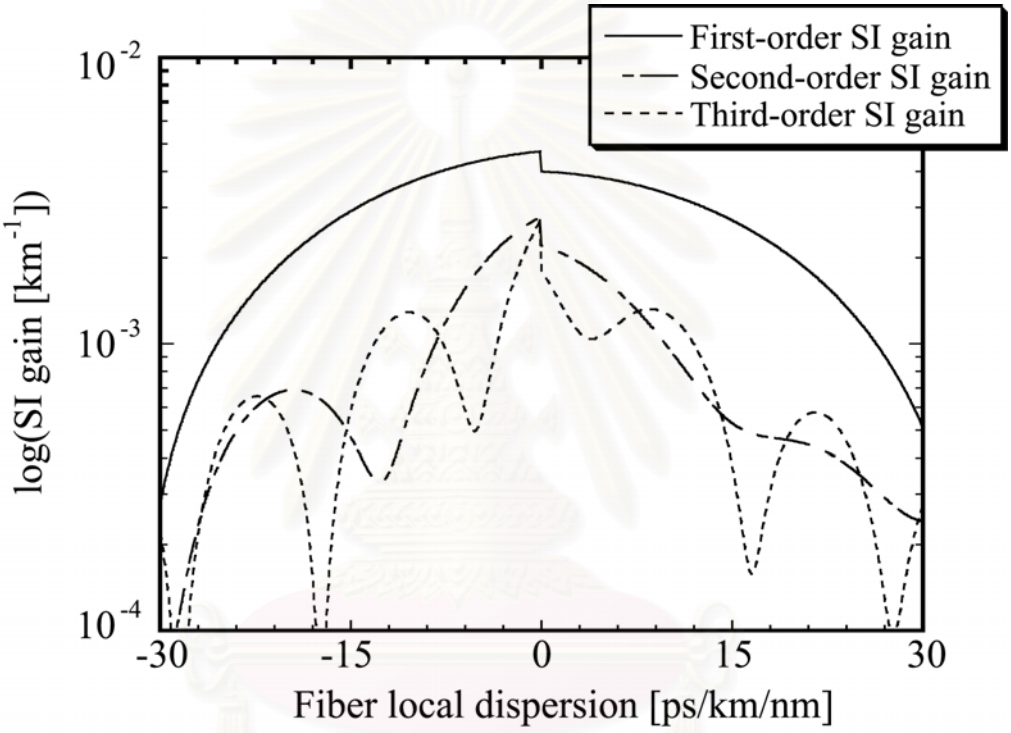

Figure 5.4: Theoretical *n* = 1, 2, and 3-order SI gain peaks at resonance frequency ω_n as a function of *D* when l_d is set at 10 km and l_f is still 40 km. Other parameters are the same as used for Fig. 5.2. All three orders are similar to Fig. 5.2 and Fig. 5.3 where the gain decreases and periodically reduces to minimum points with the increase in *D*. However, in order to achieve the magnitude of SI gain as low as those of the above two cases, relatively large *D* is required.

Quantitatively, $|G_n|$ calculated from Eq. (5-25) by replacing α_1 and γ_1 with α_2 and γ_2, and replacing α_2, γ_2, and β_{2fl} with α_1, γ_1, and $-\beta_{2fl}$ is equivalent to that obtained directly from Eq. (5-25). On the other hand, the replacement between

α_1, γ_1, β_{2fl} and α_2, γ_2, $-\beta_{2fl}$ in Eq. (5-32) yields different $|G_n|$ comparing to $|G_n|$ obtained directly from Eq. (5-32) without the replacement. Furthermore, for the case of $l_d \le l_f$, even both fiber#1 and fiber#2 possess equivalent values of α and γ, when the order of the two fibers is reversed, only the difference in the sign of *D* also leads to the different magnitude of SI gain since the power variation on each fiber is not the same.

It should be emphasized that, in this work, we focus only on the higher-order dispersion managed transmission line consisting of SMF and RDF. Since SMF and RDF possess almost equivalent absolute values of SOD and TOD with opposite signs, our analysis model shown in Fig. 5.1 is well matched with the practical transmission line composed of SMF and RDF. However, it is still worth studying SI induced from the dispersion-managed line which consists of fibers with different lengths and different amount of dispersion shifted from the average dispersion value.

Figure 5.5(a) shows the model of the dispersion-managed fiber link composed of fiber#1 and fiber#2 whose lengths are unequal. The most practical case where $l_d = l_f$ is considered. In Fig. 5.5(a), *x* is the length of fiber#1 and $l_f - x$ is the length of fiber#2. D_1 and D_2, respectively, denote the local dispersion of the fiber#1 and the fiber#2 shifted from the average dispersion D_{av}. To make the accumulated dispersion vanished at each l_d, D_2 can be written as the function of D_1 and *x* as

$$D_2 = -\frac{D_1 x}{l_f - x}. \tag{5-33}$$

Following the above derivation for the case $l_d \le l_f$, we found that SI also occurs at the frequency determined by Eq. (5-28) but, for this case, F_0 is obtained as

$$\begin{aligned} F_0 &= \frac{1}{l_f}\left\{\int_0^x \gamma_1 \exp(-\alpha_1 z)dz + \int_x^{l_f} \gamma_2 \exp(-\alpha_2 z)dz\right\} \\ &= \gamma_1\left(\frac{1-\exp(-\alpha_1 x)}{\alpha_1 l_f}\right) + \gamma_2\left(\frac{\exp(-\alpha_2 x) - \exp(-\alpha_2 l_f)}{\alpha_2 l_f}\right). \end{aligned} \tag{5-34}$$

On the other hand, G_n can be obtained as

$$G_n = \frac{1}{l_f}\int_0^x \gamma_1 \exp(-\alpha_1 z)\exp\left(-i\beta_{21}\omega^2 z\right)\exp\left(-ik_f nz\right)dz + \frac{1}{l_f}\int_x^{l_f} \gamma_2 \exp(-\alpha_2 z)\exp\left(-i\omega^2\left\{(\beta_{21}-\beta_{22})x+\beta_{22}z\right\}\right)\exp\left(-ik_f nz\right)dz, \quad (5\text{-}35)$$

where β_{21} and β_{22} are local GVD parameters of fiber#1 and fiber#2, respectively. Completing the integrations in Eq. (5-35) by using Eq. (5-6) and (5-33), we have

$$G_n = \gamma_1\left\{\frac{1-\exp(-\alpha_1 x)\exp\left(-i\left(\beta_{21}\omega^2+k_f n\right)x\right)}{\alpha_1 l_f + i\left(\beta_{21}\omega^2+k_f n\right)l_f}\right\} + \gamma_2 \exp\left(-i\omega^2\left(\frac{\beta_{21}l_f}{l_f-x}\right)x\right) \times\left\{\frac{\exp(-\alpha_2 x)\exp\left(i\left(\omega^2\left(\frac{\beta_{21}x}{l_f-x}\right)-k_f n\right)x\right)-\exp(-\alpha_2 l_f)\exp\left(i\left(\omega^2\left(\frac{\beta_{21}x}{l_f-x}\right)-k_f n\right)l_f\right)}{\alpha_2 l_f - i\left(\omega^2\left(\frac{\beta_{21}x}{l_f-x}\right)-k_f n\right)l_f}\right\}. \quad (5\text{-}36)$$

Assuming both fiber#1 and fiber#2 exhibit equivalent α and γ, then G_n depends on D_1 and x. To see the variation of SI gain with the change of both D_1 and x, the gain contour map should be used. Figure 6(b) shows the contour map of the first order SI gain peak as functions of D_1 and x. For obtaining Fig. 5.5(b), D_{av} = – 0.5 ps/km/nm, α = 0.2 dB/km, γ = 2.6 $W^{-1}km^{-1}$, and $l_d = l_f$ = 40 km are used. The gain map in Fig. 5.5(b) indicates that the use of fiber#1 that has large local dispersion with relatively long length can significantly reduce the SI gain. Quantitatively, the length of the fiber#1 should be longer than 10 km and the local dispersion $|D_1|$, which can be both normal and anomalous dispersion, should be larger than 5 ps/km/nm to assure the first order SI gain smaller than 10^{-3} km^{-1}.

For all cases, it should be noted that when D_{av} is set in anomalous dispersion region the modulation instability (MI) [4], which can be interpreted as the zero-order SI, occurs and also only be slightly reduced by relatively large *D*.

Recently, the fabrication of optical fiber with designed dispersion value has been realized [114]. This enables us constructing a dispersion-managed transmission fiber with appropriate value of dispersion in order to suppress SI effect for a given system.

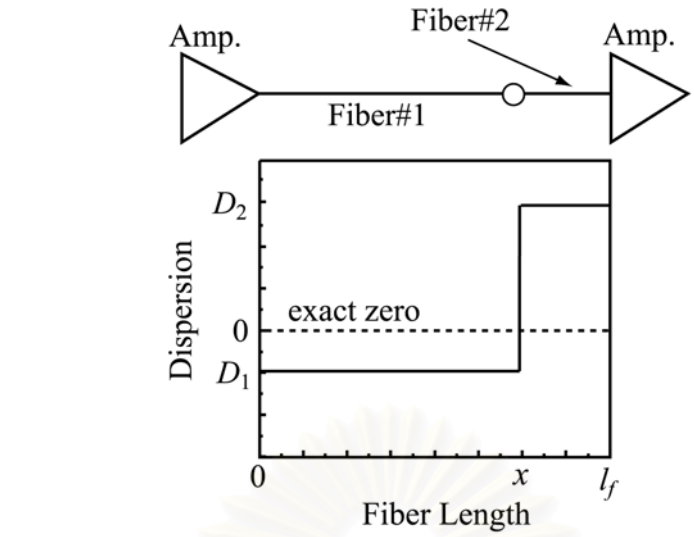

(a)

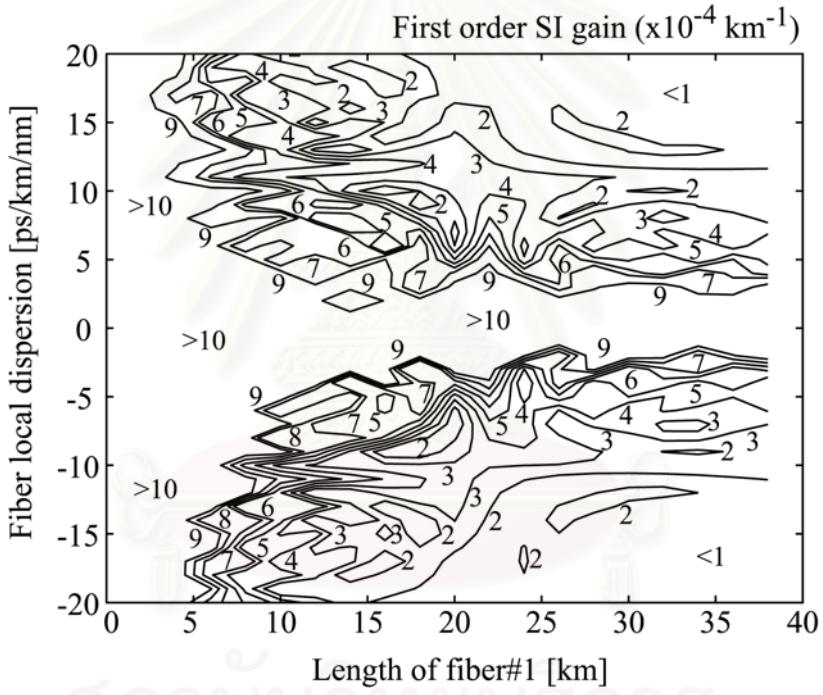

(b)

Figure 5.5: Model of dispersion-managed transmission line and its corresponding SI gain contour map. (a) shows the model of dispersion-managed transmission line composed of fiber#1 and fiber#2 whose lengths are unequal. (b) shows the contour map of the first order SI gain peak as functions of D_1 and x. The gain map indicates that the use of fiber#1 that has large local dispersion with relatively long length can significantly reduce the SI gain.

5.3 Computer Simulations

In order to confirm the validity of the proposed theory, we have performed some numerical simulations using a CW signal and amplified spontaneous emission (ASE) noise as sideband frequency source. It should be noted that the CW is used for the convenience of observing the gain and the position of SI. The main parameters used in the simulations are the same as those used in Fig. 5.2, 5.3, and 5.4. The TOD of fiber#1 and fiber#2 are set at 0.06 ps/km/nm^2 and –0.06 ps/km/nm^2, respectively. Since the two fibers have equal length so that the accumulated TOD is canceled at each dispersion compensation interval. At the output of each amplifier the ASE noise is added to the signal through the process of amplification with noise figure of 5.3 dB (n_{sp} = 1.7). The propagation of the optical signal is calculated by solving the nonlinear Schrodinger equation (NLSE) by the split-step Fourier method (SSFM) [4].

The results of the numerical simulations for several cases in terms of transmitted optical spectrum are shown in Fig. 5.6. The transmitted CW spectrum for $l_d = l_f$ = 40 km with D = 4.3 ps/km/nm and D = 21.3 ps/km/nm are shown in Fig. 7(a) and (b), respectively. Figure 5.6(c) and (d) show the results for the case $l_d > l_f$ with D = 14 ps/km/nm and $l_d < l_f$ with D = 16.7 ps/km/nm, respectively. According to Fig. 5.3, at D = 4.3 ps/km/nm, the first, second and third order SI all exhibit high gain with almost the same value. Oppositely, at D = 21.3 ps/km/nm, all the three orders of SI appear in minimum value.

As expected, in all figures, the computer simulation results of both SI gain and SI frequency are in a good agreement with the theoretical gain shown in Fig. 5.2, 5.3 and 5.4 together with Eq. (5-19) and (5-28), confirming the accuracy of our analytical derivation. For high SI gain as Fig. 5.6(a), SI arises obviously even in such relatively short transmission length (2,000 km). On the other hand, in order to observe SI for large D, it requires the transmission distance as long as 16,000 km to serve the gain as shown in Fig. 5.6(b), 8,000 km in Fig. 5-6(c) and 6,000 km in Fig. 5.6(d). This informs us that strong dispersion management fiber using such the combination of SMF and RDF can be used to suppress SI.

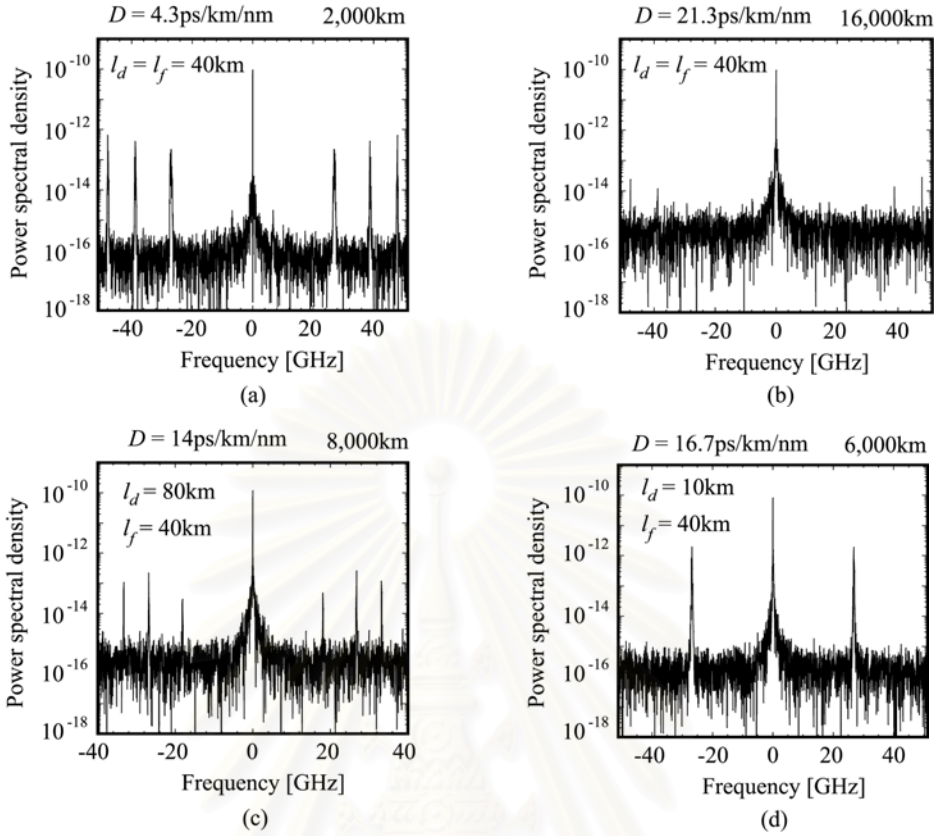

Figure 5.6: Numerical simulation results show the spectrums of optical CW signal and amplified spontaneous emission (ASE) noise transmitted in dispersion management transmission line using SMF and RDF with periodic signal amplification. (a) 2,000-km-transmitted CW spectrum for $l_d = l_f$ = 40 km with D = 4.3 ps/km/nm, (b) 16,000-km-transmitted CW spectrum for $l_d = l_f$ = 40 km with D = 21.3 ps/km/nm, (c) 8,000-km-transmitted CW spectrum for l_f = 40 km, l_d = 80 km with D = 14 ps/km/nm, and (d) 6,000-km-transmitted CW spectrum for l_f = 40 km, l_d = 10 km with D = 16.7 ps/km/nm. All simulation results, for both SI gain and SI frequency, are in a good agreement with the theoretical gain shown in Fig. 5.2, 5.3 and 5.4.

When l_d is determined, then, it is helpful to use SI gain contour map to design the operating D_{av} and P_0 at the point where the SI gain becomes as low as possible. If we consider a practical case when $l_d = l_f$, assuming that the local SOD is fixed at a

given value, the magnitude of SI gain now only depends on P_0 and D_{av}. Figure 5.7 shows the gain contour map of the first order of SI concerning the dispersion managed transmission line using the combination of SMF and RDF. It should be noted that we should concentrate to the first order SI because, practically, the low order of SI is easier to be phase-matched and causes problem in the long haul transmission than other high orders. The SMF and RDF parameters used for the calculation are the same as those have been used for fiber#1 and fiber#2, respectively. In the contour map, $|D|$ is assumed to be 17ps/km/nm with positive sign for the SMF and minus sign for the RDF.

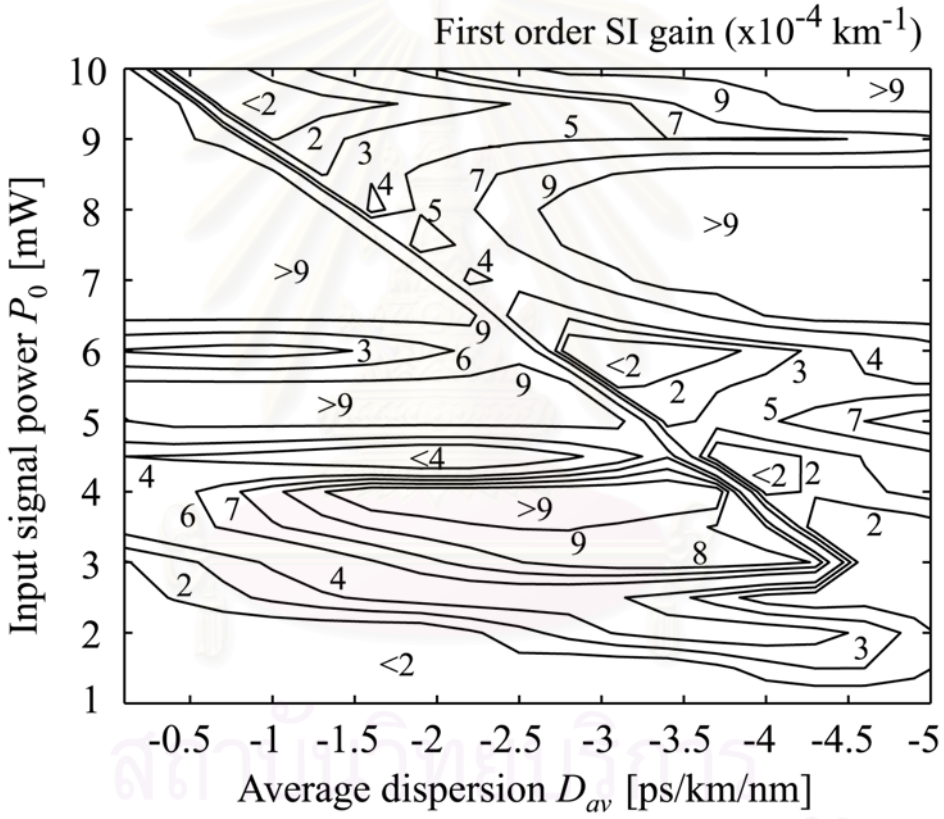

Figure 5.7: Gain contour map of the first order of SI concerning the dispersion managed transmission line consisting of SMF and RDF for $l_d = l_f$ = 40 km and $|D|$ = 17 ps/km/nm with positive sign for the SMF and minus sign for the RDF.

In Fig. 5.7, for low P_0, which is referred to relatively short transmission, SI possesses relatively low gain over a wide range of D_{av}. For high power transmission, using low D_{av} can avoid the SI gain and, at the same time, move the SI position out of the signal carrier. However, at some points of P_0, the SI gain exhibits large value even at very low D_{av}, for examples, SI gain as high as 9 x 10^{-4} km^{-1} arises from P_0 = 5 mW at D_{av} = –0.5 ps/km/nm. In order to achieve the maximum performance of the system, these operating points should be avoided. It should be noted when this periodic dispersion management using SMF and RDF is not applied to the system, the first order SI induced from only periodic amplification in dispersion-shifted fiber chain exhibits high gain larger than 10^{-3} km^{-1} even P_0 > 2 mW is used.

5.4 Effect of SI on Long Haul WDM Transmission Systems

In dispersion managed transmission system consisting of SMF and RDF, all channels experience almost the same amount of D_{av}. Thus, each channel produces its own SI that occurs at frequency shifted from carrier frequency by the same amount of frequency shift with almost the same gain. If two different channels produce SI at the same frequency, SI will cause a serious problem to the channels whose carriers are placed just at that frequency especially for the frequency where the first order SI arises.

In order to confirm our presumption, we perform computer simulations of the transmission of 4-wavelength CW signal and ASE noise. In the first calculation, we focus on the case when the first order SI gain generated from two separated channels enhances each other and positions on the other two channels. In the calculations, l_d is set equal to l_f at 40 km and other SMF and RDF parameters are the same as those used in other calculations described above. According to the contour map in Fig. 8, to investigate the problem of SI even the system is operating with condition that yields relatively low SI gain, we select P_0 = 3 mW and D_{av} = –0.5 ps/km/nm, which yields the first order SI gain about 2 x 10^{-4} km^{-1}. Using Eq. (5-28) and the calculation parameters, the first order SI will arise at ± 77.4 GHz shifted from each carrier frequency. Next, we place four channels at the frequencies –116.1 GHz, –38.7 GHz, 38.7 GHz, and 116.1 GHz shifted from the zero-dispersion wavelength 1550 nm

respectively. By this arrangement, SI produced from channel#1 and channel#3 will arise just at the position of channel#2 carrier. Similarly, SI induced from channel#2 and channel#4 will occurs just at the position of channel#5-

Figure 5.8(b) shows the spectrum of the 4-channel CW signal transmitted over 4000 km comparing with its initial shape shown in Fig. 5.8(a). By this channel allocation, the serious distortion of CW spectrum is clearly observed. In order to avoid this problem, it is necessary to arrange the channel allocation in such a way that none of the channel is placed on the SI frequency.

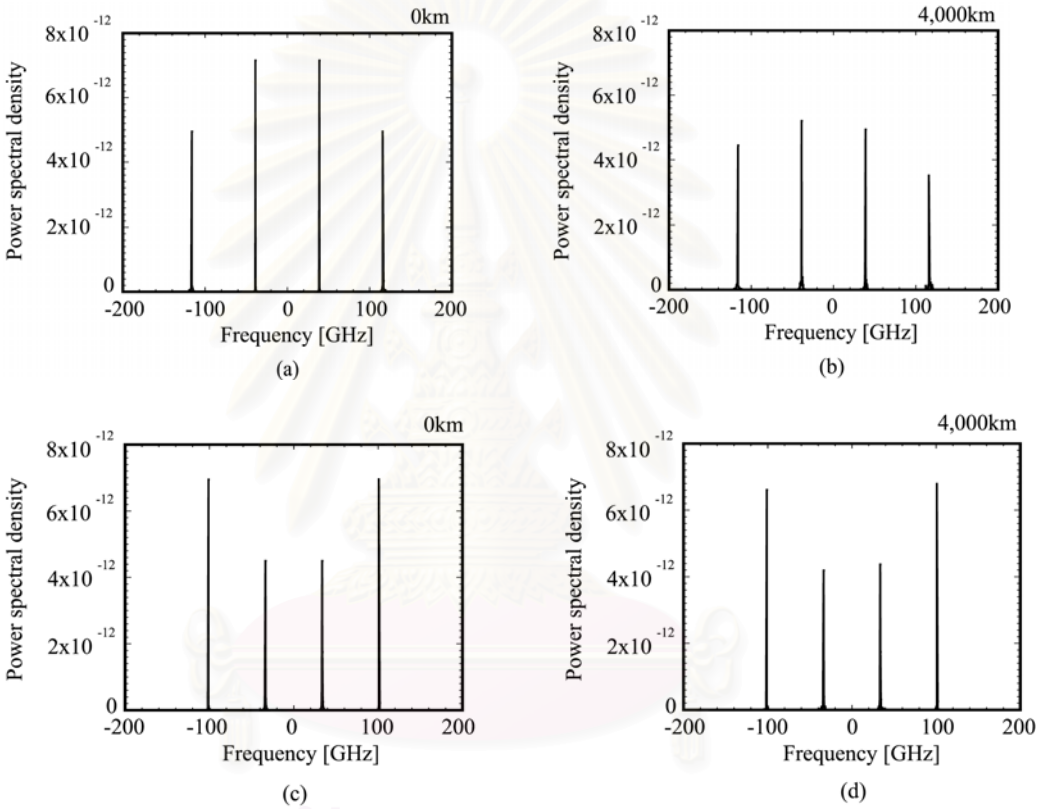

Figure 5.8: Optical spectrum of 4-channel CW signal shown in linear scale. l_d is set equal to l_f at 40 km, P_0 = 3 mW and D_{av} = –0.5 ps/km/nm. In (a) and (b) the channel spacing is set at ± 77.4 GHz where two of the first order SI from neighbor channels arise just at channel#2 and channel#3 carrier positions. (a) initial shape and (b) 4,000-km-transmitted spectrum. By this channel allocation, serious distortion of CW spectrums is clearly observed. (c) and (d), respectively, shows the initial and 4,000-km-transmitted CW spectrums simulated by decreasing 10 GHz to shift SI frequency out of signal bandwidth. The transmitted spectrum in (b) appears in more severe distorted shape than (d) because of SI.

Figure 5.8(c) and (d) respectively shows the initial four-channel CW signal spectrum and its shape after 4,000 km transmission simulated by the same parameters as Fig. 5.8(b). The channel spacing in this calculation is decreased 10 GHz resulting in the shift of SI frequency out of signal bandwidth. Comparing to Fig. 5.8(b) where the SI occurs just at the channel position, the output spectrum in Fig. 5.8(d) appears in similar shape to the initial than the case of Fig. 5.8(b), confirming the achievement of avoiding the effect of SI. In fact, as FWM among channels is easy to be phase-matched when the channel spacing becomes smaller, the decrease in channel spacing should have led to more signal distortion. However, the transmitted spectrum in Fig. 5.8(b) appears in more severe distorted shape than that of Fig. 5.8(d). This can be interpreted that the effect of SI plays a significant role in determining the transmission performance than the inter-channel FWM for this condition.

To explore the effect of SI on WDM transmission more details, we perform the calculation of the bit-error rate (BER) of the 4-channel WDM system using pseudorandom 32-bit Gaussian RZ pulse train as an input optical signal whose bit rate of each channel is equal to 10 Gbit/s. At the end of the system, the accumulated D_{av} is post-compensated by multiplying the complex amplitude of the signal with a negative amount of linearly accumulated phase shift caused by D_{av}. We assume the use of a bandwidth-adjustable optical band-pass filter (OBPF) in front of the receiver to select the passband channel. This OBPF is also always adjusted to obtain minimum BER. The receiver is modeled by 6.5-GHz-cutoff sixth-order Bessel-Thompson low-pass filter following by BER detector. For obtaining the numerical BER of the detected signal, the simulation is repeated 128 times for the same pseudo-random pulse train. The numerical *Q* factor of every bit is then individually calculated at the maximum eye-opening point of the bit period. Based on the assumption of Gaussian noise distribution, the numerical BER's are computed from the bit numerical *Q* factors and averaged over the entire bits [25].

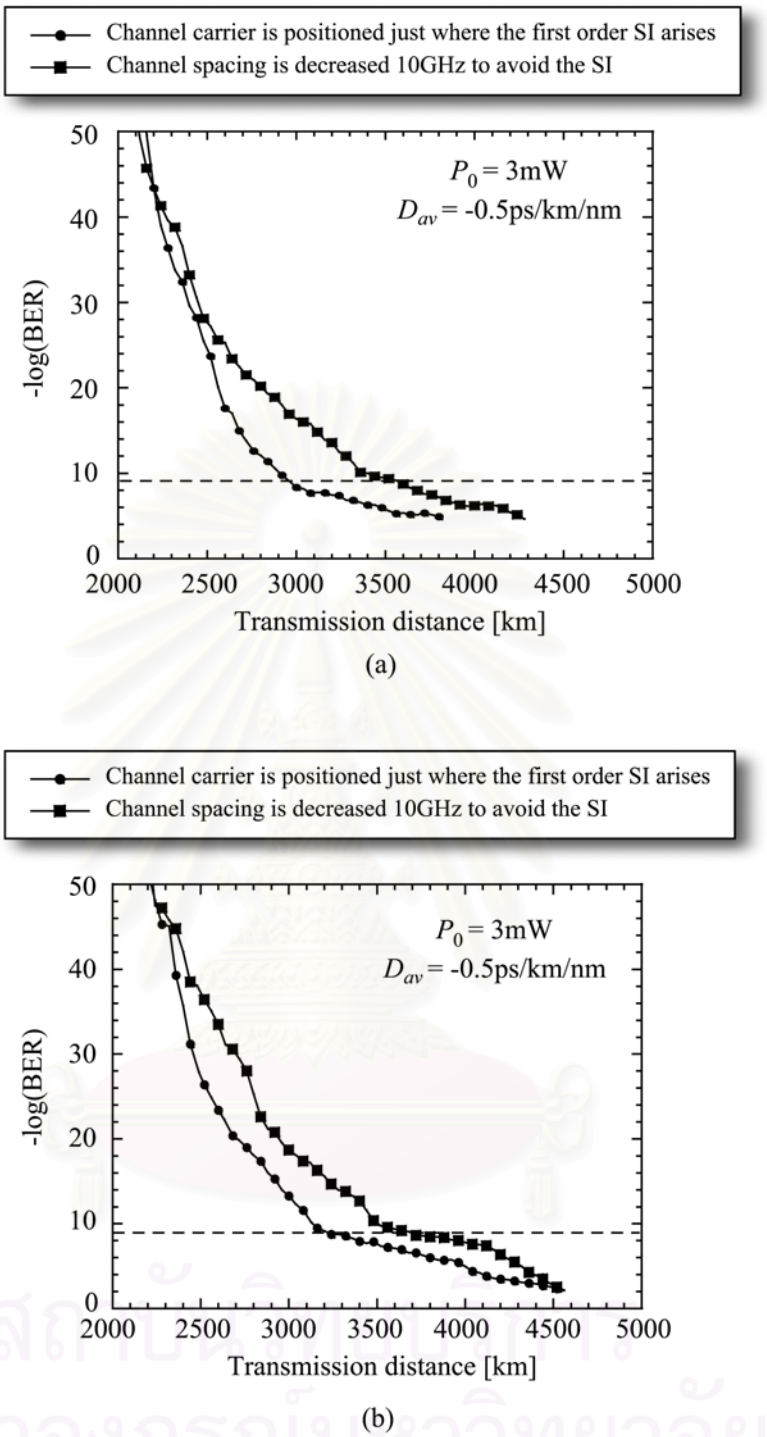

Figure 5.9: BER as a function of transmission distance calculated from the (4 x 10)-Gbit/s-32-bit RZ signal for different channel spacings. (a) and (b) show BER curves of channel#2 and channel#3, respectively. In both (a) and (b), circles show BER obtained from the system whose signal carriers are placed on the position where the SI arises while squares show BER obtained from 10-GHz-decreasing channel spacing. At BER = 10^{-9} (shown by an across dotted line) the systems where the channel allocation is re-arranged to avoid the position of SI give significantly longer transmission length.

Figure 5.9(a) and (b), respectively, shows the calculated BER curves of channel#2 and 3 as a function of transmission distance simulated by P_0 = 3 mW and D_{av} = –0.5 ps/km/nm with different channel spacing setting. The BER curves obtained from the system whose signal carriers are placed on the position where the SI arises (shown by circles) drop more rapidly than those obtained from 10-GHz-decreased channel spacing (shown by squares). If we defined the maximum transmission distance obtained at the distance where the BER reaches 10^{-9} as shown by the across dotted line, the systems where the channel allocation is arranged to avoid the position of SI yield significantly longer transmission length. We also simulated the system with P_0 = 5mW and D_{av} = –0.5 ps/km/nm that yields high SI gain. The result showed more severe degradation of BER for channel carriers positioned just on SI frequency and, on the contrary, an obvious improvement when a channel allocation is done to avoid the SI frequency. This confirms the necessity of avoiding SI in higher-order dispersion management long-haul WDM transmission systems.

5.5 Conclusion

In this chapter, we have presented the derivation of the analytical expression of the sideband instability (SI) induced from periodic signal power variation and periodic dispersion management considering when two different fibers are connected together to form the dispersion compensation link. Three possible dispersion management systems were considered: (a) system where dispersion management period is larger than amplifier spacing, (b) system where the two lengths are equal, and (c) system where amplifier spacing is larger than dispersion management period.

We found that SI frequency depends on the larger period between the amplifier spacing and the dispersion management period. The larger the variation period becomes, the SI frequency will arise closer to carrier frequency. Moreover, the gain of SI appears to be reduced with the increase of local fiber second-order dispersion (SOD). This is because the increase in the local SOD virtually shifts the order of SI to higher order resulting in the difficulty of phase-match process. The computer simulations were made and their results were in a good agreement with the derived theory.

In WDM systems that use relatively narrow channel spacing, we demonstrated that even the dispersion map is properly designed to achieve low SI gain, SI causes signal distortion to specific channels that fall just on the low order SI frequency, especially the first order. Additionally to WDM system design rules, the channel allocation must avoid the SI position in such a way that none of the channel should be lied at. The computer simulations have confirmed that BER of WDM systems whose channel location is re-arranged to avoid SI give a significant improvement of the transmission performance.

CHAPTER 6
SIMULTANEOUS SUPPRESSION OF TOD AND SI IN OPC TRANSMISSION SYSTEMS BY COMBINATION OF SMF AND RDF

In optical phase conjugation (OPC) systems, the third-order dispersion (TOD) of optical fibers and the nonlinear resonance at well-defined signal sideband frequencies called sideband instability (SI) mainly limit the transmission performance. We propose, for the first time, a scheme for simultaneous suppression of both TOD and SI in OPC systems using a periodic higher-order dispersion-managed link consisting of standard single-mode fibers (SMFs) and reverse dispersion fibers (RDFs). Computer simulation results demonstrate the possibility of 200-Gbit/s data transmission over 10,000 km in the higher-order dispersion-managed OPC system, where the dispersion map is optimized by our system design strategies [115].

6.1 Introduction

To expand both capacity and distance of ultra-high-bit-rate optical-time-division multiplexed (OTDM) transmission systems, management of second-order dispersion (SOD) and third-order dispersion (TOD) of optical fibers will be one of the key issues. For this purpose, a special dispersion compensating fiber called the reverse dispersion fiber (RDF) [58], [60] has been proposed and demonstrated. Since the standard single-mode fiber (SMF) and the RDF possess almost equivalent absolute values of SOD and TOD with opposite signs, the combination of SMF and RDF realizes a dispersion-flattened transmission line with a sufficiently low average SOD.

Several recent OTDM transmission experiments demonstrated very attractive results such as the 640-Gbit/s signal transmission over 92 km [61], and the 1.28-Tbit/s signal transmission over 70 km by using SMF and RDF [62]. In dispersion-managed soliton transmission systems, a recent numerical study showed a possibility of 320-Gbit/s transmission over 6,000 km employing short-period SOD and TOD management [63]. Even in wavelength-division multiplexed (WDM) transmission systems, the combination of SMF and RDF could achieve the data rate as high as 1 Tbit/s (104 x 10Gbit/s) over 10,000 km [104].

As an alternative approach for ultra-high bit-rate long-haul transmission, midway optical phase conjugation (OPC) is an attractive solution to compensate for

the waveform distortion induced from the interplay between the SOD and the self-phase modulation (SPM) effect [65]. Several recent works have reported broadband, wavelength-shift-free, and polarization-independent optical phase conjugators [66], [67]. These may bring the OPC system into a commercial world in the short coming future.

However, the ultimate performance of the OPC system is also limited by the TOD together with the nonlinear resonance at well-defined signal sideband frequencies induced by the periodic amplification process called the sideband instability (SI) effect [68]. Recently, we have demonstrated by a numerical simulation that a single-channel transmission with a bit rate of 100 Gbit/s can successfully achieve a transmission distance over 10,000 km with TOD compensation in the OPC system [49].

For the SI effect, Watanabe and Shirasaki have given a condition for perfect SI compensation [11]. In order to satisfy the condition, a dispersion-decreasing (SOD) fiber (DDF), whose SOD-decreasing coefficient is proportional to fiber loss coefficient, must be installed throughout the entire OPC system length. A good transmission result of 20-Gbit/s data over 3,000 km [95] was demonstrated by using a quasi-DDF in which short fibers with different dispersion values were concatenated to form the dispersion-decreasing profile. However, such an approach sounds too impractical to be employed in real systems. Moreover, the uncompensated TOD will show up to affect the long-haul transmission with the bit rate higher than 40 Gbit/s. Recently, our analysis has demonstrated a more practical way to suppress the SI by only applying strong dispersion management [51], [52]. Therefore, by using such combination of SMF and RDF in the OPC system, the simultaneous suppression of both SI and TOD can be expected.

In this chapter, we show, for the first time to our knowledge, the simultaneous suppression of TOD and SI in ultra-high-bit-rate long-haul OPC transmission systems using the dispersion-managed fiber link consisting of SMF and RDF. This paper is organized as follows. Section 6.2 reviews our previous works about the TOD compensation scheme in OPC systems and the reduction of the SI gain by employing the combination of SMF and RDF. Our main contributions presented here commence from section 6.3. In this section, we discuss the implementation of dispersion management in OPC systems. We suggest that the symmetric SOD profile with respect to the mid-point of the system is preferable in order to avoid the nonlinear

accumulation of amplifier noise when the system operates with relatively high signal intensity. The performance improvement of the 100-Gbit/s OPC system using the symmetric dispersion profile is confirmed by numerical simulations even when the dispersion map is not optimized.

In section 6.4, we discuss the optimum dispersion map design for obtaining the maximum performance in OPC systems. In section 6.5, we demonstrate that, a 200-Gbit/s data transmission over a 10,000 km distance can be achieved by simultaneously suppressing TOD and SI in OPC systems using the dispersion-managed fiber link consisting of SMF and RDF whose dispersion map is properly designed. Finally, the summary of this paper is presented in section 6.6.

6.2 Simultaneous Suppression of TOD and SI by SMF and RDF

As described above, the performance of OPC transmission systems is mainly limited by TOD and SI effect. Without TOD compensation, a 10,000-km transmission with data rate of 40 Gbit/s was achieved by following optimum design strategies to avoid the effect of SI [65]. To increase the transmission bit-rate of the 10,000-km OPC system, it is necessary to suppress both TOD and SI. In this section, we review and summarize our previous studies on the TOD compensation scheme in OPC systems [49] and the reduction of SI gain through the strong periodic dispersion-managed fiber link [51], [52].

6.2.1 TOD Compensation Scheme in OPC Systems

The accumulation characteristic of TOD in OPC systems can be discussed through three characteristic scales: the SOD length L_{d2}, the TOD length L_{d3}, and the nonlinear length L_{nl}, which are defined in [4]. In OPC systems, the SOD exists along the entire transmission length; therefore, L_{d2} becomes many times shorter than L_{nl} for the case of high bit-rate transmission. When L_{d2} is much shorter than L_{nl} and L_{d3}, the signal pulses are rapidly broadened by SOD, and their peak power decreases after transmitting for several L_{d2}. This means that the broadened pulses almost do not experience the effect of fiber nonlinearity. Thus, in ultra-high-speed OPC systems, the accumulation of the TOD-induced phase shift increases almost linearly with the transmission length at an ordinary operating signal power. The linear TOD accumulation enables us to achieve perfect TOD compensation by placing only one

compensator at any point in the line, or even freely installing distributed compensators without the necessity of concerning their intervals.

When TOD is perfectly compensated in OPC systems, the 100-Gbit/s data transmission over 10,000 km [49] can be made possible at the balance point of the improvement of signal-to-noise ratio (SNR) and the degradation from SI effect. In order to further improve the transmission performance of the TOD-compensated OPC system, the waveform distortion induced from SI effect must be overcome.

6.2.2 Reduction of Sideband Instability Gain by Strong Dispersion Management

As shown in previous chapter, the gain of SI can be practically reduced by using a strong periodic dispersion-managed transmission line such as the combination of SMF and RDF, instead of uniform dispersion line [51], [52]. This is because the increase in the local fiber SOD virtually shifts the order of SI to higher orders resulting in the difficulty of phase-match process. Furthermore, the frequency where SI arises depends on the larger period between the amplifier spacing (l_f) and the dispersion management period (l_d). The larger the variation period becomes, the closer to the carrier frequency the SI frequency arises.

In order to show the reduction of SI gain through a periodic dispersion-managed line, here we calculate the gain contour map of the first-order SI focusing on the dispersion-managed transmission line consisting of SMF and RDF. The dispersion management profile is the simple type where one SMF and one RDF with an equivalent length are only connected together. In each dispersion management period, SMF is placed before RDF at the output end of the amplifier. The placement of signal carrier frequency determines the values of the operating average SOD D_{av} and the local SOD D. In Fig. 6.1, the gain map is obtained as a function of l_d and an input signal power P_0 when D_{av} and D are given. It should be noted that we should concentrate to the first order SI because, practically, the low order of SI is easier to be phase-matched and causes more serious signal distortion in long haul transmission systems than higher order SI. The fiber loss coefficient α_1 and the fiber nonlinear coefficient γ_1 of SMF used for calculating the gain map are 0.2 dB and 1.6 $W^{-1}km^{-1}$, respectively, while α_2, γ_2 representing those of RDF are 0.25 dB and 6.8 $W^{-1}km^{-1}$,

respectively. D_{av} is set at –1 ps/km/nm and $|D|$ = 17 ps/km/nm. Comparing with these gain maps, the magnitudes of the first, second, and third-order SI gains of a non-dispersion management system as a function of the input power is shown in Fig. 12. In this case, the transmission fiber is assumed to be a dispersion-shifted fiber (DSF) with α = 0.2 dB and γ = 2.6 $W^{-1}km^{-1}$.

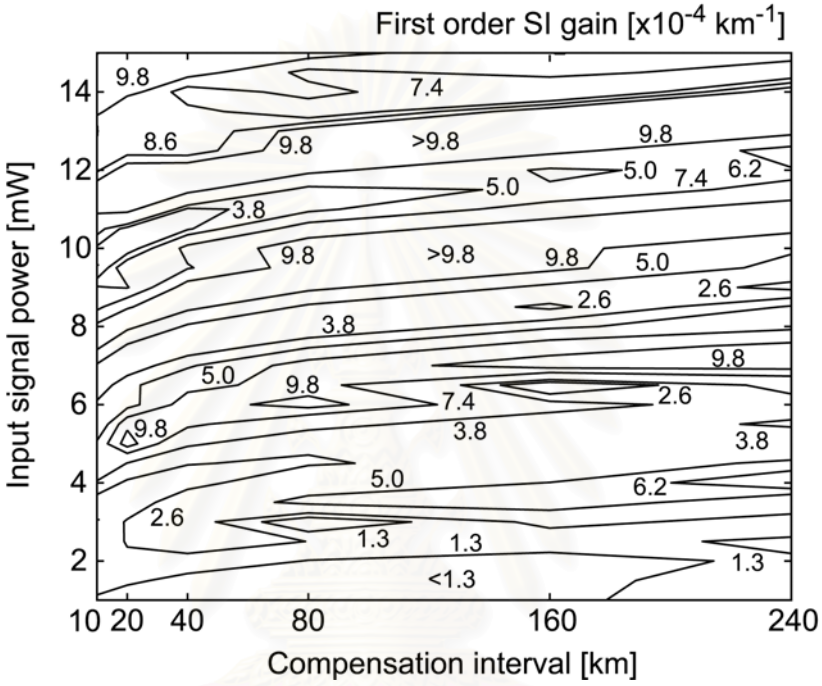

Figure 6.1: Gain contour map of the first-order SI focusing on the dispersion-managed transmission line consisting of SMF and RDF. The gain is calculated as a function of l_d and an input signal power P_0 when an average SOD D_{av} and a fiber local SOD $|D|$ are set at –1 ps/km/nm and 17 ps/km/nm, respectively.

In Fig. 6.1, for low P_0 (< 3 mW), SI possesses very low gain over a wide range of l_d ; thus, SI may not affect the signal transmission for relatively short distance systems. Even in high power transmission (from 3 mW to 15 mW), SI still exhibits relatively low gain (< 10^{-3} km^{-1}) comparing with the gain shown in Fig. 6.2 at the same P_0 . Without dispersion management, Fig. 6.2 indicates that the SI gain

almost linearly increases with P_0 and exhibits a value larger than 10^{-3} km^{-1} even for P_0 = 2 mW for the first-order SI.

The linear accumulation of TOD, together with the reduction of SI gain through strong dispersion management open a possibility of simultaneously suppressing TOD and SI in OPC systems by using the higher-order dispersion management transmission line such as the combination of SMF and RDF.

Assuming that TOD and SI are perfectly suppressed in OPC systems, there remains the problem originated from the accumulation of the transmission of amplified spontaneous emission (ASE) noise which is enhanced during the transmission by parametric interaction between SOD and SPM [65]. As shown in Fig. 6.3, the transmission of the ASE noise is not symmetrical with respect to the midpoint of the system. Thus, only part of the nonlinear enhancement can be compensated by OPC while there still exists the accumulated ASE noise, which is enhanced by the nonlinear interaction.

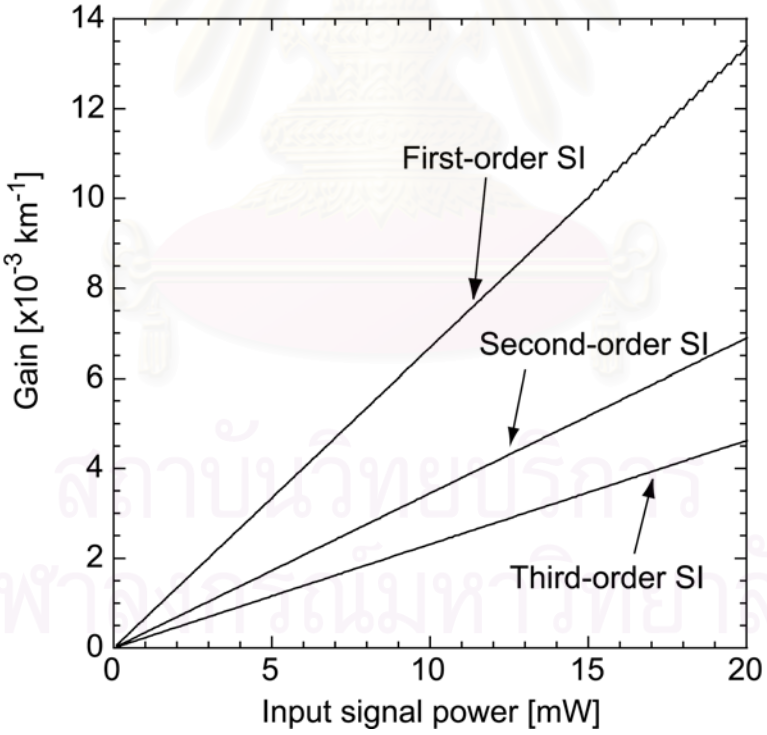

Figure 6.2: Magnitudes of the first, second, and third-order SI gains arising from a non-dispersion management system. The gains are obtained as a function of signal input power. The transmission fiber is assumed to be only DSF with α = 0.2 dB and γ = 2.6 $W^{-1}km^{-1}$.

It should be noted that this fiber nonlinearity-enhanced ASE noise cannot be suppressed by the combination of SMF and RDF. However, its harm is expected to reduce through large fiber local dispersion with sufficiently large compensation period. This is because the signal pulses are rapidly broadened by SOD, therefore, they almost do not experience the effect of fiber nonlinearity.

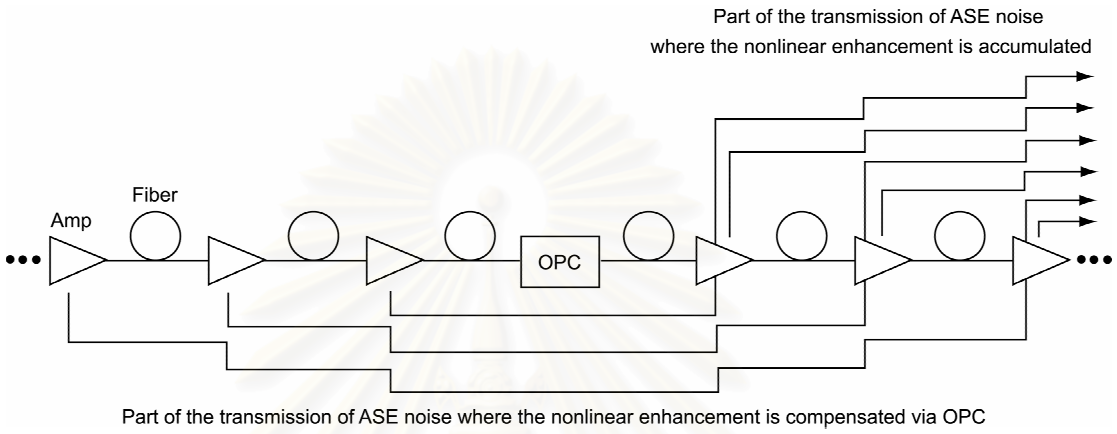

Figure 6.3: Transmission of ASE noise in OPC system. ASE noise produced from each optical amplifier is enhanced during the transmission by parametric interaction between SOD and SPM, and will accumulate to the end of system. Since the transmission of ASE noise is not symmetric with respect to the system mid-point, therefore, only part of the nonlinear enhancement can be compensated by OPC while their remains an amount of ASE noise that is enhanced by the nonlinear interaction and accumulates to the end of system.

6.3 Implementation of Dispersion Management on OPC Systems

The most practical way available now to compensate TOD for ultra-high bit-rate long-haul transmission is probably the use of the dispersion-managed fiber link such as the combination of SMF and RDF. In the previous section, we have shown that SI induced from the periodic power variation can be suppressed by using periodic dispersion management with large local dispersion. Therefore, by using such combination of SMF and RDF in OPC systems, the simultaneous compensation of both TOD and SI can be expected. Moreover, the accumulation of D_{av} will be

automatically compensated by OPC without post compensation used in ordinary dispersion management systems.

6.3.1 Possible Installing Dispersion Profiles

Figure 6.4 illustrates two possible schemes to install dispersion management in the OPC transmission system. In Fig. 6.4(a), both periodic dispersion variation and periodic power variation are in uniform distributions along the entire system length. On the other hand, in Fig. 6.4(b), the order of SMF-RDF is reversed to RDF-SMF after the midway OPC yielding the symmetric distribution of the periodic dispersion variation with respect to the system mid-point.

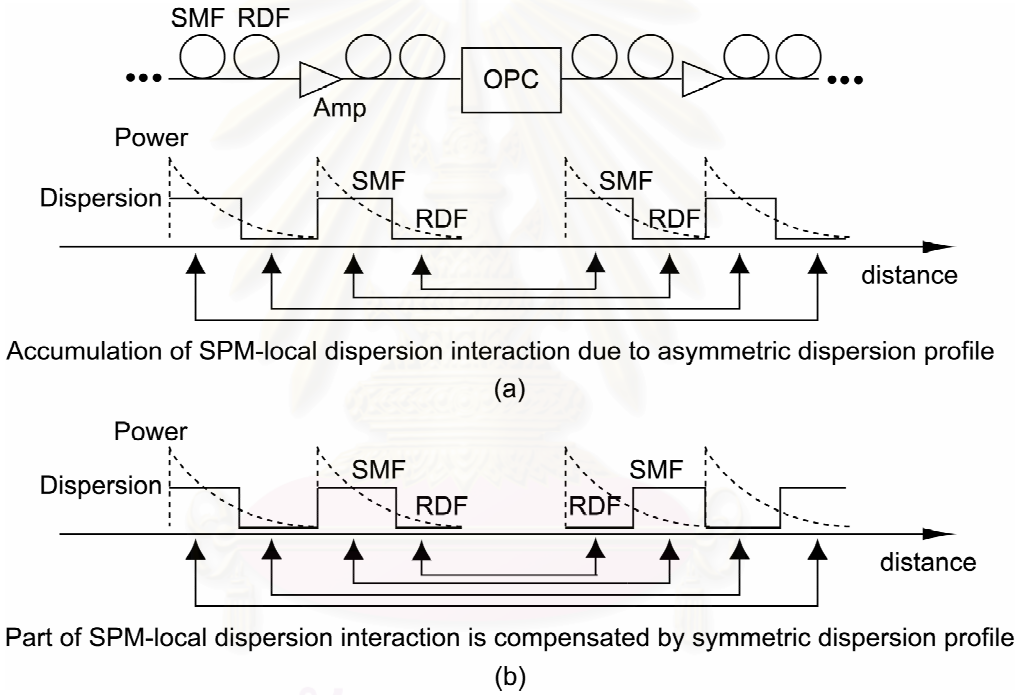

Figure 6.4: Two possible ways for implementing the dispersion management in OPC transmission system. In (a) both periodic dispersion variation and periodic power variation are in uniform distributions along the entire system length. On the other hand, in (b), the order of SMF-RDF is reversed to RDF-SMF after the system mid-point, forming the symmetric distribution of the periodic SOD variation with respect to the system mid-point. The symmetric dispersion profile in (b) gives better transmission performance than profile (a) especially when the systems operates with high signal power because part of the interaction between SPM and fiber local dispersion is compensated by OPC.

We suggest that the symmetric dispersion profile in Fig. 6.4(b) gives better transmission performance than the other profile especially for high power transmission. The reasons can be explained as follows: First, when the nonlinear length L_{nl} is longer than the periods of the variations, due to the uniform distributions in Fig. 6.4(a), each order of SI arises from one frequency determined by the two periodic perturbations and experiences the gain whose magnitude exponentially increases with the transmission length. On the other hand, for the dispersion management profile in Fig. 6.4(b), the system in the first half and second half produce their own SI at different frequencies whose separation depends on the difference in the nonlinear coefficient and the fiber loss coefficient between SMF and RDF. However, each resonance frequency experiences the SI gain only half of the system length, the signal distortion may not be so severe as that occurs from the dispersion profile in Fig. 6.4(a).

Second, for high power transmission, when L_{nl} becomes comparable or shorter than the compensation interval, the interplay between SPM and the local dispersion of each fiber occurs and causes additional signal waveform distortion. With this consideration, by constructing the symmetric dispersion compensation profile as shown in Fig. 6.4(b), part of the interaction between SPM and local dispersion of the fiber will be compensated by OPC whether the power variation distribution remains unchanged. Oppositely, for the profile in Fig. 6.4(a), this interaction will accumulate along the transmission length due to the asymmetric distribution with respect to mid-point of both periodic power variation and periodic dispersion compensation.

6.3.2 Computer Simulations

In order to evaluate our proposed SI suppression method in OPC systems, we perform a computer simulation of the transmission of 100-Gbit/s data composed of 32-bit pseudorandom Gaussian RZ pulses based on the system models in Fig. 6.6. In the calculation, we set $l_d = l_f$ = 40 km. TOD is assumed to be 0.06 ps/km/nm for SMF and -0.06 ps/km/nm for RDF. Other SMF and RDF parameters used in this simulation are the same as used above. The optical amplifier produces ASE noise with noise figure of 5.3 dB (n_{sp} = 1.7). The optical pulse at the midway of the system is conjugated by an ideal infinite-bandwidth optical phase conjugator.

When the combination of SMF and RDF is not applied for TOD compensation, the TOD compensator, placed only at the end of system, is assumed to be an ideal device that multiplies the complex amplitude of the signal with a negative amount of linearly accumulated phase shift caused by TOD. Also, for signal transmission in this case, DSF with the same parameters as the calculation above is used.

To see the efficiency of the SI suppression more obviously, the input signal power P_0 is set at 21 mW giving L_{nl} becomes equivalent to l_f. Also for all other cases, P_0 will be set at this value. Since SMF and RDF exhibit different values of α and γ, we calculate L_{nl} of the system employing SMF and RDF by using the average values of those parameters. With P_0 = 21 mW, L_{nl} of the system constructed by SMF and RDF becomes approximately 36 km, which is slightly shorter than that of DSF.

The propagation of the optical pulse is calculated by solving the nonlinear Schrodinger equation (NLSE) by the split-step Fourier method (SSFM) [4]. The integration step size of SSFM is always chosen at the value that gives a step size error less than 0.01 % [116]. The receiver is modeled by an optical band-pass filter (OBPF), a 65-GHz-cutoff sixth-order Bessel-Thompson low-pass filter, followed by a BER detector. The system performance is evaluated in terms of the numerical bit-error rate (BER). The bandwidth of the OBPF is always adjusted to obtain the minimum BER. To calculate the numerical BER of the detected signal, the simulation is repeated 128 times for the same pseudo-random pulse train. The numerical *Q* factor of every bit is then individually calculated at the maximum eye-opening point of the bit period. Based on the assumption of the Gaussian noise distribution, the numerical BER is computed from the bit numerical *Q* factor and averaged over the entire bits [50].

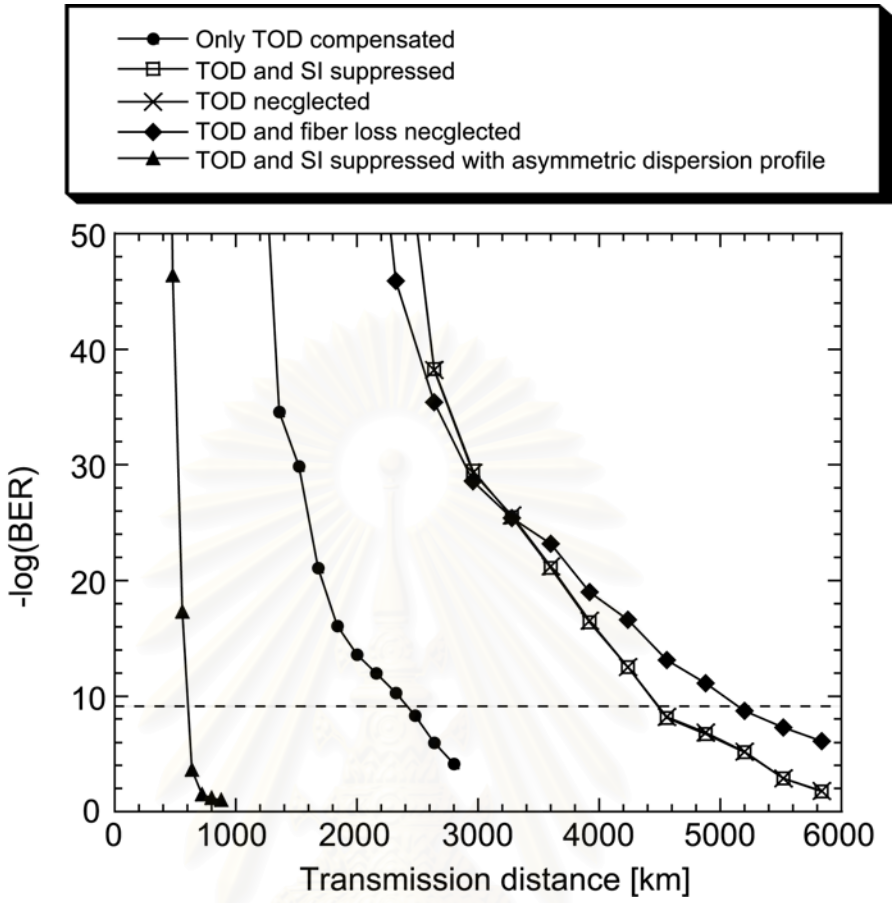

Figure 6.5: BER of several OPC systems, calculated as a function of transmission distance. For all OPC systems, the input signal power is adjusted to give L_{nl} equivalent to l_f at 40 km. Circles show BER obtained from the system where only TOD is compensated. Squares show BER of the system using SMF and RDF as transmission fiber with the symmetric dispersion management profile of Fig. 6.4(b), while triangles show BER of the system employing the asymmetric dispersion profile of Fig. 6.4(a). Crosses show BER of the system where TOD is neglected. Diamonds show BER obtained from the system where both TOD and SI are neglected. At BER = 10^{-9}, the achievable transmission length of the system using symmetric dispersion increases 2000 km longer than the system where only TOD is compensated without using SMF and RDF. Furthermore, BER of the system employing the asymmetric dispersion becomes the worst due to the accumulation of the nonlinear interaction between SPM and local fiber dispersion.

Figure 6.5 shows the calculated BER as a function of transmission distance. According to the condition $L_{nl} = l_f$, when only TOD is compensated (shown by circles), the performance of the system is limited by SI and the nonlinear distortion from the interaction between SPM and local dispersion in each segment of fiber. Thus, BER of the system in this case rapidly decreases. When the dispersion management profile in Fig. 6.4(b) is employed to the system (shown by squares), BER curve drops significantly slow. Comparing to the case without the combination of SMF and RDF, by using SMF and RDF, the achievable transmission length at BER = 10^{-9} can be further extended approximately 2000 km. Moreover, the BER curve of the system where TOD is neglected (shown by crosses) almost fits with that obtained from TOD-compensated system. This result mentions that this SI suppression method does not affect accumulation characteristics of TOD since l_d is still much shorter than the TOD length L_{d3} ($\approx$ 280 km) so that in the TOD scale, the signal propagates as if there is no dispersion management ever be installed.

On the other hand, BER of the system employing the dispersion profile of Fig. 6.4(a) (shown by triangles) obviously becomes worse than others due to the reasons described above. Furthermore, the difference in transmission distance between the BER curve obtained from the system using the dispersion profile of Fig. 6.4(b) and the BER curve obtained from the system neglecting TOD and SI (shown by diamonds) mainly comes from part of the interaction between SPM and local fiber SOD that cannot be perfectly compensated by OPC.

6.4 Optimum Dispersion Map for Higher-Order Dispersion-Managed OPC Systems Using SMF and RDF

When the combination of SMF and RDF is employed to a given system, the fiber local SOD and the average SOD are almost automatically determined by the placement of operating signal wavelength. In this case, the maximum system performance will be achieved by determining the optimum l_d and signal power. Below, we discuss the optimum dispersion map design considering the OPC systems using $l_d > l_f$, $l_d = l_f$, and $l_d < l_f$.

6.4.1 OPC Systems Using $l_d > l_f$

For given l_d ($l_d > l_f$), the increase in the signal power can help improving SNR. At the same time, when the signal power is increased until L_{nl} becomes comparable to, or shorter than l_d, the signal pulse will experience the local SOD rather than its periodic variation. In this case, SI determined by the period of l_f on each local fiber length also arises. Additionally, the signal will also be attacked by the interaction between SPM and the local SOD. Therefore, for given l_d ($l_d > l_f$), the maximum system performance will be achieved by using an optimum input power which yields the balance of the improvement in SNR and the degradation described above.

Even the use of very large l_d ($l_d > l_f$) can also help reducing the nonlinear enhancement of the ASE noise since the signal and the ASE noise will transmit through large local SOD which repeats for long length [93]. Additional to the problems discussed above, the larger l_d we use, SI, whose position is determined by l_d in this case, will occur at the frequency closer to the signal carrier. Therefore, even only a small SI gain may cause serious signal distortion. As a result, for larger l_d, the optimum signal power will exhibit lower value than that of shorter l_d. Furthermore, the system may give a good result close to the linear SNR limit for relatively low power transmission. However, the system performance will degrade very immediately after reaching the optimum signal power.

Comparing to ordinary dispersion management systems, in OPC systems, such optimum power will be found at relatively high value since dispersion exists along the transmission yielding L_{d2} several times shorter than L_{nl}, especially for the case of high bit-rate transmission.

6.4.2 OPC Systems Using $l_d = l_f$

When $l_d = l_f$, the transmission of signal is expected to give a good result since SI occurs at the furthest frequency from the signal carrier. However, the signal, in this case, keeps its high peak power during the transmission because the signal almost restores its shape at each l_f due to low average dispersion. Therefore, it is easy to be affected by the nonlinear effect. When $L_{nl} > l_d = l_f$, the nonlinear enhancement of ASE noise by the interaction between SPM and average SOD, which is more severe

than that of system with $l_d > l_f$, becomes a main problem that limits the system. Moreover, in the second half of the system, RDF, which exhibits larger nonlinear coefficient than SMF, is installed near the output of the optical amplifier according to the symmetric SOD distribution. This results in more serious enhancement of ASE noise since, in the second half, the signal and the accumulated noise will propagate through the highly nonlinear RDF where their powers are still intense. When L_{nl} approaches l_d by the use of high signal power, the interaction between SPM and fiber local SOD also arises and causes additional signal waveform distortion. By these reasons, the system constructed with $l_d = l_f$ may not be expectable to give good transmission performance comparing to $l_d > l_f$ case and even $l_d < l_f$ case.

6.4.3 OPC Systems using $l_d < l_f$

For the system with $l_d < l_f$, SI will arise at the same frequencies as those of the $l_d = l_f$ case since the position of the resonance frequency depends on the larger period between l_d and l_f. With increasing the signal input power, similar to the case of $l_d = l_f$, the problem which limits the performance of the system comes from the enhancement of the amplifier noise by the interaction between SPM and average SOD. However, even if we reverse the order of fibers after the mid-point to form symmetric dispersion profile, the nonlinear accumulation of amplifier noise will not be so severe as the case of $l_d = l_f$. This is because the signal at high peak power does not propagate on highly nonlinear RDF for a long length.

Even L_{nl} becomes very short by using relatively high input power, the interaction between the local SOD and SPM will not be so serious as the case of $l_d = l_f$. This is because the signal does not too much feel the local SOD as long as L_{nl} is still not comparable to l_d. This makes the systems with $l_d < l_f$ may yield a significant tolerance to high power transmission comparing to other cases. At given l_d ($l_d < l_f$), the optimum power will exhibit relatively high value than the case of $l_d > l_f$. However, for a low input power, the system may not give good performance comparing to the case of $l_d > l_f$ according to the interaction of SPM and average SOD.

From the above discussion, for each l_d , the optimum input power for achieving maximum transmission performance will be found at different values. One will be relatively low input power obtained for the case $l_d > l_f$. The longer l_d is, the lower the optimum power becomes. The other one will be found at relatively high value for the case $l_d < l_f$ and will be higher value with the reduction in l_d. However, the system operating with $l_d = l_f$ may not give as good result as the others.

6.5 Ultimate Performance of Higher-Order Dispersion-Managed OPC Systems

To explore the ultimate performance of the higher-order dispersion-managed OPC systems employing the combination of SMF and RDF when the systems are operating in optimum conditions, we perform extensive computer simulations of the systems with data rate of 100 Gbit/s, 160 Gbit/s, and 200 Gbit/s. The SOD profile used in the simulations is the symmetric profile shown in Fig. 6.4(b). The system parameters and fiber parameters are all the same as above calculations.

Figures 6.6, 6.7, and 6.8, respectively, show the calculated BER at 10,000 km of OPC transmission systems with data rate of 100 Gbit/s, 160 Gbit/s, and 200 Gbit/s as a function of the signal input power P_0 for several l_d (10 km, 40 km, 80 km, 160 km, and 240 km). In each figure, BER of the same OPC system neglecting the nonlinear coefficient γ is also calculated to show the linear SNR limit for comparison.

According to the simulated results of the 100-Gbit/s OPC systems shown in Fig. 6.6, for low P_0, BER of the systems with larger l_d appears in a value closer to the SNR limit because the use of large l_d can help avoiding the effect of fiber nonlinearity. For higher P_0, BER of the systems using large l_d start decaying rapidly while that of system using l_d = 10 km still shows a good result due to its tolerance to fiber nonlinearity. As discussed above, the system with l_d is set equivalent to l_f at 40 km shows the worst result. However, with defining a maximum transmission distance at BER = 10^{-9}, all 100-Gbit/s systems can achieve 10,000-km transmission for a wide range of P_0. In comparison with these results, the system using DSF

incorporated with TOD compensation can only reach 10,000 km by only P_0 = 7 mW [49]. This mentions the significant improvement of the OPC system by using the higher-order dispersion management transmission line consisting of SMF and RDF.

For the 10,000-km transmission result of 160-Gbit/s data shown in Fig. 6.7, the existence of the optimum P_0 can be observed more obviously. The systems with l_d = 240 km, 160 km, 80 km, and 10 km reach maximum performance, at BER smaller than 10^{-9}, with their own optimum P_0 at 9 mW, 10 mW, 14 mW, and 15 mW, respectively. As predicted, the optimum P_0 for longer l_d is found at lower value. However, system with l_d = 40 km no longer succeeds BER = 10^{-9} for all range of P_0.

According to this ultimate performance of dispersion-managed OPC systems, further increase in transmission bit-rate can be expected. The calculated BER of 200-Gbit/s data transmission at 10,000 km shown in Fig. 6.8 indicates the possibility of this ultra-high bit-rate long-haul transmission at BER = 10^{-9} using l_d = 240 km with P_0 = 11 mW or l_d = 10 km with P_0 = 15 mW.

To extend the bit-rate more than 200 Gbit/s in 10,000-km transmission, the easiest way may be the optimization of the average SOD value D_{av}. The increase in D_{av} can reduce the effect of fiber nonlinearity, at the same time, moving the SI which is not completely suppressed to occur more inner signal bandwidth. The optimum D_{av} will be found under the balance of these two effects.

6.6 Conclusion

In this paper, we have proposed for the first time the simultaneous suppression of two main problems, TOD and SI, in OPC transmission systems by employing the higher-order dispersion-managed fiber link consisting of SMF and RDF.

In order to implement the combination of SMF and RDF on OPC systems, we demonstrated that it is necessary to use the symmetric dispersion profile with respect to the mid-point of the system to reduce the SI gain together with the accumulation of the interplay between SPM and the fiber local dispersion. Finally, the computer simulation results have demonstrated that the 10,000-km transmission of the data rate as high as 200 Gbit/s is made possible at BER = 10^{-9} by the higher-order dispersion-managed OPC system whose dispersion map is properly designed.

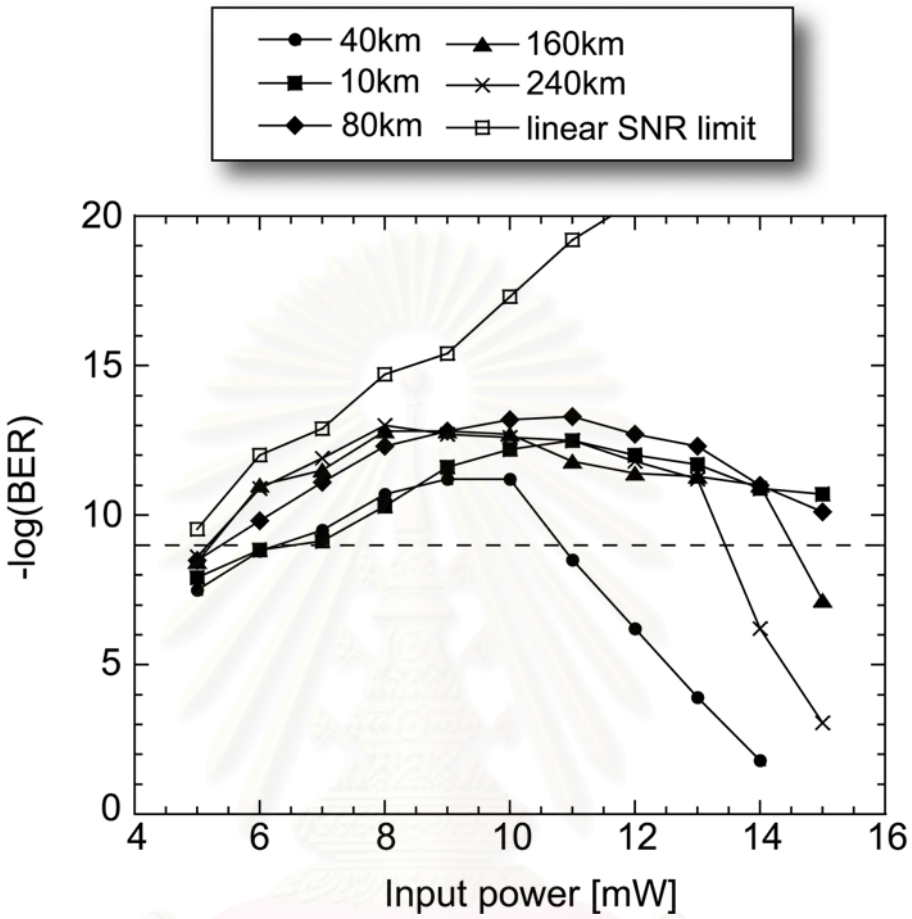

Fig. 6.6: BER of higher-order dispersion-managed 100-Gbit/s OPC transmission systems at 10,000 km as a function of the signal input power P_0 for several l_d (10 km, 40 km, 80 km, 160 km, and 240 km), comparing with the linear SNR-limited BER. At BER = 10^{-9}, all systems can achieve 10,000-km transmission for a broad range of P_0. Since the OPC system using DSF where TOD is compensated can only reach 10,000 km by only P_0 = 7 mW [49], these results show the significant improvement of OPC system by using the higher-order dispersion management transmission line consisting of SMF and RDF to eliminate both TOD and SI.

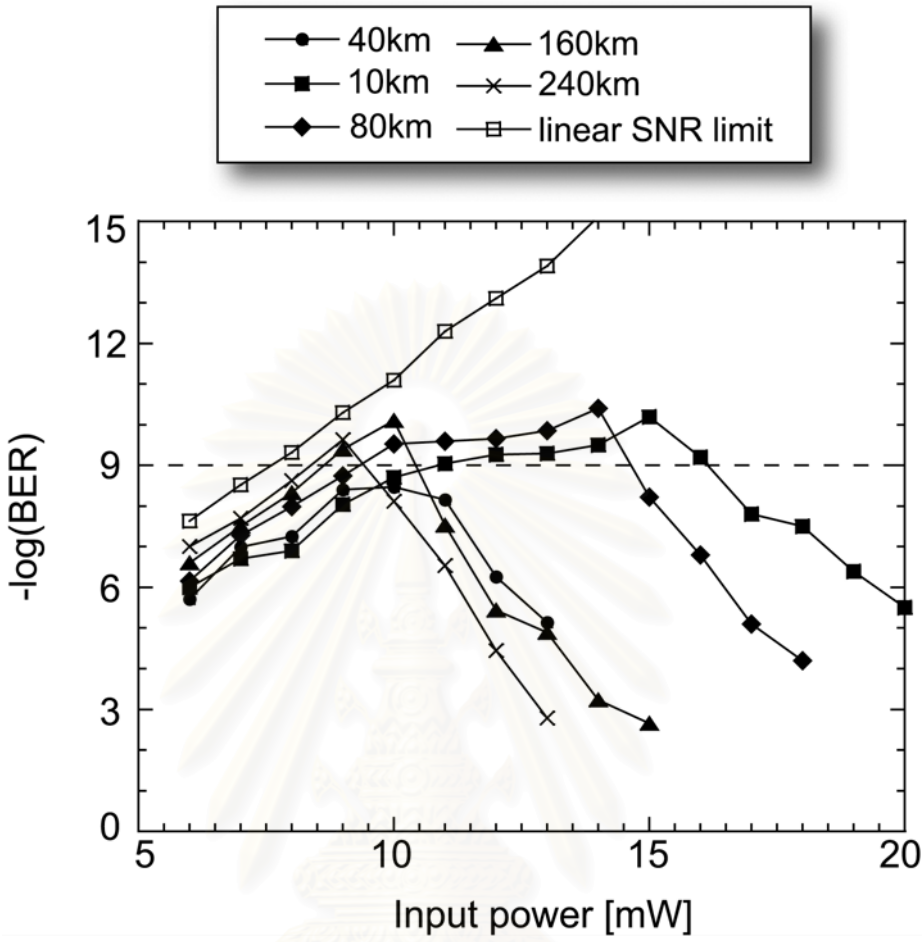

Fig. 6.7: BER of higher-order dispersion-managed 160-Gbit/s OPC transmission systems at 10,000 km as a function of the signal input power P_0 for several l_d (10 km, 40 km, 80 km, 160 km, and 240 km), comparing with the linear SNR-limited BER. The systems with l_d = 240 km, 160 km, 80 km, and 10 km reach maximum performance, with BER smaller than 10^{-9}, with the optimum P_0 at 9 mW, 10 mW, 14 mW, and 15 mW, respectively. However, system with $l_d = l_f$ = 40 km does not achieve BER = 10^{-9} for all range of P_0.

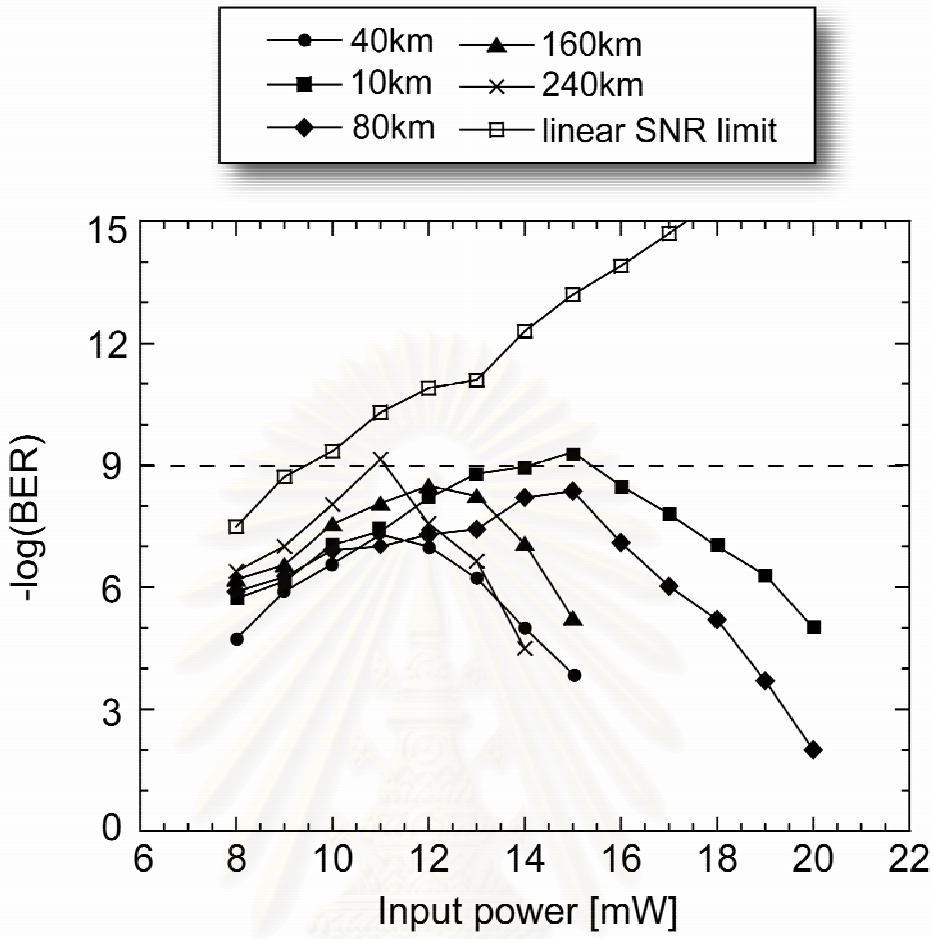

Fig. 6.8: BER of higher-order dispersion-managed 200-Gbit/s OPC transmission systems at 10,000 km as a function of the signal input power P_0 for several l_d (10 km, 40 km, 80 km, 160 km, and 240 km), comparing with the linear SNR-limited BER. The 10,000-km transmission of the data rate as high as 200 Gbit/s becomes possible at BER = 10^{-9} by using l_d = 240 km with P_0 = 11 mW or l_d = 10 km with P_0 = 15 mW in the higher-order dispersion-managed OPC transmission system.

CHAPTER 7
SUPPRESSION OF NONLINEAR WAVEFORM DISTORTION INDUCED BY KERR EFFECT IN OPC SYSTEMS USING DISTRIBUTED RAMAN AMPLIFICATION

In optical phase conjugation (OPC) systems, the third-order dispersion (TOD) of optical fibers and the nonlinear resonance at well-defined signal sideband frequencies called sideband instability (SI), which is induced by Kerr effect, mainly limit the transmission performance. We propose, for the first time, a scheme for suppression not only the SI effect but all the signal distortion induced by Kerr effect in OPC systems using distributed Raman amplification (DRA) to form a reverse power distribution in the second half of the system. In combination with TOD compensator, our simulation results demonstrate that, a 100-Gbit/s data transmission over 10,000 km with 50-km amplifier spacing and a 200-Gbit/s data transmission over 10,000 km with 40-km amplifier spacing is achieved in the OPC systems using the DRA [117].

7.1 Introduction

Broadband optical amplifier, together with broadband dispersion compensation technologies are necessary to respond the ever-increasing demand for transmission bandwidth in dense wavelength-division-multiplexed (DWDM) systems. Nevertheless, due to the difficulty in expanding the gain bandwidth of conventional erbium-doped fiber amplifier (EDFA), distributed Raman amplification (DRA) using transmission fiber is currently attracting interest [118]. This is due to the fiber Raman amplifier (FRA) offers several advantages to the EDFA, such as wider amplification bandwidth, higher optical-signal-to-noise-ratio (OSNR) which consequently results in the reduction of fiber nonlinearity and the possibility of increasing amplifier span, flexible use of signal wavelength since stimulated Raman scattering (SRS) provides gain at any wavelength with the provision of a suitable pump source. Moreover, the gain bandwidth of FRA can be designed and expanded by using multiple pumping scheme and carefully designing the relative positions and powers of the pump lights. Gain bandwidth in excess of 17 THz has been demonstrated using the FRAs pumped at multiple wavelengths [119].

Several DWDM transmission experiments have successfully achieved using the DRA, such as, 3.28 Tbit/s (82 x 40Gbit/s) over 3 x 100 km of non-zero-dispersion-shifted fiber [120] and 1.05 Tbit/s (105 x 10Gbit/s) over 8,186 km [121].

For dispersion compensation, midway optical phase conjugation (OPC) system is an attractive candidate for ultra-long-haul high-speed transmission since the signal waveform distortion induced from the interplay between fiber dispersion and the Kerr effect can be almost compensated [65]. However, the ultimate performance of the OPC system is also limited by the third-order dispersion (TOD) together with the nonlinear resonance at well-defined signal sideband frequencies induced by the periodic amplification process through the Kerr effect called the sideband instability (SI) effect [50]-[52]. Recently, we have demonstrated by numerical simulations that a single-channel transmission with a bit rate of 100 Gbit/s can succeed a transmission distance over 10,000 km by only performing TOD compensation in the OPC system [49].

For the SI effect, a condition for perfect SI suppression has been given by Watanabe and Shirasaki [95]. In order to satisfy their condition, a dispersion-decreasing fiber (DDF), whose dispersion-decreasing coefficient is exactly proportional to the fiber loss coefficient, must be installed throughout the entire OPC system length. More recently, we have demonstrated a practical way to simultaneously suppress both TOD and SI by only applying strong higher-order dispersion management using the combination of the standard single-mode fiber (SMF) and the reverse-dispersion fiber (RDF) [60], [115]. Our computer simulation result has shown that the 10,000-km transmission of the data rate as high as 200 Gbit/s is made possible by the higher-order dispersion-managed OPC system whose dispersion map is properly designed [115].

In this chapter, we propose the alternative application of DRA for compensating residual signal waveform distortion caused by the Kerr effect in ultra-long-haul high-speed OPC transmission system. The DRA in combination with optical attenuator, in this case, is used for producing the reverse periodic signal power variation on the second-half of OPC system, which results in the entirely symmetrical signal power distribution with respect to the midway OPC. By this scheme, not only the SI effect but all the signal waveform distortion induced by the Kerr effect which is accumulated from the first-half will be perfectly compensated by transmitting the conjugated signal through the second half.

This chapter is organized as follows. Section 7.2 gives the basic knowledge about the DRA using a transmission fiber. Section 7.3 devoted to the design of the DRA gain using bidirectional pumping scheme to achieve the reverse power distribution. In section 7.4, the system configuration of ultra-long haul high-speed OPC systems using the combination of DRA and optical attenuators, together with the TOD compensator is proposed for the first time to our knowledge. The simulation results obtained from the system model demonstrate that, a 100-Gbit/s data transmission over 10,000 km with 50-km amplifier spacing and 200-Gbit/s data transmission over 10,000 km with 40-km amplifier spacing can be achieved when the DRA is used to form the reverse power distribution in the second half of the OPC systems.

7.2 Distributed Raman Amplification Using Transmission Fiber

Theoretically, the nonlinear waveform distortion induced from the Kerr effect can be completely compensated by the OPC if the signal power distribution in the second half of the system mirrors the distribution in the first half [65]. For the system using cascaded lump EDFAs, such power distribution can not be realized. We propose that the use of distributed gain from Raman amplifiers or the combination of the Raman amplifiers with EDFA may bring such power distribution to reality.

Raman gain in optical fibers arises from the transfer of power from one optical beam to another that is down shifted in frequency by the energy of an optical phonon. Practically this can be produced by inject high power laser pump whose frequency is higher than the signal carrier frequency by an amount of Raman frequency shift into transmission fibers [4].

The measured Raman gain in fused silica at a pump wavelength of 1000 nm has been shown in Fig. 2.9, as a function of frequency shift from the pump. The Raman gain exhibits the gain over a large bandwidth up to 40 THz with a broad dominant peak near 13 THz.

Figure 7.1 shows several pump configurations of DRA. In Fig. 7.1, (a) shows the co-propagating pump scheme, (b) the counter-propagating pump scheme, and (c) the bidirectional pump scheme, and (d) when combined with EDFA. It was shown that co-propagating pump scheme suffers from the pump depletion than counter-propagating pump scheme. However, co-propagating pump scheme gives better SNR

than that of counter-propagating pump scheme. On the other hand, bi-directional pumping produces high gain and provides high SNR for medium pump power. For higher pump power, the counter propagating pumping yields the best in both gain and SNR [122].

The forward pump power (P_f), backward pump power (P_b), signal power (P_s), and noise power (P_n) evolutions in one link of FRA are governed by the DRA equations as shown in Eq. (7-1), (7-2), (7-3), and (7-4), respectively [125].

$$\frac{dP_f}{dz} = -\alpha_p P_f - \frac{f_p}{f_s}\frac{G_R}{K_{eff}A_{eff}} P_s P_f \,, \tag{7-1}$$

$$\frac{dP_b}{dz} = \alpha_p P_b + \frac{f_p}{f_s}\frac{G_R}{K_{eff}A_{eff}} P_s P_f \,, \tag{7-2}$$

$$\frac{dP_s}{dz} = -\alpha_s P_s + \frac{G_R}{K_{eff}A_{eff}} P_f P_s + \frac{G_R}{K_{eff}A_{eff}} P_b P_s \,, \tag{7-3}$$

$$\begin{aligned}\frac{dP_n}{dz} = {} & -\alpha_n P_n + RlP_b + \frac{G_R}{K_{eff}A_{eff}} P_f P_n + \frac{G_R}{K_{eff}A_{eff}} P_b P_n \\ & + h_p f_s \Delta f \frac{G_R}{K_{eff}A_{eff}} \left\{ 1 + \frac{1}{\exp\left(\frac{h_p\left(f_p - f_s\right)}{k_B T} \right)} \right\} P_f \\ & + h_p f_s \Delta f \frac{G_R}{K_{eff}A_{eff}} \left\{ 1 + \frac{1}{\exp\left(\frac{h_p\left(f_p - f_s\right)}{k_B T} \right)} \right\} P_b \end{aligned} \,. \tag{7-4}$$

In Eq. (7-1), (7-2), (7-3), and (7-4), z is the transmission distance, α_p, α_s, and α_n are the fiber loss coefficients at frequencies of the forward and backward pump (single wavelength pumps), signal, and noise, respectively. Similarly, f_p, f_s, and Δf are the frequencies of the pumps, signal, and the bandwidth of noise, respectively. G_R is the Raman gain coefficient at signal frequency, K_{eff} and A_{eff} the polarization factor and the effective core area, h_p, k_B, and T the Plank's constant, the Boltzman's

constant, and the temperature in Kelvin unit, and *Rl* the Rayleigh back-scattering coefficient. From the DRA equations shown above, the signal power evolution in the bi-directional pumping DRA depends on the pump powers launched into the fiber. Therefore, the signal evolution in FRA link can be designed by using appropriate pump powers.

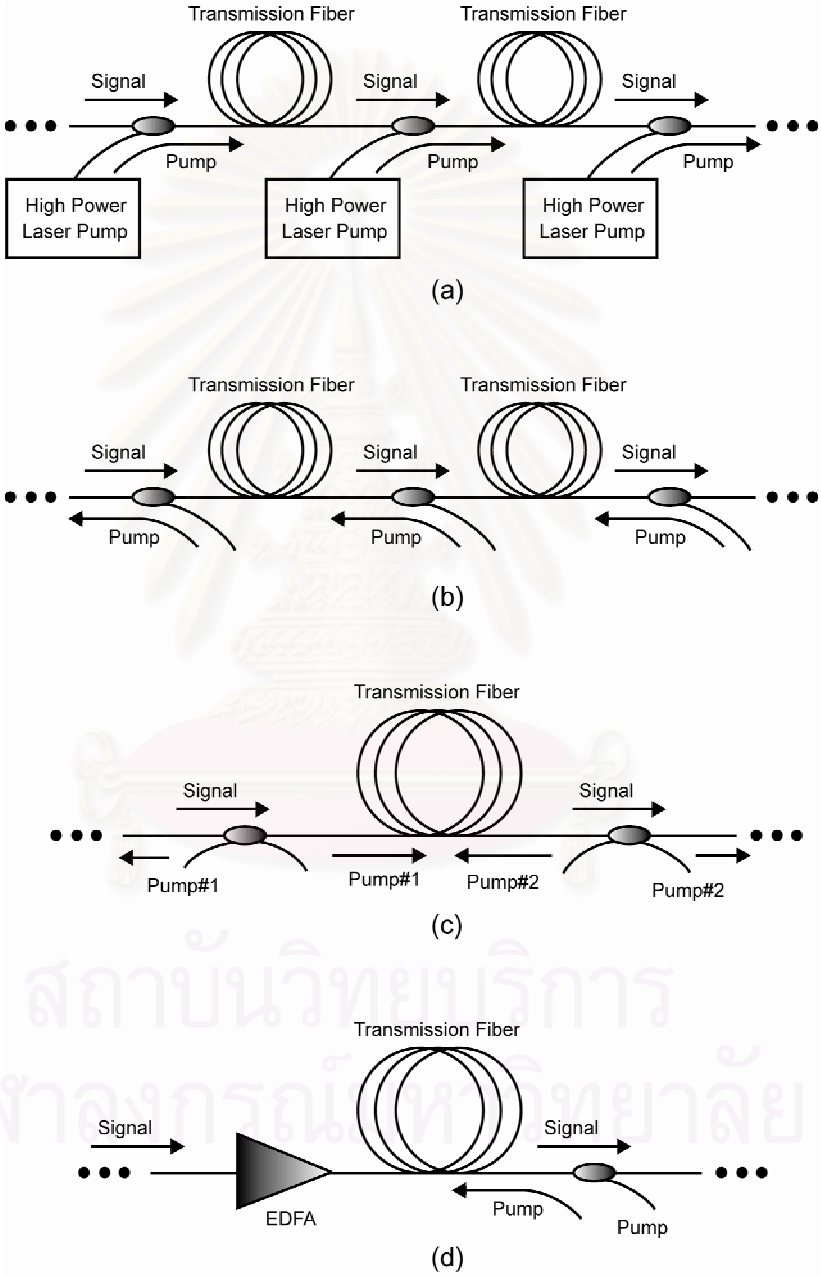

Figure 7.1: Several pump configurations of Raman amplifier. (a) shows the co-propagating pump scheme, (b) the counter-propagating pump scheme, (c) the bidirectional pump scheme, and (d) when combined with EDFA.

In Fig. 7.2, we propose a configuration which employs the DRA for obtaining symmetrical power distribution with respect to system midpoint. Comparing with the power distribution in cascaded EDFAs shown in Fig. 7.2(a), the use of bi-directional pumped DRA and optical attenuators in the second-half of the system, shown in Fig. 7.2(b) may enables us to form reverse power distribution of the first half. This reverse power distribution does not only result in the reduction of SI effect, but also provides the avoidance of all nonlinear waveform distortion induced from the Kerr effects in OPC transmission systems. With the proposed scheme, in combination with lump TOD compensators, the vanishing of both TOD and SI in OPC systems can be expected.

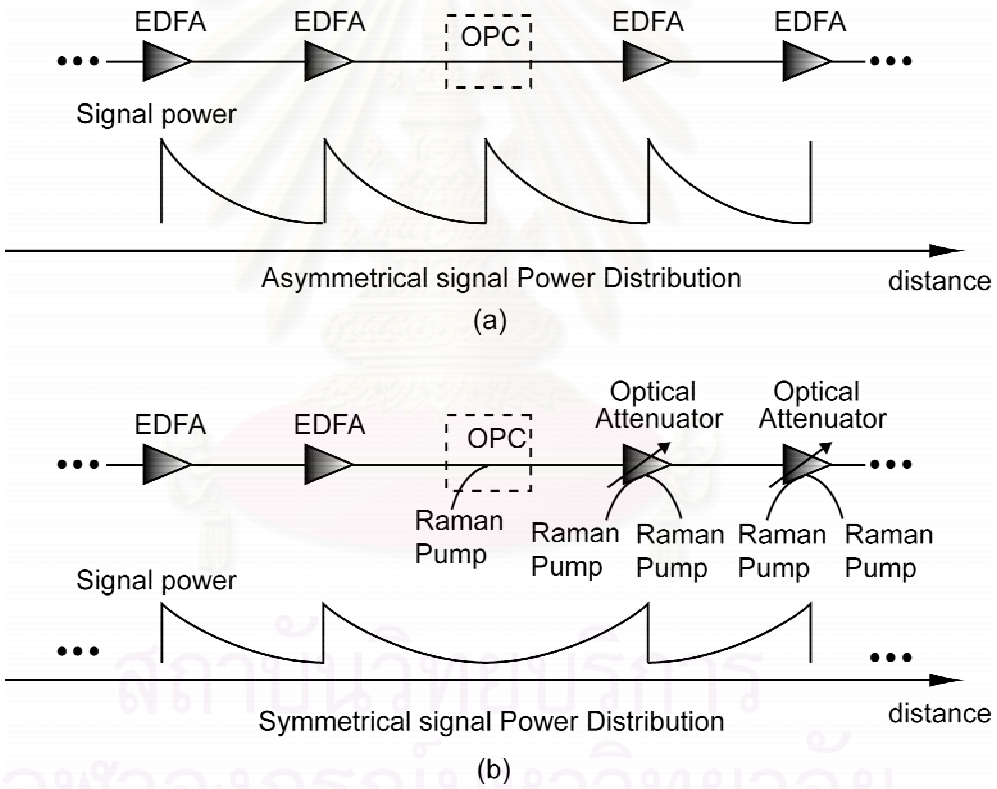

Figure 7.2: Periodic signal power variation (a) in chain of EDFA and (b) with DRA in the second half to form reverse power distribution.

7.3 Generation of Reverse Signal Power Distribution by DRA

For long distance transmission, periodic lump amplification is used for maintaining a good SNR at a receiver. The fiber loss and the periodic gain form a periodic signal power distribution along the system length, producing a periodic variation of the fiber refractive index through the nonlinear Kerr effect of an optical fiber. This process constructs a virtual grating in the transmission fiber. The resonance between the virtual grating and the signal will occur at signal sideband components whose wave vectors match with the wave vector of this virtual grating, resulting in the exponential growth of those components with transmission length.

This phenomenon is known as the sideband instability (SI), which causes signal waveform distortion if the SI arises at frequencies inside the signal bandwidth. Figure 7.2(a) shows the signal power evolution in the OPC system constructed by the chain of lossy fiber and the lump amplification. Since the signal power distribution in practical OPC systems is not symmetrical with respect to the mid-point, the SI cannot be compensated and will accumulate to the end of the system length. On the other hand, by constructing the symmetrical power distribution with respect to the midway OPC, as shown in Fig. 7.2(b), the SI induced in the first half will be compensated while the signal propagates through the second half of OPC system. In order to obtain such symmetrical power distribution, the signal transmission through the second half requires a distributed gain whose gain coefficient is equal to the loss coefficient of the fiber used in the first half. However, such reverse power distribution can never be realized if a lossy fiber and lump amplification is used for signal transmission.

Here, we bring the reverse power distribution into the real world by using the bidirectional pumping DRA. Since the signal power evolution in FRA depends on the pump powers launched into the fiber, there should exists the appropriate pump powers which give the reverse power distribution. To find out those powers, we numerically calculate the signal power transmission in one span DRA using the model based on the DRA equations presented in [123]. We assume the use of a single wavelength pump light because the Raman gain bandwidth of about 2 THz, which is sufficiently broad and flat enough for single channel data rate used in our simulations, can be produced by only single wavelength pumping. The signal wavelength is 1,550 nm. The pump wavelength is 1,450 nm, which is corresponding to the 13.2-THz-up-shift

from signal carrier frequency. Two pump lights are launched into the input end of fiber, which propagates forward, and the output end of fiber, which propagates backward. The model in [123] also accounts for the temperature-dependent spontaneous Raman scattering noise and the Rayleigh back scattering with multiple reflections, which are considered as noise. For simplicity, the evolution of signal power and noise are treated separately because the noise effects has little influence on the distributed Raman gain spectrum and the signal evolution [124], [125]. In our calculations, the Raman gain spectrum with polarization factor of 2, and the attenuation spectrum of silica fiber shown in [2] is taken. The fiber is the dispersion-shifted fiber (DSF) with effective core area A_{eff} = 50 μ m^2. The signal and noise evolution is computed by integrating the FRA equations using the fourth-order Runge-Kutta (RK4) method [94] with the integration step size of 10 m.

In order to obtain the reverse power distribution from the FRA, we first calculate the target reverse power distribution $P_{ref}^{sig}(z)$ with a given input signal power P_{rev}^{sig} and keep it as reference. It should be noted that P_{rev}^{sig} refers to the signal power at the output end of fiber span for the case of ordinary lump amplification, which can be calculated by $P_{rev}^{sig} = P_{pump}^{sig} \exp(-\alpha L)$, where P_{pump}^{sig} is the signal input power for lump amplification, α the fiber loss coefficient, and L the amplifier span. Then, the FRA equations are solved iteratively until we obtain the bidirectional input pump powers (P_+ : forward pump power and P_- : backward pump power), which yield least normalized root-mean-square error $Err(P_+, P_-)$ defined as

$$Err(P_+, P_-) = \sqrt{\frac{\int_0^L \left| P_{Raman}^{sig}(P_+, P_-, z) - P_{ref}^{sig}(z) \right|^2 dz}{\int_0^L \left| P_{ref}^{sig}(z) \right|^2 dz}} \times 100\%, \qquad (7\text{-}5)$$

where $P_{Raman}^{sig}(P_+, P_-, z)$ represents the reverse power distribution obtained by DRA.

Table 7.1 shows the optimum P_+ and P_- and their corresponding $Err(P_+, P_-)$ at several P_0 for L = 40 km and 50 km. $Err(P_+, P_-)$ becomes larger for higher value of P_0. At given P_0, the use of 50-km span yields larger $Err(P_+, P_-)$ than that of the 40-km span. We also calculate $Err(P_+, P_-)$ from the 80-km span. $Err(P_+, P_-)$ larger than 30 % is resulted from such long span. For instance, Fig. 7.3 and 7.4 shows the reverse

power distribution from DRA with $Err(P_+, P_-)$ of about 7.3 %, compared with the reference calculated by P_0 = 5 mW and L = 40 km and the corresponding pump power evolutions. The reverse power distribution obtained from DRA is almost curve-fitted with the reference, indicating the possibility of generating reverse power distribution by DRA. It should be noted that we also explore the backward and forward pumping schemes. However, the reverse power distribution with sufficiently low error cannot be constructed by these two schemes.

Table 7.1: Raman pump powers for constructing reverse power distribution.

	Amplifier span 40 km			**Amplifier span 50 km**		
Input signal power [mW]	**Forward pump power [mW]**	**Backward pump power [mW]**	**Error [%]**	**Forward pump power [mW]**	**Backward pump power [mW]**	**Error [%]**
3	120	127	6.9	146	152	11.9
4	120	130	7.1	145	155	12.3
5	127	122	7.3	145	158	12.6
6	127	124	7.3	157	142	12.7
8	126	129	7.4	156	148	12.7
10	125	134	7.7	155	154	12.9

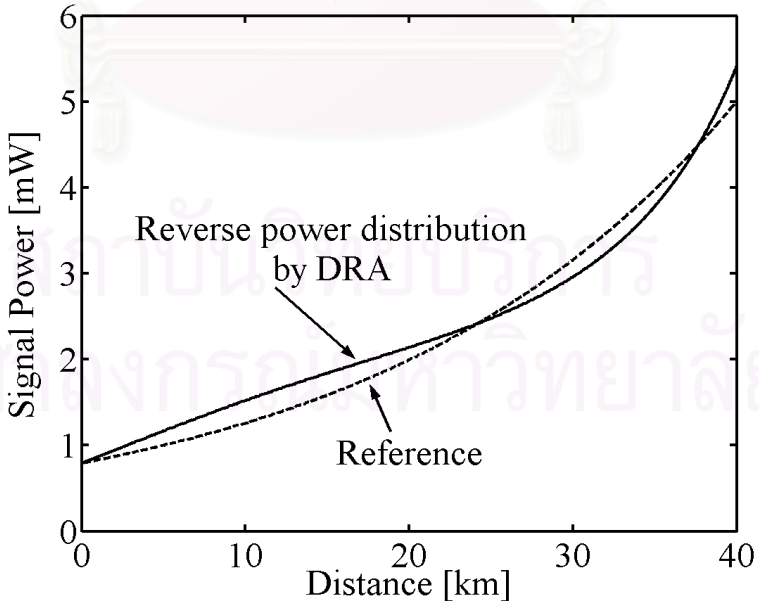

Figure 7.3: Reverse power distribution formed by DRA for signal input power of 5 mW.

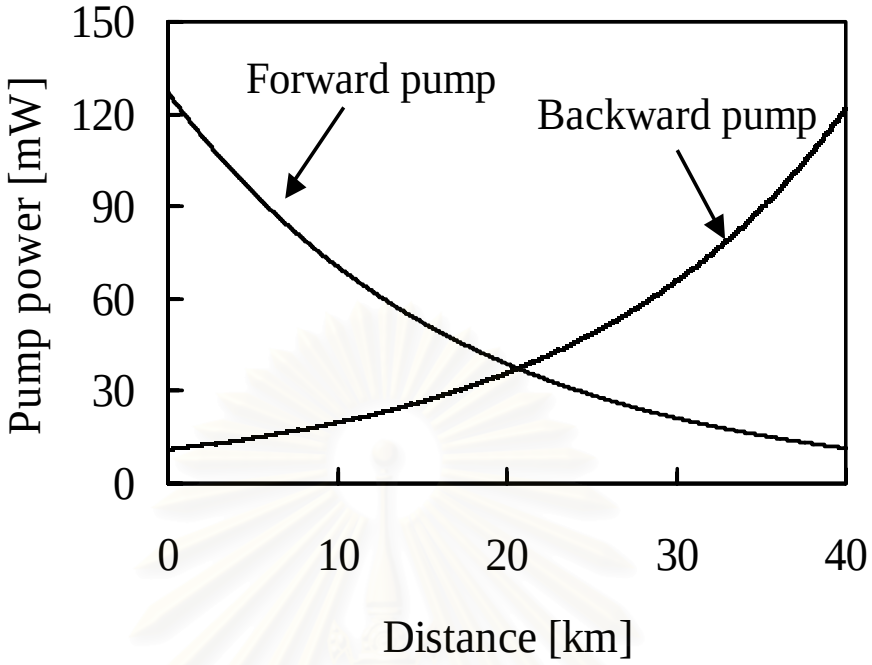

Figure 7.4: Pump power evolutions for constructing the reverse power distribution in Fig. 7.3.

7.4 Computer Simulations of OPC Transmission Systems Using DRA

After we obtain the optimum Raman bi-directional pump powers for producing the reverse power distribution, the DRA is implemented on the second half of OPC system to form the symmetrical power distribution with respect to the system midpoint. The model of OPC system using DRA in the second half is shown in Fig. 7.2(b). The fist half consists of chain of transmission fibers and optical amplifiers. In the second half, at each span end, the optical attenuator is installed to reduce the signal power to make the reverse power distribution periodic. At the end of system, the TOD compensator is placed to reset the accumulated TOD. It should be noted that the accumulation of TOD in OPC systems has been theoretically shown to be linear [49], thus, only one linear TOD compensator is needed and can be installed anywhere in the system for perfect compensation.

In order to evaluate the performance improvement using our proposed method, we perform a computer simulation of the optical signal transmission in OPC systems based on the model in Fig. 7.2(b). The optical signal composed of 32-bit

pseudorandom Gaussian RZ pulses. The transmission fiber is the DSF with the operating dispersion D = -1ps/km/nm, the TOD = 0.06 ps/km/nm, and the nonlinear coefficient γ = 2.6 $W^{-1}km^{-1}$. Other parameters used in this simulation are the same as used for integrating the FRA equations above. For the first half of the system, the optical signal propagation is simulated by solving the nonlinear Schrodinger equation (NLSE) with the split-step Fourier method (SSFM) [4]. The integration step size of the SSFM is set at the value that gives the step size error less than 0.1 % [116]. The optical amplifier produces ASE noise with noise figure of 5.3 dB (n_{sp} = 1.7). The optical pulse at the midway of the system is conjugated by an ideal infinite-bandwidth optical phase conjugator.

To simulate the signal propagation in the FRAs in the second half, some following modifications are needed. The distributed gain for each step of the SSFM is calculated from the FRAs equations with the RK4, then, the distributed gain is acted as a gain/loss in the NLSE for that step. Similarly, the amount of noise generated within the step length of FRA is also computed from Raman equations with the RK4, then, is used for calculating the varience of the Gaussian distribution of ASE noise which will be randomly added to the signal bandwidth at end of that step.

The TOD compensator, placed only at the end of system, is assumed to be an ideal device that multiplies the complex amplitude of the signal with the negative amount of linearly accumulated phase shift caused by the TOD. The bandwidth of the optical band-pass filter, which is placed at the output end of the fiber, is always adjusted to obtain the minimum BER. The receiver is modeled by the 65-GHz-cutoff sixth-order Bessel-Thompson low-pass filter followed by the BER detector. For obtaining the numerical BER of the detected signal, the numerical Q factor of every bit is individually calculated at the maximum eye-opening point of the bit period. Based on the assumption of Gaussian noise distribution, the numerical BER is computed from the bit numerical Q factors and averaged over the entire bits [25].

Figure 7.5 shows the calculated BER at 10,000 km of the OPC systems using DRA as a function of the signal input power launched to the first half. In Fig. 7.5, for low input signal power, BER of the systems using the reverse power distribution reduce as the input signal power increase owing to the improvement in SNR, together with the suppression of SI. In fact, assuming that the TOD and the SI are perfectly suppressed in OPC systems, there remains the problem originated from the

accumulation of noise which is nonlinearly enhanced during the transmission by the parametric interaction between dispersion and SPM [65], [93], [115]. Since the transmission of the ASE noise is not symmetrical with respect to the midpoint of the system. Thus, only part of the nonlinear enhancement can be compensated by OPC while there still exists the accumulated ASE noise, which is enhanced by the nonlinear interaction.

Therefore, for high input signal power, the BER becomes saturate because the nonlinear enhancement of noise, as well as the increase in error in forming the reverse power distribution become significant and start to affect the system performance. When we further increase the signal power, these two effects mainly cause signal distortion, therefore, the BER degrades rapidly. However, with defining a maximum transmission distance at BER = 10^{-9}, the 100-Gbit/s systems using the reverse power distribution with the amplifier span of 40 km can achieve 10,000-km transmission for a wide range of input signal power (2 – 10 mW).

In comparison with these results, the same OPC system using the DSF and the lump amplifiers incorporated with the TOD compensation can only achieve the 10,000-km transmission by using only input signal power of 7 mW [49]. This mentions the significant improvement of the OPC system by using the DRA. On the other hand, for the system with the amplifier spacing of 50 km, the 10,000-km transmission can be achieved with BER = 10^{-9} at the input signal power of only 4 mW. This is mainly resulted from larger error in constructing the reverse power distribution compared to the 40-km span. We also calculate the BER of the systems using the 80-km span. Because the error in forming the reverse power distribution becomes even larger than 30 % for signal power all input signal powers, therefore, we cannot achieve BER = 10^{-9}. However, the result has demonstrated the possible in expanding the span length of 10 km when the DRA is used.

For the 40-km span, the further increase in transmission data rate is expectable using the DRA. The calculated BER of 160-Gbit/s and 200-Gbit/s data transmission at 10,000 km shown in Fig. 7.5 indicate the possibility of such ultra-high bit-rate long-haul transmission at BER = 10^{-9} using the signal input power = 4 mW and 5 mW for the 160-Gbit/s and the 200-Gbit/s data, respectively.

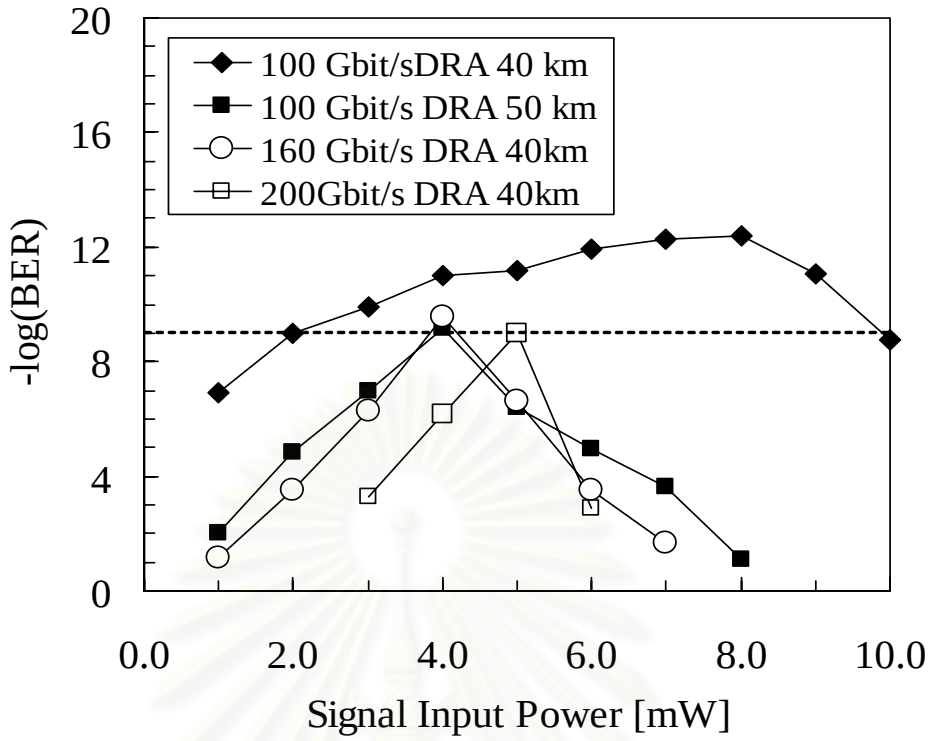

Figure 7.5: BER of optical signal after transmitted 10,000 km through OPC systems using DRA.

In [115] we have also demonstrated the possibility of 10,000-km transmission of the data rate 200 Gbit/s by simultaneously suppressing both TOD and SI in OPC transmission systems employing the higher-order dispersion management fiber link consisting of SMF and RDF. Although, such method can only reduce the SI effect, it realizes such ultra-high bit rate transmission because the harm of fiber nonlinearity-enhanced ASE noise is also reduced through large fiber local dispersion of SMF and RDF. On the other hand, by using the DRA, the signal and noise propagates under small value of uniform dispersion for entire length of system, therefore, the nonlinearity-enhanced noise may be almost as strong as the system using the periodic EDFA. However, the DRA in the second half, where the accumulated noise becomes large and is enhanced by the fiber nonlinearity, produces lower noise than the chain of periodic EDFA. Moreover, the SI is almost perfectly suppressed, thus, the 200-Gbit/s data transmission over 10,000 km can also be made possible by this method.

7.5 Conclusion

We have demonstrated the performance improvement of ultra-long-haul high-bit-rate OPC transmission systems by employing the DRA to suppressing signal waveform distortion caused by the Kerr effect. The pump powers of the bi-directional pumping DRA were designed for producing the reverse periodic signal power variation on the second-half of the systems in order to construct entirely symmetrical power distribution with respect to the system midpoint. Incorporated with the TOD compensator, our simulation results have shown possibilities of the 100-Gbit/s data transmission over a 10,000 km with the 50-km amplifier span and the 200-Gbit/s data transmission over 10,000 km with the 40-km amplifier span.

CHAPTER 8
FINITE-DIFFERENCE TIME-DOMAIN SIMULATION OF SLOWLY-VARYING ENVELOPE PULSE PROPAGATION IN RELATIVELY LONG NONLINEAR OPTICAL FIBER

We propose the use of several algorithms of the finite-difference time-domain (FDTD) method for simulating pulse propagation in relatively long fiber. The results are compared with the results from the split-step Fourier method (SSFM). The numerical results of 5-ps FWHM single optical pulse propagation in dispersion compensated fiber span using the FDTD method have shown a possibility of the calculation over several ten kilometers with acceptable accuracy. The algorithms studied in this chapter are the explicit FDTD, the implicit FDTD, and the FDTD employing the Crank-Nicholson (CN) scheme. We have modified these algorithms to be the implicit-1, implicit-2, CN-1, CN-2, CN-3, CN-4, and CN-5 FDTD in order to make them suitable for solving the nonlinear Schrodinger equation (NLSE) which is separated into two coupled equations for the real and imaginary part of the optical signal.

8.1 Introduction

Propagation of slowly varying envelope optical signal in optical fibers is governed by the well-known partial differential equation called nonlinear Schrodinger equation (NLSE) [4]. Since the NLSE does not have an analytic solution, the use of numerical method is necessary. The most commonly used numerical algorithm for solving the NLSE is the split-step Fourier method (SSFM) [4], in which the fiber is divided into small sections with a length called the step size. Each section exhibits only the dispersive or nonlinear effects which act on the propagating signal separately. The accuracy of the SSFM solution increases with the reduction of the step size.

Although the SSFM has become the standard method for analyzing almost all problems of signal propagating in optical fibers, it is quite inconvenient for those who are not good at computer programming, and also who only aim to study simple problems and want to know the approximate solutions immediately. This is because it is very complicated and tough to implement the SSFM algorithm into

computational program. It can take more than a week to develop several hundred lines of a simulation program based on SSFM algorithm and then validating it before it starts to work properly.

As an alternative method for studying optical field propagation, the finite-difference time-domain (FDTD) method [69] has been widely used for analyzing and designing several structures of short-scale optical waveguides and devices [70], [71]. Since the FDTD algorithm is much easier and simpler for implementing than the SSFM, by using the FDTD, it is possible to develop the calculation program which consumes not more than 20 lines in only an hour. The basic principle of FDTD is to discretize both time and space into small cells and then applying the central difference approximations for both temporal and spatial derivatives. Recently, a 12-fs ultra-broadband optical pulse propagation in optical fiber is also studied using the FDTD for directly solving Maxwell's equations [72].

In this chapter, we propose the use of FDTD for solving the NLSE and demonstrate that the FDTD can be sufficiently applied to simulate the optical pulse propagation in relatively long fiber under acceptable accuracy. The paper is organized as follows. Section 8.2 of this paper mainly devotes to the use of the explicit FDTD method for solving the NLSE. After the discretization of the NLSE and the employment of central difference approximation in the NLSE, through the explicit FDTD algorithm, the NLSE is transformed into first-order linear equation with initial problem. Furthermore, we also introduce a practical condition for determining spatial step size of FDTD. Then, the problem based on the propagation of 5-ps single optical pulse over 50-km dispersion compensated fiber link is modeled. The calculation error caused by the choice of spatial step size is quantified. Next, the simulation results, together with the comparison with those obtained from the SSFM are shown and discussed.

Several algorithms have been invented to reduce the accumulated error due to the choice of the calculation step such as the implicit FDTD [69], the Crank-Nicholson scheme [69], the Douglas scheme [126], [127], and other algorithm [71]. In section 8.3 and 8.4 of this chapter, we study the use of the implicit FDTD and the Crank-Nicholson (CN) scheme for solving the NLSE. We modify these algorithms to be the implicit-1, implicit-2, CN-1, CN-2, CN-3, CN-4, and CN-5 FDTD in order to make them suitable for solving the NLSE which will be separated into two coupled equations for the real and imaginary part of the optical signal. Similar to section 8.2,

the same problem of pulse propagation is simulated. The characteristic of the accumulation error, as well as the difference between the results obtained by the FDTD and the SSFM are shown and discussed. Next, the comparison between all the proposed FDTD algorithms and also the SSFM are discussed in section 8.5. Finally, the summary of this paper is made at section 8.6.

8.2 Explicit FDTD

We should start from the NLSE for the slowly-varying envelope signal function $A(z,T)$ propagating along *z* axis

$$\frac{\partial A}{\partial z} = -\frac{\alpha}{2}A - \frac{i}{2}\beta_2 \frac{\partial^2 A}{\partial T^2} + \frac{1}{6}\beta_3 \frac{\partial^3 A}{\partial T^3} + i\gamma |A|^2 A, \tag{8-1}$$

where β_2 is the group-velocity dispersion (GVD) parameter, β_3 the higher-order GVD parameter, α the fiber loss coefficient, and γ the nonlinear coefficient. To apply the explicit FDTD method to Eq. (8-1), time domain discretization is made with the step of ΔT, and the corresponding index *n*, giving $T = n\Delta T$ (*n* = 1, 2, 3, …). Similarly, the propagation distance is discretized with the step Δz, and the spatial index *k*, therefore, $z = k\Delta z$ (*k* = 1, 2, 3, …). Then, after discretization, $A(z,T)$ becomes $A^k(n)$. Following FDTD algorithm, Eq. (8-1) becomes

$$\begin{aligned}\frac{A^{k+1}(n) - A^k(n)}{\Delta z} = &-\frac{\alpha}{2}A^k(n) - \frac{i}{2}\beta_2 \frac{A^k(n+1) - 2A^k(n) + A^k(n-1)}{(\Delta T)^2} \\ &+ \frac{1}{6}\beta_3 \frac{A^k(n+2) - 2A^k(n+1) + 2A^k(n) - A^k(n-1)}{(\Delta T)^3} \\ &+ i\gamma \left|A^k(n)\right|^2 A^k(n),\end{aligned} \tag{8-2}$$

Since $A(z,T)$ is complex function, we will split $A^k(n)$ into its real and imaginary components

$$A^k(n) = A^k_{real}(n) + iA^n_{imag}(n). \tag{8-3}$$

Substituting Eq. (8-3) into Eq. (8-2), we obtain two coupled explicit FDTD equations

$$
\begin{aligned}
A_{real}^{k+1}(n) = A_{real}^{k}(n) &- \frac{1}{2}\alpha\Delta z A_{real}^{k}(n) \\
&+ \frac{\beta_3\Delta z}{6(\Delta T)^3}\left\{A_{real}^{k}(n+2) - 2A_{real}^{k}(n+1) + 2A_{real}^{k}(n-1) + A_{real}^{k}(n-2)\right\} \\
&+ \frac{\beta_2\Delta z}{2(\Delta T)^2}\left\{A_{imag}^{k}(n+1) - 2A_{imag}^{k}(n) + A_{imag}^{k}(n-1)\right\} \\
&- \gamma\Delta z\left|\left(A_{real}^{k}(n)\right)^2 + \left(A_{imag}^{k}(n)\right)^2\right| A_{imag}^{k}(n)
\end{aligned}
\quad . \qquad (8\text{-}4)
$$

$$
\begin{aligned}
A_{imag}^{k+1}(n) = A_{imag}^{k}(n) &- \frac{1}{2}\alpha\Delta z A_{imag}^{k}(n) \\
&+ \frac{\beta_3\Delta z}{6(\Delta T)^3}\left\{A_{imag}^{k}(n+2) - 2A_{imag}^{k}(n+1) + 2A_{imag}^{k}(n-1) + A_{imag}^{k}(n-2)\right\} \\
&- \frac{\beta_2\Delta z}{2(\Delta T)^2}\left\{A_{real}^{k}(n+1) - 2A_{real}^{k}(n) + A_{real}^{k}(n-1)\right\} \\
&+ \gamma\Delta z\left|\left(A_{real}^{k}(n)\right)^2 + \left(A_{imag}^{k}(n)\right)^2\right| A_{real}^{k}(n)
\end{aligned}
\quad . \qquad (8\text{-}5)
$$

In Eq. (8-4) and (8-5), it is worth noted that, to obtain the signal spectra, the fast-Fourier transform (FFT) algorithm can be used to transform $A^k(n)$ at arbitrary distance to obtain its spectra. Then the time resolution ΔT is determined by the spectral window W with the relation $W = 1/\Delta T$. On the other hand, it is quite difficult to determine the spatial step Δz because there is no specific Courant condition [2] to guide us, as was the case in Maxwell's equations simulation. We propose here a practical approach to determine reasonable Δz by defining the normalized spatial step q

$$
q = \left|\frac{1}{2}\alpha\Delta z\right| + \left|\frac{\beta_3\Delta z}{6(\Delta T)^3}\right| + \left|\frac{\beta_2\Delta z}{2(\Delta T)^2}\right| + \gamma\Delta z\left|\left(A_{real}^{k}(n)\right)^2 + \left(A_{imag}^{k}(n)\right)^2\right|_{\max} << 1 . \qquad (8\text{-}6)
$$

Our concept is very simple and similar to FDTD numerical stability theorem [2]. That is, a stable solution to Eq. (8-4) and (8-5) will be obtained if q becomes much less than unity.

The problem model used for simulations is the propagation of optical single pulse in dispersion compensated fiber link composed of dispersion-shifted fiber (DSF) and dispersion compensator. The length of one span is 50 km. The optical signal is 5-ps full-width-half-maximum (FWHM) single pulse with Gaussian shape. The input power of the pulse is 10 mW. The parameters used in the simulations are typical dispersion-shifted fiber parameters: α = 0.2 dB/km, β_2 = 0.26 ps^2/km (corresponding to the second-order dispersion (SOD) or the dispersion = -0.2

ps/km/nm), β_3 = 0.11 ps^3/km (corresponding to dispersion slope or the third-order dispersion (TOD) = 0.06 ps/km/nm^2), and γ = 2.6 W^{-1}km^{-1}. The dispersion compensator used in simulations is assumed to be an ideal device that multiplies the complex amplitude of the signal with a negative amount of linearly accumulated phase shift caused by the SOD. This compensator is placed at the end of 50-km span. Also, one lump optical amplifier placed at the end of 50-km span. The amplifier produces gain of 10 dB without amplifier noise for compensating the fiber loss of 50-km span.

The time window is 50 ps and is sampled to 512 discrete points giving $\Delta T \approx 0.1$ ps, which yields the spectral window width $W \approx 10$ THz. The propagation of the optical pulse is calculated by solving the NLSE using both above proposed FDTD method and SSFM. To quantify the error caused by the choice of the spatial step size of both FDTD and NLSE, the normalized root-mean-square error $E(\Delta z)$, which is defined in [116],

$$E(\Delta z) = \sqrt{\sum_{i=1}^{n} \left| A_{sim}^{k}(\Delta z; i) - A_{exact}^{k}(\Delta z; i) \right|^2 \Big/ \sum_{i=1}^{n} \left| A_{exact}^{k}(\Delta z; i) \right|^2} , \qquad (8\text{-}7)$$

where $A_{sim}^{k}(\Delta z; i)$ represents the discretized output pulse obtained by simulation, and $A_{exact}^{k}(\Delta z; i)$ the exact solution. It should be noted that and $A_{exact}^{k}(\Delta z; i)$ is approximated by $A_{exact}^{k}(\Delta z_{ref}; i)$, where Δz_{ref} is 5 times smaller than the so far smallest step size for which $E(\Delta z)$ has been estimated.

Figure 8.1 shows $E(\Delta z)$ of the single pulse after propagating for one span as the function of q simulated by the FDTD method. Both $E(\Delta z)$ and q in Fig. 8.1 are shown in logarithm scale. The result indicates that $E(\Delta z)$ increases almost linearly with the spatial step size. The smaller the error is, the closer the numerical result gets closed to the exact solution. However, there becomes a question that how much the error can be acceptable.

Figure 8.2 shows the output pulse shape computed by setting q = 1.7x10^{-2} (shown by solid line), comparing with the output pulse waveform simulated by reducing q to 3.4x10^{-3}, which is 5 times smaller (shown by dotted line). In this case, $E(\Delta z)$ obtained from q = 1.7x10^{-2} is around the value of 1.2x10^{-2}. From Fig. 8.2, the propagated pulses appear with slight asymmetrical broadening induced from higher-

order GVD. Excepting small distinction around peak point of the pulse, the pulse waveform calculated by using $q = 1.7\text{x}10^{-2}$ is almost fitted with that obtained from $q = 3.4\text{x}10^{-3}$. To further decreasing q much shorter than this value may result only a little more difference. However, the result from Fig. 8.2 informs us that with error of about 10^{-2}, we are sufficiently able to attain nearly the exact solution.

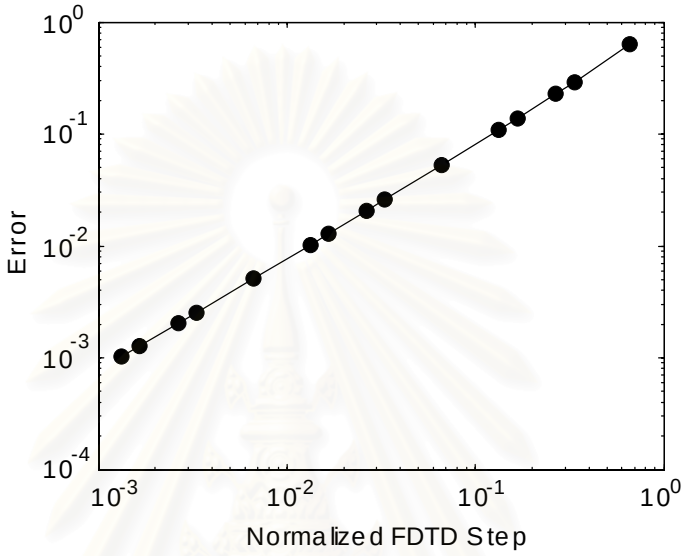

Figure 8.1: $E(\Delta z)$ of the single pulse after propagating for one span as the function of q shown in logarithm scale simulated by the FDTD method. $E(\Delta z)$ increases almost linearly with the spatial step size.

Figure 8.3 compares $E(\Delta z)$ from the explicit FDTD method with the SSFM as a function of spatial step size Δz. At the same Δz, the SSFM produces much smaller $E(\Delta z)$ and converges to the exact solution more rapid than the FDTD method. At $\Delta z = 10^{-2}$, $E(\Delta z)$ of the SSFM exhibits a value lower than 10^{-8}, while that obtained from the FDTD is as large as 10^{-1}. Therefore, by the explicit FDTD method, in order to achieve an equal $E(\Delta z)$ to the SSFM, it is clearly that extremely small Δz is required, resulting in significant increase in computation time.

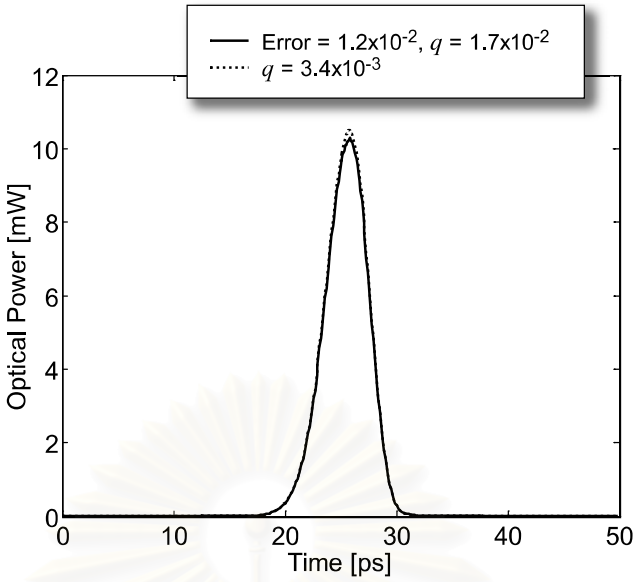

Figure 8.2: Output pulse shape calculated by the explicit FDTD method with q = 1.7x10^{-2} (shown by solid line), comparing with output pulse shape simulated by q = 3.4x10^{-3} (shown by dotted line). $E(\Delta z)$ of q = 1.7x10^{-2} is about 1.2x10^{-2}. Small difference around peak point of the pulse is observed. However, the exact solution is almost obtained with error of about 10^{-2}.

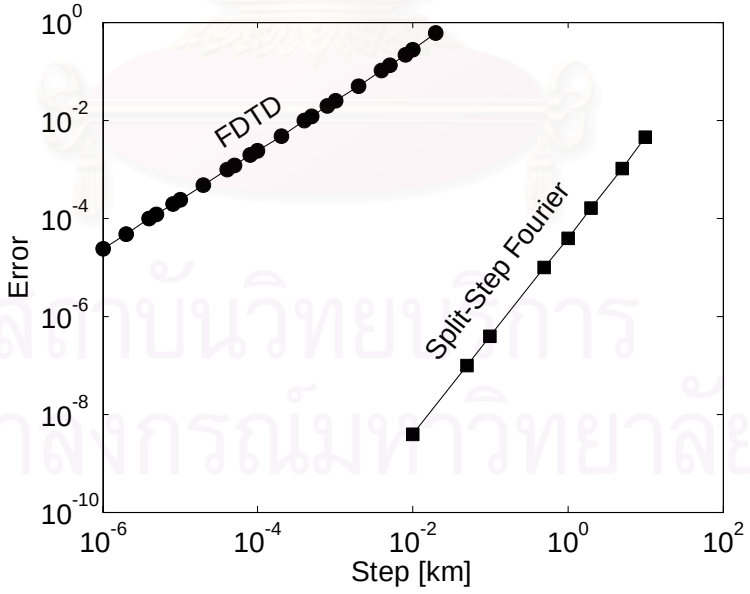

Figure 8.3: $E(\Delta z)$ calculated from the explicit FDTD method and the SSFM as a function of spatial step size. The SSFM yields much smaller $E(\Delta z)$ and converges to the exact solution more rapid than the explicit FDTD method.

Figure 8.4 shows the comparison of computation time between the explicit FDTD method and SSFM method as a function of $E(\Delta z)$. Although, the computation time used by both methods increase almost linearly with the reduction of $E(\Delta z)$. As expected, at equal value of $E(\Delta z)$, the explicit FDTD method consumes much calculation time than the SSFM. However, with the rapid progress in the performance improvement of nowadays computers, in such a case of simulation of pulse propagation in fiber span which is not so long, such drawback in computation time may not disturb those who use the explicit FDTD method too much rather than being annoyed in wasting much time transforming the SSFM into computer code. For instance, running the simulations on MS. Visual C++ on Window XP using CPU Pentium IV 2 GHz with 512 MB memory take computation time below 1 s for the SSFM and about 10 s for the explicit FDTD method at the same $E(\Delta z)$ of about 10^{-2}.

Next, we explore how far the explicit FDTD method can be used to compute the pulse propagation. Assuming the SSFM is the most accurate method for simulating pulse propagation in optical fibers, the difference between results obtained from the explicit FDTD method and the SSFM is investigated. Figure 8.5 shows the 50-km-transmitted pulse waveform calculated by the explicit FDTD method using q = $3.4\text{x}10^{-4}$ (shown by solid line), comparing with that calculated by the SSFM with Δz = 10 m. $E(\Delta z)$ of both waveform are $2.4\text{x}10^{-4}$ and $3.9\text{x}10^{-9}$, for the explicit FDTD method and the SSFM, respectively. According to Fig. 8.5, the difference in results between two algorithms is observed. To determine an amount of difference between the explicit FDTD method and the SSFM, we should define the FDTD-to-SSFM error using Eq. (8-7) by changing the reference term $A^k_{exact}(\Delta z; i)$ with $A^k_{SSFM}(\Delta z; i)$, where $A^k_{SSFM}(\Delta z; i)$ is obtained from SSFM. By this definition, the FDTD-to-SSFM error of the two pulse waveforms in Fig. 8.5 is about $7.9\text{x}10^{-2}$.

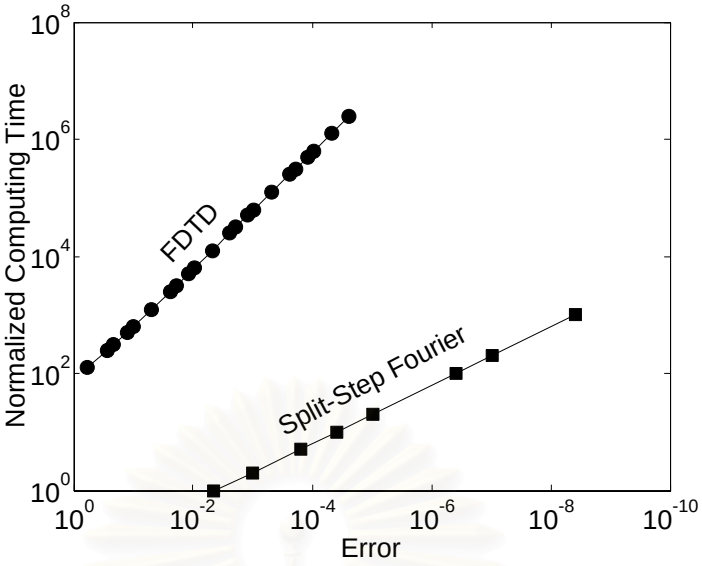

Figure 8.4: Comparison of computation time between the explicit FDTD method and the SSFM method as a function of $E(\Delta z)$. At equal $E(\Delta z)$, the explicit FDTD method consumes much calculation time than the SSFM.

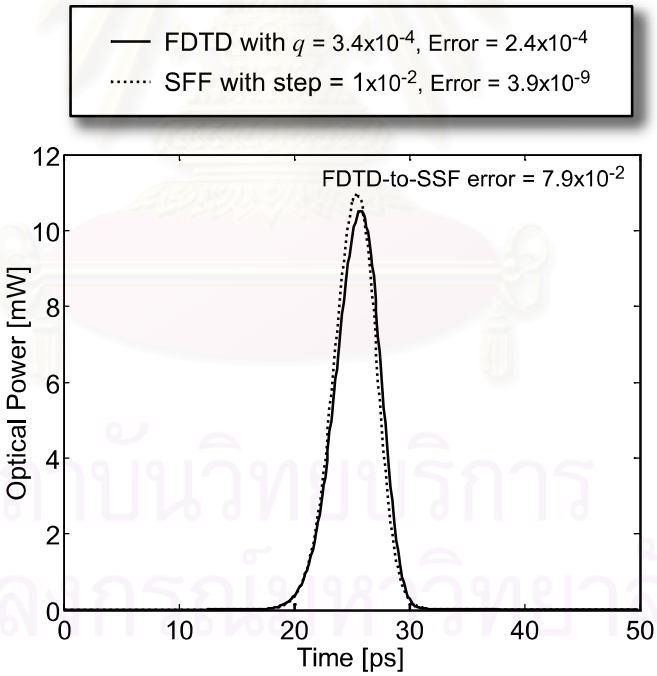

Figure 8.5: 50-km-transmitted pulse waveform calculated by the explicit FDTD method using q = 3.4x10^{-4} (shown by solid line), comparing with that calculated by the SSFM with Δz = 10 m. $E(\Delta z)$ of both waveform are 2.4x10^{-4} and 3.9x10^{-9}, for the explicit FDTD method and the SSFM, respectively. FDTD-to-SSFM error of the two pulse waveforms is about 7.9x10^{-2}.

Figure 8.6 show the explicit-FDTD-to-SSFM error as a function of propagation distance for several q values. In this case the pulse is transmitted for two spans (100 km) with additional one lump noiseless optical amplifier placed at 100 km. The result from Fig. 8.6 mentions that the FDTD-to-SSFM error become greater with propagation distance. The increase in spatial step size Δz can only slightly reduce this error. For relatively small q, even we further reducing q by 20 times ($q = 6.8\text{x}10^{-3}$ shown by squares to $q = 3.4\text{x}10^{-4}$ shown by diamonds), the corresponding FDTD-to-SSFM error at arbitrary distance is almost not changed.

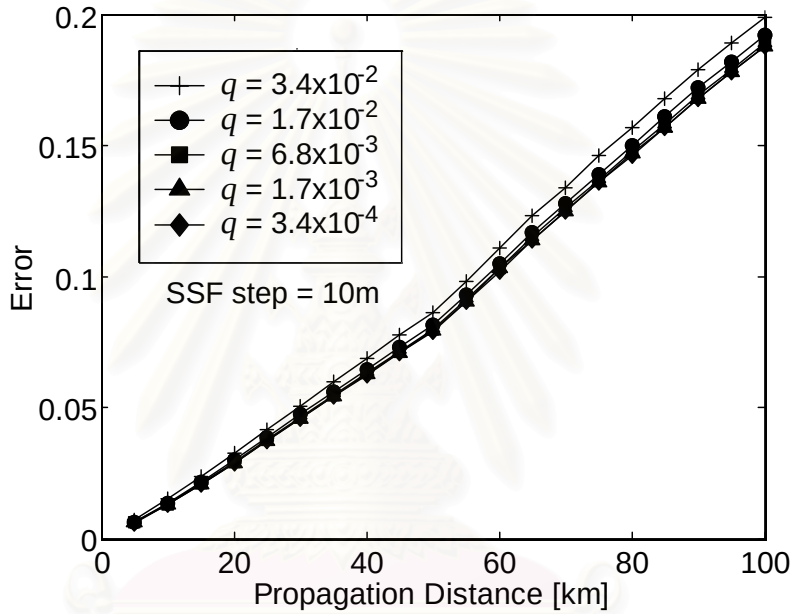

Figure 8.6: FDTD-to-SSFM error as a function of propagation distance for several q values. The pulse is transmitted for two spans (100km). FDTD-to-SSFM error becomes greater with propagation distance. The increase in spatial step size Δz can only slightly reduce this error. If we consider the FDTD-to-SSFM error is the most serious limit of the explicit FDTD method, the simulation using the explicit FDTD method can only be applied for a fiber length of several ten kilometers.

8.3 Implicit FDTD

The concept of implicit FDTD is to use the next step solution to calculate the next step solution itself. It has been shown that the use of the implicit FDTD can reduce the error caused by the choice of a step size. At the same step size, the implicit FDTD

gives more accurate result than the explicit FDTD. However, the accumulative characteristics of these two methods are the same.

Using the implicit FDTD, Eq. (8-2) is rewritten to be

$$\frac{A^{k+1}(n)-A^{k}(n)}{\Delta z}=-\frac{\alpha}{2}A^{k+1}(n)-\frac{i}{2}\beta_2\frac{A^{k+1}(n+1)-2A^{k+1}(n)+A^{k+1}(n-1)}{(\Delta T)^2}$$
$$+\frac{1}{6}\beta_3\frac{A^{k+1}(n+2)-2A^{k+1}(n+1)+2A^{k+1}(n)-A^{k+1}(n-1)}{(\Delta T)^3} \quad (8\text{-}8)$$
$$+i\gamma\left|A^{k+1}(n)\right|^2A^{k+1}(n),$$

It should be noted that the suffix *k* on the right hand side of Eq. (8-8) is only replaced by *k*+1.

After splitting $A^{k}(n)$ as well as $A^{k+1}(n)$ into its real and imaginary components using Eq. (8-3), we obtain two coupled implicit FDTD equations

$$A_{real}^{k}(n)=A_{real}^{k+1}(n)+\frac{1}{2}\alpha\Delta zA_{real}^{k+1}(n)$$
$$-\frac{\beta_3\Delta z}{6(\Delta T)^3}\left\{A_{real}^{k+1}(n+2)-2A_{real}^{k+1}(n+1)+2A_{real}^{k+1}(n-1)+A_{real}^{k+1}(n-2)\right\}$$
$$-\frac{\beta_2\Delta z}{2(\Delta T)^2}\left\{A_{imag}^{k+1}(n+1)-2A_{imag}^{k+1}(n)+A_{imag}^{k+1}(n-1)\right\} \quad (8\text{-}9)$$
$$+\gamma\Delta z\left|\left(A_{real}^{k+1}(n)\right)^2+\left(A_{imag}^{k+1}(n)\right)^2\right|A_{imag}^{k+1}(n)$$

$$A_{imag}^{k}(n)=A_{imag}^{k+1}(n)+\frac{1}{2}\alpha\Delta zA_{imag}^{k+1}(n)$$
$$-\frac{\beta_3\Delta z}{6(\Delta T)^3}\left\{A_{imag}^{k+1}(n+2)-2A_{imag}^{k+1}(n+1)+2A_{imag}^{k+1}(n-1)+A_{imag}^{k+1}(n-2)\right\}$$
$$+\frac{\beta_2\Delta z}{2(\Delta T)^2}\left\{A_{real}^{k+1}(n+1)-2A_{real}^{k+1}(n)+A_{real}^{k+1}(n-1)\right\} \quad (8\text{-}10)$$
$$-\gamma\Delta z\left|\left(A_{real}^{k+1}(n)\right)^2+\left(A_{imag}^{k+1}(n)\right)^2\right|A_{real}^{k+1}(n)$$

From Eq. (8-9) and (8-10), to obtain $A^{k+1}(n)$, we establish two coupled implicit FDTD matrix equations for the real part and imaginary part with each equation has *n* unknown variables as shown below,

$$\begin{bmatrix} & A & \end{bmatrix}\begin{bmatrix} A_{real}^{k+1}(1) \\ A_{real}^{k+1}(2) \\ A_{real}^{k+1}(3) \\ \vdots \\ A_{real}^{k+1}(n) \end{bmatrix}+\begin{bmatrix} & B & \end{bmatrix}\begin{bmatrix} A_{imag}^{k+1}(1) \\ A_{imag}^{k+1}(2) \\ A_{imag}^{k+1}(3) \\ \vdots \\ A_{imag}^{k+1}(n) \end{bmatrix}=\begin{bmatrix} A_{real}^{k}(1) \\ A_{real}^{k}(2) \\ A_{real}^{k}(3) \\ \vdots \\ A_{real}^{k}(n) \end{bmatrix}, \quad (8\text{-}11)$$

$$\begin{bmatrix} & A' & \end{bmatrix}\begin{bmatrix} A_{imag}^{k+1}(1) \\ A_{imag}^{k+1}(2) \\ A_{imag}^{k+1}(3) \\ \vdots \\ A_{imag}^{k+1}(n) \end{bmatrix}+\begin{bmatrix} & B' & \end{bmatrix}\begin{bmatrix} A_{real}^{k+1}(1) \\ A_{real}^{k+1}(2) \\ A_{real}^{k+1}(3) \\ \vdots \\ A_{real}^{k+1}(n) \end{bmatrix}=\begin{bmatrix} A_{imag}^{k}(1) \\ A_{imag}^{k}(2) \\ A_{imag}^{k}(3) \\ \vdots \\ A_{imag}^{k}(n) \end{bmatrix}. \quad (8\text{-}12)$$

The matrix A, B, A', and B' are all $n \times n$ matrix. The components of matrix A which are not zero are

$$a_{i,i} = 1 + \frac{1}{2}\alpha\Delta z \text{, for } i = 1, 2, 3,\ldots, n, \quad (8\text{-}13)$$

$$a_{i,i+1} = \frac{\beta_3 \Delta z}{3\Delta T^3} \text{, for } i = 1, 2, 3,\ldots, n\text{-}1, \quad (8\text{-}14)$$

$$a_{i,i+2} = -\frac{\beta_3 \Delta z}{6\Delta T^3} \text{, for } i = 1, 2, 3,\ldots, n\text{-}2, \quad (8\text{-}15)$$

$$a_{i+1,i} = -\frac{\beta_3 \Delta z}{3\Delta T^3} \text{, for } i = 1, 2, 3,\ldots, n\text{-}1, \quad (8\text{-}16)$$

$$a_{i+2,i} = \frac{\beta_3 \Delta z}{6\Delta T^3} \text{, for } i = 1, 2, 3,\ldots, n\text{-}2. \quad (8\text{-}17)$$

The components of matrix B which are not zero are

$$b_{i,i} = -\gamma\left\{\left|A_{real}^{k+1}(i)\right|^2 + \left|A_{imag}^{k+1}(i)\right|^2\right\}\Delta z - \frac{\beta_2 \Delta z}{\Delta T^2} \text{, for } i = 1, 2, 3,\ldots, n, \quad (8\text{-}18)$$

$$b_{i,i+1} = \frac{\beta_2 \Delta z}{2\Delta T^2} \text{, for } i = 1, 2, 3,\ldots, n\text{-}1, \quad (8\text{-}19)$$

$$b_{i+1,i} = \frac{\beta_2 \Delta z}{2\Delta T^2} \text{, for } i = 1, 2, 3,\ldots, n\text{-}1, \quad (8\text{-}20)$$

The components of matrix A' which are not zero are

$$a'_{i,i} = 1 + \frac{1}{2}\alpha\Delta z \text{ , for } i = 1, 2, 3,\ldots, n, \tag{8-21}$$

$$a'_{i,i+1} = \frac{\beta_3 \Delta z}{3\Delta T^3} \text{, for } i = 1, 2, 3,\ldots, n\text{-}1, \tag{8-22}$$

$$a'_{i,i+2} = -\frac{\beta_3 \Delta z}{6\Delta T^3} \text{ , for } i = 1, 2, 3,\ldots, n\text{-}2, \tag{8-23}$$

$$a'_{i+1,i} = -\frac{\beta_3 \Delta z}{3\Delta T^3} \text{ , for } i = 1, 2, 3,\ldots, n\text{-}1, \tag{8-24}$$

$$a'_{i+2,i} = \frac{\beta_3 \Delta z}{6\Delta T^3} \text{, for } i = 1, 2, 3,\ldots, n\text{-}2. \tag{8-25}$$

The components of matrix B' which are not zero are

$$b'_{i,i} = \gamma\left\{\left|A^{k+1}_{real}(i)\right|^2 + \left|A^{k+1}_{imag}(i)\right|^2\right\}\Delta z + \frac{\beta_2 \Delta z}{\Delta T^2} \text{ , for } i = 1, 2, 3,\ldots, n, \tag{8-26}$$

$$b'_{i,i+1} = -\frac{\beta_2 \Delta z}{2\Delta T^2} \text{ , for } i = 1, 2, 3,\ldots, n\text{-}1, \tag{8-27}$$

$$b'_{i+1,i} = -\frac{\beta_2 \Delta z}{2\Delta T^2} \text{ , for } i = 1, 2, 3,\ldots, n\text{-}1, \tag{8-28}$$

For given fiber parameters and A^k, in order to solve the above two equations for obtaining the next step solution A^{k+1}, some algorithms must be used for modifying Eq. (8-11) and (8-12). This is because, for example, to obtain A^{k+1}_{real}, the second term on the left hand side of Eq. (8-11), which is dependent on A^{k+1}_{imag} must be available first. Similarly, to calculate A^{k+1}_{imag}, the second term on the left hand side of Eq. (8-12), which is dependent on A^{k+1}_{real} must be also obtained before. Furthermore, in matrix *B*, $b_{i,i}$ and $b'_{i,i}$ require the calculation of $\left|A^{k+1}_{real}(i)\right|^2 + \left|A^{k+1}_{imag}(i)\right|^2$, which will not be exactly obtained unless we have both A^{k+1}_{real} and A^{k+1}_{imag} before. For overcoming these problems, we proposed two schemes, which will be assigned the names as the implicit-1 FDTD and the implicit-2 FDTD.

8.3.1 Implicit-1 FDTD

The algorithm of the implicit-1 FDTD, as shown in Fig. 8.7 is very simple. A^k_{real} and A^k_{imag} are used instead of A^{k+1}_{real} and A^{k+1}_{imag} in the second terms including the

calculation of $\left|A_{real}^{k+1}(i)\right|^2 + \left|A_{imag}^{k+1}(i)\right|^2$ inside the matrix B and B', respectively. Then, Eq. (8-11) and (8-12) will be solve to obtain A_{real}^{k+1} and A_{imag}^{k+1}, which become A_{real}^{k} and A_{imag}^{k} for next step.

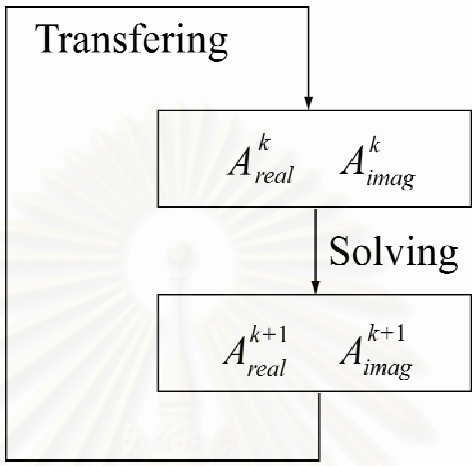

Figure 8.7: Algorithm of the implicit-1 FDTD.

Figure 8.8 shows the accumulated step size error of the explicit FDTD in percentage unit for the single pulse propagation in two spans (100 km), as a function of distance for several step sizes

For comparison, Fig. 8.9 shows the accumulated step size error of the implicit-1 FDTD in percentage unit for the single pulse propagation in two spans, as a function of distance for several step sizes. The results are obtained by solving Eq. (8-11) and (8-12) by using Gaussian elimination with backsubstitution with scaling and pivoting [94]. Although the error increases with transmission distance and then rapidly arises at a distance that is shorter for larger step size, the error causes by the implicit-1 FDTD is approximately 10 times smaller than the error from using the explicit FDTD.

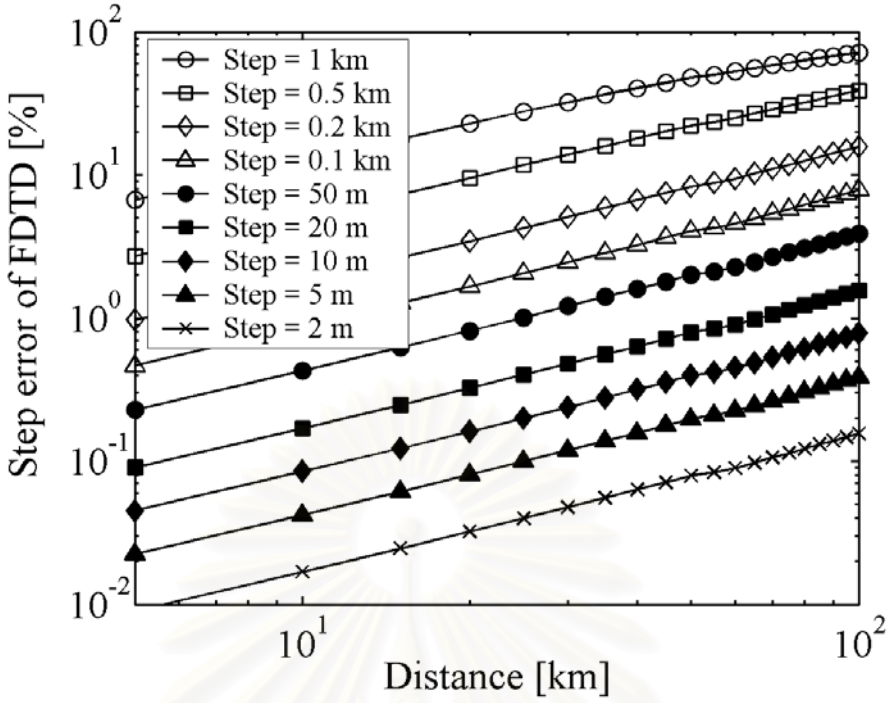

Figure 8.8: Step size error of the explicit FDTD in percentage unit for the single pulse propagation for 100 km as a function of distance for several step sizes.

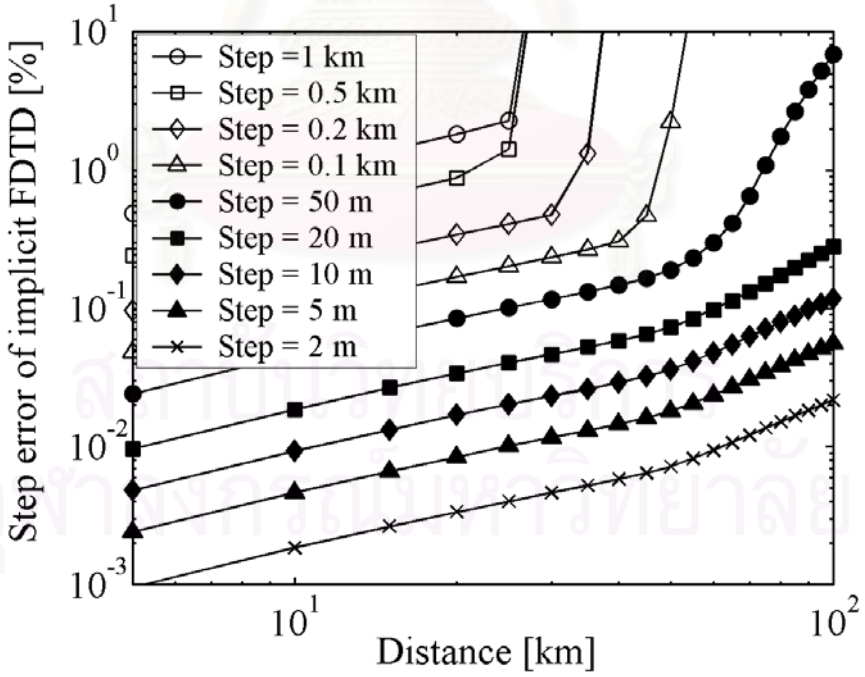

Figure 8.9: Accumulated step size error of the implicit-1 FDTD in percentage unit for the single pulse propagation for 100 km as a function of distance for several step sizes.

Figure 8.10 shows the accumulated explicit-FDTD-to-SSFM error in percentage unit for the single pulse propagation in two spans, as a function of distance for several step sizes. Although, the error almost increases linearly with transmission distance, similar to Fig. 8.6, the increase in size Δz can only slightly reduce this error. The error converges to a value for a given distance, for examples, 7.6 % for 50 km and 17.8 % for 100 km transmission.

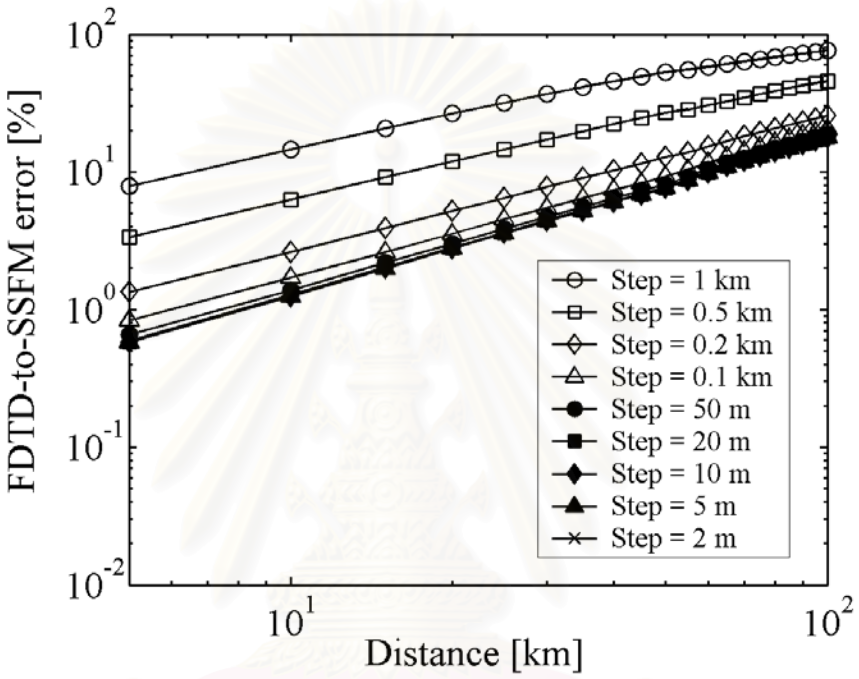

Figure 8.10: Accumulated explicit-FDTD-to-SSFM error in percentage unit for the single pulse propagation for 100 km as a function of distance for several step sizes.

In comparison with the result in Fig. 8.10, Fig. 8.11 shows the accumulated implicit-FDTD-to-SSFM error in percentage unit for the single pulse propagation in two spans, as a function of distance for several step sizes. For larger step size (> 0.2 km), this error increases rapidly when the pulse propagates for a distance. However, for smaller step size (< 0.2 km) the error also saturates to a value which is almost the same as the case of explicit FDTD. For examples, the error becomes 7.6 % for 50 km and 17.8 % for 100 km transmission.

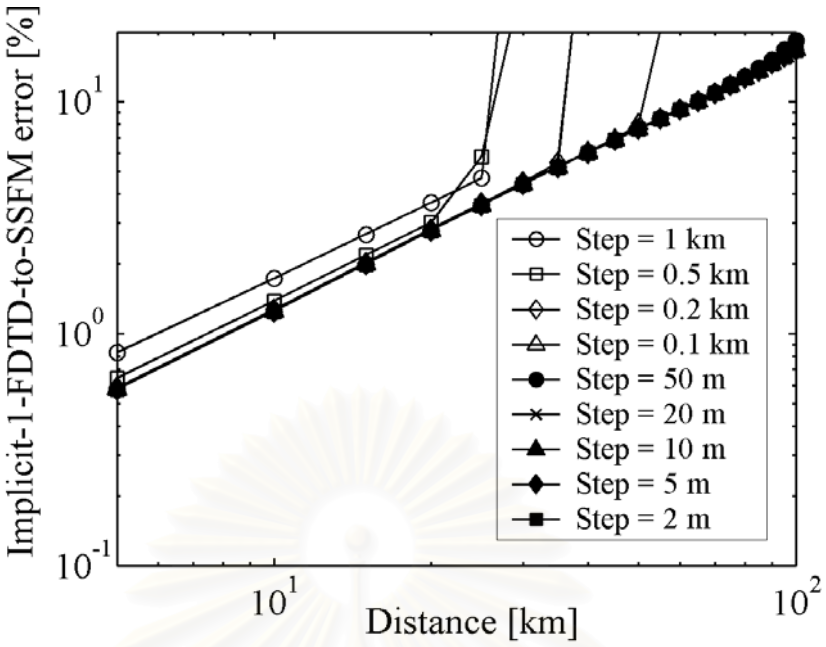

Figure 8.11: Accumulated implicit-FDTD-to-SSFM error in percentage unit for the single pulse propagation for 100 km as a function of distance for several step sizes.

8.3.2 Implicit-2 FDTD

The algorithm of the implicit-2 FDTD, as shown in Fig. 8.12, is more complicated than the implicit-1 FDTD. For the first step of calculation, A^2_{real} is calculated by using A^1_{real} and A^1_{imag}. Then, A^2_{imag} is obtained by using A^2_{real} in the second term of the left hand side of Eq. (8-12). It should be noted that $\left|A^2_{real}(i)\right|^2 + \left|A^2_{imag}(i)\right|^2$ is approximated by $\frac{1}{2}\left\{\left|A^2_{real}(i)\right|^2 + \left|A^1_{imag}(i)\right|^2 + \left|A^1_{real}(i)\right|^2 + \left|A^1_{imag}(i)\right|^2\right\}$. For next step, A^2_{real} and A^2_{imag} are employed to calculate A^3_{real} from Eq. (8-11). A^3_{imag} is then obtained by using A^2_{real}, A^2_{imag}, and A^3_{real} through Eq. (8-12). This calculation repeats continuously until A^n_{real} and A^n_{imag} are obtained.

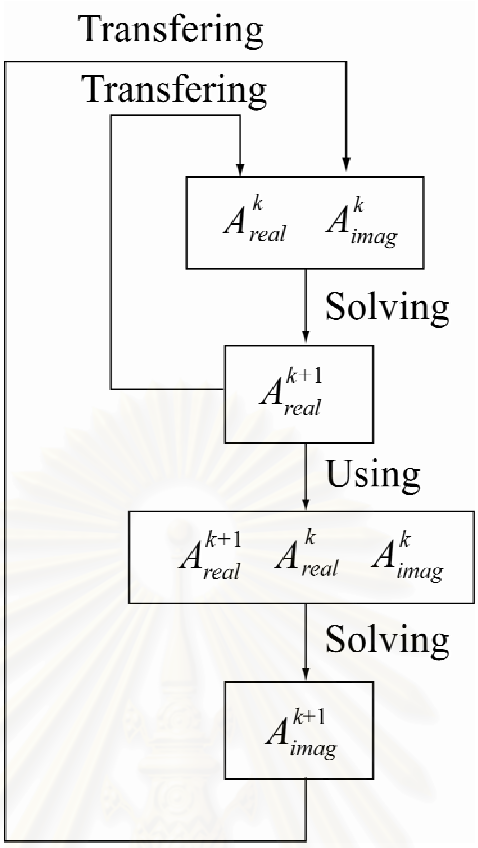

Figure 8.12: Algorithm of the implicit-2 FDTD.

Figure 8.13 shows the accumulated step size error of the implicit-2 FDTD in percentage unit for the single pulse propagation in two spans, as a function of distance for several step sizes. The increase in error is almost the same as that of the implicit-1 FDTD. However, the implicit-2 FDTD results slightly better error for a given step size than the result from the implicit-1 FDTD. Figure 8.14 shows the accumulated implicit-2-FDTD-to-SSFM error in percentage unit for the single pulse propagation in two spans, as a function of distance for several step sizes. Similar to the implicit-1 FDTD, the reduction in the step size can only slightly reduce the difference of the result from FDTD and the SSFM. For the step larger than 0.2 km, this error increases rapidly when the pulse propagates for a distance. However, the distance that the error rapidly arises is longer than that of the implicit-1 FDTD.

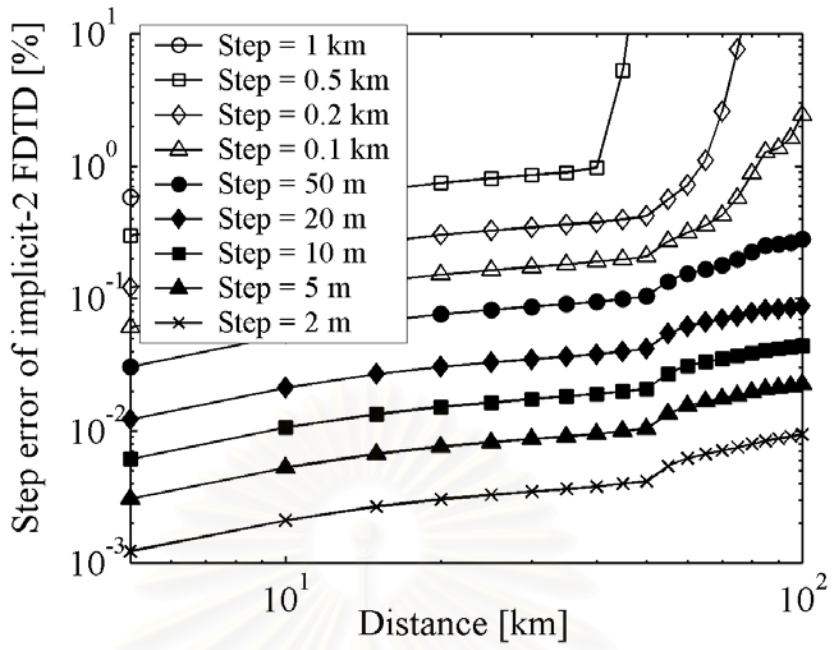

Figure 8.13: Accumulated step size error of the implicit-2 FDTD in percentage unit for the single pulse propagation for 100 km as a function of distance for several step sizes.

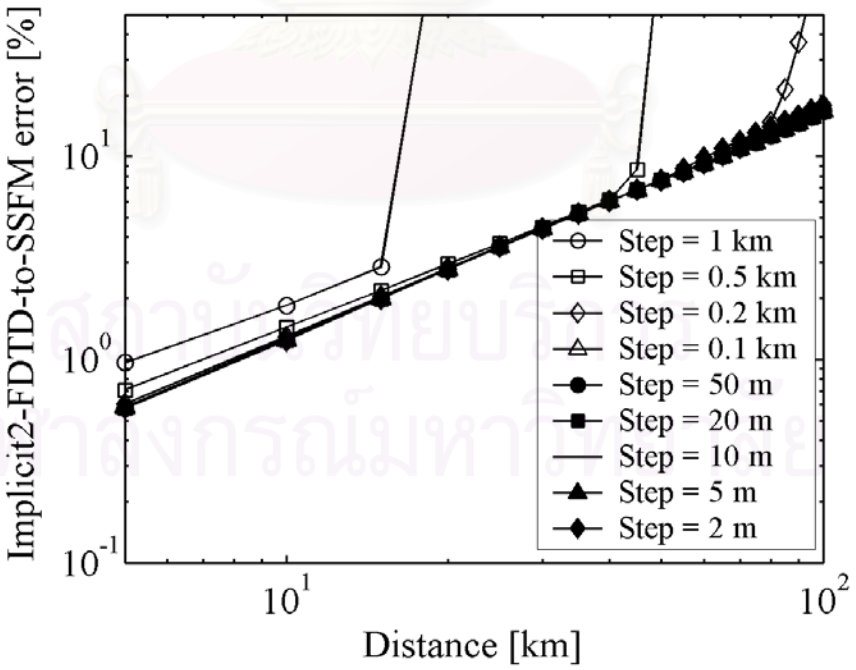

Figure 8.14: Accumulated implicit-2-FDTD-to-SSFM error in percentage unit for the single pulse propagation for 100 km as a function of distance for several step sizes.

8.4 FDTD Employing Crank-Nicholson Scheme

Crank-Nicholson (CN) scheme is well known for a method that can sufficiently reduce the accumulated error caused by the choice of step size in FDTD algorithm. The concept of CN scheme is to use the average value between the solution and the solution of the next step for estimating the solution of the next step.

Employing the CN scheme, Eq. (8-2) is modified to be

$$\begin{aligned}\frac{A^{k+1}(n)-A^{k}(n)}{\Delta z} &= -\frac{\alpha}{2}\left\{\frac{A^{k+1}(n)+A^{k}(n)}{2}\right\}\\ &-\frac{i}{2}\beta_2\left\{\begin{array}{l}\dfrac{A^{k+1}(n+1)-2A^{k+1}(n)+A^{k+1}(n-1)}{2(\Delta T)^2}\\ +\dfrac{A^{k}(n+1)-2A^{k}(n)+A^{k}(n-1)}{2(\Delta T)^2}\end{array}\right\}\\ &+\frac{1}{6}\beta_3\left\{\begin{array}{l}\dfrac{A^{k+1}(n+2)-2A^{k+1}(n+1)+2A^{k+1}(n)-A^{k+1}(n-1)}{2(\Delta T)^3}\\ +\dfrac{A^{k+1}(n+2)-2A^{k+1}(n+1)+2A^{k+1}(n)-A^{k+1}(n-1)}{2(\Delta T)^3}\end{array}\right\}\\ &+i\gamma\left|\frac{A^{k+1}(n)+A^{k}(n)}{2}\right|^2\left\{\frac{A^{k+1}(n)+A^{k}(n)}{2}\right\},\end{aligned} \tag{8-29}$$

After splitting $A^{k}(n)$ and $A^{k+1}(n)$ into its real and imaginary parts using Eq. (3), we obtain two coupled implicit FDTD equations

$$\begin{aligned}&A_{real}^{k+1}(n)+\frac{1}{4}\alpha\Delta z A_{real}^{k+1}(n)\\ &-\frac{\beta_3\Delta z}{12(\Delta T)^3}\left\{A_{real}^{k+1}(n+2)-2A_{real}^{k+1}(n+1)+2A_{real}^{k+1}(n-1)+A_{real}^{k+1}(n-2)\right\}=A_{real}^{k}(n)\\ &-\frac{1}{4}\alpha\Delta z A_{real}^{k}(n)+\frac{\beta_3\Delta z}{12(\Delta T)^3}\left\{A_{real}^{k}(n+2)-2A_{real}^{k}(n+1)+2A_{real}^{k}(n-1)+A_{real}^{k}(n-2)\right\}\\ &+\frac{\beta_2\Delta z}{2(\Delta T)^2}\left\{\frac{A_{imag}^{k+1}(n+1)-2A_{imag}^{k+1}(n)+A_{imag}^{k+1}(n-1)+A_{imag}^{k}(n+1)-2A_{imag}^{k}(n)+A_{imag}^{k}(n-1)}{2}\right\}\\ &-\gamma\Delta z\left|\frac{\left(A_{real}^{k+1}(n)\right)^2+\left(A_{imag}^{k+1}(n)\right)^2+\left(A_{real}^{k+1}(n)\right)^2+\left(A_{imag}^{k+1}(n)\right)^2}{2}\right|\left\{\frac{A_{imag}^{k+1}(n)+A_{imag}^{k+1}(n)}{2}\right\}\end{aligned} \tag{8-30}$$

$$
\begin{aligned}
&A_{imag}^{k+1}(n)+\frac{1}{4}\alpha\Delta z A_{imag}^{k+1}(n)\\
&-\frac{\beta_3\Delta z}{12(\Delta T)^3}\left\{A_{imag}^{k+1}(n+2)-2A_{imag}^{k+1}(n+1)+2A_{imag}^{k+1}(n-1)+A_{imag}^{k+1}(n-2)\right\}\\
&=A_{imag}^{k}(n)-\frac{1}{4}\alpha\Delta z A_{imag}^{k}(n)\\
&+\frac{\beta_3\Delta z}{12(\Delta T)^3}\left\{A_{imag}^{k}(n+2)-2A_{imag}^{k}(n+1)+2A_{imag}^{k}(n-1)+A_{imag}^{k}(n-2)\right\}\\
&-\frac{\beta_2\Delta z}{2(\Delta T)^2}\left\{\frac{A_{real}^{k+1}(n+1)-2A_{real}^{k+1}(n)+A_{real}^{k+1}(n-1)+A_{real}^{k}(n+1)-2A_{real}^{k}(n)+A_{real}^{k}(n-1)}{2}\right\}\\
&+\gamma\Delta z\left|\frac{\left(A_{real}^{k+1}(n)\right)^2+\left(A_{imag}^{k+1}(n)\right)^2+\left(A_{real}^{k+1}(n)\right)^2+\left(A_{imag}^{k+1}(n)\right)^2}{2}\right|\left\{\frac{A_{real}^{k+1}(n)+A_{real}^{k+1}(n)}{2}\right\}
\end{aligned}
\tag{8-31}
$$

Similar to the case of the implicit FDTD, to obtain $A^{k+1}(n)$, two coupled implicit FDTD matrix equations originated by Eq. (8-30) and (8-31) is formed for the real part and imaginary part with each equation has *n* unknown variables as shown below,

$$
\begin{aligned}
&\begin{bmatrix} & & \\ & A & \\ & & \end{bmatrix}\begin{bmatrix} A_{real}^{k+1}(1)\\ A_{real}^{k+1}(2)\\ A_{real}^{k+1}(3)\\ \text{M}\\ A_{real}^{k+1}(n)\end{bmatrix}=\begin{bmatrix} & & \\ & B & \\ & & \end{bmatrix}\begin{bmatrix} A_{real}^{k}(1)\\ A_{real}^{k}(2)\\ A_{real}^{k}(3)\\ \text{M}\\ A_{real}^{k}(n)\end{bmatrix}\\
&+\begin{bmatrix} & & \\ & C & \\ & & \end{bmatrix}\begin{bmatrix} A_{imag}^{k+1}(1)\\ A_{imag}^{k+1}(2)\\ A_{imag}^{k+1}(3)\\ \text{M}\\ A_{imag}^{k+1}(n)\end{bmatrix}+\begin{bmatrix} & & \\ & C & \\ & & \end{bmatrix}\begin{bmatrix} A_{imag}^{k}(1)\\ A_{imag}^{k}(2)\\ A_{imag}^{k}(3)\\ \text{M}\\ A_{imag}^{k}(n)\end{bmatrix}.
\end{aligned}
\tag{8-32}
$$

$$\begin{bmatrix} & A' & \end{bmatrix}\begin{bmatrix} A_{real}^{k+1}(1) \\ A_{real}^{k+1}(2) \\ A_{real}^{k+1}(3) \\ \text{M} \\ A_{real}^{k+1}(n) \end{bmatrix} = \begin{bmatrix} & B' & \end{bmatrix}\begin{bmatrix} A_{real}^{k}(1) \\ A_{real}^{k}(2) \\ A_{real}^{k}(3) \\ \text{M} \\ A_{real}^{k}(n) \end{bmatrix}$$
$$+\begin{bmatrix} & C' & \end{bmatrix}\begin{bmatrix} A_{imag}^{k+1}(1) \\ A_{imag}^{k+1}(2) \\ A_{imag}^{k+1}(3) \\ \text{M} \\ A_{imag}^{k+1}(n) \end{bmatrix} + \begin{bmatrix} & C' & \end{bmatrix}\begin{bmatrix} A_{imag}^{k}(1) \\ A_{imag}^{k}(2) \\ A_{imag}^{k}(3) \\ \text{M} \\ A_{imag}^{k}(n) \end{bmatrix} \quad (8\text{-}33)$$

The matrix A, B, A', and B' are all $n \times n$ matrix. The components of matrix A which are not zero are

$$a_{i,i} = 1 + \frac{1}{4}\alpha\Delta z, \text{ for } i = 1, 2, 3, \ldots, n, \quad (8\text{-}34)$$

$$a_{i,i+1} = \frac{\beta_3 \Delta z}{6\Delta T^3}, \text{ for } i = 1, 2, 3, \ldots, n\text{-}1, \quad (8\text{-}35)$$

$$a_{i,i+2} = -\frac{\beta_3 \Delta z}{12\Delta T^3}, \text{ for } i = 1, 2, 3, \ldots, n\text{-}2, \quad (8\text{-}36)$$

$$a_{i+1,i} = -\frac{\beta_3 \Delta z}{6\Delta T^3}, \text{ for } i = 1, 2, 3, \ldots, n\text{-}1, \quad (8\text{-}37)$$

$$a_{i+2,i} = \frac{\beta_3 \Delta z}{12\Delta T^3}, \text{ for } i = 1, 2, 3, \ldots, n\text{-}2. \quad (8\text{-}38)$$

The components of matrix B which are not zero are

$$b_{i,i} = 1 - \frac{1}{4}\alpha\Delta z, \text{ for } i = 1, 2, 3, \ldots, n, \quad (8\text{-}39)$$

$$b_{i,i+1} = -\frac{\beta_3 \Delta z}{6\Delta T^3}, \text{ for } i = 1, 2, 3, \ldots, n\text{-}1, \quad (8\text{-}40)$$

$$b_{i,i+2} = \frac{\beta_3 \Delta z}{12\Delta T^3}, \text{ for } i = 1, 2, 3, \ldots, n\text{-}2, \quad (8\text{-}41)$$

$$b_{i+1,i} = \frac{\beta_3 \Delta z}{6\Delta T^3}, \text{ for } i = 1, 2, 3, \ldots, n\text{-}1, \quad (8\text{-}42)$$

$$b_{i+2,i} = -\frac{\beta_3 \Delta z}{12\Delta T^3}, \text{ for } i = 1, 2, 3, \ldots, n\text{-}2. \quad (8\text{-}43)$$

The components of matrix C which are not zero are

$$c_{i,i} = -\frac{\gamma}{4}\left\{\left|A_{real}^{k+1}(i)\right|^2 + \left|A_{imag}^{k+1}(i)\right|^2 + \left|A_{real}^{k}(i)\right|^2 + \left|A_{imag}^{k}(i)\right|^2\right\}\Delta z - \frac{\beta_2 \Delta z}{2\Delta T^2},$$

for i = 1, 2, 3,…, n, (8-44)

$$c_{i,i+1} = \frac{\beta_2 \Delta z}{4\Delta T^2}, \text{ for } i = 1, 2, 3,\ldots, n\text{-}1, \quad (8\text{-}45)$$

$$c_{i+1,i} = \frac{\beta_2 \Delta z}{4\Delta T^2}, \text{ for } i = 1, 2, 3,\ldots, n\text{-}1, \quad (8\text{-}46)$$

The components of matrix A' which are not zero are

$$a'_{i,i} = 1 + \frac{1}{4}\alpha\Delta z, \text{ for } i = 1, 2, 3,\ldots, n, \quad (8\text{-}47)$$

$$a'_{i,i+1} = \frac{\beta_3 \Delta z}{6\Delta T^3}, \text{ for } i = 1, 2, 3,\ldots, n\text{-}1, \quad (8\text{-}48)$$

$$a'_{i,i+2} = -\frac{\beta_3 \Delta z}{12\Delta T^3}, \text{ for } i = 1, 2, 3,\ldots, n\text{-}2, \quad (8\text{-}49)$$

$$a'_{i+1,i} = -\frac{\beta_3 \Delta z}{6\Delta T^3}, \text{ for } i = 1, 2, 3,\ldots, n\text{-}1, \quad (8\text{-}50)$$

$$a'_{i+2,i} = \frac{\beta_3 \Delta z}{12\Delta T^3}, \text{ for } i = 1, 2, 3,\ldots, n\text{-}2. \quad (8\text{-}51)$$

The components of matrix B' which are not zero are

$$b'_{i,i} = 1 - \frac{1}{4}\alpha\Delta z, \text{ for } i = 1, 2, 3,\ldots, n, \quad (8\text{-}52)$$

$$b'_{i,i+1} = -\frac{\beta_3 \Delta z}{6\Delta T^3}, \text{ for } i = 1, 2, 3,\ldots, n\text{-}1, \quad (8\text{-}53)$$

$$b'_{i,i+2} = \frac{\beta_3 \Delta z}{12\Delta T^3}, \text{ for } i = 1, 2, 3,\ldots, n\text{-}2, \quad (8\text{-}54)$$

$$b'_{i+1,i} = \frac{\beta_3 \Delta z}{6\Delta T^3}, \text{ for } i = 1, 2, 3,\ldots, n\text{-}1, \quad (8\text{-}55)$$

$$b'_{i+2,i} = -\frac{\beta_3 \Delta z}{12\Delta T^3}, \text{ for } i = 1, 2, 3,\ldots, n\text{-}2. \quad (8\text{-}56)$$

The components of matrix C' which are not zero are

$$c'_{i,i} = \frac{\gamma}{4}\left\{\left|A^{k+1}_{real}(i)\right|^2 + \left|A^{k+1}_{imag}(i)\right|^2 + \left|A^{k}_{real}(i)\right|^2 + \left|A^{k}_{imag}(i)\right|^2\right\}\Delta z + \frac{\beta_2 \Delta z}{2\Delta T^2},$$

$$\text{for } i = 1, 2, 3, \ldots, n, \tag{8-57}$$

$$c'_{i,i+1} = -\frac{\beta_2 \Delta z}{4\Delta T^2}, \text{ for } i = 1, 2, 3, \ldots, n\text{-}1, \tag{8-58}$$

$$c'_{i+1,i} = -\frac{\beta_2 \Delta z}{4\Delta T^2}, \text{ for } i = 1, 2, 3, \ldots, n\text{-}1. \tag{8-59}$$

Similar to the case of the implicit FDTD, some algorithms must be used for solving Eq. (8-32) and Eq. (8-33) because, to obtain the next step solution A^{k+1}, we have to use A^{k+1} itself for computing the second and third term in Eq. (8-32) and (8-33) before. For this purpose, we present here 5 algorithms for solving Eq. (8-32) and (8-33). The algorithms are named as CN-1, CN-2, CN-3, CN-4, and CN-5.

8.4.1 CN-1 FDTD

The concept of the CN-1 FDTD algorithm is shown in Fig. 8.15. For the first step of calculation, A^2_{real} is calculated by using A^1_{real} and A^1_{imag} instead of A^2_{real} and A^2_{imag}. Then, A^2_{imag} is obtained by using A^2_{real} A^1_{real}, and A^1_{imag} in the second and the third term of the right hand side of Eq. (8-33). For next step, A^2_{real} and A^2_{imag} are used instead of A^3_{real} and A^3_{imag} while A^1_{real} and A^1_{imag} are used instead of A^2_{real} and A^2_{imag} in the second and the third term of the right hand side of Eq. (8-32) for calculating A^3_{real} from Eq. (8-32). A^3_{imag} is then obtained by using A^2_{real}, A^2_{imag}, and A^3_{real} from Eq. (8-33). This process will repeat continuously until A^n_{real} and A^n_{imag} are obtained.

Figure 8.16 shows the accumulated step size error of the CN-1 FDTD in percentage unit for the single pulse propagation in two spans, as a function of distance for several step sizes. The CN-1 FDTD yields less error than that of the implicit FDTD when the same step size is used. However, if we look at Fig. 8.17, which shows the accumulated CN-1-FDTD-to-SSFM error in percentage unit for the single pulse propagation in two spans as a function of distance for several step sizes, the error becomes larger than 100 % at a distance of about 60 km for all of step size values. Moreover, the use of larger step size results in slightly smaller different from the result from the SSFM. This indicates that the CN-1 FDTD gives the solution that is much different from the solution from the SSFM.

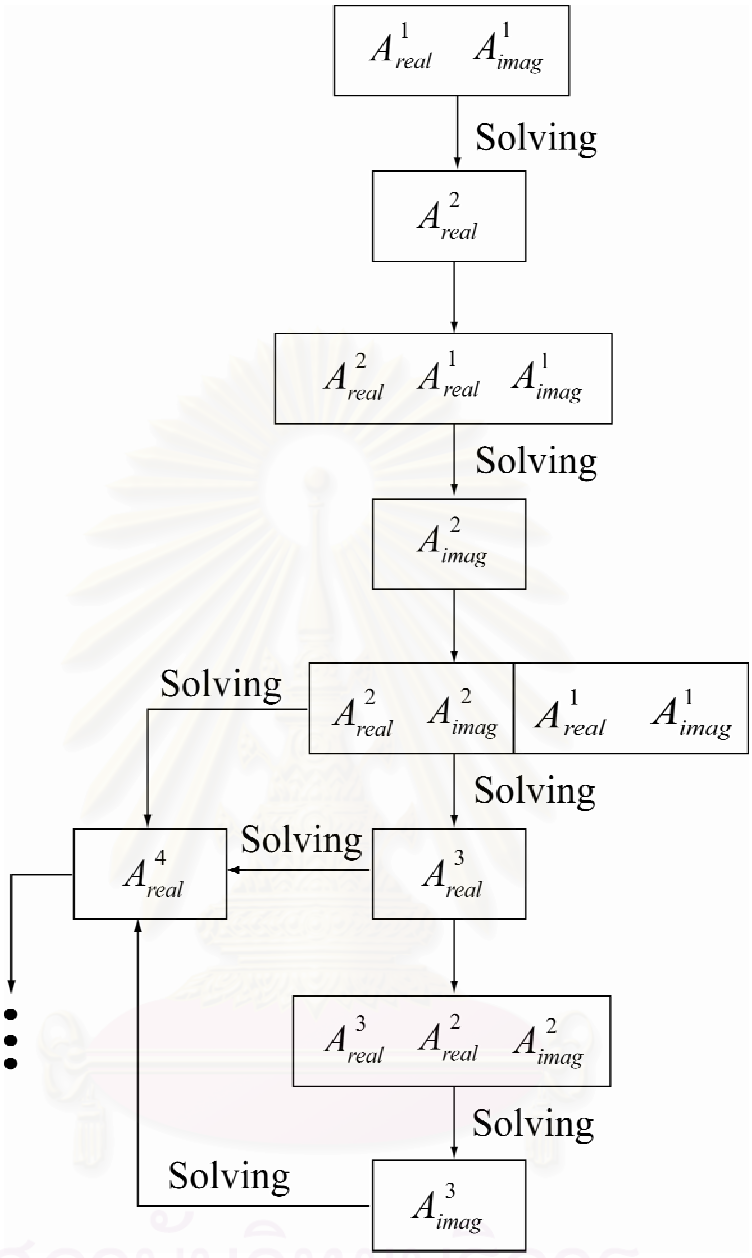

Figure 8.15: Algorithm of the CN-1 FDTD.

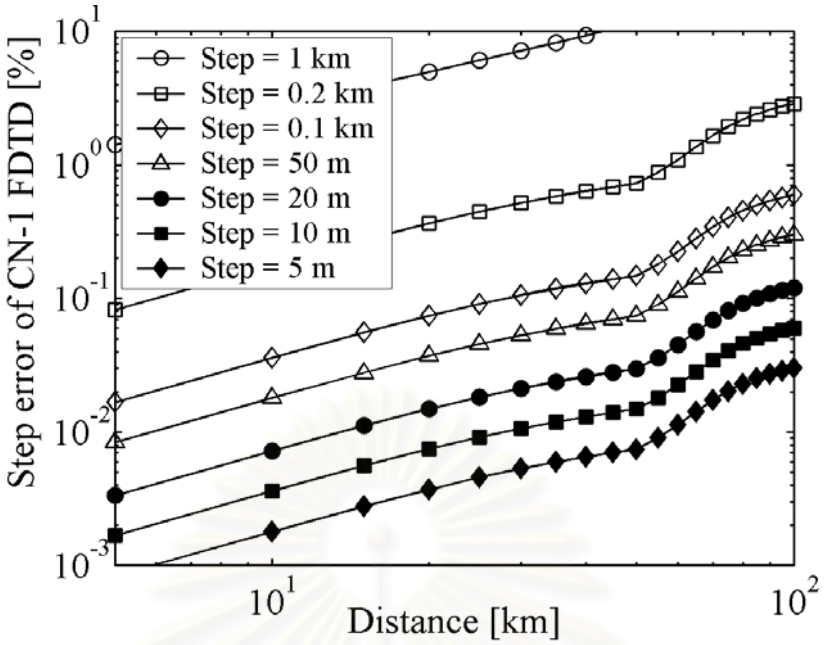

Figure 8.16: Accumulated step size error of the CN-1 FDTD in percentage unit for the single pulse propagation for 100 km as a function of distance for several step sizes.

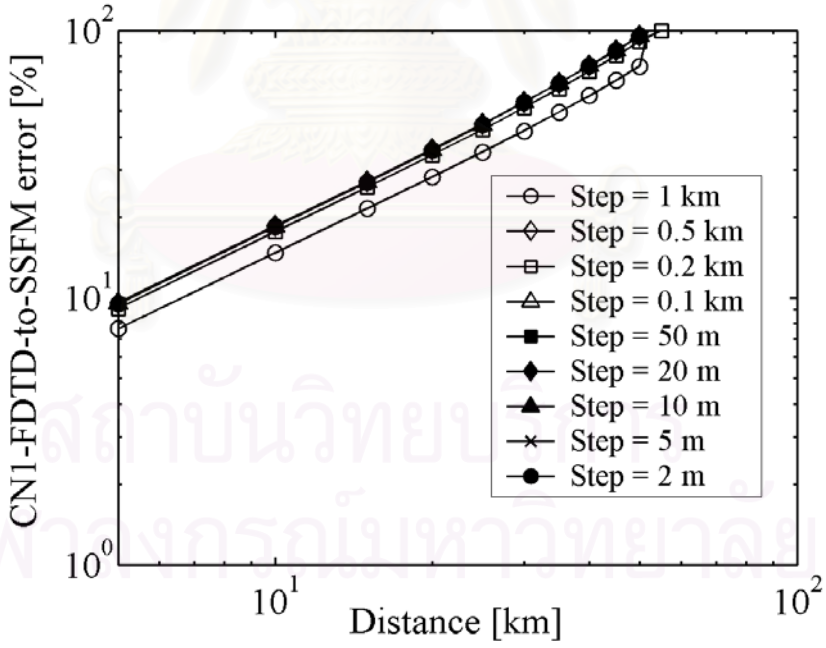

Figure 8.17: Accumulated CN-1-FDTD-to-SSFM error in percentage unit for the single pulse propagation for 100 km as a function of distance for several step sizes.

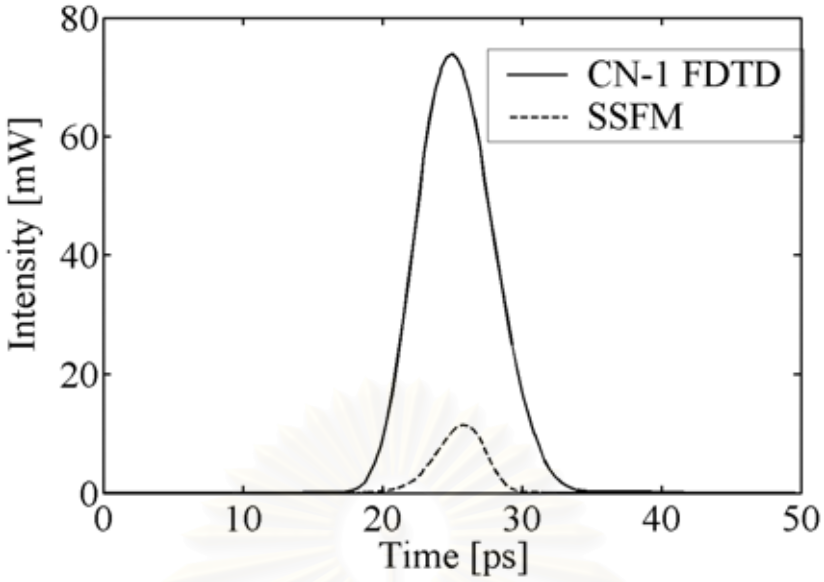

Figure 8.18: Comparison of pulse shapes at the output end of 100-km fiber calculated by the CN-1 FDTD and the SSFM.

Figure 8.18 shows the pulse shapes at the output end of 100-km fiber calculated by the CN-1 FDTD compared with that calculated by the SSFM. The pulse obtained from the CN-1 FDTD exhibits the power as large as 70 mW although its power that we launched into the input end is only 10 mW. This is impossible because a gain medium is not installed except the amplifiers which we use only to compensate the span loss. Therefore, we can conclude that the CN-1 FDTD that we proposed gives the result that is not accurate. On the other hand, for the result obtained from the SSFM, the result is reasonable because the output pulse has the peak power value very close to 10 mW.

8.4.2 CN-2 FDTD

The algorithm that we call CN-2 FDTD is the same as that of the implicit-1 FDTD which is shown in Fig. 8.7. This CN-2 FDTD is much simpler than the CN-1 FDTD. In CN-2 FDTD, A_{real}^{k} and A_{imag}^{k} is used instead of A_{real}^{k+1} and A_{imag}^{k+1} for calculating A_{real}^{k+1}. Then, A_{real}^{k} and A_{imag}^{k} is used instead of A_{real}^{k+1} and A_{imag}^{k+1} again for obtaining A_{imag}^{k+1}. This calculation repeats continuously until we obtain A_{real}^{n} and A_{imag}^{n}.

Figure 8.19 shows the accumulated step size error of the CN-2 FDTD in percentage unit for the single pulse propagation in two spans, as a function of distance

for several step sizes. The step error increases with transmission distance and arises rapidly at a distance that is shorter for larger step size. Although the CN-2 FDTD gives sufficiently as small error as those of the implicit FDTD and the CN-1 FDTD, the error is slightly larger than that of the CN-1 FDTD at the same step size. Figure 8.20 shows the accumulated CN-2-FDTD-to-SSFM error in percentage unit for the single pulse propagation in two spans as a function of distance for several step sizes. The error is almost the same at the error causes by using the implicit FDTD.

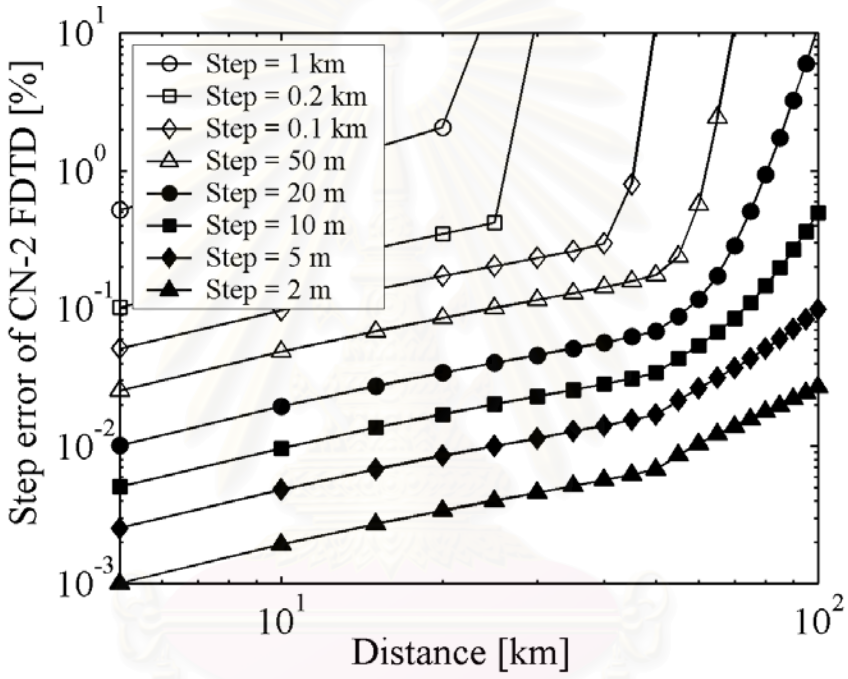

Figure 8.19: Accumulated step size error of the CN-2 FDTD in percentage unit for the single pulse propagation for 100 km as a function of distance for several step sizes.

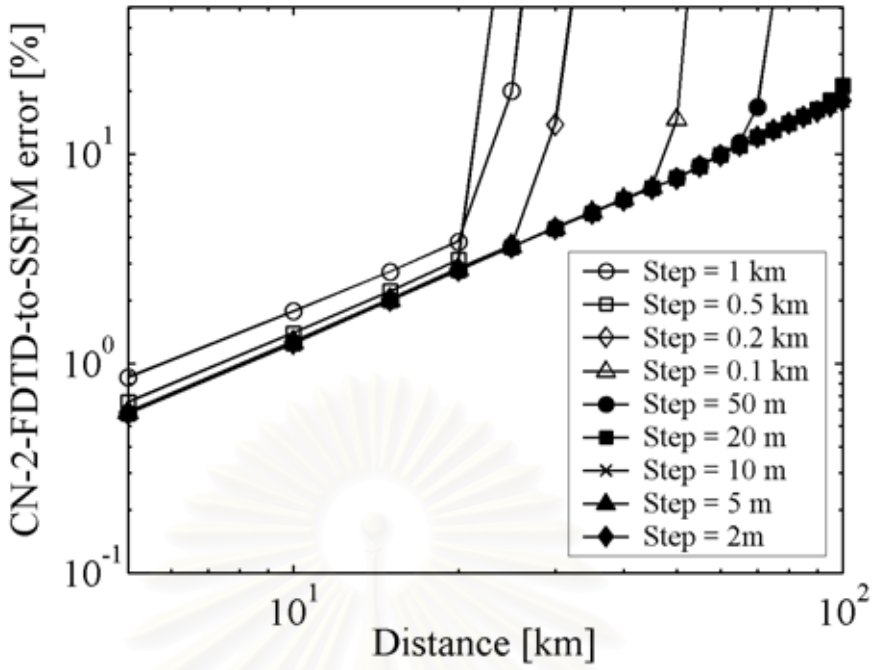

Figure 8.20: Accumulated CN-2-FDTD-to-SSFM error in percentage unit for the single pulse propagation for 100 km as a function of distance for several step sizes.

8.4.3 CN-3 FDTD

The concept of the CN-3 FDTD algorithm is the same as the implicit-2 FDTD which is shown in Fig. 8.12. For the first step of calculation, A_{real}^2 is calculated by using A_{real}^1 and A_{imag}^1 instead of A_{real}^2 and A_{imag}^2. Then, A_{imag}^2 is obtained by using A_{real}^2 A_{real}^1, and A_{imag}^1 in the second and the third term of the right hand side of Eq. (8-33). For next step, A_{real}^2 and A_{imag}^2 are used instead of A_{real}^3 and A_{imag}^3 in the second and the third term of the right hand side of Eq. (32) for calculating A_{real}^3 from Eq. (8-32). A_{imag}^3 is then obtained by using A_{real}^2, A_{imag}^2, and A_{real}^3 from Eq. (8-33). This process will repeat continuously until A_{real}^n and A_{imag}^n are obtained.

Figure 8.21 shows the accumulated step size error of the CN-3 FDTD in percentage unit for the single pulse propagation in two spans, as a function of distance for several step sizes. Comparing to other types of the CN FDTD which we have proposed, the CN-3 FDTD gives the error that is smaller than the CN-2 FDTD but slightly larger than the CN-1 FDTD. Figure 8.22 shows the accumulated CN-3-FDTD-to-SSFM error in percentage unit for the single pulse propagation in two spans

as a function of distance for several step sizes. The error is almost the same at the error causes by using the implicit FDTD and the CN-2 FDTD.

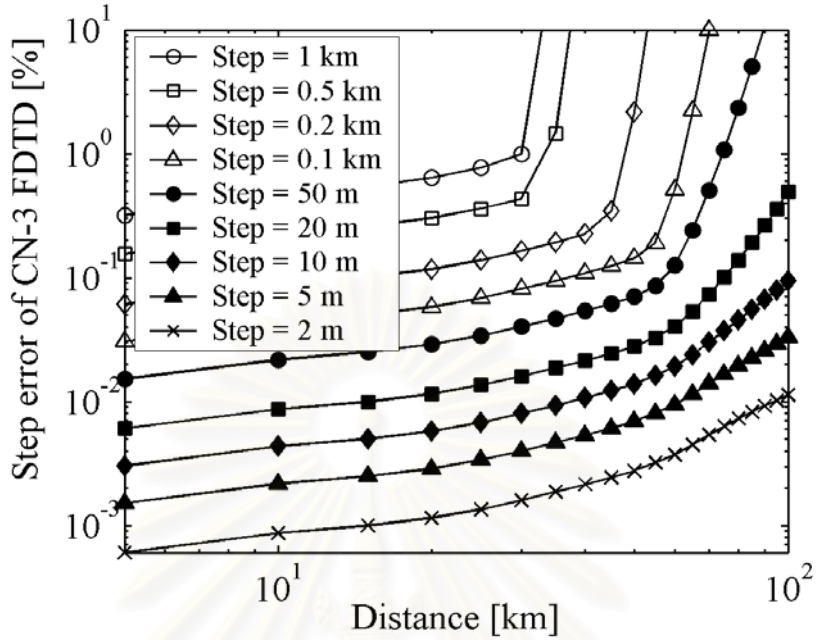

Figure 8.21: Accumulated step size error of the CN-3 FDTD in percentage unit for the single pulse propagation for 100 km as a function of distance for several step sizes.

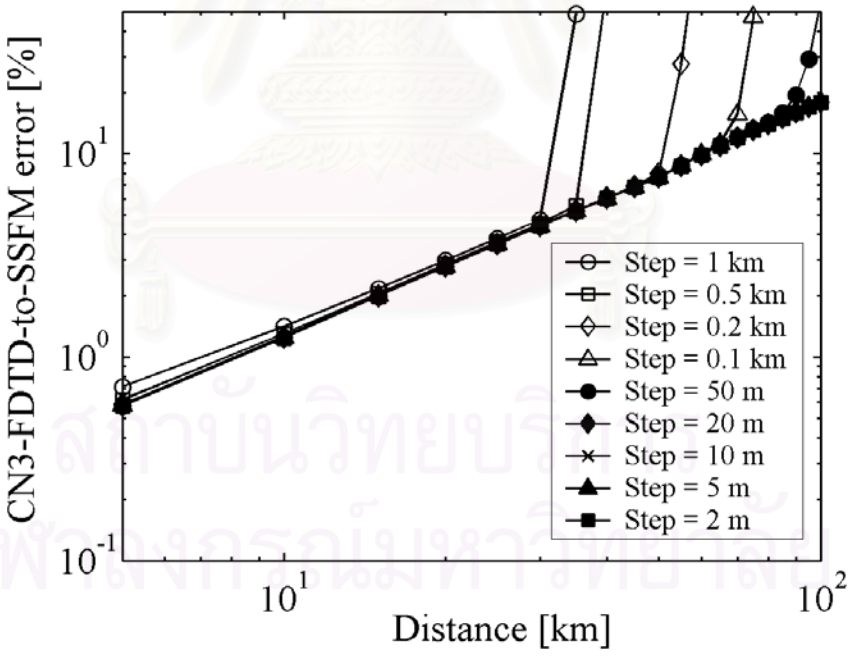

Figure 8.22: Accumulated CN-3-FDTD-to-SSFM error in percentage unit for the single pulse propagation for 100 km as a function of distance for several step sizes.

8.4.4 CN-4 FDTD

The concept of the CN-4 FDTD algorithm is shown in Fig. 8.23. The algorithm starts by the estimation of A_{real}^{2} by using A_{real}^{1} and A_{imag}^{1} instead of A_{real}^{2} and A_{imag}^{2}. Then, A_{imag}^{2} is obtained by using A_{real}^{2} A_{real}^{1}, and A_{imag}^{1} in the second and the third term of the right hand side of Eq. (8-33). For next step, A_{real}^{2} and A_{imag}^{2} are used in the second and the third term of the right hand side of Eq. (8-32) to obtain A_{real}^{2} again. In the next step A_{real}^{3} and A_{imag}^{3} is similarly calculated through this process. The calculation will repeat continuously until A_{real}^{n} and A_{imag}^{n} are obtained. Since we have to solve the CN FDTD equations 3 times (Eq. (8-32), Eq. (8-33), and Eq. (8-33)) for the estimation of A_{real}^{k+1} and A_{imag}^{k+1} for each step, it consumes the computation time about 1.5 times longer than other CN FDTD algorithm.

Figure 8.24 shows the accumulated step size error of the CN-4 FDTD in percentage unit for the single pulse propagation in two spans, as a function of distance for several step sizes. The CN-4 FDTD yields larger error than other FDTD algorithm. Moreover, similar to the result from CN-1 FDTD, the accumulated CN-4-FDTD-to-SSFM error as a function of distance in Fig. 8.25 shows a very high error closed to 100 % for long distance caused by this algorithm.

Figure 8.26 shows the pulse shapes at the output end of 100-km fiber calculated by the CN-4 FDTD compared with that calculated by the SSFM. The peak power of the pulse calculated by the CN-4 FDTD reduces significantly to be about 1 mW. Similar to the case of the CN-1 FDTD, this is also not reasonable because we compensate for the span loss by optical amplification. Therefore, the CN-4 FDTD algorithm is also the one that we have to avoid.

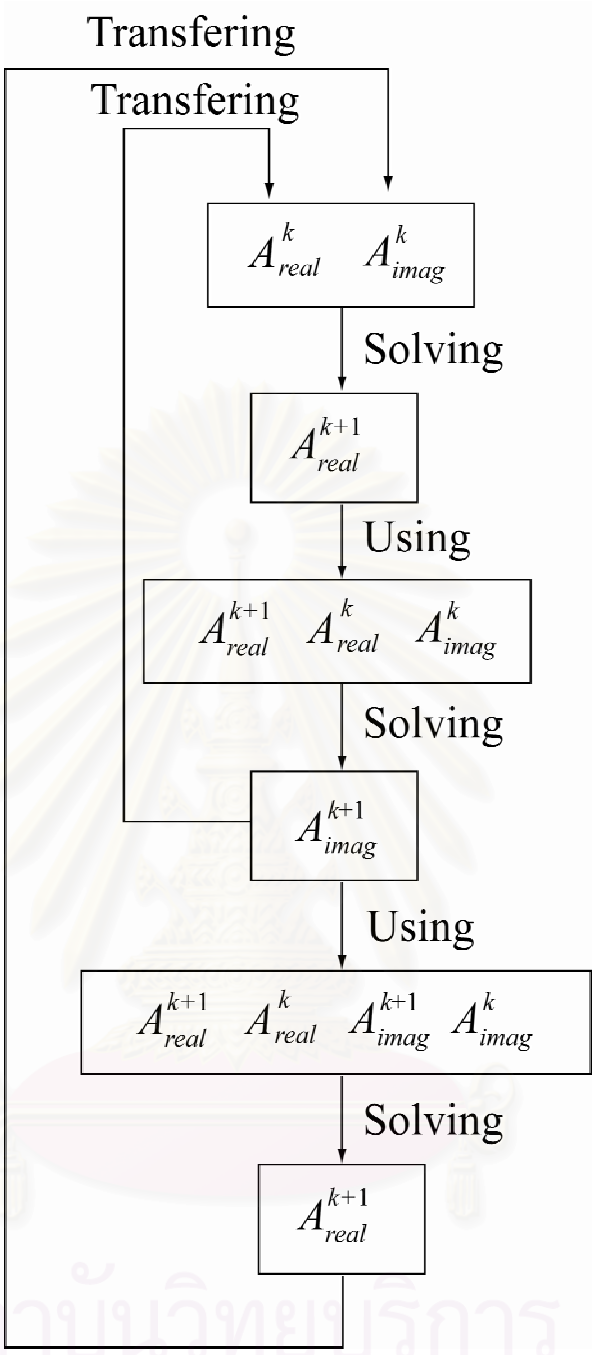

Figure 8.23: CN-4 FDTD algorithm.

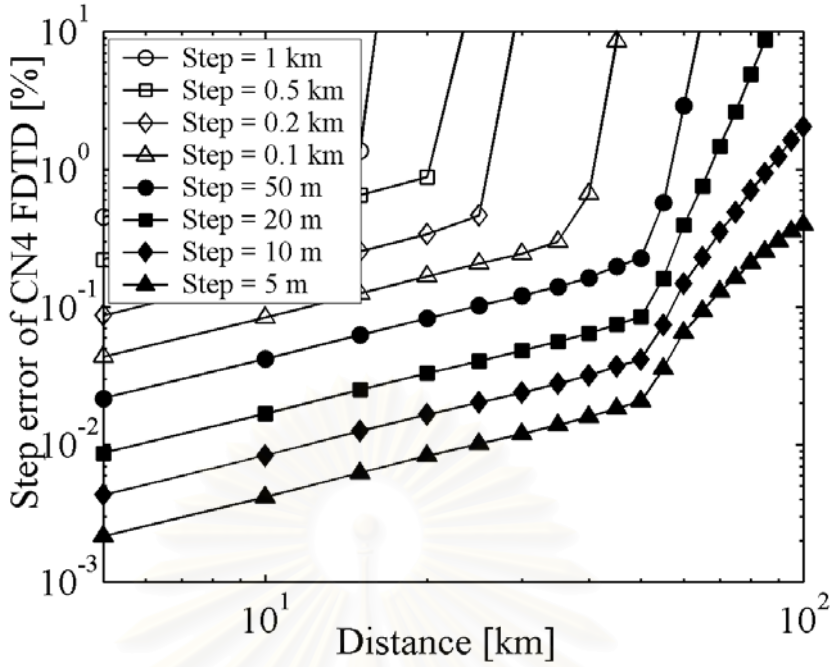

Figure 8.24: Accumulated step size error of the CN-4 FDTD in percentage unit for the single pulse propagation for 100 km as a function of distance for several step sizes.

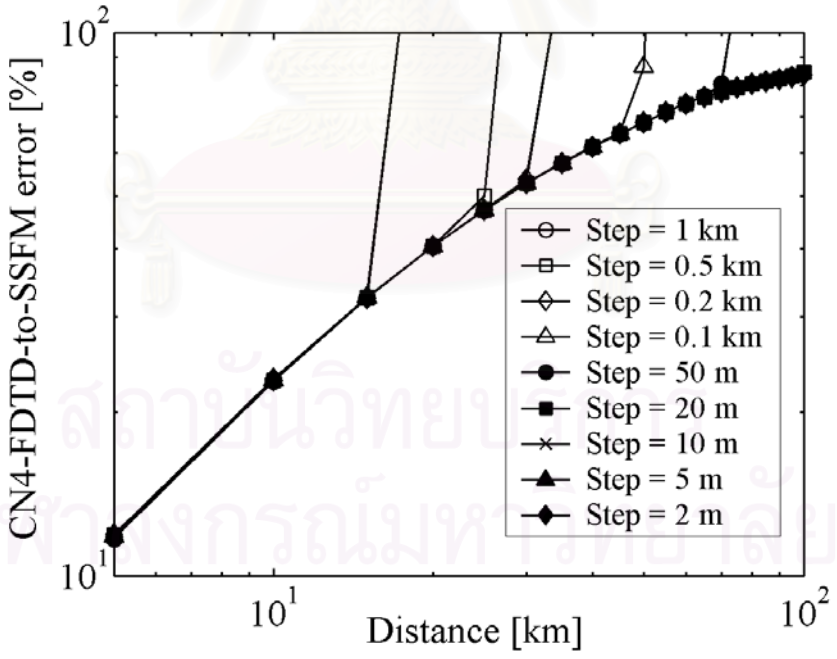

Figure 8.25: Accumulated CN-4-FDTD-to-SSFM error in percentage unit for the single pulse propagation for 100 km as a function of distance for several step sizes.

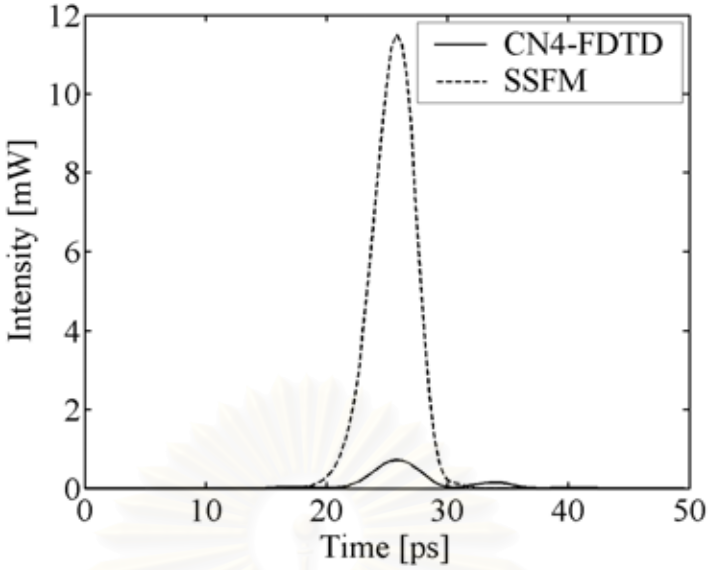

Figure 8.26: Comparison of pulse shapes at the output end of 100-km fiber calculated by the CN-4 FDTD and the SSFM.

8.4.5 CN-5 FDTD

The concept of the CN-5 FDTD algorithm is shown in Fig. 8.27. In the first step of calculation, A_{real}^{2} is computed by using A_{real}^{1} and A_{imag}^{1} instead of A_{real}^{2} and A_{imag}^{2} in the second and the third term of the right hand side of Eq. (8-32). Then, A_{imag}^{2} is estimated by using A_{real}^{2}, A_{real}^{1}, and A_{imag}^{1} in the second and the third term of the right hand side of Eq. (8-33). For next step, A_{real}^{2} and A_{imag}^{2} are used in the second and the third term of the right hand side of Eq. (8-33) to obtain A_{imag}^{3}. Then A_{imag}^{3}, A_{real}^{2} and A_{imag}^{2} is used to calculate A_{real}^{3} from Eq. (8-32). Similarly for each next step, A_{real}^{k+1} and A_{imag}^{k+1} are alternatively obtained until the last step that we reach A_{real}^{n} and A_{imag}^{n}.

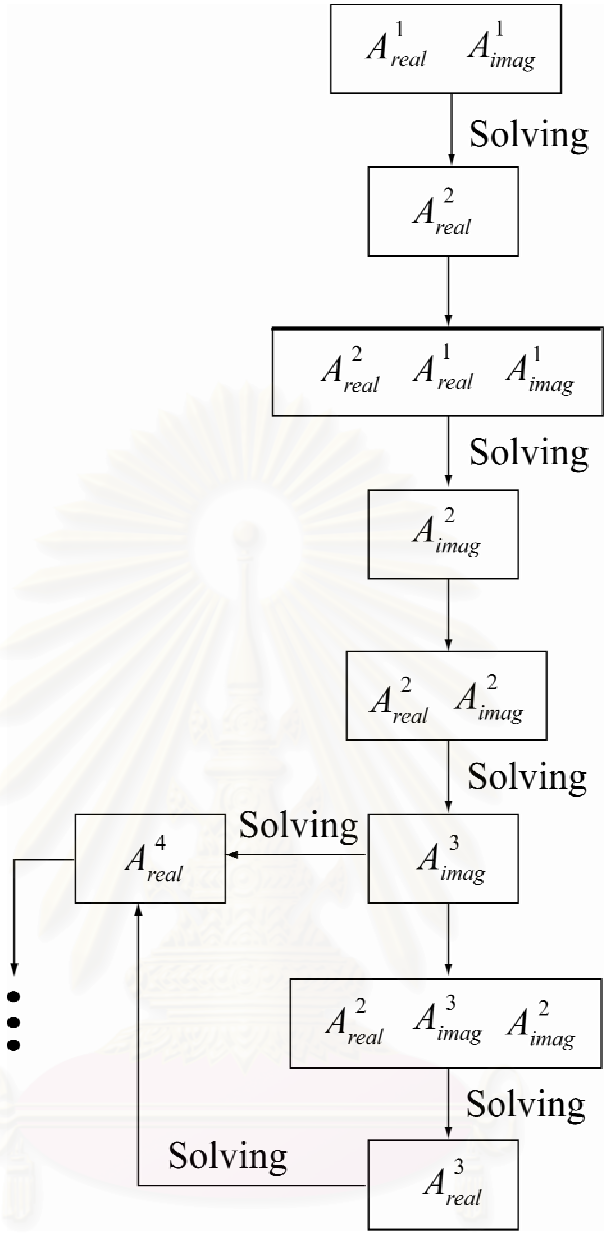

Figure 8.27: CN-5 FDTD algorithm.

Figure 8.28 shows the accumulated step size error of the CN-5 FDTD in percentage unit for the single pulse propagation in two spans, as a function of distance for several step sizes. Although for relatively large step size, the error increases very rapidly, the use of relatively small step size (< 10 m) brings the error to be lower than other FDTD algorithm. Figure 8.29 shows the accumulated CN-5-FDTD-to-SSFM error in percentage unit for the single pulse propagation in two spans as a function of distance for several step sizes. The error is almost the same at the error causes by using other FDTD algorithm except the CN-1 and CN-4 FDTD.

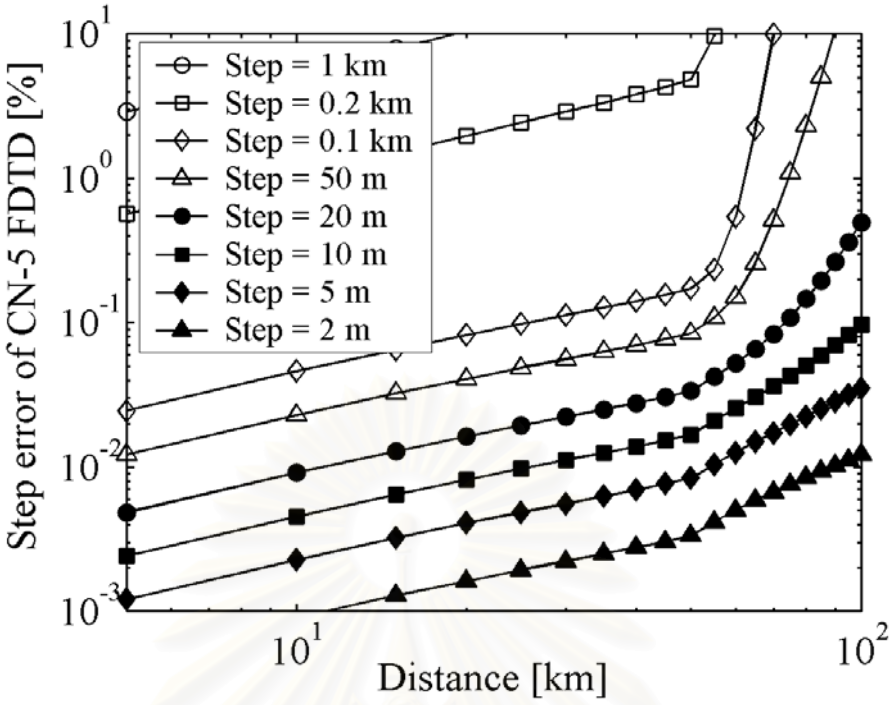

Figure 8.28: Accumulated step size error of the CN-5 FDTD in percentage unit for the single pulse propagation for 100 km as a function of distance for several step sizes.

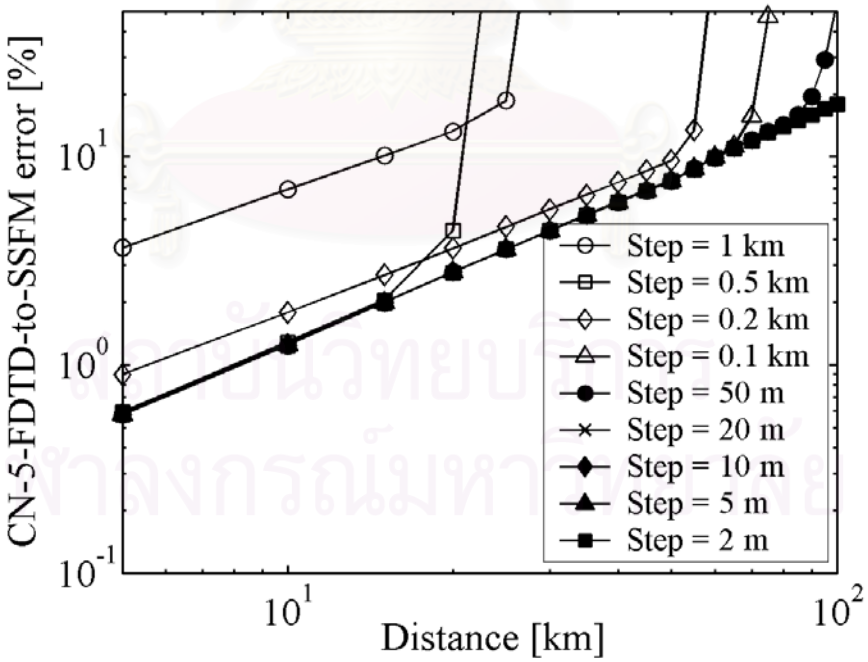

Figure 8.29: Accumulated CN-5-FDTD-to-SSFM error in percentage unit for the single pulse propagation for 100 km as a function of distance for several step sizes.

8.5 Comparison among Proposed FDTD Algorithms

Figure 8.30 shows the comparison between proposed algorithms in term of the step error as a function of transmission distance by using the calculation step size 10 m. For only the explicit FDTD, the step error increases almost linearly with the transmission distance. At a distance shorter than 50 km, all the non-explicit FDTDs give the errors which are more than 10-time lower than the explicit FDTD. However, when the distance becomes longer than 50 km, all the non-explicit FDTDs result the errors which are rapidly increases with the distance and become closer to the error caused by the explicit FDTD for case of the CN-2 DTD at 100 km or even larger than the explicit FDTD for the case of the CN-4 FDTD at 100 km. For a distance shorter than 50 km, the CN-1, CN-3, and CN-5 yield sufficiently small error while, for a distance longer than 50 km, the implicit-1 and implicit-2 FDTD give the errors smaller than those from all of the CN FDTD.

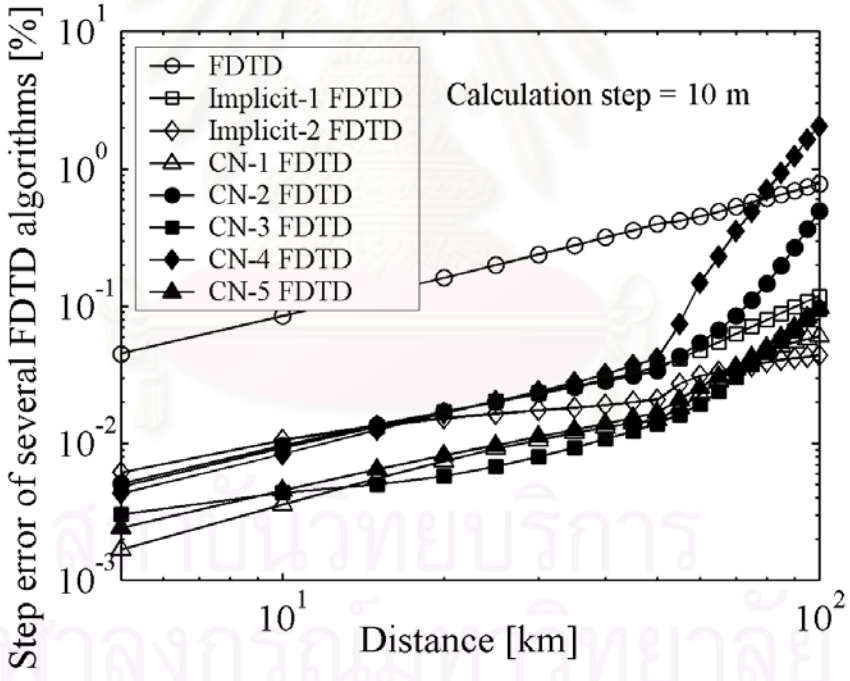

Figure 8.30: Comparison between proposed algorithms in term of the step error as a function of transmission distance by using the calculation step size 10 m.

Figure 8.31 shows the comparison of the differences from the SSFM caused by the proposed algorithms as a function of transmission distance by using the calculation step size 10 m. The CN-1 and CN-2 gives very large differences from the

result from the SSFM. The differences become larger than 100 % for a distance shorter than 100 km for these two algorithms. For other algorithms, almost the same differences from the SSFM are obtained. It should be noted that the explicit FDTD results slightly larger error than those obtained from other algorithms except the CN-1 and CN-4 FDTD for a distance larger than 60 km.

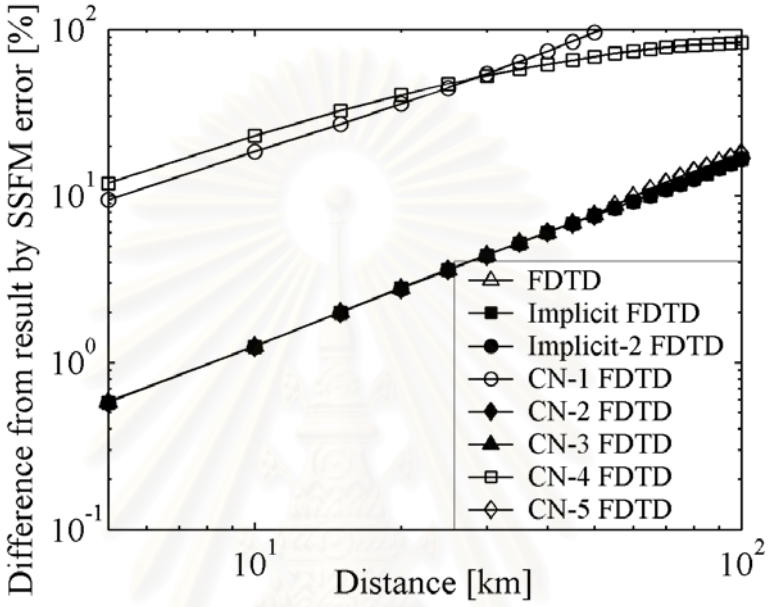

Figure 8.31: Comparison of the differences from the SSFM caused by the proposed algorithms as a function of transmission distance by using the calculation step size 10 m.

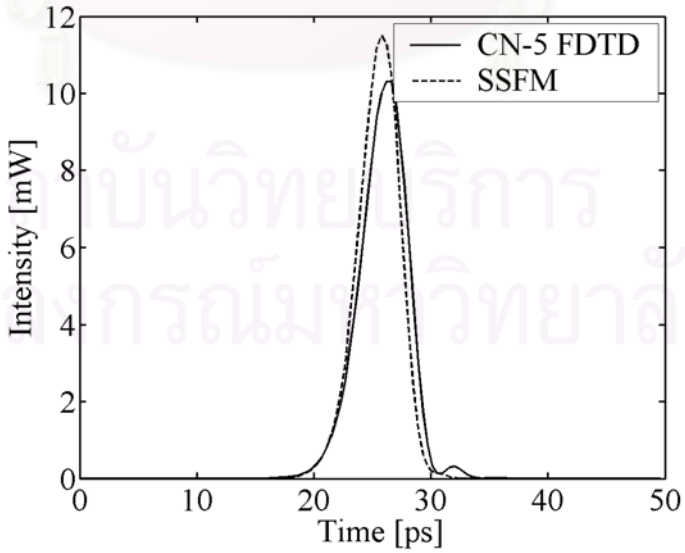

Figure 8.32: Pulse shapes at the output end of 100-km fiber calculated by the CN-5 FDTD and the SSFM.

As a representative of the result of calculation from FDTD method, Fig. 8.32 shows the pulse shape at the output end of 100-km fiber calculated by the CN-5 FDTD compared with the result from the SSFM. Although the difference between these two pulse shapes is about 18 %, the result from the CN-5 FDTD looks sufficiently similar to the result from SSFM. Thus, we can almost get the information about the pulse after propagation though we choice the FDTD for computation. For the result from the CN-5 FDTD, the effect of the dispersion slope on pulse propagation is obviously seen from the small pulse generated at the tail of the pulse. On the other hand, we cannot observe the small pulse when the SSFM is used.

Table 8.1 shows the comparison among the normalized computation times consumed by the proposed FDTDs at arbitrary distance with the same step size. The normalized time is obtained as the ratio between the computation time used by the FDTD algorithm and the computation time used by the SSFM. Except the explicit FDTD, the proposed FDTD algorithms use much longer computation time than the SSFM. Although, the explicit FDTD uses shorter computation time than the SSFM when the same step size is used, the explicit FDTD causes almost 10^8 –time larger than the SSFM as shown in Fig. 8.4. The CN-4 FDTD uses longer computation time than other algorithms because, in order to obtain A_{real}^{k+1} and A_{imag}^{k+1} from A_{real}^{k} and A_{imag}^{k}, three steps of calculation are needed.

Table 8.1: Comparison among the normalized computation times used by the proposed FDTD algorithms.

Algorithms	SSFM	Exp	Imp-1	Imp-2	CN-1	CN-2	CN-3	CN-4	CN-5
Normalized computation times	1	0.2	177.8	188.9	188.9	188.9	188.9	277.8	188.9

8.6 Conclusion

In this chapter, the use of FDTD method for solving the NLSE in order to simulate pulse propagation in relatively long optical fiber has been studied. For the simplest explicit FDTD, we have defined the normalized spatial step size which should be determined much shorter than unity in order to attain the numerical stability. In comparison with SSFM, the SSFM is obviously superior to the explicit FDTD method

in both error and computation time. Taking into account the difference between the result obtained from the explicit FDTD and the SSFM or the FDTD-to-SSFM error, the numerical results of 5-ps FWHM single optical pulse propagation in dispersion compensation fiber span using FDTD method has shown a possibility of the calculation over several ten kilometers before this error approaches 20 %.

Next, two algorithms (implicit FDTD, and Crank-Nicholson) for reducing the error due to the choice of calculation step size in the explicit FDTD method are employed and compared. We have modified these algorithms to be the implicit-1, implicit-2, CN-1, CN-2, CN-3, CN-4, and CN-5 FDTD in order to make them suitable for solving the NLSE which is separated into two coupled equations for the real and imaginary part of the optical signal. For the explicit FDTD, the step size error increases linearly with the transmission distance, while for the implicit and CN FDTD, the step size error also increases linearly with the transmission but rapidly arises at a shorter distance when larger step size is used. However, both implicit and CN FDTD give significantly smaller step size error than the explicit FDTD at the same step size. For the comparison of the computation time when the same step size is used, the explicit FDTD consumes the smallest computation time than other methods including the SSFM because of its simplicity in algorithm.

It has been widely recognized that the SSFM is the method that gives the sufficient accuracy for the calculation result of pulse propagation in long nonlinear optical fiber, since the CN-1 and CN-4 FDTD yield the results that differ from the result obtained from the SSFM more than 100 % for the propagation of the single pulse over 100 km, we can mention that the algorithms such as the CN-1 and CN-4 FDTD that we have proposed should be avoided. For other algorithms, the differences in the results compared to the SSFM are almost the same at about 18 % for 100-km propagation. This indicates that if we consider the FDTD-to-SSFM error is the most serious limit of the FDTD method, the simulation using the FDTD method can only be applied for a fiber length of several ten kilometers. Nevertheless, it is a matter of exactness which those who compute required for the solution. Also, if possible, it is still necessary to compare the results from both FDTD method and SSFM with the experiment result in order to justify which gives more accurate solution.

According to all results shown above, although the FDTD method was shown to be difficult to be utilized to simulate pulse propagation in very long optical fiber

transmission system, the FDTD method can be employed for studying signal propagation in short distance systems, fiber devices, fiber amplifiers, and also studying other nonlinear effects in optical fiber by additionally including interesting terms to the NLSE. The significant advantage of the FDTD method to the SSFM is that the FDTD method is much easy to implement than the SSFM. Therefore the calculation results can be immediately seen without wasting too much time in programming before starting to simulate.

The FDTD method is also capable to be applied to the case of multi-bit signal or even WDM signal transmission. This can be realized by only reducing the time sampling resolution and the corresponding spatial step size since such multi-bit signal and WDM signal are represented by larger bandwidth than the bandwidth of single pulse.

CHAPTER 9
DISCUSSION:
GETTING CLOSER TO THE REAL WORLD

In this dissertation, we proposed the practical schemes for improving the transmission performance of the OPC systems. The numerical method is used for proving the effectiveness of our proposed schemes. We should state that, by our numerical results, we assure the performance improvement of the systems using our proposed schemes, but we do not aim to assure the achievable data rates shown in this dissertation. In fact, we have modeled the systems as much practical as possible. Moreover, the major effects that cause significant signal distortions are all considered. Thus, we believe that, in the real world, the performance of the system may differ from the calculated results not too much.

In all calculations in this dissertation, some minor factors, which can also cause the signal distortions, have been neglected. This is because such factors do not play dominant roles in limiting system performance comparing with the problems induced from the TOD and SI effect. However, in order to fulfill the completeness of this dissertation, in this section, we note about such factors and how they affect an OPC system.

The polarization mode dispersion (PMD) has been recognized as a significant problem limiting the transmission of such ultra-high bit-rate data. In this thesis, we do not take PMD into account in the calculations. For the higher-order-dispersion-managed OPC systems using the combination of SMF and RDF, which is proposed in chapter 6, it has been shown that, without compensation, PMD of the dispersion-managed transmission fiber using SMF and RDF is as small as 0.03 ps/$\sqrt{\text{km}}$ [61]. Thus, by incorporating with PMD compensation, the performance of the higher-order-dispersion-managed OPC systems may not be degraded too much. In chapter 7, we have proposed the use of DRA in OPC systems. In this case, we assume the use of DSF for signal transmission. The DSF, in fact, exhibits larger PMD than the combination of SMF and RDF. For the design of the power distribution in a link of DRA, we have considered the PMD by including the PMD factor of 2 in the DRA equations. Therefore, the power distribution obtained by the DRA in the real world

may only slightly be affected by the PMD. However, for the signal transmission in DSF with data rate larger than 100 Gbit/s, the PMD compensation may be necessary.

In all calculations shown above, for simplicity, the optical phase conjugator is assumed to be ideal because we aim to focus on the effectiveness of our proposed methods for suppressing the problems induced from the TOD and the SI. Practically, if we use the optical nonlinearity for producing the conjugated replica of the signal, the SNR of the signal will unavoidably decreases due to the poor conversion efficiency. This will cause poorer BER than the results we have shown in this thesis.

Furthermore, in our calculations, we neglect the spatial fluctuation of local fiber SOD. This effect can also cause significant signal distortion in OPC systems. For the systems where the SOD fluctuation period is shorter than the nonlinear length: L_{nl}, the SOD fluctuation has a little influence on signal transmission because, the SOD fluctuation can be averaged out in the nonlinear scale. Then, the signal almost feels the average SOD rather than the SOD fluctuation while propagating in such systems. On the other hand, the SOD variation whose period is comparable or longer than L_{nl} will cause significant signal distortion. For the case of a higher-order-dispersion-managed OPC system using the SMF and RDF, since the nonlinear coefficient of RDF is larger than that of SMF, the SOD fluctuation on the RDF will result more severe degradation than that occurs in the SMF and DSF.

The signal distortion caused by the SOD fluctuation can be reduced by using the transmission fibers with a relatively large SOD. Since the combination of SMF and RDF yields large local fiber SOD, moreover, in all calculations, we set the average SOD value: D_{av} at -1 ps/km/nm for both cases of OPC systems using SMF and RDF and OPC systems using DSF, we believe that the influence of the SOD fluctuation is sufficiently suppressed in our proposed systems.

According to the results obtained from chapter 6, relatively high input signal powers (> 10 mW) are required for achieving BER < 10^{-9}. The stimulated Brillouin scattering (SBS) effect [4] is also one of the main factors that place the upper limit for the usable input signal power. For the problem induced from the SBS, we have estimated the SBS threshold powers [128], [129] of the RDF for several data rates used in our simulations because the RDF is more nonlinear than the SMF. The SBS thresholds for the case of 100-Gbit/s, 160-Gbit/s, and 200-Gbit/s data are approximately 51 mW, 81 mW, and 102 mW, respectively. Therefore, we can

conclude that the SBS can be neglected for all values of the signal input powers used in our calculations.

The fourth-order dispersion, which exhibits a value around 4×10^{-4} ps/km/nm^3 [62] for DSF, has been shown to affect the propagation of such a femto-second pulse (pulse width < 1 ps). For non-OPC systems, using the fourth-order dispersion value 4×10^{-4} ps/km/nm^3 for the pulse width of 2.5 ps (data rate 200 Gbit/s) and the transmission distance of 10,000 km, the maximum delay between signal spectral components can be estimated to be approximately 131 ps. Thus, the fourth-order dispersion will also cause the signal distortion for such a 200-Gbit/s data transmission over 10,000 km. However, the NLSE, which is numerically solved in this dissertation, includes the dispersive effects up to only the third-order. This is because the OPC can perfectly compensate for the dispersion whose order is an even number (2^{nd}, 4^{th}, 6^{th},…) [4]. Therefore, we can neglect the fourth-order dispersion in both higher-order dispersion-managed OPC systems and OPC systems using DRA. Especially for the higher-order dispersion-managed OPC systems, practically the TOD almost vanishes by the combination of the SMF and RDF. Therefore, the dispersion whose order is higher than the TOD can be completely neglected.

The optical phase conjugator should be exactly placed at the system midpoint or nearest to the system midpoint in order to utilize the full performance of the OPC scheme. In case that the optical phase conjugator has to be installed at the point deviated from the midpoint, it is necessary to compensate the amount of the unbalance SOD accumulation between the accumulated SOD in the first half and the second half because the lengths of the first half and the second half become no longer equal. With respect to the position of the optical phase conjugator, the additional signal distortion will be induced from the interaction between the fiber SOD and the Kerr effect on the unbalance section. Therefore, the larger the position of the optical phase conjugator deviates from the system midpoint, the more serious such signal distortion degrades the system performance. The deviation of the optical phase conjugator from the exact midpoint of the system should be much smaller than the nonlinear scale of the system in order to reduce the nonlinear waveform distortion occurring in the unbalance section.

For practical installation, the optical phase conjugator should be placed at the same point of the optical amplifiers. Therefore, the optical phase conjugator will be

moved out of the midpoint with the step of one amplifier span. For the higher-order dispersion-managed OPC systems whose the dispersion management period is larger than the amplifier span, we have to move the optical phase conjugator with a length step of one dispersion management period in order to keep the symmetrical distribution of the dispersion management profile with respect to the optical phase conjugator. This will cause more severe signal distortion for larger dispersion management period. According to the installed dispersion management profile shown in Fig. 6.4(b), for the higher-order dispersion-managed OPC systems whose the dispersion management period is equal to, or smaller than the amplifier span, the optical phase conjugator should be moved to the second half in order to shorten the transmission where the RDFs, whose nonlinear coefficient is larger than the SMFs, are located near the output of amplifiers. Then, the signal distortion due to the interaction between the Kerr effect and the SOD on the unbalance transmission section will be reduced.

Figure 9.1 shows the example of OPC system configuration where the optical phase conjugator is moved to the second half. The transmission length of the first half is L_1, while that of the second half is L_2, resulting in the unbalance section of $L_1 - L_2$ located at the input end of fiber. The operating dispersion is $-D$, therefore, at the end of the system, the SOD with amount of $-D(L_1 - L_2)$ is necessary to add in order to balance the accumulated SOD in the first half and the second half.

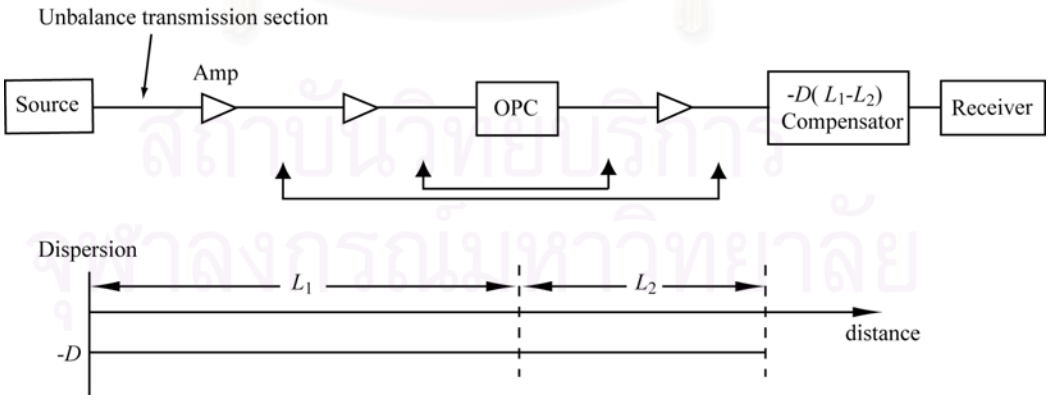

Figure 9.1: Example of OPC system configuration where the optical phase conjugator is moved to the second half.

It has been shown that the RDF can be manufactured to have almost perfect compensation of the TOD when combining with the SMF. The average remained TOD becomes as small as 3.3×10^{-5} ps/km/nm^2 [62]. Using this value, the TOD length for the data rate of 200 Gbit/s is as long as 60,000 km. Since the longest transmission length in this dissertation is 10,000 km, we can neglect the slight mismatch between the dispersion characteristic of SMF and RDF. Therefore, in this dissertation, we have assumed that the dispersion characteristic of RDF is a complete reverse of SMF. The effect of the imperfect match of the cascaded SMFs and RDFs on signal transmission, however, can be considered as the random variation of the TOD. For OPC systems, since we have proved that the accumulation characteristic of the TOD is almost linear in chapter 4 and in [49], this problem can be completely overcome by only adjusting the amount of TOD that will be compensated at the TOD compensator.

It is common and practical to construct a system with equal amplifier spacing. This is because the accumulated amount of the ASE noise at the receiver becomes minimum for only the system using the equal amplifier spacing. Moreover, it will be easy and convenient to design the gain of an optical amplifier for equal amplifier spacing. However, randomly slight deviation of the amplifier position may possibly occur in the real world. Comparing to a system using equal amplifier spacing, since the amount of the accumulated noise in a system using unequal amplifier spacing is larger, the SNR at the receiver will be poorer than the system using equal amplifier spacing. Moreover, as shown in Fig. 9.2 for the occurrence of the SI effect, the signal power variation in a chain of the randomly unequal amplifier spacing produces the virtual grating in transmission fiber. This virtual grating has a form of randomly nonlinear-chirped grating [130] through the Kerr effect. The nonlinear resonance, which is assisted by this randomly nonlinear-chirped grating, will arise at many signal sideband spectral components around the carrier frequency. Although, the gain of this type of SI is not so large as the SI gain for the case of the equal amplifier spacing, the gain of the SI from the unequal amplifier spacing exhibits very broad bandwidth. Therefore, the severe spectral broadening will be resulted from the unequal amplifier spacing.

In OPC systems, although either the strong higher-order dispersion management or the DRA is very effective for suppressing the SI, however, the system

performance cannot be expected as high as the OPC systems using the equal amplifier spacing.

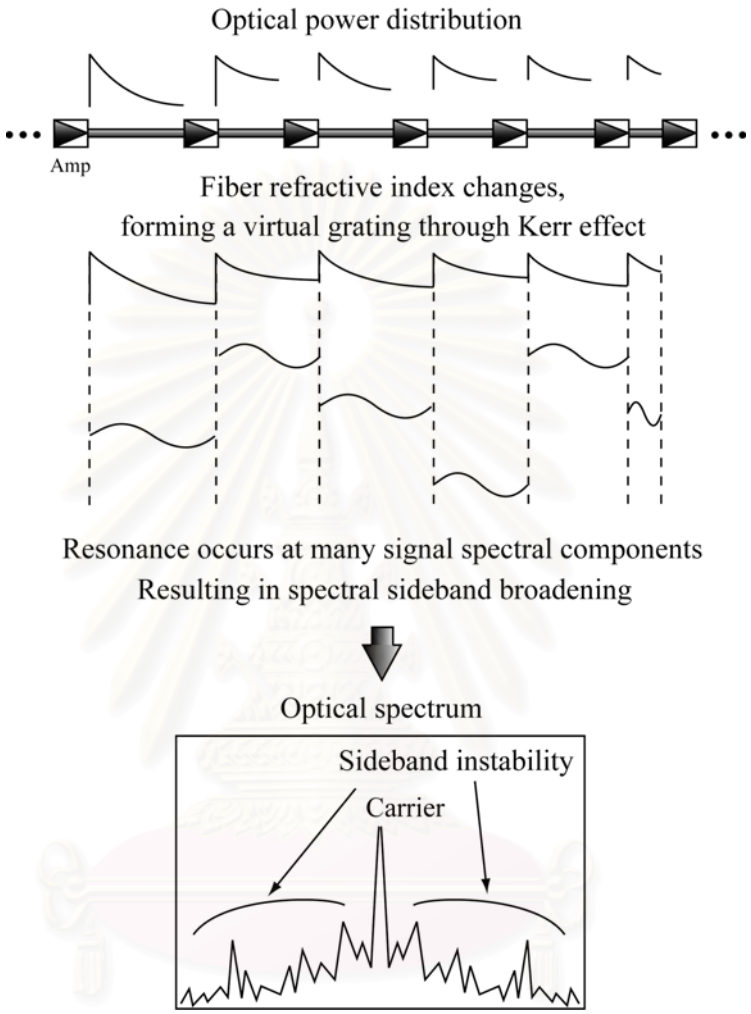

Figure 9.2: The occurrence of SI for a system using nonuniform amplifier spacing.

The spectral linewidth of the optical source is not taken into account in this dissertation for the sake of simplicity. The source spectral linewidth is directly responsible for the dispersion effect and the amount of noise entering the signal bandwidth. For the data rates used in this dissertation, in combination with the TOD compensation, the signal will restore its spectral width to its initial linewidth after transmitting in our proposed OPC systems because the all order of dispersion is almost perfectly compensated. Therefore, only the degradation of the SNR at the

receiver is still left to consider when the linewidth of the optical source is taken into account.

The optical loss due to signal reflections at connection parts on a system is also neglected in this dissertation. To overcome this additional loss, it is necessary to increase the gain of the optical amplifiers. This results in larger amount of the ASE noise generated through high optical gain. Therefore, this problem also causes the degradation of the SNR at the receiver.

CHAPTER 10
CONCLUSION AND SUGGESTIONS FOR FURTHER IMPROVEMENT

10.1 Summary of the Dissertation

In this dissertation, performance improvement of ultra-long-haul high-bit-rate optical transmission system using midway OPC was studied. The serious limitations of OPC system are mainly resulted from TOD and SI effect. We have shown that the accumulation characteristic of the TOD in OPC transmission systems is almost linear as long as the SOD length is much shorter than the nonlinear length. This fact gave us a possibility to install only one of the linear TOD compensator at any point in the system for perfect TOD compensation. By assuming the ideal TOD compensator, the computer simulation result has shown the possibility of a data transmission over 10,000 km with data rate of 100 Gbit/s based on TOD compensated OPC systems.

We have presented the derivation of the analytical expression of the sideband instability (SI) induced from periodic signal power variation and periodic dispersion management when two different fibers are connected together to form the dispersion compensation link. Three possible dispersion management systems were considered: (a) system where dispersion management period is larger than amplifier spacing, (b) system where the two lengths are equal, and (c) system where amplifier spacing is larger than dispersion management period.

We found that SI frequency depends on the larger period between the amplifier spacing and the dispersion management period. The larger the variation period becomes, the SI frequency will arise closer to carrier frequency. Moreover, the gain of SI appears to be reduced with the increase of local fiber second-order dispersion (SOD). This is because the increase in the local SOD virtually shifts the order of SI to higher order resulting in the difficulty of phase-match process. The computer simulations were made and their results were in good agreement with the derived theory.

In WDM systems that use relatively narrow channel spacing, we demonstrated that even the dispersion map is properly designed to achieve low SI gain, SI causes signal distortion to specific channels that fall just on the low order SI frequency, especially for the first order. In addition to WDM system design rules, the channel

allocation must avoid the SI position in such a way that none of the channels should be lied at. The computer simulations have confirmed that a WDM system, whose channel location is re-arranged to avoid SI, give a significant improvement of the transmission performance.

Next we proposed for the first time the simultaneous suppression of the two main problems, TOD and SI, in OPC transmission systems by employing higher-order dispersion management fiber link consisting of SMF and RDF. In order to implement the combination of SMF and RDF on OPC systems, we demonstrated that it is necessary to use symmetric dispersion profile with respect to mid-point of the system to reduce SI gain together with the accumulation of the interplay between SPM and each fiber local dispersion. According to the numerical computation results, a 100-Gbit/s data transmission in OPC system that employs the SMF+RDF-dispersion-managed link without optimizing the dispersion map has achieved the transmission length at BER = 10^{-9} over 2,000 km longer than the system where SI is not suppressed, although the nonlinear length of the system is set comparable to the amplifier spacing.

Next, we have introduced the system design approaches to achieve the maximum system performance considering the determination of dispersion management period l_d and the corresponding signal input power. Such maximum performance can be achieved by using optimum input power, which will be found at relatively low value for the case of $l_d > l_f$ and at relatively high value for the case of $l_d < l_f$. The computer simulation results have demonstrated that the 10,000-km transmissions of 100-Gbit/s data, 160-Gbit/s data and even the data whose data rate as high as 200 Gbit/s become possible by the dispersion-managed OPC system whose dispersion map is properly designed.

Figure 10.1 shows the recent significant progresses in single channel transmission data rate and distance. From figure 10.1, our result has recorded the highest bit-rate-distance product that has been proposed by computer simulation up to now. Also shown in the same figure, L. J. Richardson, et. al. have numerically demonstrated the transmission of a 320-Gbit/s data over the distance of 6,000 km [64]. The bit-rate-distance product of their work (1,920 Tbit$\cdot$km/s) is only 4 % smaller than our work (2,000 Tbit$\cdot$km/s). However, their proposed scheme is very impractical comparing with our proposed scheme. This is because, in their work, the

320-Gbit/s soliton signal is propagated through a chain of very-short period higher-order dispersion management. In one link of 50-km amplifier spacing, the period of such higher-order dispersion management is assumed to be as much as 64 periods. Furthermore, the absolute fiber local SOD and the average SOD have to be strictly set at about 1.2 ps^2/km and -0.001 ps^2/km, respectively. This is very difficult to manufacture such higher-order dispersion-managed fibers. Moreover, since their scheme requires relatively small values of the fiber local SOD and the average SOD, the random dispersion fluctuation will easily cause the deviation of such fiber local SOD and average SOD from the designed values. Therefore, in the real world, the soliton may be destroyed after only propagating for several amplifier spans.

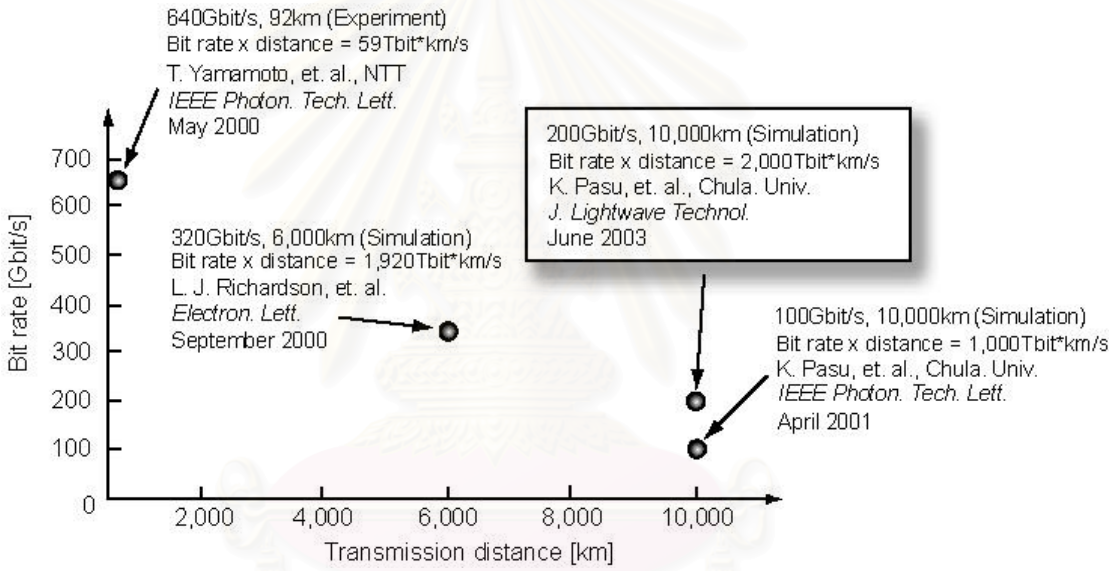

Figure 10.1: Recent significant progresses in single channel transmission data rate and distance. Our result has recorded the highest bit-rate-distance product that has been proposed by computer simulation up to now.

The performance improvement of the OPC transmission system by employing distributed Raman amplification (DRA) was also studied. We produced the reverse periodic signal power variation on the second-half of the systems in order to construct entirely symmetrical power distribution with respect to the system midpoint by using appropriate pump powers of the bi-directional pumping DRA. As a result, all signal waveform distortions caused by the Kerr effect are compensated through the midway OPC. Incorporated with the TOD compensator, our simulation results have shown

possibilities of the 100-Gbit/s data transmission over a 10,000 km with the 50-km amplifier span and the 200-Gbit/s data transmission over 10,000 km with the 40-km amplifier span.

Next, to develop the simple numerical algorithm for calculating signal transmission in optical fibers, we studied the use of finite-difference (FDTD) method for solving the nonlinear Schrodinger equation (NLSE) in order to simulate pulse propagation in relatively long optical fiber. The algorithms studied in this chapter are the explicit FDTD, the implicit FDTD, and the FDTD employing the Crank-Nicoleson (CN) scheme. We have modified these algorithms to be the implicit-1, implicit-2, CN-1, CN-2, CN-3, CN-4, and CN-5 FDTD in order to make them suitable for solving the NLSE. The model of a 5-ps full-width-half-maximum (FWHM) single optical pulse propagation in dispersion compensated fiber span was used for simulation. The numerical results of using these proposed FDTD algorithms are compared with the results obtained by using the split-step Fourier method (SSFM). Taking into account the differences of result from the SSFM, our developed FDTD algorithm have shown a possibility of the calculation over several ten kilometers with acceptable accuracy. Therefore, we should mention that the FDTD method can be employed for studying signal propagation in short distance systems, fiber devices, fiber amplifiers, and also studying other nonlinear effects in optical fiber by additionally including interesting terms to the NLSE. The significant advantage of the FDTD method to the SSFM is that the FDTD method is much easier to implement than the SSFM. Therefore the calculation results can be immediately seen without wasting too much time in programming before starting to simulate.

10.2 Suggestions for Further Work

We give the suggestions for further work as follows.

1. **The optimum operation SOD for OPC systems:** To extend the performance of the OPC systems more than what we have derived, the easiest way may be the optimization of the average SOD value D_{av}. The increase in D_{av} can reduce the effect of fiber nonlinearity either the case for using the combination of SMF and RDF or the case of using the DRA, at the same time, moving the SI which is not completely suppressed to occur more inner signal bandwidth. The optimum D_{av} will be found under the balance of these two effects.

2. **The optimum symmetrical power distribution by DRA:** Since the power distribution in a link of transmission fiber with DRA can be designed by using appropriate input pump powers, there should exist the symmetrical power distribution constructed by the DRA that gives the least difference from the target power distribution though high input signal power or large DRA span is required. This optimum symmetrical power distribution will yield better performance on both the increasing transmission data rate and the extension of the DRA span because the Kerr effect will be almost completely compensated through the OPC. For examples in Fig. 10.2, we propose two configurations, which employ the DRA for obtaining symmetrical power distribution with respect to system midpoint. In Fig. 10.2 (a) and (b), a flat power distribution and a uniform power distribution may also be constructed by using the bi-directional pumping schemes.
3. **Wavelength division multiplexing:** Since all the systems considered in this work are single channel transmission systems, for future works, we suggest the study on the use of higher-order dispersion-managed OPC scheme on long-haul wavelength division multiplexing (WDM) transmission systems. In this case, design strategies for signal channel allocation that avoids the position of SI should be considered.
4. **DRA with ultra-broadband, flat-gain, and symmetrical power distribution by multi-wavelength pumping scheme:** To support the data transmission using OPC with DRA in WDM scheme, the DRA that exhibits ultra-broadband, flat-gain, symmetrical-power-distribution should be used. This can be realized by using the multi-wavelength pumping scheme with carefully designing the wavelength and the power of each pump.

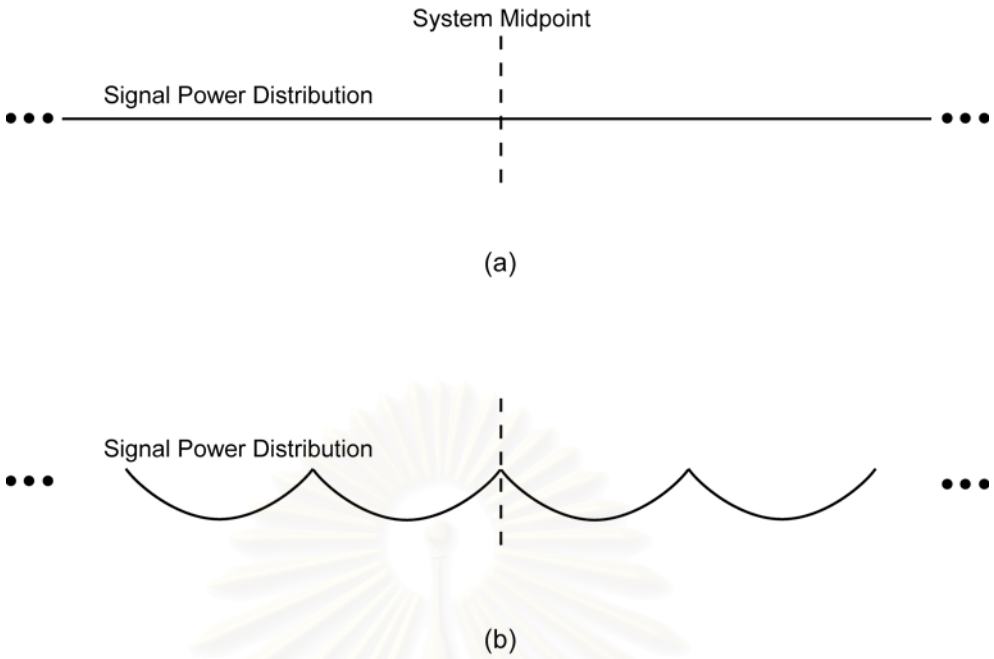

Figure 10.2: Two symmetrical power distributions, with respect to system midpoint, which can be constructed by employing the DRA, (a) flat power distribution and (b) uniform power distribution.

REFERENCES

[1] T. Naito, N, Shimojoh, T. Tanaka, H. Nakamoto, M. Doi, T. Ueki, and M. Suyama. 1 Terabit/s WDM transmission over 10,000km. Proc. European Conf. on Opt. Commun. (ECOC'99), PD2-1, Nice France, Sept. 26-30, 1999: pp. 24-25.

[2] S. Walker, L. C. Blank, L. Bicker, and R. Garnham. Transmission and signal precessing techniques for gigabit lightwave systems. J. Lightwave Technol., vol. LT-4, 1986: pp. 759-766.

[3] A. F. Elrefaie, R. E. Wagner, D. A. Atlas, and D. G. Daut. Chromatic dispersion limitations in coherent lightwave transmission systems. J. Lightwave Technol., vol. 6, 1988: pp. 704-709.

[4] G. P. Agrawal. Nonlinear Fiber Optics. 3rd Ed.: New York, Academic Press, 2001.

[5] G. P. Agrawal. Fiber-optic communication systems. 2nd Ed.: New York, Academic Press, 1997.

[6] R. Chraplyvy. Limitations on lightwave communications imposed optical-fiber nonlinearities. J. Lightwave Technol., vol. 8, 1990: pp. 1548-1557.

[7] D. Marcuse, A. R. Chraplyvy, and R. W. Tkach. Effect of fiber nonlinearity on long-distance transmission. J. Lightwave Technol., vol. 9, 1991.

[8] J. P. Hamaide, Ph. Emplit, J. M. Gabriagues. Limitations in long haul IM/DD optical fibre systems caused by chromatic dispersion and nonlinear Kerr effect. Electron. Lett., vol. 26, 1990: pp. 1451-1452.

[9] K. Kikuchi. Enhancement of optical-amplifier noise by nonlinear refractive index and group-velocity dispersion of optical fibers. IEEE Photon. Technol. Lett., vol. 5, 1993: pp. 221-223.

[10] C. Lorattanasane and K. Kikuchi. Parametric instability of optical amplifier noise in long-distance optical transmission systems. IEEE J. Quantum Electron., vol. 33, 1997: pp. 1068-1074.

[11] S. Bigo, O. Leclerc, E. Desurvire. All-optical fiber signal processing and regeneration for soliton communications. IEEE J. on Selected Topics in Quantum Electron. vol. 3, no. 5, 1997: pp. 1208-1223.

[12] C. R. Giles and E. Desurvire. Propagation of signal and noise in concatenated Erbium-doped fiber optical amplifiers. J. Lightwave Technol., vol. 9, 1991: pp. 147-154.

[13] B. J. Ainslie. A review of the fabrication and properties of Erbium-doped fibers for optical amplifiers. J. Lightwave Technol. vol. 9, 1991: pp. 220-227.

[14] C. R. Giles and E. Desurvire. Modeling Erbium-doped fiber amplifiers. J. Lightwave Technol., vol. 9, 1991: pp. 271-283.

[15] M. Potenza. Optical fiber amplifiers for telecommunication systems. IEEE Communication Magazine. August, 1996: pp. 96-102.

[16] R. S. Tucker, G. Eisenstein, and S. K. Corotky. Optical time-division multiplexing for very high bit-rate transmission. J. Lightwave Technol., vol. 6, 1988: pp. 1737-1749.

[17] G. P. Agrawal. Nonlinear pulse distortion in single-mode optical fibers at the zero-dispersion wavelength. Phys. Rev. A, vol. 33, 1986: pp. 1765-1776.

[18] D. Marcuse. Single-channel operation in very long nonlinear fibers with optical amplifiers at zero dispersion. J. Lightwave Technol., vol. 9, 1991: pp. 356-361.

[19] T. Matsuda, A. Naka and S. Saito. 10Gbit/s, 6000km NRZ and 4400km RZ signal transmission experiments at zero-dispersion wavelength. Electron. Lett., vol. 32, 1996: pp. 229-231.

[20] D. Marcuse. Bit-error rate of lightwave systems at the zero dispersion wavelength. J. Lightwave Technol., vol. 9, 1991: pp. 1330-1334.

[21] N. Kikuchi and S.Sasaki. Fiber nonlinearity in dispersion-compensated conventional fiber transmission. Electron. Lett., vol. 32, 1996: pp. 570-572.

[22] R. J. Nuyts, Y. K. Park, and P. Gallion. Dispersion equalization of a 10Gbit/s repeatered transmission system using dispersion compensating fibers. J. Lightwave Technol., vol. 15, 1997: pp. 31-41.

[23] M. Murakami, T. Matsuda, H. Maeda, and T. Imai. Long-haul WDM transmission using higher order fiber dispersion management. J. Lightwave Technol., vol. 18, no. 9, 2000: pp. 1197-1204.

[24] M. Murakami, K. Suzuki, H. Maeda, T. Takahashi, A. Naka, N. Ohkawa, and M. Aiki. High speed TDM-WDM techniques for long-haul submarine optical amplifier systems. Optic. Fiber Technol., vol. 3, no. 4, 1997: pp. 320-338.

[25] X. Wang, K. Kikuchi, and Y. Takushima. Analysis of dispersion-managed optical fiber transmission system using non-return-to-zero pulse format

and performance restriction from third-order dispersion. IEICE Trans. Electron., vol.E82-C, no.8, 1999: pp.1407-1413.

[26] K. Mukasa, R. Sugizaki, S. Hayami, and S. Ise. Dispersion-managed transmission lines with reverse-dispersion fiber. Furukawa Review, no. 19, 2000: pp. 5-9.

[27] C. Lin, H. Kogelnik, and L. G. Cohen. Optical-pulse equalization of low-dispersion transmission in single-mode fibers in the 1.3-1.7 μm spectral region. Opt. Lett., vol. 5, 1980: pp. 476-478.

[28] H. Izadpanah, C. Lin, J. L. Gimlett, A. J. Antos, D. W. Hall, and D. K. Smith. Dispersion compensation in 1310nm-optimized SMFs using optical equalizer fiber, EDFA's and 1310/1550nm WDM. Electron. Lett., vol. 28, 1992: pp. 1469-1471.

[29] H. Izadpanah, E. Goldstein, and C. Lin. Broadband multiwavelength simultaneous dispersion compensation near 1550nm through single-mode fiber optimized for 1310nm. Electron. Lett., vol. 29, 1993: pp. 364-365.

[30] A. R. Chraplyvy, A. H. Gnauck, R. W. Tkach, R. M. Derosier, C. R. Giles, B. M. Nyman, G. A. Ferguson, J. W. Sulhoff, and J. L. Zyskind. One-third terabit/s transmission through 150km of dispersion 150km of dispersion-managed fiber. IEEE Photon. Technol. Lett., vol. 7, 1995: pp. 98-100.

[31] S. Kawanishi, H. Takara, O. Kamatani, T. Morioka, and M. Saruwatari. 100Gbit/s 560km optical transmission experiment with 80km amplifier spacing employing dispersion management. Electron. Lett., vol. 32, 1996: pp. 470-471.

[32] N. Kikuchi and S.Sasaki. Fiber nonlinearity in dispersion-compensated conventional fiber transmission. Electron. Lett., vol. 32, 1996: pp. 570-572.

[33] R. J. Nuyts, Y. K. Park, and P. Gallion. Dispersion equalization of a 10Gbit/s repeatered transmission system using dispersion compensating fibers. J. Lightwave Technol., vol. 15, 1997: pp. 31-41.

[34] Stern, J. P. Heritage, R. N. Thurston, and S. Tu. Self-phase modulation and dispersion in high data rate fiber-optic transmission systems. J. Lightwave Technol., vol. 8, 1991: pp. 1009-1016.

[35] C. Kurtzke. Suppression of fiber nonlinearities by appropriate dispersion management. IEEE Photon. Technol. Lett., vol. 5, no. 10, 1993: pp. 1250–1253.

[36] A. Hasegawa and F. Tappert, " Transmission of stationary nonlinear optical pulses in dispersive dielectric fibers, " Appl. Phys. Lett., vol. 23, pp. 142-144, 1973.

[37] L. F. Mollenauer, R. H. Stolen, and J. P. Gordon. Experimental observation of picosecond pulse narrowing and soliton in optical fibers. Phys. Rev. Lett., vol. 45, 1980: pp. 1095-1098.

[38] N. J. Doran, and K. J. Blow. Solitons in optical communications. IEEE J. Quantum Electron., vol. QE-19, 1983: pp-1883-1888.

[39] M. Nakazawa, Y. Kimura, K. Suzuki. Soliton transmission at 20Gbit/s over 2000km in Tokyo metropolitan optical network. Electron. Lett., vol. 31, 1995: pp. 1478-1479.

[40] Y. Takushima, X. Wang, and K. Kikuchi. Transmission of 3ps dispersion-managed soliton pulses over 80km distance under influence of third-order dispersion. Electron. Lett., vol. 35, no. 9, 1999: pp.739-740.

[41] I. Morita, K. Tanaka, N. Edagawa, and M. Suzuki. 40Gbit/s single-channel soliton transmission over 10,200km without active inline transmission control. Proc. of 24th European Conference on Optical Communication (ECOC'98), Postdeadline paper, Madrid, Spain, Sept. 20-24, 1998: pp.49-51,

[42] A. Hasegawa and Y. Kodama. Guiding-center soliton in optical fibers. Opt. Lett., vol. 15, 1990: pp. 1443-1445.

[43] K. J. Blow and N. J. Doran. Average soliton dynamics and the operation of soliton systems with lumped amplifiers. IEEE Photon. Technol. Lett., vol. 3, 1991, pp. 369-371.

[44] L. F. Mollenauer, S. G. Evangelides, and H. A. Haus. Long-distance soliton propagation using lumped amplifiers and dispersion-shifted fiber. J. Lightwave Technol., vol. LT-9, 1991: pp. 194-197.

[45] Y. Kodama and K. Nozaki. Soliton interaction in optical fibers. Opt. Lett., vol. 12, 1987: pp. 1038-1040.

[46] J. P. Gordon and H. A. Haus. Random walk of coherently amplified solitons in optical fiber transmission. Opt. Lett., vol. 11, 1986: pp. 665-667.

[47] D. Marcuse. An alternative derivation of the Gordon-Haus effect. J. Lightwave Technol., vol. 10, 1992: pp. 273-278.

[48] C. Lorattanasane and K. Kikuchi. Design theory of long-distance optical transmission systems using midway optical phase conjugation. J. Lightwave Technol., vol. 15, 1997: pp. 948-955.

[49] P. Kaewplung, T. Angkaew, and K. Kikuchi. Feasibility of 100-Gb/s 10000-km single-channel optical transmission by midway optical phase conjugation in corporated with third-order dispersion compensation. IEEE Photon. Technol. Lett., vol. 13, no. 4, 2001: pp. 293–295.

[50] F. Matera, A. Mecozzi, M. Romagnoli and M. Settembre. Sideband instability induced by periodic power variation in long distance fiber links. Opt. Lett., 18, 1993: pp. 1499-1501.

[51] P. Kaewplung, T. Angkaew, and K. Kikuchi. Sideband instability in the presence of periodic power variation and periodic dispersion management. Proc. Opt. Fiber Comm. (OFC'2001), Anaheim, CA, Mar. 17-22, 2001: paper WDD32.

[52] P. Kaewplung, T. Angkaew, and K. Kikuchi. Complete analysis of sideband instability in chain of periodic dispersion-managed fiber link and its effect on higher-order dispersion-managed long-haul wavelength division multiplexed systems. OSA/IEEE J. Lightwave Technol., vol. 20, no. 11, 2002: pp. 1895-1907.

[53] Y. Takushima, X. Wang, and K. Kikuchi. Transmission of 3ps dispersion-managed soliton pulses over 80km distance under influence of third-order dispersion. Electron. Lett., vol.35, no.9, 1999: pp.739-740.

[54] I. Morita, K. Tanaka, N. Edagawa, and M. Suzuki. 40Gbit/s single-channel soliton transmission over 10,200km without active inline transmission control. Proc. 24th European Conference on Optical Communication (ECOC'98), Postdeadline paper, Madrid, Spain, Sept. 20-24, 1998: pp.49-51.

[55] T. Imai, T. Komukai, and M. Nakazawa. Second- and third-order dispersion compensation of picosecond pulses achieved by combining two nonlinearly chirped fibre Bragg gratings. Electron. Lett., vol. 34, no. 25, 1998: pp. 2422-2423.

[56] A. H. Gnauck, J. M. Wiesenfeld, L. D. Garrett, M. Eiselt, F. Forghieri, L. Arcangeli, B. Agogliata, V. Gusmeroli, and D. Scarano. 16x20-Gb/s, 400km WDM transmission over NZDSF using a slope-compensating fiber-grating module. IEEE Photon. Technol. Lett., vol. 12, 2000: pp. 437-439.

[57] M. Jablonski, Takushima, Y, and Kikuchi, K. The realization of all-pass filters for third-order dispersion compensation in ultrafast optical fiber transmission systems. J. Lightwave Technol., vol. 19, no. 8, 2001: pp. 1194-1205.

[58] M. Morimoto, I. Kobayashi, H. Hiramatsu, K. Mukasa, R. Sugizaki, Y. Suzuki, Y. Kamikura. Development of dispersion compensation cable using reverse dispersion fiber. Proc. of Fifth Asia-Pacific Conference on Communications, 1999 and Fourth Optoelectronics and Communications Conference (APCC/OECC '99), vol. 2, 1999: pp. 1590-1593.

[59] K. Mukasa, R. Sugizaki, S. Hayami, and S. Ise. Dispersion-managed transmission lines with reverse-dispersion fiber. Furukawa Review, no. 19, 2000: pp. 5-9.

[60] M. Kazunori, T. Yagi. Dispersion flat and low nonlinear optical link with new type of reverse dispersion fiber (RDF-60). Proc. Opt. Fiber Comm. (OFC'2001), Anaheim, CA, Mar. 17-22, 2001: paper TuH7.

[61]T. Yamamoto, E. Yoshida, K. R. Tamura, K. Yonenaga, and M. Nakazawa. 640-Gbit/s optical TDM transmission over 92 km through a dispersion-managed fiber consisting of single-mode fiber and " reverse dispersion fiber ". IEEE Photon. Technol. Lett., vol. 12, 2000: pp. 353–355.

[62] M. Nakazawa, T. Yamamoto, and K. R. Tamura. 1.28Tbit/s-70km OTDM transmission using third- and Fourth-order simultaneous dispersion compensation with a phase modulator. Electron. Lett., vol. 36, no. 24, 2000: pp. 2027-2029.

[63] B. Mikkelsen, G. Raybon, R. J. Essiambre, A. J. Stentz, T. N. Nielsen, D. W. Peckham, L. Hsu, L. Gruner-Nielsen, K. Dreyer, and J. E. Johnson. 320-Gb/s single-channel pseudo linear transmission over 200km of nonzero-dispersion fiber. IEEE Photon. Technol. Lett., vol. 12, no. 10, 2000: pp. 1400–1402.

[64] L. J. Richardson, W. Forysiak, and K. J. Blow. Single channel 320Gbit/s short period dispersion managed transmission over 6000km. Electron. Lett., vol. 36, no. 24, 2000: pp. 2029-2030.

[65] C. Lorattanasane and K. Kikuchi. Design theory of long-distance optical transmission systems using midway optical phase conjugation. J. Lightwave Technol., vol. 15, 1997: pp. 948-955.

[66] H. C. Lim, F. Futami, K. Taira, and K. Kikuchi. Broad-band mid-span spectral inversion without wavelength-shift of 1.7-ps optical pulses using a highly-nonlinear fiber Sagnac interferometer. IEEE Photon. Technol. Lett., vol. 11, 1999: pp. 1405-1407.

[67] H. C. Lim and K. Kikuchi. A filter-free scheme for orthogonally-pumped, polarization-insensitive optical phase conjugation of broad-band optical signals. IEEE Photon. Technol. Lett., vol. 13, no. 5, 2001: pp. 481-483.

[68] F. Matera, A. Mecozzi, M. Romagnoli and M. Settembre. Sideband instability induced by periodic power variation in long distance fiber links. Opt. Lett., 18, 1993: pp. 1499-1501.

[69] A. Taflove. Computational Electrodynamics The Finite-Difference Time-Domain Method: Boston, London, Artech House, 1995.

[70] Y. Yuan, R. Jambunathan, J. Singh, and P. Bhattacharya. Finite-difference time-domain analysis and experimental examination of the performance of a coupled-cavity MQW laser/active waveguide at 1.54 μ m. IEEE J. Quantum electron., vol. 33, 1997: pp. 408-415.

[71]J. Shibayama, T. Takahashi, J. Yamauchi, and H. Nakano. Efficient time-domain finite-difference beam propagation methods for the analysis of slab and circularly symmetric waveguides. IEEE/OSA J. Lightwave Technol., vol. 18, 2000: pp. 437-442.

[72] S. Nakamura, Y. Koyamada, N. Yoshida, N. Karasawa, H. Sone, M. Ohtani, Y. Mizuta, R. Morita, H. Shigekawa, and M. Yamashita. Finite-difference Time-domain calculation with all parameters of Sellmeier's fitting equation for 12-fs laser pulse propagation in a silica fiber. IEEE Photon. Technol. Lett., vol. 14, 2002: pp. 480-482.

[73] M. Ohashi, K. shiraki, and K. Tajima. Optical loss property of single-mode fiber. J. Lightwave Technol., vol. 10, 1992: pp. 539-543.

[74] G. P. Agrawal. Nonlinear pulse distortion in single-mode optical fibers at the zero-dispersion wavelength. Phys. Rev. A, vol. 33, 1986: pp. 1765-1776.

[75] R. S. Tucker, G. Eisenstein, and S. K. Corotky. Optical time-division multiplexing for very high bit-rate transmission. J. Lightwave Technol., vol. 6, 1988: pp. 1737-1749.

[76] E. Lichtman, R. G. Waarts, and A. A. Friesem. Stimulated Brillouin Scattering excited by a modulated pump wave in single-mode fibers. J. Lightwave Technol., vol. 7, 1988: pp. 171-174.

[77] W. L. Barnes, S. B. Poole, J. E. Townsend, L. Reekie, D. J. Taylor, and D. N. Payne. Er^{3+}-Yb^{3+} and Er^{3+}-doped fiber lasers. J. Lightwave Technol., vol. 7, 1989: pp. 1461-1465.

[78] K. Smith, J. R. Armitage, R. Wyatt, N. J. Doran, and S. M. J. Kelly. Erbium-doped fiber soliton laser. Electron. Lett., vol. 26, 1990: pp. 1149-1151.

[79] M. Nakazawa, Y. Kimura, and K. Suzuki. Ultralong dispersion-shifted erbium doped fiber amplifier and its application to soliton transmission. IEEE J. Quantum Electron., vol. QE-26, 1990: pp. 2103-2108.

[80] L. F. Mollenauer, M. J. Neubelt, S. G. Evangelides, J. P. Gordon. J. R. Simpson and L. G. Cohen. Experimental study of soliton transmission over more than 10000km in dispersion-shifted fiber. Opt. Lett., vol. 15, 1990: pp. 1203-1205.

[81] L. F. Mollenauer, B. M. Nyman, M. J. Neubelt, G. Raybon, and S. G. Evangelides. Demonstration of soliton transmission at 2.4Gbit/s over 12000km. Electron. Lett., vol. 27, 1991: pp. 178-179.

[82] K. Inoue. Four-wave mixing in an optical fiber in the zero-dispersion wavelength region. J. Lightwave Technol., vol. 10, 1992: pp. 1553-1561.

[83] R. H. Stolen and J. E. Bjorkholm. Parametric amplification and frequency conversion in optical fibers. IEEE J. Quantum Electron., vol. QE-18, 1982: pp. 1062-1071.

[84] Inoue, H. Toba, and K. Oda. Influence of fiber four-wave mixing in multichannel FSK heterodyne envelope detection transmissions. J. Lightwave Technol., vol. 10, 1992: pp. 350-360.

[85] R. W. Tkach, A. R. Chaplyvy, F. Forghieri, A. H. Gnauck, and R. M. Derosier. Four-photon mixing and high-speed WDM systems. J. Lightwave Technol., vol. 13, 1995: pp. 841-849.

[86] J. P. Gordon and L. F. Mollenauer. Phase noise in photonic communications systems using linear amplifiers. Opt. Lett., vol. 15, 1990: pp. 1351-1353.

[87] D. Marcuse. Bit-error rate of lightwave systems at the zero dispersion wavelength. J. Lightwave Technol., vol. 9, 1991: pp. 1330-1334.

[88] S. Ryu. Signal linewidth broadening due to fiber nonlinearities in long-haul coherent optical fiber communication systems. Electron. Lett., vol. 27, 1991: pp. 1527-1529.

[89] M. Murakami and S. Saito. Evolution of field spectrum due to fiber-nonlinearity-induced phase noise in in-line optical amplifier systems. IEEE Photon. Technol. Lett., vol. 4, pp. 1269-1272, 1992: pp. 1269-1272.

[90] S. Ryu. Signal linewidth broadening due to nonlinear Kerr effect in long-haul coherent systems using cascaded optical amplifiers. J. Lightwave Technol, 1992: pp. 1450-1457.

[91] S. Ryu. Change of field spectrum of signal light due to fiber nonlinearities and chromatic dispersion in long-haul coherent systems using in-line optical amplifiers. Electron. Lett., vol. 28, 1992: pp. 2212-2213.

[92] K. Kikuchi. Enhancement of optical-amplifier noise by nonlinear refractive index and group-velocity dispersion of optical fibers. IEEE Photon. Technol. Lett., vol. 5, 1993: pp. 221-223.

[93] C. Lorattanasane and K. Kikuchi. Parametric instability of optical amplifier noise in long-distance optical transmission systems. IEEE. J. Quantum Electron., vol. 33, 1997: pp. 1068-1074.

[94] W. H. Press, S. A. Teukolsky, W. T. Vettering, and B. P. Flannery Numerical Recipes in C: The art of scientific computing: 2nd Ed., New York, Cambridge University Press, 1992.

[95] S. Watanabe and M. Shirasaki. Exact compensation for both chromatic dispersion and Kerr effect in a transmission fiber using optical phase conjugation. J. Lightwave Technol., vol. 14, 1996: pp. 243-248.

[96] R. W. Tkach, A. R. Chaplyvy, F. Forghieri, A. H. Gnauck, and R. M. Derosier. Four-photon mixing and high-speed WDM systems. J. Lightwave Technol., vol. 13, 1995: pp. 841-849.

[97] N. Kikuchi, K. Sekine, and S. Sasaki. Analysis of cross-phase modulation (XPM) effect on WDM transmission performance. Electron. Lett., vol. 33, 1997: pp. 653-654.

[98] D. Marcuse. Single-channel operation in very long nonlinear fibers with optical amplifiers at zero dispersion. J. Lightwave Technol., vol. 9, 1991: pp. 356-361.

[99] N. Kikuchi and S.Sasaki. Fiber nonlinearity in dispersion-compensated conventional fiber transmission. Electron. Lett., vol. 32, 1996: pp. 570-572.

[100] R. J. Nuyts, Y. K. Park, and P. Gallion. Dispersion equalization of a 10Gbit/s repeatered transmission system using dispersion compensating fibers. J. Lightwave Technol., vol. 15, 1997: pp. 31-41.

[101] M. Murakami, T. Matsuda, H. Maeda, and T. Imai. Long-haul WDM transmission using higher order fiber dispersion management. J. Lightwave Technol., vol. 18, no. 9, 2000: pp. 1197-1204.

[102] M. Murakami, K. Suzuki, H. Maeda, T. Takahashi, A. Naka, N. Ohkawa, and M. Aiki. High speed TDM-WDM techniques for long-haul submarine optical amplifier systems. Optic. Fiber Technol., vol. 3, no. 4, 1997: pp. 320-338.

[103] N. S. Bergano, C. R. Davidson, M. A. Mills, P. C. Corbett, R. Menges, J. L. Zyskind, J. W. Shulhoff, A. K. Srivastava, and C. Wolf. Long-haul transmission using 10Gb/s channels: 160Gb/s(16x10Gb/s) 6000km demonstration. Proc. OAA'97: Postdeadline paper PD-9.

[104] T. Naito, N, Shimojoh, T. Tanaka, H. Nakamoto, M. Doi, T. Ueki, and M. Suyama, " 1 Terabit/s WDM transmission over 10,000km. Proc. European Conf. on Opt. Commun. (ECOC'99). Nice France, Sept. 26-30, 1999, PD2-1: pp. 24-25.

[105] F. M. Madani and K. Kikuchi. Design theory of long-distance WDM dispersion-managed transmission system. J. Lightwave Technol., vol. 17, 1999: pp. 1326-1335.

[106] K. Tanaka, T. Tsuritani, N. Edagawa, and M. Suzuki. 320Gbit/s (32x10.7Gbit/s) error-free transmission over 7,280km using dispersion flattened fiber link with standard SMF and slope compensating DCF. Proc. ECOC'1999, Nice, France, Sep. 26-30, 1999: pp. II-180-181

[107] T. Tsuritani, N. Takeda, K. Imai, K. Tanaka, A. Agata, I. Morita, H. Yamauchi, N. Edagawa, and M. Suzuki. 1Tbit/s (100x10.7Gbit/s) transoceanic transmission using 30nm-wide broadband optical repeaters with Aeff -

enlarged positive dispersion fibre and slope-compensating DCF. Proc. European Conf. on Opt. Commun. (ECOC’99), Nice France, Sept. 26-30, 1999, PD2-1: pp. 38-39.

[108] H. Nakamoto, T. Tanaka, N. Shimojoh, T. Naito, I. Yokota, A. Sugiyama, T. Ueki, and M. Suyama. 1.05Tbit/s WDM transmission over 8,186km using distributed Raman amplifier repeaters. Proc. Opt. Fiber Comm. (OFC’2001), Anaheim, CA, Mar. 17-22, 2001: paper TuF6

[109] E. Shibano, S. Nakagawa, T. Kawazawa, H. Taga, and K. Goto. 96x11.4Gbit/s transmission over 3,800km using C-band EDFA and non-zero dispersion shifted fiber. Proc. Opt. Fiber Comm. (OFC’2001), Anaheim, CA, Mar. 17-22, 2001: paper TuN2

[110] C. Kurtzke and K. Peterman. Impact of fiber four-photon mixing on the design of n-channel megameter optical communication systems. Proc. Opt. Fiber Comm. (OFC’93), San Jose, CA, Feb. 21-26, 1993: paper FC3.

[111] C. Kurtzke. Suppression of fiber nonlinearities by appropriate dispersion management. IEEE Photon. Technol. Lett., vol. 5, no. 10, 1993: pp. 1250–1253.

[112] K. Kikuchi, C. Lorattanasane, F. Futami, and S. Kaneko. Observation of quasi-phase matched four-wave mixing assisted by periodic power variation in a long-distance optical amplifier chain. IEEE Photon. Technol. Lett., vol. 7, no. 11, 1995: pp. 1378–1380.

[113] N. J. Smith and N. J. Doran. Modulation instability in fibers with periodic dispersion management. Opt. Lett., vol. 21, 1996: pp. 570-572.

[114] T. Okano, T. Ooishi, T. Kato, Y. Yokoyama, M. Yoshida, Y. Takahashi, Y. Makio, and M. Nishimura. Optimum dispersion of non-zero dispersion shifted fiber for high bit rate DWDM systems. Proc. Opt. Fiber Comm. (OFC’2001), Anaheim, CA, Mar. 17-22, 2001: paper TuH4

[115] P. Kaewplung, T. Angkaew, and K. Kikuchi. Simultaneous suppression of third-Order dispersion and sideband instability in single-channel optical fiber transmission by midway optical phase conjugation systems employing higher-order dispersion management. IEEE/OSA J. Lightwave Technol., vol. 21, no. 6, 2003: pp. 1465-1473.

[116] C. J. Rasmussen. Simple and fast method for step size determination in computations of signal propagation though nonlinear fibres. Proc. Opt. Fiber Comm. (OFC'2001), Anaheim, CA, Mar. 17-22, 2001: paper WDD29-1.

[117] P. Kaewplung, T. Angkaew. 200-Gbit/s, 10,000-km single-channel transmission by midway OPC system using distributed Raman amplifiers. Proc. Opto-Electronic Communication Conference (OECC'2003), Shianghai, China, October 13-16, 2003.

[118] M. N. Islam. Raman amplifiers for telecommunications. IEEE J. Selected Topics in Quantum Electron., vol. 8, no. 3, 2002: pp. 548-559.

[119] D. Bayart, P. Baniel, A. Bergonza, J. Y. Boniort, P. Bousselet, L. Garca, D. Hamoir, F. Lepringard, A. L. Sauza, P. Nouchi, F. Roy, and P. Sillard. Broadband optical fiber amplification over 17.7 THz range. Electron. Lett., vol. 36, 2000: pp. 1569-1671.

[120] T. N. Nielsen, A. J. Stents, K. Rottwitt, D. S. Vengsarkar, Z. J. Chen, P. B. Hansen, J. H. Park, K. S. Feder, S. Cabot, S. Stulz, D. W. Peckham, L. Hsu, C. K. Kan, A. F. Judy, S. Y. Park, L. E. Nelson, and L. G. Nielsen. 3.28-Tb/s transmission over 3 x 100 km of nonzero-dispersion fiber using dual C- and L-band distributed Raman amplification. IEEE Photon. Technol. Lett., vol. 12, pp. 1079–1081, 2000.

[121] H. Nakamoto, T. Tanaka, N. Shimojoh, T. Naito, I. Yokota, A. Sugiyama, T. Ueki, and M. Suyama. 1.05Tbit/s WDM transmission over 8,186km using distributed Raman amplifier repeaters. Proc. Opt. Fiber Comm. (OFC'2001), Anaheim, CA, Mar. 17-22, 2001: paper TuF6.

[122] E. A. Kunarajah, J. J. Lepley, and A. S. Sidiqui. An accurate numerical model for distributed Raman amplifiers. Proc. 27th Eur. Conf. on Opt. Comm. (ECOC'01), Amsterdam, Denmark, 2001: paper Tu.L.3.6.

[123] H. Kidorf, K. Rottwitt, M. Nissov, M. Ma, and E. Rabarijaona. Pump interactions in a 100-nm bandwidth Raman amplifier. IEEE Photon. Technol. Lett., vol. 11, 1999: pp. 530–532.

[124] V. E. Perlin and H. G. Winful. Optimal design of flat-gain wide-band fiber Raman amplifiers. IEEE J. Lightwave Technol., vol. 20, 2002: pp. 250-254.

[125] V. E. Perlin and H. G. Winful. On distributed Raman amplification for ultrabroad-band long-haul WDM systems. IEEE J. Lightwave Technol., vol. 20, 2002: pp. 409-416.

[126] J. Yamauchi, J. Shibayama, and H. Nakano. Modified finite-difference beam propagation method based on the generalized Douglas scheme for variable coefficients. IEEE Photon. Technol. Lett., vol. 7, 1995: pp. 661–663.

[127] J. Yamauchi, J. Shibayama, O. Saito, O. Uchiyama, and H. Nakano. Improved finite-difference beam-propagation method based on the generalized Douglas scheme and its application to semivectorial analysis. IEEE J. Lightwave Technol., vol. 14, 1996: pp. 2401-2406.

[128] Y. Aoki, K. Tajima, and I. Mito. Input power limits of single-mode optical fibers due to stimulated Brillouin scattering in optical communication systems. J. Lightwave Technol., vol. 6, 1988: pp. 710-719.

[129] D. A. Fishman and J. A. Nagel. Degradations due to stimulated Brillouin scattering in multigigabit intensity-modulated fiber-optic systems. J. Lightwave Technol., vol. 11, 1993: pp. 1721-1728.

[130] G. P. Agrawal. Applications of Nonlinear Fiber Optics.: New York, Academic Press, 2001.

APPENDIX

PUBLICATIONS

International Periodical Journals

1. P. Kaewplung, T. Angkaew, and K. Kikuchi, “ Feasibility of 100-Gb/s 10,000-km single-channel optical transmission by midway optical phase conjugation incorporated with third-order dispersion compensation, ” *IEEE Photon. Technol. Lett*., vol. 13, no. 4, pp. 293–295, 2001.
2. P. Kaewplung, T. Angkaew, and K. Kikuchi, “ Complete analysis of sideband instability in chain of periodic dispersion-managed fiber link and its effect on higher-order dispersion-managed long-haul wavelength division multiplexed systems, ” *IEEE/OSA J. Lightwave Technol.*, vol. 20, no. 11, pp. 1895-1907, 2002.
3. P. Kaewplung, T. Angkaew, and K. Kikuchi, “ Simultaneous suppression of third-Order dispersion and sideband instability in single-channel optical fiber transmission by midway optical phase conjugation systems employing higher-order dispersion management, ” *IEEE/OSA J. Lightwave Technol.*, vol. 21, no. 6, pp. 1465-1473, 2003.

International Conference Proceedings

1. P. Kaewplung, T. Angkaew, and K. Kikuchi, “ Sideband instability in the presence of periodic power variation and periodic dispersion management, ” in *Proc. OSA Optical Fiber Communication conference (OFC’2001),* Anaheim, CA, Mar. 17-22, 2001, paper WDD32.
2. P. Kaewplung, T. Angkaew, and K. Kikuchi, “ 200-Gbit/s, 10,000-km single-channel transmission by midway OPC system using distributed Raman amplifiers, ” *in Proc. Opto-Electronic Communication Conference (OECC’2003),* Shianghai, China, October 13-16, 2003.
3. P. Kaewplung, T. Angkaew, and K. Kikuchi, “ Finite-difference time-domain computation of pulse propagation in relatively long nonlinear optical fiber, ” *in Proc. IEEE Asia-Pacific Communication Conference (APCC’2003),* Penang, Malaysia, September 21-24, 2003.

Domestic Conference Proceedings

1. P. Kaewplung, T. Angkaew, and K. Kikuchi, " Effect of sideband instability on long-haul DWDM optical fiber transmission systems employing higher-order dispersion management (Best paper award), " *in Proc. of 25th Electrical engineering conference (EECON25)*, 21-22 Nov 2002, Hadyai, Songkla, Thailand.
2. P. Kaewplung, T. Angkaew, and K. Kikuchi, " Simultaneous suppression of third-Order dispersion and sideband instability in long-haul ultra-High speed midway optical phase conjugation systems using higher-order dispersion management, " *in Proc. of 25th Electrical engineering conference (EECON25)*, 21-22 Nov 2002, Hadyai, Songkla, Thailand.
3. P. Kaewplung, T. Angkaew, and K. Kikuchi, "Feasibility of 200-Gbit/s, 10,000-km single-Channel optical fiber transmission using midway optical phase conjugation incorporated with third-order dispersion compensation and distributed Raman amplification, " *in Proc. of 26th Electrical engineering conference (EECON26)*, 6-7 Nov 2003, Chaum, Petchburi, Thailand.

Award

1. BEST PAPER AWARD of telecommunication engineering session in *25th Electrical engineering conference (EECON25)*, 23-24 Nov 2000, Hadyai, Songkla, Thailand under the topic: " Effect of Sideband Instability on Long-haul DWDM Optical Fiber Transmission Systems Employing Higher-Order Dispersion Management

BIOGRAPHY

Pasu Kaewplung was born in Bangkok, Thailand, in December 1971. He received B.S. and M.S. degrees in electrical engineering from Yokohama National University, Yokohama, Japan, in 1996 and 1998, respectively. From April 1998 to March 2000, he had been doing research in Research Center for Advanced Science and Technology (RCAST) at the University of Tokyo, Japan. In April 2000, he joined the Department of Electrical Engineering as a Lecturer at Chulalongkorn University, Bangkok, Thailand. He is also currently pursuing the Ph.D. degree in electrical engineering at Chulalongkorn University.

His research activities have been devoted to long-distance large-capacity optical fiber transmission systems, dispersion compensations, and the applications of nonlinear optical effects.